Through-Thickness Compression Testing and Theory of Carbon Fibre Composite Materials

A thesis submitted to the University of Manchester for the degree of

Doctor of Philosophy

in the Faculty of Engineering and Physical Sciences

2011

Luke Francis Thompson

School of Mechanical, Aerospace and Civil Engineering

List of Contents

Word Count: 68,358

Nomenclature

Abbreviations

2-D	Two dimensional
3-D	Three dimensional
ASTM	American Society for Testing and Materials
Ave	Average
CFRP	Carbon fibre reinforced polymer
CLT	Classical laminate theory
C_v	Coefficient of variation
DERA	Defence Evaluation and Research Agency
FE	Finite element
FEA	Finite element analysis
FRP	Fibre reinforced polymer
Max	Maximum
Min	Minimum
PAN	Polyacrylonitrile (carbon fibre basis)
QI	Quasi-isotropic
RTM	Resin transfer moulding
RVE	Repeating volume element
TLR	Translaminar reinforcement
UD	Unidirectional
V_f^f	Fibre volume fraction
V_f^m	Matrix volume fraction
V_f^z	Z-pin volume fraction

Material Characteristics

E_i	Young's modulus in the *i* direction
v_{ij}	Poisson's ratio in the *ij* plane
G_{ij}	Shear modulus in the *ij* plane
σ_i	Direct stress in the *i* direction
τ_{ij}	Shear stress in the *ij* plane
ε_i	Direct strain in the *i* direction
γ_{ij}	Shear strain in the *ij* plane
$[C]$	Stiffness matrix
$[S]$	Compliance matrix
C_0^*	Walpole's overall constraint tensor
κ_0	Walpole's comparison material bulk modulus
μ_0	Walpole's comparison material shear modulus
c_r	Walpole's constituent volume fraction notation
$[T]$	Coordinate transformation matrix
$[Q]$	Lamina stiffness matrix
x, y, z	Global coordinates
1, 2, 3	Lamina coordinates
u, v, w	Global displacements in the *x*, *y* and *z* directions respectively

Other Symbols

K	Gauge factor (strain gauge)
R	Electrical resistance
V_{out}	Output voltage
V_{in}	Input voltage
σ_{sd}	Standard deviation
μ_{m}	Mean

List of Tables

Appendices

List of Figures

Chapter 1

Chapter 2

Chapter 3

Chapter 4

Chapter 5

Chapter 6

Chapter 7

Chapter 8

Appendices

Abstract

This study investigates the through-thickness behaviour of carbon/epoxy laminates. A through-thickness compression test regime was conducted utilising three specimen designs, which are waisted, hollow cylindrical and cubic specimens. An assessment and comparison of each specimen is given regarding their advantages and disadvantages in characterising the through-thickness response of $[+45/-45/90/0]_s$ quasi-isotropic AS4/8552 carbon/epoxy laminates.

A finite element (FE) study of the three specimens is presented which results in specimen geometries that provided a macroscopically uniform stress response throughout the gauge length whilst also minimising other features such as stress concentrations. Further to the final geometries being presented, the method of manufacture for the laminate and machining processes for each of the specimens is given.

A mesoscopic FE study is presented relating to the free-edge effects induced by through-thickness loading in quasi-isotropic laminates. The results presented show that free-edge effects will be present in the test specimens and will have a larger overall impact on the hollow cylindrical specimen. The free-edge effects also increase the stress concentrations present in the corners of the waisted and cubic specimens.

Characteristic stress strain curves are presented for each specimen with strain data taken from post yield strain gauges attached to the specimens. The extracted initial Young's modulus E_z and Poisson's ratios v_{zx} and v_{zy} show a small variation between specimens. The strength values for the three specimens vary greatly with the waisted specimen being the strongest and cylindrical specimen the weakest, indicating that the chosen specimen geometry dominates failure. The experimental data will be used for test case 12 in the Second World Wide Failure Exercise (WWFE-II).

A study is presented to predict the effective elastic properties of Z-pinned laminates. The materials under consideration are UD and $[0/90]_s$ cross-ply AS4/3501-6 carbon/epoxy laminates. Estimates on the effective properties are provided by two FE approaches and two analytical bounding approaches; namely Voigt and Reuss bounds and Walpole's bounding theory. The two FE approaches are based on extreme assumptions about the in-plane fibre volume fraction in the presence of Z-pins and provide a tight range of values in which the real result should lie. Furthermore, whilst the bounding methods are simple and in the case of Young's moduli produce very wide bounds the selection of the suitable bound result can lead to a good estimate in comparison with the FE data. Typically the best bounding method result for each elastic property is within 10% of the FE predictions.

Declaration

No portion of the work referred to in this thesis has been submitted in support of an application for another degree or qualification of this or any other university or other institute of learning.

Copyright

Acknowledgments

First of all I would like to thank all of the people at the University of Manchester who have helped me through the course of this project. Particular thanks must go Fahad Almeskari with whom I have shared many academic and theological debates. I shall sincerely miss our ‘discussions’.

Of all the people at the university my biggest thanks must go to my Supervisor, Shuguang Li. His support, guidance and technical knowledge have been invaluable during this project and his enthusiasm has never failed to cheer me up, even at the worst of times.

I must also extend thanks to the EPSRC and QinetiQ for kindly providing financial support and in particular I would like to thank Sam Kaddour from QinetiQ. He has provided great insights into various aspects of composite materials and his hard work on the World Wide Failure Exercise never fails to astound me. I must also thank Mike Hinton and Paul Smith for allowing me to join them, along with Shuguang and Sam at World Wide Failure Exercise meetings. Despite the very early morning drives to London and Surrey, I have thoroughly enjoyed my time with the WWFE guys and can only hope that I have helped them with their valuable work. It has been a pleasure to be involved with the project.

I would also like to express my appreciation to all of my family and friends. I have to thank Liam and Chris, with whom I shared a house during the project, for providing constant comic relief. Maybe one day we’ll get to Laos, Chad and Denmark!

A great deal of thanks must also go to my girlfriend Clare. She has always been there when I’ve called on her and I can only thank her for her great patience with me over the last few years.

Finally I must thank my brother Greg for all of his support and also my mother Liesje. No matter when or where, I know I can always rely on these two people to help me out.

1 Introduction

1.1 Background

1.1.1 Composite Materials

Composites are created by combining two or more constituents to form a solid material and are designed to take the benefits of the constituent phases, for example; weight, strength or cost. Many different materials are used to make composites including traditional use of wood (a natural composite), mud and straw, concrete and additives such as steel as well as more 'modern' composite materials such as fibre glass or carbon fibre.

There are various types of modern composite material many of which have a polymer matrix and some sort of inclusion. Most commonly modern composites are classed in the three following ways:

- Particulate
- Sandwich
- Fibre

Particulate composites have been used in a wide array of applications such as buildings, structures and in the aerospace industry. Generally it is reported that particulate composites are utilised as a money saving exercise. Although this is very common these composites are also designed with overall material properties in mind and in certain cases cost is not the main consideration. Particulate composites can be made from a wide variety of constituents. These particulates can be manmade, such as coated calcium carbonate, glass or polymers; or natural inclusions such as stone or diamond.

Sandwich composites are used as building materials, for furniture and have been used in engineering applications in areas such as aerospace. Generally sandwich composites are comprised of a light weight core such as a honeycomb structure, foam or balsa wood. The core is then covered in a facing or skin which is usually stiffer than the core. Materials such as fibre reinforced composites, metal and wood are typically used as facing layers. Sandwich composites are designed for

strength with the system acting like an I-beam construction. The facings prevent bending of the material and can take in-plane loading while the core improves the compressive loading response and can help improve impact absorption.

Fibre reinforced composites can be split into two main groups:

- Short fibres
- Long/continuous fibres

Short fibre composites are commonly, but not always, manufactured using E-glass (electrical grade) fibres a few millimetres long (although many other materials are used). Short fibre composites do not offer the same mechanical advantages as continuous fibre composites such as high specific modulus and high specific strength. However, if the short fibres are aligned they can provide the composite with better mechanical properties than each individual constituent provides. A major advantage of short fibre composites over continuous fibre materials is that they are more easily mass-produced. Various systems, including both thermosetting and thermoplastic matrix composites, can be injection moulded along with short fibres which is not possible for continuous fibre composites.

Long/continuous fibre composites have the distinct advantage over short fibre systems in that they can be designed to meet the specific requirements of a product in terms of stiffness and weight. This makes continuous fibre composites an excellent tool for designers as it enables them to design highly efficient structures. These advantages come at a cost, however, since continuous fibre composites can be very expensive to produce. Due to their extensive use in industry and the need for more information, the work for this study focuses on long fibre reinforced composites.

1.1.2 Long Fibre Reinforced Polymers

Fibre Reinforced Polymer (FRP) composites were developed 50-60 years ago with military applications the first major beneficiaries of the newly designed materials. Carbon Fibre composites also played a large role in the space race of the ‘60s. Traditionally people perceive FRPs to be used for their strength and weight and whilst this is true in this instance, one of the main reasons for the use of

carbon fibre was also its thermal conductivity properties. On re-entry to the Earth's atmosphere the craft has to withstand immense heat. During this time the resin on the outer surface will burn off with lots of heat being expelled during this process. The material below the surface is then protected from the heat and so the craft can return safely to Earth.

From the 1970s and '80s composites were beginning to be used extensively in commercial aircraft from large manufacturers such as Airbus, Antonov and Boeing. In more recent years the media have increasingly picked up on the use of composite materials in aerospace applications. The Airbus 'A380' caught the public's imagination due to its sheer size and the Boeing '787 Dreamliner' was marketed as being a sleek, new and completely modern aircraft. In both cases, the media paid particular attention to the lightweight composite materials that made up large sections of these new aircraft structures.

Much media coverage has also been given to the race for commercial space tourism. One of the leading efforts is that of Virgin Galactic. The craft Virgin Galactic is using, WhiteKnightTwo and SpaceShipTwo, built by Scaled Composites, received huge amounts of media coverage. One of the primary reasons for this coverage is the bodies and structures of both craft are made entirely from composite materials.

Use of FRPs has long since deviated from just aerospace applications. Boat hulls have long been constructed using fibrous composite materials. Fibreglass composites have been used extensively in boat building for some time and in the last 20 years carbon and Kevlar composites have started to be used more and more due to their increased stiffness and lightness compared to traditional materials.

It is widely recognised that many racing cars are constructed using carbon fibre composites and their current safety record is very good owing to the materials used and design considerations. Composites have also been widely used in pieces of sports equipment such as golf clubs, rackets, kayaks, bicycles and many more. All of these uses have helped composites become a viable and leading material choice for many new applications prompting much further research and investment in the industry.

1.1.2.1 Fibre Reinforced Polymer Manufacture

There are various ways in which long fibre composite materials can be manufactured. The manufacture process chosen depends largely on the product being made. When designing for structural applications designers often start with continuous fibre composites. The manufacture of these materials requires processes which can apply the material accurately to gain the desired benefits by placing the fibres in specific orientations.

Common products manufactured with FRPs include pipes, fuel tanks, rocket casings, drive-shafts, ballistics launchers and structural supports. The link between all of these applications is that they have a cylindrical cross section. The easiest method of producing these shapes is by a process known as *filament winding*. In this process a shell structure is created by wrapping a fibre around a mandrel to create a cylindrical structure. The fibre orientation can be altered by controlling the rotation of the mandrel and speed of the fibre feeding device.

In the filament winding process there are two clear methods of applying the matrix material. The first is through wet winding and the second is through the use of pre-impregnated strips of the material (pre-pregs). During the wet winding method fibres are pulled through a bath or over a roller containing liquid resin. The fibres are then placed onto the mandrel. When using pre-pregs the pre-preg tape is first run through a heater to make the polymer 'mobile' and then the tape is applied to the mandrel. This heating process means that in general using pre-pregs for filament winding is a slower process than wet winding. The filament winding process can also be used to make more complex shapes by using machines such as a five axis winding machine. This allows for features to be created along the cylinder and can be used to create products such as prosthetic limbs.

Pultrusion is a further method of manufacture and is similar to extrusion used for forming plastics and metals. Generally this method produces unidirectional (UD) continuous fibre products although it is possible to include other orientations and fabrics. Through this process it is possible to create mostly structural components such as I, L and U-beams, cylinders, and bars. These cross-sections are pultruded and then cut to the correct length.

One of the classic methods of FRP manufacture is the *hand layup* process. In this process a release surface is placed onto a mould and resin is placed on top of this. The reinforcing material (which can be in various forms e.g. cloth or random fibres) is placed onto the resin and a roller is used to remove the excess resin. Many layers can be built up until the desired material layup is reached. The composite is cured and removed from the mould. This process has the advantage that irregular shapes can be made with varying layups and reinforcing materials used but it is also very labour intensive and the reinforcement content of the final product is generally low (20-35% by volume) which means that reinforcement advantages are limited compared to other production techniques.

Other common manufacturing processes for FRPs are moulding processes such as *vacuum bag moulding*, *autoclave moulding*, *die moulding* and *resin transfer moulding*(RTM). The first three processes mostly use pre-preg materials placed into or on a mould and the material is cured under pressure. In die moulding the pressure is applied by male and female die plates whereas in vacuum bag moulding and autoclave moulding pressure is applied by means of a vacuum with autoclave moulding being able to produce parts with greater fibre volume fractions compared to vacuum bag moulding. These processes are used extensively in the aerospace and automotive industries. Resin transfer moulding is similar to die moulding but the fibres are preformed to the desired shape. This allows the component to be formed under relatively low pressures which in turn allows the moulds to be made from cheaper materials than in die moulding.

Long fibre composites can be very expensive to produce due to the complex design and manufacture processes involved with these materials. However, the ability to design highly efficient structures in terms of their size to weight ratio has ensured that FRPs are a widely used choice of material in many industries.

1.1.2.2 Carbon Fibre

This study analyses the through-thickness behaviour of carbon/epoxy laminates and a brief history of carbon fibre is presented here. The first known carbon fibres were produced by Thomas Edison in the 1890s[1]. These were

created by carbonising natural materials such as bamboo and their first use was for filaments in electric light bulbs. It was soon found that carbon fibres did not have a long lifespan as a filament for light bulbs and they were soon forgotten. Carbon fibre as we know it today was first developed in the late 1950s. The first fibres had relatively low strength values but due to their potential, further research was conducted. Eventually fibres were fabricated with high strength at Rolls Royce and the Royal Aircraft Establishment in Farnborough, UK. These were created using polyacrylonitrile (PAN) as a raw material and is the most common method of producing high modulus carbon fibres (other methods of carbon fibre manufacture exist). The raw material is drawn into a fibre and heated under tension and then going through various heat treatments it obtains a strong molecular structure.

Carbon fibres are similar to graphite; in a single carbon crystal the atoms are in the form of hexagonal arrays and are held together with very strong covalent bonds. Different planes are linked with weak van der Waals bonds. In graphite the layers remain relatively flat and hence the material 'slips' quite easily, meaning a graphite fibre is relatively weak in the axial direction. A schematic of the arrangement of carbon atom basal planes is shown in Figure 1.1 and it can be seen that the layers are packed irregularly. This irregularity prevents layers from 'slipping' resulting in a material with very high axial strength which is exploited in Carbon Fibre Reinforced Polymers (CFRP).

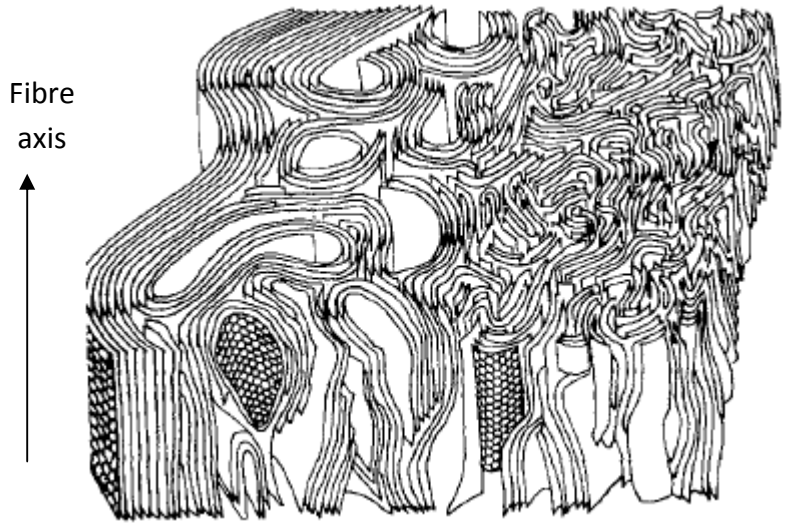

Figure 1.1: Schematic image of the structure of a carbon fibre [2]

1.2 Scope of the Thesis

1.2.1 Through-Thickness Testing of Carbon Fibre Reinforced Composites

Traditionally, composite materials have been used for minor applications in larger structures, for example as a covering or as a filler material. However, as understanding of the materials has increased it is being used more for primary structures. This can most evidently be seen in the aerospace industry where Boeing and Airbus have created the 787 Dreamliner (Boeing) and the A380 and A400M (Airbus); the wing and box sections in particular are now made using entirely composite constructions (replacing traditional metallic constructions). Due to this increased use of composite materials it is important that engineers have the most up to date test data and material characteristics data to work with. Modern finite element codes rely on input values to provide a reliable material response and hence many design applications also rely on these reliable material data.

As well as material properties there is also a call for accurate material behaviour/strength predictions for composites. In order to help assess the current state of composite failure theories the Second World Wide Failure Exercise (WWFE-II) was set up[3]. This exercise will compare various failure theories with benchmark triaxial test data. Due to a lack of data available to the organisers of WWFE-II a through-thickness compression test regime will be carried out here to provide data for test case 12 of WWFE-II.

Chapters 2, 4, 5, 6 and 7 of this thesis will look at composites testing and will focus in particular on through-thickness compression testing of carbon fibre reinforced polymers (CFRPs). Existing works will be examined and their merits and pitfalls discussed. The objective is to explore the most suitable test methods for observing the through-thickness behaviour of CFRPs. The results from the testing (including that to be used in WWFE-II) will be presented and discussed with attention paid to the repeatability of the tests in order that an optimal specimen can be recommended for future testing.

An extensive FE analysis is presented in conjunction with the test regime in order to optimise the specimen geometries before testing. The FE analysis is also used to assess any practical issues to do with the specimens selected. Furthermore, FE analysis is used to observe the presence of free-edge effects within the gauge length of the specimens with conclusions drawn as to the impact of these stresses.

1.2.2 Property Prediction for Three Dimensional (Z-pinned) Composites

As the use of composite materials grows and the application of these materials becomes more complex the design of the materials also advances. One of the advancements to traditional FRPs is the use of through-thickness reinforcement in the form of tufts and Z-pins. When advancements like this are made the current analysis techniques must be examined to assess their relevance to these new materials.

Chapters 3 and 8 of this thesis will examine three dimensional composites: what are they and how are they analyzed. For this study the emphasis is on the prediction of the elastic properties of Z-pinned CFRPs. Classic Voigt and Reuss bounds are presented as well as Walpole's bounds to assess their suitability for analysing these materials. Furthermore, the cases examined are also analysed using an existing semi-homogeneous FE modelling technique as well as a new set of models based on a mesoscopic approach. Assumptions are presented on the role of the in-plane fibres in the Z-pin region demonstrating the importance of this parameter.

Conclusions are drawn as to the features of each of the FE models and how these features affect the property predictions. The FE results are compared to the bounding methods' results to demonstrate the effectiveness of the analytical methods.

2 Through-Thickness Testing of Fibre Reinforced Composites

The through-thickness testing carried out in this thesis relates to pure through-thickness compression after a request from the organisers of the Second World Wide Failure Exercise (WWFE-II) to provide high quality test data in this domain. A brief history of the WWFE is presented to give the reader an idea of the importance of the present experimental work with regards to benchmarking of composite failure theories. A brief introduction to composites testing is also given, highlighting the reasons why new specimens need to be developed for through-thickness testing. This is followed by a presentation of the through-thickness compression test methods and experimental data available in the literature. This literature survey is used to select specimen designs for further investigation in order that they can be directly compared and analysed as well as be used to provide data for WWFE-II.

2.1 The World Wide Failure Exercise

2.1.1 The First World Wide Failure Exercise

The First World Wide Failure Exercise (WWFE-I) was published in a special issue of Composites, Science and Technology in 1998[4]. The decision to conduct WWFE-I was taken after a meeting of experts in 1991 where a key question was asked: '*do any of the failure theories for FRPs work?*'[4]. After the meeting it was clear that there were certain issues to resolve. Firstly, whether the failure theories worked or not seemed irrelevant as there was a lack of faith from industry in the available failure theories. This lack of faith was exacerbated by the lack of a definition of failure. As an example a piece of sporting equipment may be considered to have failed if its stiffness reduces by a certain percentage. A pipe designer however, may consider failure as liquid escaping through the walls of a pipe. These are clearly very different definitions of failure and consideration needs to be taken when assessing failure theories as to how they classify failure.

As stated in the first exercise, the question '*do any of the failure theories for FRPs work?*' may seem like a simple question to answer due to the amount of literature available on the subject. However, looking at the literature the reviews of theories available to the authors of the exercise were selective in the cases chosen as demonstrated by the references in the first exercise[5-8]. Hinton, Soden and Kaddour (from here on to be referred to as 'the organisers') conducted WWFE-I to overcome the existing problems and to help with the drive for a definitive answer to the question of whether failure theories for FRPs work. During the planning of the first exercise the organisers finalised an eight point instruction list to be followed in order to conduct an unbiased review of the available failure theories. In summary these instructions were[4]:

1. The organisers must remain truly independent from the participants.
2. The originators of the theory must carry out the calculations in order to avoid any misinterpretation.
3. All theories must be used to predict the same parameters for the same test cases in order that comparisons between theories are possible.
4. In order to test the range of a given theory it must be tested over a wide range of cases and problems which will highlight differences and similarities between theories. Theories must be tested to the full by considering laminate and loading conditions which will show any discriminating features
5. The test cases must be selected by the organisers so that the cases do not favour any particular theory.
6. High quality experimental data should exist for all the cases being solved theoretically. This will enable theories to be benchmarked against test data rather than against other theories.
7. Theoretical predictions should first be made 'blind'. The participants must not have knowledge of the experimental results for the cases until their papers are submitted to avoid any possibility of results being 'tuned'.
8. The difference between 'blind' and 'tuned' predictions must be made clear.

WWFE-I was the first exercise to use such a stringent set of instructions and it was this that ultimately brought about its success.

The first exercise concentrated on biaxial test cases only[9]. This was deemed to be a suitable starting point in order to assess the state of FRP failure theories. It was also important that the scale of the task was not overbearing on the prospective participants so the organisers focused on one area. The exercise was initially split into two parts; part A was made up of papers from participants presenting their blind predictions with an overall comparison between the different theories for each case given by the organisers[9]. Part B compared the theories to the experimental data and gave the participants a chance to comment on their theories and the test data and allowed them the opportunity to tweak their results[10, 11].

The organisers managed to gather eleven participants for parts A and B including theories from Tsai, Rotem, Puck and Zinoviev amongst others[12-23]. After the review of part B it was clear that some theories stood out from the rest. These were the theories put forward by Puck, Zinoviev and Tsai[17, 19, 23]. The organisers commented that these three theories provided predictions for all the cases and were regularly amongst the best predictions for initial and final failure. They were also noted as being good at predicting other parameters such as the mode and sequence of failure. It should be noted that other theories such as that put forward by McCartney were never intended to predict results for all of the cases in WWFE-I and it is a testament to these contributors that they attempted the exercise at all.

Subsequent to parts A and B the organisers conducted part C to the first exercise[24]. This came about in light of new theories emerging in the literature and the invitation to take part was accepted by four new participants[25-28]. The same processes for parts A and B were followed by the participants and from these four new theories those by Bogetti and Cuntze were singled out for praise along with the three leading theories from parts A and B[25, 26].

WWFE-I was, and still is, a stand-out piece of work in the field of composites. More than ten years on from the publication of part A, the first

exercise is still regarded as the most comprehensive and highest quality piece of work in assessing the state of failure prediction for FRPs[29].

2.1.2 The Second and Third World Wide Failure Exercises

Owing to the success of the first exercise the organisers announced plans for two more exercises to further the knowledge of the capabilities of various failure theories. The second exercise has been developed to assess the current theories for their effectiveness of analysing cases of triaxial loading conditions[3]. The third exercise has been designed to assess the current theories for the ability to predict damage of composites[30]. Of the two new exercises WWFE-II is the most closely linked to WWFE-I and provides the next step in the overall picture of the state of FRP failure theories. It was started slightly earlier than WWFE-III and is due for publication in the summer of 2011.

The key difference between WWFE-I and WWFE-II is that the first exercise was concerned only with in-plane loading and response whereas the second exercise is concerned with triaxial loading and 3-D stress response. During the first exercise many of the participants presented simplified three dimensional theories and hence the starting point for WWFE-II was to invite the participants of the first exercise to take part in the second. Six of the participants accepted (or nominated someone to stand in for them) and along with these six a further six participants with new theories or modelling techniques were also confirmed as taking part. The final list of participants can be seen in ref[31]. These participants come from a range of countries and institutions so should provide a broad view of the state of failure theories for FRPs.

The third exercise aims to validate failure theories which the contributors claim are capable of predicting damage under loading such as delamination from transverse cracks, matrix crack initiation and propagation and deformation up to fracture. As with the other exercises a range of test cases were chosen on a range of laminates in order to fully test the theories. Again, a large number of participants were invited to take part from various countries and covering academia, industry

and software houses. In total it was reported that 17 participants were due to take part[32].

The eight point instruction list set out for the first exercise is being followed for the second and third exercises. Of interest to the author was instruction 6:

'High quality experimental data should exist for all the cases being solved theoretically. This will enable theories to be benchmarked against test data rather than against other theories.'

The organisers of the WWFE had selected the cases for both WWFE-II and WWFE-III but did not have the required experimental data for the twelfth and final case in WWFE-II. The proposed test case was based on a through-thickness compression test on cross-ply, $[0/90]_s$ laminates. In response to this the author has been working with the organisers of the exercises to supply the required experimental data.

2.2 Testing of Composites

Before materials are tested it is important to understand why testing is required. Engineers generally need to design products which are fit for purpose, cost effective and material efficient. To do this engineers require specific information on the material they are designing with. Certainly in structural applications this requires that the material being used is understood mechanically, in order that the final product is able to carry out its duties effectively for its expected life-span. When designing a structure of a given material it is important that the engineer has access to information such as the elastic moduli, strengths and ductility among others. For this mechanical testing is required.

In many of their applications, FRPs are used as load-bearing primary or sub-structures. In their initial use this was due to their favourable in-plane strength to weight ratio. This is reflected in the mathematical analysis of composites where Classical Laminate Theory (CLT) is commonly used. CLT uses certain assumptions such as the laminate to be analysed must be thin, all displacements are small compared to the thickness of the laminate, and transverse normal strains ε_z are zero after deformation. Another assumption is that there is perfect bonding

between the different layers of the laminate (a full list of the basic assumptions and a full explanation of CLT can be found from pg 158 of ref[33]). These assumptions break the analysis down to a 2-D problem (an in-plane problem) which is adequate for a large number of applications. This is also reinforced by the early testing of composites where tests designed for homogeneous and isotropic materials such as metals and plastics were adapted for use with FRPs. These tests were concerned with the in-plane properties only. As confidence in the use of FRPs has grown, the number of applications for which FRPs have become a prime material choice has also grown. This has led to large primary structures being constructed using FRPs and so analysis techniques must also advance to cater for these new applications.

It is possible to find plenty of work on composites testing in text books and conferences dedicated to composites testing[33-36]. There is however one common factor between the references available and this is that they do not include much, if any work on through-thickness testing of composite materials. Ref[35] does give some details of various through-thickness test methods but the list is by no means exhaustive. Through-thickness issues can arise in many uses of fibrous composites. Items such as pressure vessels, submersible marine craft and thick hulled boats can be subject to large through-thickness stresses and commonly these are analysed by costly design, make and test approaches. Moreover free-edge effects under in-plane loading can give rise to out of plane stresses (i.e. through-thickness stresses) at the free-edges of multi-angled laminates[37]. This can provide a real problem for designers as these interlaminar stresses can cause local delaminations between layers of the laminate. These local delaminations can act as initiation sites for complete failure of the material and should be prevented. There is extensive work in the literature relating to free-edge effects as a result of in-plane loading and for further information on this phenomenon the reader is directed to references[37-45].

As mentioned in Chapter 2.1.2 WWFE-II requires through-thickness test data for benchmark cases; this highlights another reason for testing. Many current failure theories require prior knowledge of material properties in order to be used. These properties include the Young's Moduli E_1, E_2 and E_3; the shear moduli G_{12}, G_{13}

and G_{23}; the Poisson's ratios ν_{12}, ν_{13}, and $\nu_{23,}$ and tensile, compressive and shear strength values. These values must be obtained through reliable testing methods. As the in-plane properties have been studied extensively it is now important that reliable test methods to obtain through-thickness mechanical properties are developed, studied and utilised. This is particularly important for benchmarking of failure theories as a theory can be made to predict any number of results but without a comparison to reliable test data it should never be trusted.

Having established why testing of FRPs is important the next task is to investigate what test methods already exist to obtain through-thickness properties. The literature review in this chapter focuses on providing an in-depth background to through-thickness compression test methods in order that the most suitable methods can be selected for further investigation.

2.3 Through-Thickness Testing of FRP Laminates

As with all mechanical testing there are three areas of focus; shear, tensile and compressive testing. In order to fully characterise the behaviour of a material all three load types must be considered. In the current work only through-thickness compressive loading is considered. This was due to a request from the organisers of the WWFE-II to provide high quality through-thickness compression test data on carbon/epoxy laminates as the data they desired was not available. Furthermore through-thickness compression testing is relevant in the current time due to the increasing use of CFRPs in primary structures. As a result, it is prudent to expect that CFRP materials may be subject to high through-thickness compressive loads.

As a result the following literature survey covers only through-thickness compressive test methods and data. In order to aid the reader in grasping the state of through-thickness testing as a whole, the author has included tables summarising the test specimens, materials and results that have been presented in the literature for through-thickness shear and tension testing; these are included in Appendices 1 and 2 along with the references.

2.4 Through-Thickness Compressive Testing

A big issue regarding through-thickness compression testing is that there are currently no standards in place. Through-thickness compression testing has not been covered in as much detail as through-thickness tension and shear testing and consequently there are fewer specimens and fewer accounts of them (as observed by the number of tensile and shear works presented in Appendices 1 and 2). The compressive strength of FRPs (particularly multiaxial laminates) is generally very high and this means that it is very difficult to get pure compressive failure from an indirect specimen (indirect approaches have received relatively wide coverage for through-thickness tension) leaving direct specimens as the chosen through-thickness compressive test method in the literature. The use of direct loading specimens only has limited the number of specimen designs available compared to through-thickness tensile testing. Accounts of through-thickness compression experiments are generally more recent compared to through-thickness tension and shear. In recent times, as the use of composites has been moved to larger, more complex structures such as aircraft structures, boat hulls and thick pressure submarine hulls, the through-thickness compression properties have become more important.

2.4.1 Parallel Sided Specimen

The parallel sided specimen is the most widely reported through-thickness compressive test specimen in the literature. It comes in various forms with square, rectangular or cylindrical cross sections and a range of thicknesses. The general form is similar to that shown in Figure 2.1. The first account of the parallel sided specimen used for through-thickness compression testing is from Guo *et al*[46]. The group tested graphite/epoxy specimens cut from 15mm thick cylinders with cross-ply and quasi-isotropic layups. Specimens had end blocks bonded to their tops and bottoms to reduce stress concentrations. Strain readings were taken using 3mm strain gauges on three faces and Moiré interferometry on the fourth face. From the Moiré interferometry *V* field displacement Guo *et al* found that the interlaminar shear strains between the +45°/-45° layers in the quasi-isotropic laminate could be high relative to the applied through-thickness compressive

stress. These stresses do not appear through the centre of the specimen and are free-edge effects. High shear stresses were also found along the free-edges between the 0° and 90° layers in the cross ply specimen. Guo *et al* reported a through-thickness Young's modulus of 11.7GPa. No information was given on the scatter of results, the mode of failure or the strength of the specimens.

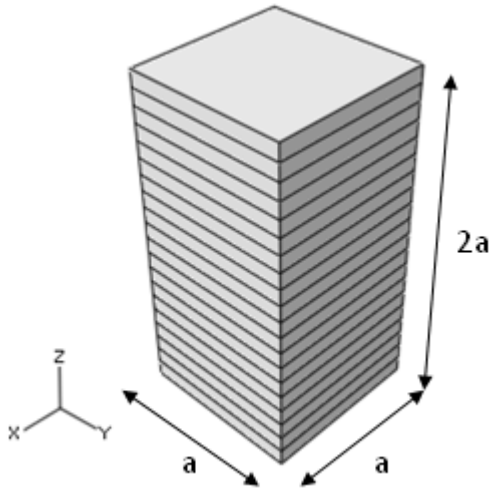

Figure 2.1: Common form of the parallel sided specimen

Lodeiro *et al* [47] tested parallel sided specimens of various materials. UD carbon/epoxy, chopped strand mat, glass fabric/epoxy, discontinuous glass fibre and random glass fibre mat laminates were tested. Specimens were tested with heights of 20mm and 40mm to observe any size effects and all tests were conducted using a four pillar die set to reduce the risk of offset loading. Biaxial strain gauges were bonded to the centre of each of the gauge faces of the specimen with results for each gauge averaged per specimen. For certain materials the specimens were made by bonding together thin laminates to create thick material, although no indication is given as to which materials these were. Lodeiro *et al* concluded that the parallel sided specimen was suitable for obtaining the through-thickness elastic properties but not through-thickness compressive strength values. The Young's modulus and Poisson's ratio results for compression agreed well with the tensile tests carried out. The compressive strength of the 40mm UD carbon/epoxy parallel sided specimens was 263MPa which was substantially lower than the values of 297MPa and 343MPa found for the waisted and cylindrical waisted specimens respectively. This lower strength value was likely

caused by stress concentrations that form at the ends of the specimen where contact is made with the loading plate and the authors state in the reference that the parallel sided specimen should not be used for strength testing.

Mespoulet *et al* tested cross-ply parallel sided specimens under through-thickness compression and tension[48]. Similar to Lodeiro *et al* the specimens were tested using a four pillar die set with hardened steel loading platens. No recess or bonding was used to fix the specimen to the loading apparatus. The through-thickness Young's modulus obtained from compressive testing was 9.9GPa which compared well with the value of 9.8GPa obtained from the through-thickness tensile tests. Although these findings cannot confirm the experimental approach on their own they do suggest that there are no issues with the application of loading or the specimen geometry. The group highlighted that free-edge effects were present but did not give any further details regarding the impact of these effects on the results.

A further account of the parallel sided specimen was given by Park and Lee[49]. They tested multiple specimens manufactured using carbon-phenolic woven materials using Rayon and PAN based fibres. Laminates with thicknesses of 12mm and 24mm were tested. The specimens were tested by compressing them between two steel collars with grease applied to the interface between the specimens and loading plate to reduce friction. A comparative study was also conducted using a self aligning device to reduce any uneven loading. Park and Lee found that the application of grease improved the strength of the specimens from 249MPa to 258MPa and also improved repeatability. The gain in strength was deemed to be statistically irrelevant but the increase in repeatability was important. Similar results were found for quasi-isotropic laminates. After these initial tests all subsequent specimens were greased and strain gauged on all four sides. It was observed that due to difficulties placing the specimens into the centre of the self aligning loading device the strengths measured using this approach were lower and produced more scatter than the results obtained using the standard machine set-up. After this, tests were carried out without the self aligning fixture. During subsequent testing failure was seen to occur in two modes, horizontal

splitting between plies and angular splitting where failure is caused by both matrix cracking and fibre breakage. Subsequent FE analysis demonstrated that the stress concentrations dispersed sufficiently quickly that both the 12mm and 24mm thick specimens were deemed suitable.

Kim *et al*[50] tested parallel sided specimens with both square and cylindrical cross sections. The group followed the finding by Park and Lee that specimens with a width to height aspect ratio of 1:1 were suitable to obtain through-thickness properties and used 10mm tall specimens. UD, cross-ply and quasi-isotropic laminates were tested made from UD laminae or fabric layers. Kim *et al* also followed Park and Lee with regards the loading of the specimen. No self aligning fixture was used; the specimens were greased at each end and loaded between two steel loading plates. The highest strength was found in the cylindrical cross-ply laminate where there was a strength increase over the UD specimen because the angled plies prevent matrix cracks from propagating through the specimen. Final fracture occurred only after fibre breakage. Kim *et al* also commented that the cross ply and quasi-isotropic specimens were subject to free-edge effects but did not give any details of their impact.

Roy and Kim tested 50.88mm tall parallel sided specimens made from AS4/3501-6 carbon/epoxy laminates[51]. They tested specimens with two different cross-sectional areas: 36mm^2 and 9mm^2. Furthermore, cross-ply and quasi-isotropic laminates were examined. The group used an IITRI compression test fixture and it was found that an increase in cross-sectional area lead to an increase in the measured strength. In the cross-ply laminates strengths rose from 775MPa to 975MPa and in the quasi-isotropic laminates strengths rose from 900MPa to 1100MPa. Comparison of the results with failure predictions highlighted that failure was considered to be an interactive failure mode.

Kitching *et al*[52] tested three chopped strand mat glass/epoxy through-thickness compressive specimens in total. These had a cross-section of 25.4x25.5mm on average and a height of 76.2mm. They found good consistency between the failure stress of each specimen with an average value of 250MPa. It

was also noted that there was some non-linearity in the strain readings. The authors suggest that this may be due to disintegration of the material, but they also comment that further investigation was needed. Moreover, it was also found that the through-thickness compressive strength was greater than the in-plane compressive strength, which was associated with splitting of layers in the laminate.

Tagarielli *et al*[53] tested square and cylindrical cross-section parallel sided blocks made from HTS-268-1200/977-2 $[0/45/-45]_{ns}$ carbon/epoxy laminates. The square blocks measured 4.2x4.2x5mm and the cylindrical specimens had a height of 12mm and a diameter of 4.7mm. The immediate issue with these specimens is that the small cross-sections could be severely affected by free-edge effects. Specimens were loaded by steel loading plates and were lubricated to reduce any frictional effects. The authors noted that both specimens exhibited strain hardening and that failure occurred due to a shear mechanism. Furthermore it was reported that the specimens were stronger than flat dog bone specimens which were also tested.

2.4.2 Waisted Specimen

The waisted specimen has been widely used for through-thickness tensile testing but there are only two accounts known to the author of the waisted specimen being used for through-thickness compression testing. These were tests carried out alongside through-thickness tensile tests by Lodeiro *et al*, Ferguson *et al* and Mespoulet *et al*[47, 48, 54]. The results presented by Lodeiro *et al* and Ferguson *et al* are identical to each other as the work was carried out as part of the same grant[47, 54].

The waisted specimens used by Ferguson *et al* (and Lodeiro *et al*) for through-thickness compression were also used for tensile testing. The standard specimen can be seen in Figure 2.2. Specimens were loaded via two steel loading plates in a four pillar die set to avoid any uneven loading. The specimens used had a rectangular cross-section which was implemented for two reasons. The major factor was that a FE study showed that the rectangular cross-section increased the uniformity of the stress response in the gauge length by 35% compared to square

cross-sectioned specimens. The second reason was that a rectangular cross-section provides a built in means of distinguishing between the *x* and *y* axis of the specimen. This is particularly useful when testing UD composites. Failure was deemed to have occurred by a matrix shearing mechanism which was identifiable due to the 45° fracture surfaces. In all cases failure initiated at the radii at the end of the gauge length.

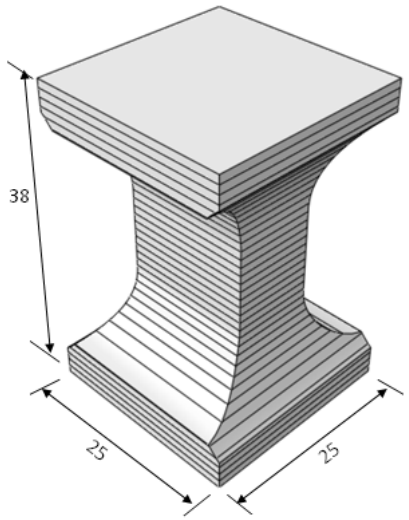

Figure 2.2: Waisted specimen used by Ferguson *et al*[54]

The standard and miniature specimens failed in the same manner for UD specimens and the material properties obtained were in reasonable agreement. However, the results for the miniature specimen showed it to have a consistently lower modulus than the standard specimens. The through-thickness material properties obtained from compression testing were in good agreement with the results obtained for through-thickness tension and the C_v values given in the reference also indicate that the waisted specimen provides readily repeatable results for the standard size specimen. C_v values for the miniature specimens were higher and this is likely due to the effects of microscopic material flaws which could induce stress variations, contributing to changes in strength and stiffness of the specimens.

Ferguson *et al* also commented on the failure surface for UD carbon/epoxy and [0/90] woven glass/epoxy laminates. It was found that the fracture surface of

these materials under compression was at an angle of 45° as shown in Figure 2.3. Failure is through the matrix material and the fracture planes run parallel to the fibres leading to the conclusion that shear stresses are responsible for failure. No discussion is given on the fracture of fibres which must be present in the [0/90] laminates.

Mespoulet *et al* tested UD carbon/epoxy waisted specimens with an elliptical profile and a thickness of 17mm[48]. The specimens were tested using a four pillar subpress with hardened steel plates although unlike the tests by Ferguson *et al* no recess was used to locate the specimens in the test jig. The strength of these specimens averaged 321MPa which is in reasonable agreement with Ferguson *et al*. Furthermore the measured compressive moduli E_3 was almost identical to the tensile modulus at 9.9GPa. The group reported that bending was not a problem during testing and C_v values were reported to be around 10%. This is substantially higher than the C_v values reported by Ferguson *et al* and could have been caused by the small specimen size prompting concerns that the specimen may be subject to size effects. The gauge length cross-section measured just 4x4mm and as a result it is likely that the specimens were severely affected by free-edge effects.

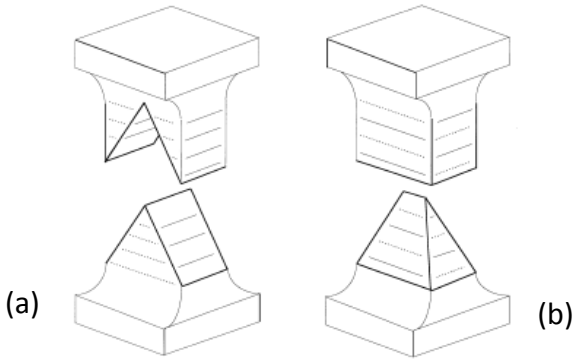

Figure 2.3: Typical fracture surfaces from through-thickness compressive loading for; (a) UD carbon/epoxy, (b) [0/90] woven glass/epoxy[54]

Tagarielli *et al*[53] tested flat dog bone specimens constructed from HTS-268-1200/977-2 $[0/45/-45]_{ns}$ (where ns means non symmetric laminate) carbon/epoxy laminates. The specimens had a gauge cross section measuring

5x3.5mm and a gauge length of 12mm, and were tested with '*plies angled at 0°, 15° and 45° from the z axis*' (angles referred to as θ). This means that in-plane fibres were layered parallel to the *xy* plane, and with an angle of 15 or 45 between the fibres and the *xy* plane. In all experiments the specimens were gripped, rather than resting on loading plates. This gripping process could lead to poor stress formation within the specimens due to the forces they exert. It was observed that failure occurred at a strain of 5% for θ=45 and at 15% for θ=0. Ultimate failure was deemed to have occurred by the propagation of an interlaminar crack. The stress strain curves showed severe non-linearity which does not agree with results elsewhere in the literature which suggests some problems with the results. This could be due to the small gauge cross-section in which free-edge effects are likely to be severe.

2.4.3 Hollow Cylinder Specimen

There is one account in the literature of a hollow cylinder being used for through-thickness compression testing given by DeTeresa *et al*[55]. The specimen was tested under combined through-thickness compression and shear in order to assess the response of FRPs to this loading case. The hollow cylinder had square ends which were used to apply torque to provide the interlaminar shear stress as shown in Figure 2.4. Some simple analysis provided in the reference is required to obtain the shear stress from the applied torque on the cylinder. Four materials; T300/F584 and IM7/8551-7 carbon/epoxies and S2-glass-epoxy and E-glass-vinylester fabric were used with various lay-ups tested and all specimens were created from thick laminates (rather than thin laminates stuck together). Specimens were tested using an MTS servohydraulic biaxial test machine to apply torque and compression and during testing a constant through-thickness stress was applied and then torque was increased up to failure. It was found that when through-thickness compression was applied, the shear strength and ductility of the specimens was increased. When the compressive stress approached the compressive strength of the material the gain in shear strength dropped away and under all compressive stresses a softening effect was witnessed. As the through-thickness stress was increased the material failure went from clear interlaminar

failure to material 'crushing'. The maximum increase in shear strength was found for quasi-isotropic T300/F584 material where the shear strength value increased by 340%. Unfortunately no discussion was given to the results of pure compression using these specimens. The thickness of the gauge length walls was only 2.55mm and as with the waisted specimen tested by Mespoulet *et al* it is believed that the DeTeresa specimen may be severely affected by edge effects. This is examined in Chapter 6.

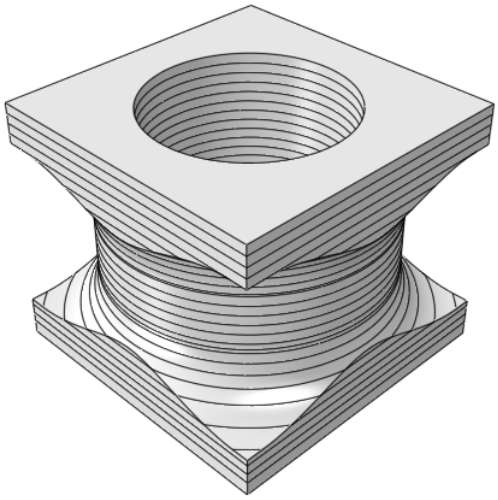

Figure 2.4: Hollow cylinder specimen used by DeTeresa *et al*[55]

2.5 Summary of Through-Thickness Testing in the Literature

Table 2-1 summarises the available through-thickness compressive test data discussed in the literature review. The aim of this is to provide a table of reference including all the known through-thickness compressive test data. For completeness, tables summarising the available through-thickness tensile and shear data are presented in Appendix 1 and 2 respectively.

Table 2-1: Summary of available through-thickness compression test data

Author	Specimen Design and Dimensions	Material/Lay-up	Strength (C_v (%))	E_z GPa (C_v (%))	v_{zx} (C_v (%))	v_{zy} (C_v (%))	Failure Mode	Notes
Kitching *et al*[52] 1984	Parallel sided specimens 25.4x26.5x84.9mm 26.4x26.4x76.4mm 28.1x30.9x87.8mm	E-glass chopped strand mat	250	6.028	0.25	-	-	Also tested materials under tension, torsion and 3 and 4 point bending.
Guo *et al*[46] 1992	Parallel sided short block - 15x13x13mm	IM6/2258 $[90_2/0_2/+45_2/-45_2]_n$ $[90_4/0_2]_n$	- -	11.7 10.6	0.064 0.051	0.078 0.08	-	Also tested in-plane compression
Roy and Kim[51] 1994	Parallel sided specimens Height = 50.88mm Depth = 6.35mm Width = 1.4mm and 5.75mm	AS4/3501-6 [0/90] Width = 1.4mm Width = 5.75mm [0/90/45/-45] Width = 1.4mm Width = 5.75mm	 775 975 900 1100	 - - - -	 - - - -	 - - - -	Thicker specimens were deemed to be stronger due to their better bucking stability	Through-thickness properties obtained from through-thickness tensile tests.
Ferguson *et al*[54] 1998	RARDE waisted specimen Standard: Height = 38mm End tab: 25x25x4mm Gauge length: 16x10x12mm Radius section: Long side, height=9mm radius = 9mm Short side, Height = 9mm Radius = 12mm Miniature: Standard dimensions divided by 2	Carbon/Epoxy pre-preg [0] Standard# Miniature# E-G/Epoxy UD filament wound [0] Standard Miniature E-G/Epoxy woven pre-preg [0/90] Standard E-G/Epoxy woven fabric [0/90] Standard# E-G/Polyester random chopped filaments Standard#	297 (1.8) 283 (4.4) 180 (2.5) 183 (2.1) 455 (4.0) 545 (1.4) 202 (5.2)	10.3 (2.3) 9.6 (4.6) 23.3 (3.5) 19.1 (6.1) 10.7 (3.7) 11.8 (1.7) 6.2 (4.8)	0.02 (23) 0.018 (42) 0.11 (15) 0.10 (8.1) 0.17 (3.0) 0.19 (2.5) 0.23 (16)	0.50 (2.6) 0.51 (6.6) 0.33(3.4) 0.34 (3.5) 0.19 (1.5) 0.18 (2.4) 0.23 (16)	Angled fracture surface present on all specimens. This occurred due to a matrix shearing mechanism. Failure preferentially initiated at the radii at the end of the gauge length. In UD carbon/epoxy failure surface was generally confined to the resin region. In UD glass/epoxy specimens the failure surface was more 'loose' due to separation of the fibres and matrix.	Also conducted through-thickness tensile tests. Where standard specimens used 5-6 specimens tested. Where miniature specimens used 6 specimens tested Fibre volume fraction and void content measured for analysis purposes

Table 2-1 continued

Ferguson *et al*[54] 1998 *Continued*		E-G/Polyester Sheet mould compound - random short fibres Miniature E-G/Nylon-66 Injection moulded – random short fibres Miniature E-G/Polypropylene – continuous swirl mat Miniature	241 (8.1) 187 (2.4) 129 (6.5)	7.5 (4.7) 4.2 (2.1) 3.3 (12)	0.17 (16) - -	0.17 (52) - -	In 0/90 woven specimens failure shear plane propagated in warp and weft directions with lots of debris on the fracture surface.	
Lodeiro *et al*[47] 1999	Parallel sided short blocks – heights: 40mm and 20mm† Sandwich parallel block – height: 40mm† Circular waisted block – height: 40mm†	T300 UD Carbon Fibre/Epoxy Parallel Block (40mm) Parallel Block (20mm) Sandwich Parallel Block (40mm) Circular Waisted Block (40mm) Circular Waisted Block (20mm) Chopped Strand Mat Parallel Block (40mm) Circular Waisted Block (40mm) 2x2 Twill Glass Fabric/Epoxy Parallel Block (40mm) Circular Waisted Block (40mm) Discontinuous Glass Fibre/Nylon 66 Parallel Block (20mm) Circular Waisted Block (20mm) Random Glass Fibre Mat/Polypropylene Parallel Block (20mm) Circular Waisted Block (20mm)	 263±3 256±6 258±8 343±7 344±10 211±6 236±10 588±29 543±5 190±8 195±5 181±14 210±9	 10.0±0.1 9.9±0.1 10.0 - - 6.3±0.3 - 12.4 - 4.3 - 4.2 -	 0.022±0.001 0.020±0.001 0.020 - - 0.29±0.04 - 0.21 - 0.21 - 0.27 -	 0.52±0.01 0.56±0.01 0.52 - - 0.29±0.04[+] - 0.21[+] - 0.44 - 0.27[+] -	Failure of parallel sided specimens initiated at the specimen ends due to stress concentrations between the specimen and loading plates. Failure of the circular waisted specimens occurred at the radius roots/mid-section due to reduction in cross-sectional area and stress concentrations. All specimens failed due to shear cracking at 30-45°.	Presented results for Through-thickness tension, compression and shear. Various specimen types used for each material.

Table 2-1 continued

Mespoulet *et al*[48] 2000	Elliptical waisted specimens – 8x8x17mm with 4x4mm cross-section at gauge length	T300/914 carbon fibre/epoxy pre-pregs [0] UD	321 (9.3)	9.9 (3.1)	-	-	-	Also tested through-thickness shear and tension.
Zhao[56] 2002	Bolted single-lap joint specimen†	IM7/8552 [0] [0/90] [0/±45/90] [0/±30/±60/90]	 300§ 1185§ 1200§ 1290§	 9§ 14.8§ 15.3§ 14.8§	 - - - -	 - - - -	-	Study to observe lap joint, bolted composites
DeTeresa *et al*[55] 2004	Hollow cylinder specimens – Inner diameter = 1.59cm Outer diameter = 2.1cm Fillet radius = 0.635cm Gauge length = 0.635cm	T300/F584 pre-preg $[45/0/-45/90]_{xs}$ IM7/8551-7 (not tested under pure compression) $[0/90]_{xs}$ $[45/0/-45/90]_{xs}$ E-Glass plain-weave fabric-vinyl ester $[90_2/\pm45]_{xs}$ S2-glass/DER-332 $[90_2/\pm45]_{xs}$	 833 >552 >552 417 421	 - - - - -	 - - - - -	 - - - - -	Combined through-thickness compression and interlaminar shear tests showed large amounts of material crushing on the fracture surface. No details given on the failure surface under pure compression.	Study was to observe the effect of applying a constant through-thickness compressive load on the shear strength of composite laminates.
Park & Lee[49] 2005	Parallel sided short blocks - square cross-section 12x12x24mm (T) 12x12x12mm (S)	PAN based carbon-phenolic woven composite $[0]_{32}$ (PZS) $[0]_{64}$ (PZT) $[0/90]_{16}$ (PCS) $[0/90]_{32}$ (PCT) $[\pm45]_{16}$ (PAS) $[\pm45]_{31}$ (PAT) $[-45/0/45/90]_{4s}$ (PQS) $[-45/0/45/90]_{8s}$ (PQT) Rayon based carbon-phenolic woven composite $[0]_{28}$ (RZS) $[0]_{56}$ (RZT)	 807 - 842 - - - 897 - 396 396	 - - - - - - - - - -	 - - - - - - - - - -	 - - - - - - - - - -	Two failure modes witnessed; horizontal splitting and angular splitting. Horizontal splitting was caused by delamination between plies whilst angular splitting was caused by a combination of matrix cracking and fibre breakage.	Studied effects of friction between specimens and loading plates as well as effects of specimen thickness and stacking sequence. Also studied the effects of testing using a self-aligning test fixture.

Table 2-1 continued

Park & Lee[49] 2005 *Continued*		$[0/90]_{14}$ (RCS) $[0/90]_{28}$ (RCT) $[\pm45]_{14}$ (RAS) $[\pm45]_{28}$ (RAT) $[-45/0/45/90/45/0/-45]_{2s}$ (RQS) $[-45/0/45/90/45/0/-45]_{4s}$ (RQT)	400* 395* - 393 373 373	- - - - - -	- - - - - -	- - - - - -		
Kim *et al*[50] 2010	Parallel sided short blocks – square and cylindrical cross-section Square: 10x10x10mm Cylinder: h=10mm, d=10mm	UD USN150 $[0]_{80}$ $[0/90]_{40}$ $[-45/0/45/90]_{10s}$ Plain Weave CF3327 $[0]_{48}$ $[0/90]_{24}$ $[-45/0/45/90]_{12s}$ Twill Weave CF3326 $[0]_{48}$ $[0/90]_{24}$ $[-45/0/45/90]_{12s}$	 200 1400 1200b 800 800 800 800 830 800	 10.2 12.2 12.2 11 11 10.7 13 11.9 11.8	 - - - - - - - - -	 - - - - - - - - -	UD materials failed through transverse matrix cracking. Final failure of cross-ply and quasi-isotropic occurred through interlaminar shear failure and fibre breakage	Square cross-section block tested with fibres running parallel to x-axis and at 45° to the x-axis
Tagarielle et al[53] 2010	Parallel sided short blocks - square and cylindrical cross-section Square: 4.2x4.2x5mm Cylinder: h=12mm, d=4.7mm Dog Bone Gauge length dimensions 5x3.5x12mm†	HTS-268-1200/977-2 $[0/45/-45]_{ns}$ carbon/epoxy laminates Dog Bone θ=0° θ=15° θ=45° Parallel sided square Parallel sided cylinder	 440* 340* 180* 650* 490*	 9.49* 9.49* 9.49* 9.49* 9.49*	 - - - - -	 - - - - -	Failure due to interlaminar cracking at 45°. Same mode found in all specimens but dog bone specimens should a greater non-linear response showing plasticity from loads of 200MPa	Also tested specimens under tension and shear
	In-plane ply angles from *z*-axis, θ=0°, 15° and 45°							

* Value extracted from graph in reference, † No other dimensions given, # Results from the same tests were also reported by Lodeiro *et al*, + Assumed from material symmetry, § Assumed value for indication, only relative values given in reference

2.6 Free-edge Effects Induced by Through-Thickness Loading

A common problem associated with testing of FRP laminates is the presence of free-edge effects. Many attempts have been made to evaluate the out-of-plane stresses induced at the free-edges of composite laminates under in-plane loading. These have been both analytical solutions and finite element analysis[37-45, 57-64]. However, none of these works have attempted to address the problems of free-edge effects induced by through-thickness loading.

Accounts on the investigation of free-edge effects induced from through-thickness loading are very limited in the literature. Guo *et al* used Moiré interferometry to observe the surface displacements of one side of quasi-isotropic and cross-ply parallel sided specimens under through-thickness compression[46]. They observed the presence of shear strains across the specimen surface which reduced close to the corners of the specimen. The transverse strains were reported to be very small and almost constant across the surface of the specimens. The through-thickness strain was reported to be lowest in the 0° layers and largest in the 90° layers. The cross-ply laminates investigated Guo *et al* showed large interlaminar shear stresses at the interface between plies. They noted that when load was applied, the surface of the specimen became undulated. The ridge and valley formation is created due to the differing Poisson's ratios between the axial and transverse directions in the plies.

A further account of free-edge effects induced by through-thickness loading was given by Park and Lee[49]. The account is only brief but shows finite element models of quasi-isotropic and cross-ply laminates and presents the interlaminar shear stress across the face of the specimen. The focus of the work does not appear to be free-edge effects but concentrates on stress distributions which lead to through-thickness compressive failure with respect to stacking sequence. However, the stress results presented are all edge stresses. The work used a $1/8^{th}$ model making use of the symmetry of the different lay-ups. No mention was given of the boundary conditions used and one must be very careful with application of loading and boundary conditions, such that the type of symmetry i.e. reflectional or translational is considered. Models were created using C3D20R elements but there

is some ambiguity as to the number of elements per layer in the models. In one sentence it is stated that the models were created with four elements per ply in the thickness direction. However, in a subsequent sentence the authors explain that the graphs presented use two data points from each ply because one ply was modelled using two elements in the thickness direction.

In the FE analysis carried out by Park and Lee, it was observed that the through-thickness stress σ_{33} became stable after three plies. It was also found that the through-thickness compressive stress σ_{33} and the in-plane shear stress τ_{12} did not vary much with respect to the stacking sequence of fabric composites. The pair examined laminates with two reinforcement materials, namely PAN based fibres and Rayon based fibres. It was observed that the interlaminar shear stresses in quasi-isotropic PAN based systems were similar to those found for cross-ply woven laminates with the same reinforcing fibres. However, in the case of Rayon fibre based systems the interlaminar shear stresses were higher in the quasi-isotropic model compared to the cross-ply and UD models examined. The conclusion was that the through-thickness compressive strength of carbon-phenolic woven composites is dependent on the stacking sequence and the fibre material as opposed to the composite thickness. This was determined due to the correlation between experimental through-thickness compressive strengths and FEA interlaminar shear stresses.

2.7 Chosen Specimens for Through-Thickness Compression Testing

In the present study through-thickness compression tests are carried out using waisted, parallel sided and hollow cylindrical specimens. The waisted specimen has provided the most consistent results in the literature whilst the parallel sided specimens have been used multiple times to observe the through-thickness behaviour of composite laminates. In the current study a robust finite element study is provided to justify the final specimen geometries and lay further weight to the standardisation of these specimens. Furthermore, by testing these specimens side by side a direct comparison regarding material properties and failure modes will be applicable.

The cylindrical specimen has also been selected for further investigation. This was chosen to observe the specimens response to pure through-thickness compression. Currently the only account available focuses on combined compression and shear loading and no sufficient discussion is given regarding the stress response under pure compressive loading. It is important that a robust analysis of the specimen be produced in order to clarify any existing or new experimental data that may have been obtained using the hollow cylinder specimen. Furthermore, this specimen will also be tested using the same material and lay-up as the waisted and parallel sided specimens so the results should be comparable.

2.8 Conclusion

Fewer test specimens have been used to obtain through-thickness compressive properties of FRPs compared to through-thickness tension. However, in light of the lack of through-thickness compressive test data the organisers of the WWFE-II have requested that a new through-thickness compression test regime be carried out.

The parallel sided specimen has been the most commonly used specimen for through-thickness compression testing. The specimens discussed here ranged in thickness from 10mm to 24mm thick which is at the thinner end of laminates for direct through-thickness testing. The specimen is also relatively easy to manufacture. There appears to be some confusion in the literature with groups such as Lodeiro *et al* stating that the parallel sided specimen cannot be used to obtain through-thickness compressive strength values due to stress concentrations, but Kim *et al* completed a strength study using only parallel sided specimens. However, results presented by Lodeiro *et al* demonstrate that the strength of parallel sided specimens is 10% and 25% lower than plain and cylindrical waisted specimens respectively. This reduction is due to end effects present in the parallel sided specimen caused by contact with the loading plates.

The waisted specimen was tested under compression by Ferguson *et al* and Lodeiro *et al*. The waisted specimens discussed in the literature range from 20mm

to 40mm in thickness and although the waisted specimen is more difficult to manufacture than the parallel sided specimen, the benefit is that the stress concentrations at the ends of the specimen are reduced. Therefore the waisted specimen should provide a more pure strength result. In general the C_v values for the waisted specimen are lower than in parallel sided specimens demonstrating greater repeatability which is of course desirable in any series of tests.

A hollow cylinder specimen has been presented by DeTeresa *et al* for combined through-thickness compression and shear loading. The specimen was used to prove that when the material is subject to through-thickness compression the shear strength improves. Unfortunately the reference focuses only on the strength under combined loading with no discussion given on the pure compressive results.

An often cited issue with through-thickness testing is the presence of free-edge effects. This has only been studied experimentally by Guo *et al* using Moiré interferometry. This work confirmed the presence of free-edge effects and highlighted that large interlaminar shear stresses were present under through-thickness loading. Other work relating to free-edge effects due to through-thickness loading are restricted to FE observations although similar findings to Guo *et al* have been found[49].

The waisted, parallel sided and hollow cylinder specimens will all be investigated in this study. This will allow for a comparison which should highlight the advantages and disadvantages of each specimen. Furthermore the study should provide clarification of the usefulness of the cylindrical specimen for through-thickness testing as well as justification for the selected geometries.

3 Properties of Three Dimensional Composite Materials

3.1 Three Dimensional Composites

The previous chapter and further work in this thesis is concerned with through-thickness compression of carbon fibre composite materials. Through-thickness properties are of concern due to the increasing use of FRPs in primary load bearing structures and as a result engineers have sought to improve the through-thickness properties of composite materials. During the course of this project the author undertook meetings at QinetiQ, The University of Manchester and The University of Surrey to discuss and review the World Wide Failure Exercise. Whilst the focus of these meetings was on tri-axial and through-thickness loading of conventional laminates, discussion often turned to the effectiveness of through-thickness reinforcement methods. Through-thickness reinforcement may be seen as the gradual progression of composite materials as engineers look to reap the benefits of these materials in greater structural circumstances. An issue that presents itself is the lack of information in this arena. Therefore it was decided that the problem should be tackled from the start. This start is commonly with the in-plane elastic characteristics of the material. It is widely known that through-thickness reinforcement will improve the through-thickness performance of carbon fibre composites, but existing work has often overlooked the effect on the in-plane properties. Hence, the current study looks at predicting the effect on the in-plane elastic properties by introducing through-thickness reinforcement. The desired outcome is that the reader will gain a greater understanding of such materials and how the in-plane elastic properties may be predicted.

The simplest form of through-thickness reinforcement is of Z-pins (Z-pinning), stitching and tufting with examples of each shown in Figure 3.1. All three of these reinforcement types are similar and relatively easy to apply but all have distinctive differences.

3.1.1 Stitching

The earliest account of stitch/Z-pin/tuft reinforcement was from Huang *et al*[65]. Steel wires were embedded into a carbon/epoxy laminate at ±45° and then cured.

It was found that the interlaminar shear strength could be improved by up to 50% when the steel wires were used as delamination propagation was slowed down. However, in this early work the wires were embedded by hand which was too labour intensive to become a viable engineering solution. To improve the production method Mignery *et al* used an industrial sewing machine to stitch Kevlar threads into a carbon/epoxy laminate prior to curing[66]. They found that although delamination was not completely prevented by through-thickness stitching it did slow down the delamination process. In general there are three types of stitch used to provide through-thickness reinforcement for composites.

The lock stitch is shown in Figure 3.1(b), with the other stitch types being the modified lock stitch and the chain stitch. Stitches can be applied to both pre-form and pre-preg materials and from a manufacturing point of view pre-pregs are desirable as the process time is quicker. However, work by Lee and Liu, and Chung *et al* has indicated that when pre-pregs are stitched, the uncured resin causes damage to the in-plane fibres during the stitching process[67, 68]. It is also important that the needle material will not cause damage to the laminate material. Another important factor in stitching is that access is required to both sides of the laminate. This can make complex structures very difficult or even impossible to manufacture using stitching techniques.

A good account of the advantages and disadvantages of stitching has been given by Dransfield *et al*[69]. Key advantages identified were: the ease of manufacture, the possibility of joining laminates to create a structure, the ability to fine tune material characteristics by adjusting stitch density, a positive influence on free-edge effects and the increase in delamination resistance. Generally stitching adds one step to the production process prior to curing, therefore the manufacture process is not altered significantly. The stitching process can also be automated with the stitch density altered in this step to enable fine tuning of material features such as delamination strength and in-plane properties in order to produce composites that are developed specifically for purpose. Another distinct advantage is that once the pre-form/pre-preg has been stitched it holds its shape and is able to be handled during the rest of the manufacture process[70].

The disadvantages of stitching given by Dransfield *et al* include the trade off that must be taken between the in-plane and interlaminar properties. Work by Farley *et al* demonstrated that the compressive strength of cross-ply laminates was reduced by around 30% when stitching was present, although the compression after impact strength increased by 75% and 95% for carbon and Kevlar stitches respectively[71]. Other problems highlighted are that the stitching process can damage the existing in-plane fibres and introduce material discontinuities which cause stress concentrations. Moreover, the presence of stitches can introduce resin rich areas and the surface loop introduced on the surface of the laminate can introduce fibre kinking on the outer layers of the composite. As a result of this final problem Farley and Dickinson investigated the effect of machining the surfaces of the cured laminate in order to eliminate the surface loops[72]. The machined specimens exhibited a greater compressive strength than the unmachined examples. The machined specimens are essentially tufted composites (as discussed in Chapter 3.1.3).

3.1.2 Z-pins

Z-pin reinforcement is the cheapest process in terms of initial capital investment as it can be incorporated into the standard autoclave process (as shown in Figure 4.2) with no extra manufacturing equipment required. Z-pins are commercially produced by passing the chosen fibres through a resin bath and pultruding the impregnated tows into rods of material between 0.15 and 1mm in diameter[73]. The rods are then placed into foam with the fibre density and length being controlled during this process with Z-pin densities ranging from 0.5-10% and thicknesses ranging from 1-51mm. The foam block contains a low density and medium density foam where the low density foam is designed to collapse easily under pressure to aid insertion of the Z-pins into the laminate. The medium density foam prevents buckling of the Z-pins during the insertion process. In order to place the Z-pins into the laminate, pre-preg material is vacuum bagged with the Z-pin pre-form placed on top. A release layer is placed between the pre-form and the laminate to avoid any damage or contamination. During the curing process the heat begins to melt and soften the pre-form foam and under the applied pressure

of the auto-clave process the Z-pins are driven in to the laminate. The Z-pins can be manufactured from carbon/epoxy, glass/epoxy, titanium, stainless steel and other materials and their use is not restricted to pre-preg laminates[74].

3.1.3 Tufting

Tuft reinforcement is similar to stitching. Unlike stitching though, where access to both sides of the laminate is required, tufting only requires access to one side. The issue with this is that the process relies on friction from the fibres to prevent the tuft from lifting back out of the laminate with the needle. A holding material such as foam can also be used if the friction of the fibres is not enough to prevent this from happening. Dell'Anno *et al* recommend using loosely woven dry pre-forms to avoid damaging the laminate material as detailed in the stitching process[75]. The surface loops can be removed pre or post curing but removing the loops post curing would appear to be advantageous as it reduces the risk of damaging the laminate or tufts whilst it is in its loose uncured form.

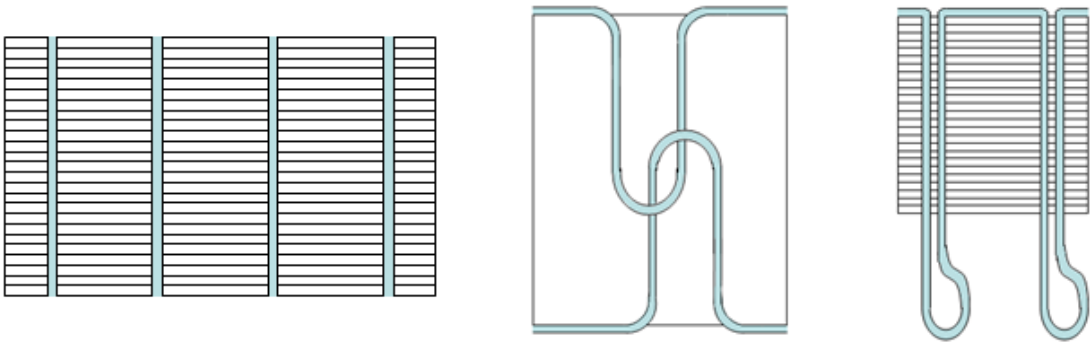

Figure 3.1: Examples of through-thickness reinforcement; (a) Z-pins, (b) Lock stitches, (c) Tufting

3.1.4 Woven, Braided and Knitted Systems

Woven, braided and knitted composites are all similar to each other and as with stitches, Z-pins and tufting they are used due to their good impact resistance and damage tolerance properties compared to conventional laminates. In woven composites the warp and weft fibre bundles are positioned at 90° to one another as shown in Figure 3.2. Woven systems can incorporate many layers of warp and weft fibre bundles woven together to create thicker materials. Woven composites are typically created as dry cloth. The cloth can then be placed into a mould to

make complex shapes. One of the problems with woven composites is that matrix pockets are unavoidable and the fibre volume fraction is less than for laminates made from UD layers[76].

Braided composites have fibre bundles orientated at various angles unlike the constraint of 0° and 90° in woven composites. A good account of the history of braided composites is given by Li *et al*[77]. There are two main processes which can be used to create 3-D braided composite structures, namely the two-step and four-step processes. Typically braided composites are in shapes with square or cylindrical cross-sections due to the common automated braiding processes but they can be used to make more complex shapes such as I-beams and cones. Examples of square and circular cross section braiding techniques are given by Li *et al*, Wang and Wang, and Tang and Postle[77-79]. Due to the nature of the braiding process, dry pre-forms are made and then resin is injected in a process such as Resin Transfer Moulding (RTM) where the final shape of the composite part is created during the consolidation phase[80]. Braided pre-forms use continuous fibres with the fibre direction constantly changing in all directions and as a result there is generally a good balance between in-plane and out of plane properties unlike in stitched composites.

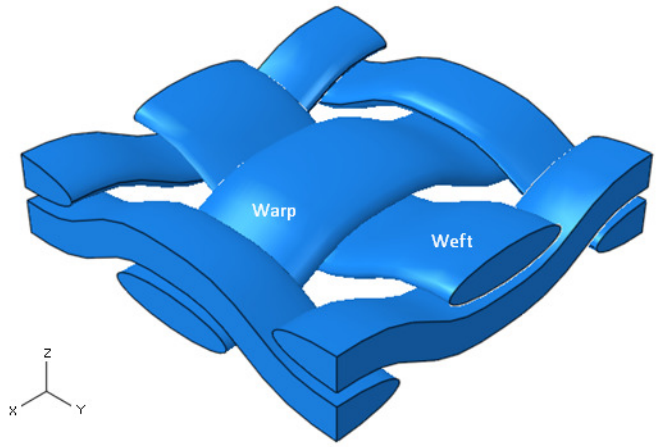

Figure 3.2: Typical woven composite model

Knitted composites are formed in a similar way to braided composites in that a dry pre-form is created and then it is taken through a resin injection process and consolidated. In terms of production there are advantages in that production

machinery can be adapted from the textiles industry to create knitted preforms from carbon, glass and aramid fibres. Other advantages are that complex shapes can be readily produced. This can be done in two ways; firstly, the cloth can be formed into complex shapes during the knitting process and then consolidated. Secondly, for very complex shapes flat cloth can be placed around a mould due to the good drapability of flat knitted fabrics[81]. However, distinct flaws have been found with knitted composites due to their comparatively poorer in-plane properties compared to more conventional laminates[82, 83]. This comes as a result of the tight curves of the fibres produced by the weave resulting in the stiff in-plane fibre properties not being used efficiently within the structure. Chou *et al* also demonstrated poor fatigue life characteristics of knitted composites and highlighted that during the knitting process the fibres can become damaged, similar to problems that can be encountered during stitching[84].

3.2 Analysis of Three Dimensional Composites

Having presented various types of through-thickness reinforcement the focus for the rest of the study on such composites will be on Z-pinned composites. These have been chosen due to a relative lack of study in the literature and because they can provide through-thickness reinforcement with relatively simple manufacture methods. Although the concentration of this study is Z-pinned laminates it is believed that the outcomes are likely to be applicable to tufted composites as well. They may also be applicable to stitched composites but the stitch geometry on the top and bottom surface will introduce features which will not be present in the current study.

The remainder of the literature survey details numerical and analytical approaches which have been, or can be used to predict the elastic properties of Z-pinned laminates.

3.2.1 Numerical Analysis

3.2.1.1 Dickinson *et al* Unit Cell Model for Z-pinned Laminates

A common approach to analysing three-dimensional composite materials is the finite element method. Dickinson *et al* conducted a finite element study of Z-

pin reinforced composites[85]. They used a unit cell approach which is common in the literature and examined further in Chapter 3.2.1.5. The initial work in the reference highlights the presence of resin rich zones surrounding the Z-pin (Z-pin is referred to as translaminar reinforcement, TLR by Dickinson) as indicated in Figure 3.3. The resin rich zones were modelled due to photographic observations. In the vast majority of cases presented, the ratio of the inclusion length (l) to the Z-pin diameter (d) was equal to 5 and the Z-pin volume fraction (V_f^z) was 1.9% (l and d are defined in Figure 3.4). In one other case the l/d value was set to 3.5 but the Z-pin V_f^z was also changed to 4.9%. In two cases the Z-pin orientation was altered from the z-axis by 15° and 45° respectively.

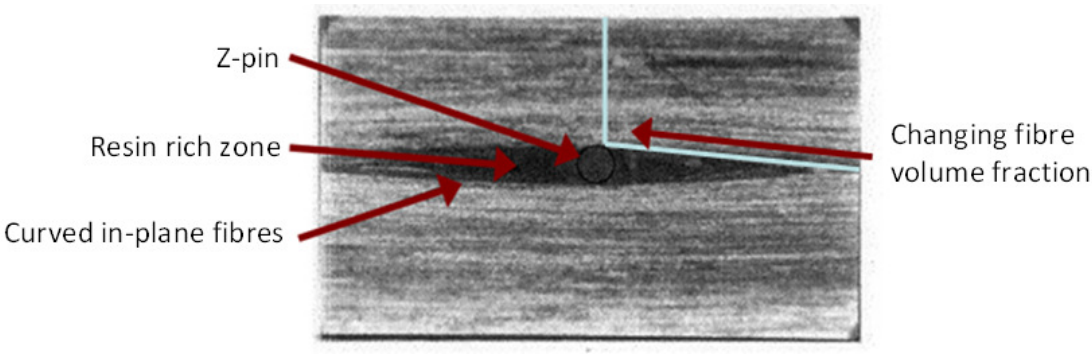

Figure 3.3: Microscopic picture of a UD laminate with Z-pin demonstrating the resin rich zone and in-plane fibre displacement[86]

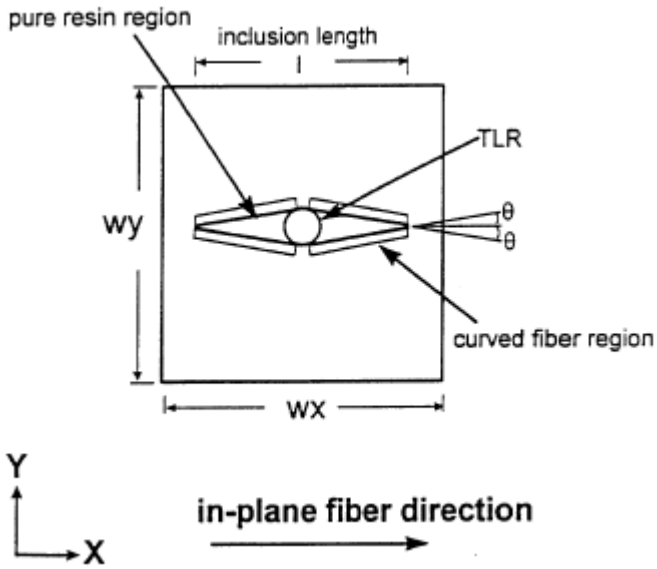

Figure 3.4: Schematic produced by Dickinson *et al* showing Z-pin(TLR), resin rich zone and curved fibre region[85].

Figure 3.4 shows a schematic of the FE modelling approach used by Dickinson *et al*. The Z-pin (shown as TLR [translaminar reinforcement] in the above image) is set with the desired diameter and the value of the inclusion length is set from the desired *l/d* ratio. From the end point of *l,* a line is drawn which hits a tangential point on the circumference of the Z-pin. The angle that this line makes with the *x*-axis is defined as θ. There are then four curved fibre regions extending from the resin rich zone tip to the tangent point with the Z-pin. In these zones the in-plane fibres are assumed to be orientated in the θ direction. The depth of this region was kept constant at a value of 1/4*d* where *d* is the diameter of the Z-pin reinforcement.

All the unit cell models examined were constructed using eight noded three-dimensional solid elements and a swept mesh was used. In the account a macrostress was applied and the unit cell constrained such that the deformation was controlled. The displacements on the boundaries of the unit cell were then used to calculate the macrostrains from which the elastic properties could be obtained. As well as the unit cell models, Dickinson *et al* also used the commercially available TEXCAD to get results for all cases such that a comparison with the FE results could be drawn[87]. TEXCAD is essentially similar to the rule-of-mixtures approach. In four control cases without Z-pins it was found that the FE and TEXCAD results were in good agreement.

Four laminate lay-ups were considered by Dickinson *et al*: [0] UD, [0/90] cross-ply, [45/-45] angle-ply and a [+45/0/-45/90] quasi-isotropic laminate. In all cases the laminate under consideration had the material properties of AS4/3501-6. Four through-thickness reinforcing materials were considered, Kevlar/epoxy, carbon/epoxy, titanium and steel. The carbon/epoxy Z-pin was used in the majority of cases with the other three being used in one case each to observe their effect on the elastic properties of [0/90] laminates. The material properties used for the unit cell models were taken from manufacturers' product information sheets and from the following references by Naik[88, 89].

The results presented by Dickinson *et al* show that with the inclusion of a carbon/epoxy Z-pin the in-plane stiffness, E_x and E_y of each laminate considered reduced by a small amount except for E_y in the UD laminate. The reason for the reduction of the in-plane stiffness was given to be due to the replacement of in-plane fibre material with softer Z-pins. The reason given for the slight increase in E_y in the UD material was that the introduction of Z-pins would restrict the contraction of the laminate in the *z* direction. As a result there is an extra resistance to the load in the *y* direction and therefore a gain in E_y is witnessed. The in-plane effects observed were reasonably limited with the largest difference in stiffness being 7% between the pinned and unpinned models. In all cases there was a substantial increase, between 23% and 27%, in E_z when Z-pins were included. The shear modulus values G_{xy}, G_{xz} and G_{yz} all reduced by a small amount for the same issues that caused reductions in E_x. The reported decrease in shear stiffness is only very small and one may expect that G_{xz} and G_{yz} may not change at all. In fact they may increase due to the inclusion of through-thickness reinforcement. However, there is little in the way of experimental evidence to characterise the shear response of Z-pinned laminates as discussed in Chapter 3.3.

Two FE models were created with the Z-pin angle rotated by 15° from the *z* axis in one model and by 45° in the second model. The FE models demonstrated that as the angle was increased the through-thickness stiffness E_z decreased due to the reduction in stiffness of the Z-pin at these angles. Only a small effect was witnessed with respect to the shear modulus G_{xz} with the value increasing as the Z-pin angle was increased

Two models were created to examine the effect of a change in Z-pin diameter. One model used a Z-pin with a 0.3% V_f^z and a second model housed a Z-pin with a V_f^z of 4.9%. The model with the larger Z-pin V_f^z used a smaller resin rich zone in order to keep the unit cell outer geometry to the original dimensions. It was observed that both the FE and TEXCAD results showed a decrease of the in-plane stiffness E_x and E_y when the Z-pin volume was increased. In all cases the TEXCAD models produced lower in-plane stiffness results, which was put down to the TEXCAD model not taking account of the curvature of the in-plane fibres around

the through-thickness reinforcement. Both the FE and TEXCAD models showed large increases in E_z with an increase in Z-pin V_f^z due to the addition of material with high stiffness in the *z* direction.

In models with differing Z-pin materials it was noted that as the stiffness of the reinforcement was increased the drop in E_x and E_y compared to the control cases reduced. The result seen was more effective in the TEXCAD models as the low stiffness of the resin rich zone and the high stiffness of the Z-pins are balanced by each other. By comparison in the FE model, the Z-pin could not contribute to the in-plane stiffness due to the shielding provided by the resin rich zone.

The final cases reported were with respect to the curvature of the in-plane fibres surrounding the Z-pin reinforcement and the resin rich zone. One model was created without the fibre curvature and one without both the fibre curvature and resin rich zone. For E_x, E_y and E_z very little difference was found between each of the three models. This was particularly true for the FE models. It was observed that in the model without fibre curvature the shear modulus G_{xy} decreased, demonstrating that the curved fibres contribute to the in-plane shear stiffness of the laminate.

3.2.1.2 Grassi *et al* Unit Cell Model for Z-pinned Laminates

Grassi *et al* conducted a similar FE study to Dickinson *et al*, using the same materials and lay-ups[86]. The model created by Grassi *et al* used 20-noded solid elements with three possible Z-pin locations and a Z-pin V_f^z of 2%. Input material properties were taken from the work by Dickinson *et al*[85] and Sun and Vaidya[90]. The work focused on the stress distribution close to the Z-pins and the interlaminar stress variation at the free-edge of the model. The results of the basic laminates containing Z-pins were almost identical to those produced by Dickinson *et al* and were also in good agreement with in-plane properties measured using a closed form solution following Lin and Chan[91]. The closed form solution, similar to TEXCAD was based on the rule of mixtures approach.

In the examination of stresses around the Z-pin the *z* axis reinforcement was seen to absorb up to 25% of the strain deformation energy in the unit cell.

Shear effects were also present here so the recommendation was that when selecting Z-pin materials the compatibility with the laminate should be considered for the strength of the bond between the materials.

In the investigation of the interlaminar stress variation, pins were modelled at three distances from the free-edge: 1.25, 0.69 and 0.25mm. Following the observation by Hu and Soutis[92] that free-edge effects extend a distance of two ply thicknesses into a laminate the authors predicted that only the Z-pin at a distance of 0.25mm to the free-edge would give a relevant result. Subsequent graphs demonstrated that this was the case and the effect of having a Z-pin in the [0°/90°] cross-ply laminates at this location was to reduce the shear stress τ_{yz}. It was also indicated that interlaminar stresses were picked up by the Z-pin close to the free-edge and that delamination damage due to through-thickness forces was likely to initiate from the resin rich zone surrounding the Z-pin. Similar results in stress reduction were found in the [±45°] laminates.

3.2.1.3 In-Plane Fibre Misalignment Assumption for Modelling Z-pinned Laminates

One key feature of the models presented by Dickinson *et al* and Grassi *et al* is the assumption of the in-plane fibre volume fraction in the location of the Z-pin. This is discussed in Chapter 3.3 which demonstrates an uncertainty about the reaction of the in-plane fibres to the insertion of Z-pins. Basic assumptions that can be used are that in the region of the Z-pin the in-plane fibre volume fraction can become greater due to fibre bunching or reduce due to fibre spreading. Although the difference in fibre volume fraction V_f^f may be small it should none the less be incorporated. Due to the use of a homogeneous composite material in the Dickinson and Grassi models it is observed that as the Z-pin volume is increased, the in-plane fibre volume fraction in the laminate in the region of the Z-pin reduces. This happens because the in-plane composite material is replaced by the Z-pin material. This is a major assumption and the result is that in their predictions the modulus *E* in the in-fibre direction reduces by a significant amount when Z-pins are introduced. In the example of a UD AS4/3501-6 laminate containing a T300/9310 Z-pin with a 2% volume fraction the results of Grassi and Dickinson

show a decrease in E_x by around 2.5GPa. This agrees with experimental work by Troulis[93] but not with experimental results presented by Steeves and Fleck[94] who demonstrated that although the in-plane strength was reduced in the presence of Z-pins, the in-plane modulus E_x showed a minimal increase compared to unpinned laminates. These works are further discussed in Chapter 3.3.

3.2.1.4 Meso-Scale Modelling of 3-D Composites

Lomov *et al* demonstrated a meso-scale orientation averaging (OA) model approach to analysing three-dimensional composites[95]. The reference includes discussion of woven composites but the approach shown also includes a discussion of stitched composites. The approach focuses on the internal structure of the material to form a solution. The work in the reference provides many further references of modelling complex fibre geometries which are beyond the scope of this thesis. The authors set out by producing a road map for the production of a unit cell. The linear approach put forward by Lomov *et al* (a damage approach is also given but damage is not considered here) is outlined in Figure 3.5. When modelling structural stitches the authors state that the stitches cause the in-plane fibres to deviate from their path, causing fibre free zones referred to in the reference as 'openings'. The assumption given is that the fibre volume fraction of the in-plane fibres will increase around the stitch. Note that this is a differing assumption to that used by Dickinson *et al* where no 'fibre bunching' is modelled.

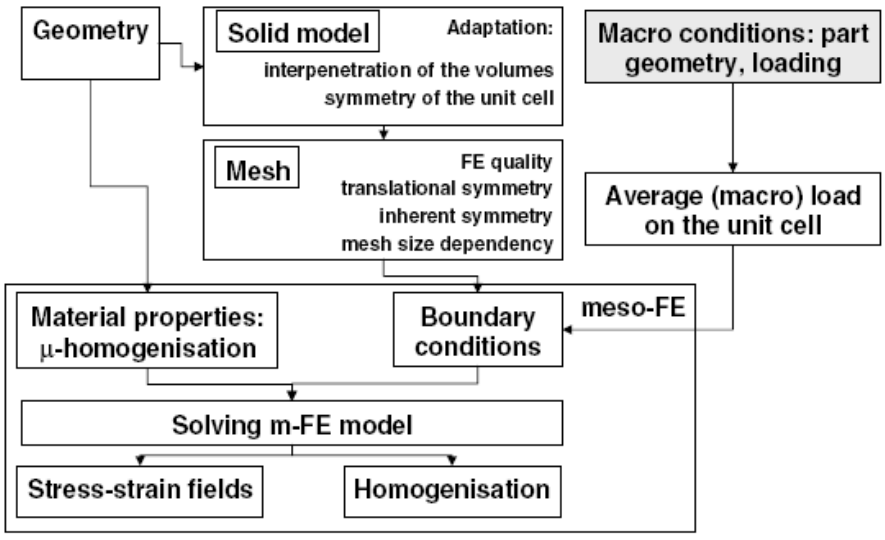

Figure 3.5: Road Map for linear meso-FE modelling produced by Lomov *et al*[95]

In the meso-scale approach the material is split into small UD sub cells incorporating geometric features such as resin rich zones. The stiffness matrix of the material is then calculated in the FE analysis based on known empirical formulae such as those proposed by Hashin, and Chamis[96-99]. In the results Lomov *et al* reported good agreement between the FE and the formulae of Chamis for Young's moduli and shear moduli but the Poisson's ratio v_{23} showed a noticeable variation. Two FE packages (ANSYS and SACOM) were used to carry out the analysis. The results showed good agreement between FE, experimental and CLT values for the Young's moduli and reasonable agreement for the Poisson's ratio values.

Bogdanovich provided a good account of the various approaches used to model 3-D woven type composites[100](and references therein). The methods presented are generally a lot more complex than is required to model Z-pinned laminates. In the current context a unit cell containing both in-plane fibres and Z-pinning can be modelled owing to the relatively simple internal geometry of the material. This modelling technique would provide an alternative to the Dickinson approach and should not increase the complexity of the FE models by any considerable amount.

3.2.1.5 Unit Cell/RVE Construction

The FE approaches discussed above all rely on unit cell analysis to obtain the effective elastic properties. There are a couple of key factors in the construction of a unit cell. The first is to correctly break down a large structure to a smaller repeating volume element (RVE) or unit cell. It is important at this time to be sure of the symmetry that has been used to reach the final unit cell geometry. The second task is to apply the appropriate boundary conditions for the unit cell under consideration. Only application of the appropriate boundary conditions will lead to an accurate result, and clearly the boundary conditions will differ depending on the unit cell geometry and symmetry properties.

Taking the example of Li[101], if one assumes a two-dimensional microstructure of a square lay-out containing equally spaced, equally sized inclusions then a square grid used to reduce the problem size can be moved anywhere within the *xy* plane without affecting the translational symmetry properties of the unit cell as shown in Figure 3.6(b). When the unit cell is to be meshed for FE analysis the most desirable solution is to choose a unit cell whose boundaries do not intersect the boundaries of the inclusion. The desirable unit cell choice is presented in Figure 3.6(c).

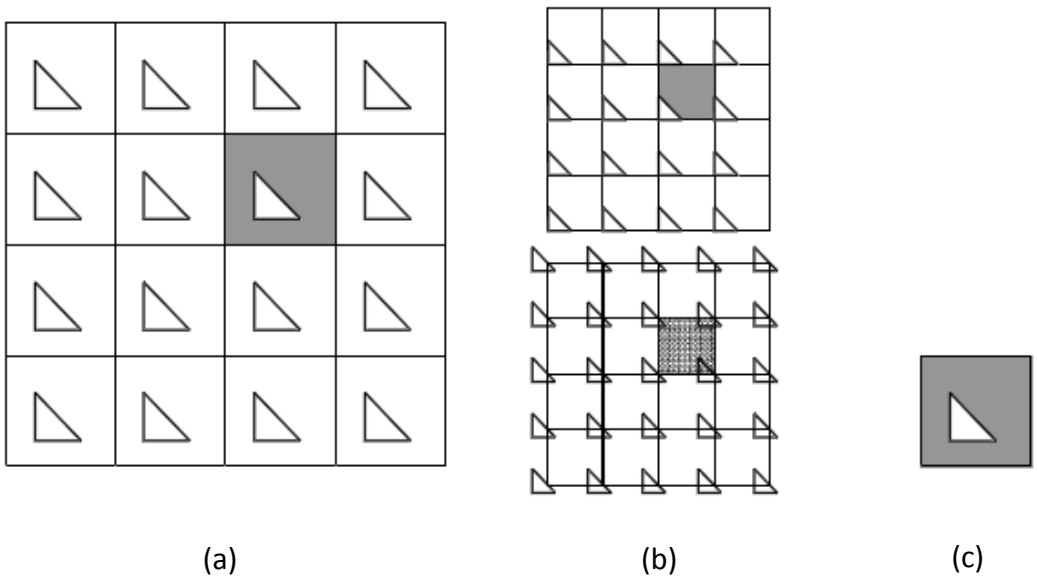

Figure 3.6: 2D unit cell generation for square packed inclusion arrangement; (a) tessalation grid, (b) movement of grid without affecting the translation symmetry properties of the unit cell, (c) desirable unit cell geometry[101]

If the microstructure shown in Figure 3.6 is idealised to the form shown in Figure 3.7, then the smallest unit cell using just translational symmetries is shown in Figure 3.7(b). By making use of reflectional symmetries the unit cell can be reduced to that shown in Figure 3.7(c). The unit cells shown in Figure 3.6(c) and Figure 3.7(c) now look identical but it is important to recall the symmetry processes used to obtain the unit cells. This affects the boundary conditions that need to be implemented; the unit cell in Figure 3.6(c) requires boundary conditions with equations relating the displacements on opposite sides of the unit cell. Due to the reflectional symmetry this is not required for the unit cell in Figure 3.7(c). A second issue with the unit cell utilising reflectional symmetry is that some microscopic

strain states are anti-symmetric and as a result the number of boundary conditions can change depending on the loading case.

Reflectional symmetry may also be taken advantage of by having the unit cell geometry intersect the inclusion as shown in Figure 3.8. The final unit cell is classed as a quarter size and is only possible where the inclusions have symmetric properties. In the context of fibre based composite systems this is useful as the fibres are often assumed to be circular or elliptical in shape which can allow this kind of symmetry to be used.

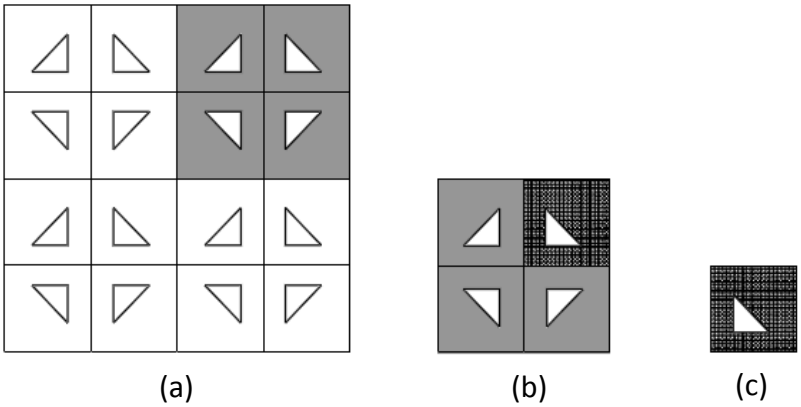

Figure 3.7: 2D unit cell generation for square packed inclusion arrangement with reflectional symmetry; (a) tessalation grid, (b) smallest unit cell using translational symmetry, (c) reduced unit cell size using reflectional symmetry[101]

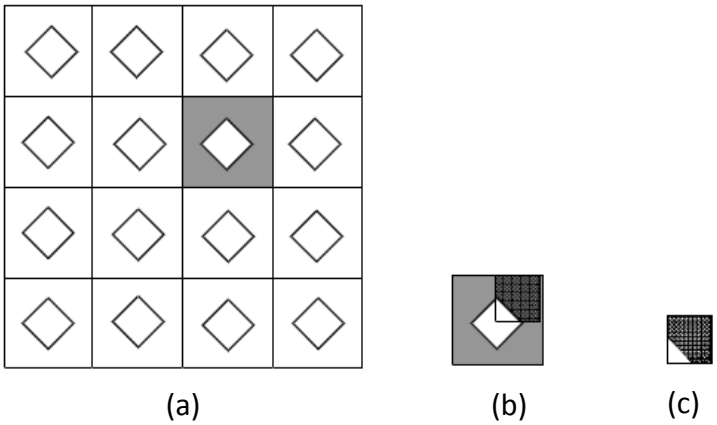

Figure 3.8: 2D unit cell generation for square packed inclusion with reflectional symmetry through the inclusion; (a) tessalation grid, (b) smallest unit cell using translational symmetry, (c) reduced unit cell size using reflectional symmetry through the inclusion[101]

In the current work the unit cells produced have to be three dimensional due to the form of the reinforcement i.e. the inclusion of in-plane fibres and through-thickness reinforcement. Therefore the boundary conditions for 3-D unit cells are explored.

3.2.1.5.1 3-D Unit Cell Constructed Using Translation Symmetry Only

When modelling a UD material using a unit cell approach the general formulation is to use a 2-D unit cell as this has enough information to characterise the materials. This is covered by Li with many other works cited within this reference[102]. In order to find work on the construction of 3-D unit cells one must look towards unit cells for particle reinforced composites for a wide range of references[103-108] (and references therein). There are also a handful of references relating to unit cells for woven composites[95, 109, 110]. The application of boundary conditions is dependent on the smallest available unit cell. The smallest unit cells can vary greatly in their geometry going from simple cubic formations for cubic particle arrangements to multi-faceted cells for arrangements such as body centred cubic and face centred cubic packings[111]. In the present application the unit cells can be restricted to simple cubic packaging as the simplest formulations so the boundary and loading conditions investigated are for simple cubic packing only.

A good account of the construction of a 3-D unit cell using only translational symmetry is given by Li and Wongsto[111]. Following their approach a cubic packing of particles (these particles can be in the form of fibre-like cylinders) can lead to a cubed Voronoi cell such as that shown in Figure 3.9. This cell is bounded by three sets of planes, namely

$$\begin{aligned} x &= \pm b \\ y &= \pm b \\ z &= \pm b \end{aligned} \qquad \textbf{3-1}$$

where b is the largest radius of a particle or cylinder which will fit into the unit cell.

A major part of using a unit cell approach is the application of appropriate displacement boundary conditions. To do this, one must define the translational symmetry. In the present case if the unit cell shown in Figure 3.9 is taken with an arbitrary point *P* then any point *P** within the material but outside of the unit cell can be found as the image of *P* under a translational symmetry. The coordinates of the points are related by the following expression given by Li and Wongsto[111]

$$\left(x^*, y^*, z^*\right) = \left(x + 2ib, y + 2jb, z + 2kb\right) \qquad \textbf{3-2}$$

where *P** is *i*, *j* and *k* unit cells away from *P* in the *x*, *y* and *z* directions respectively.

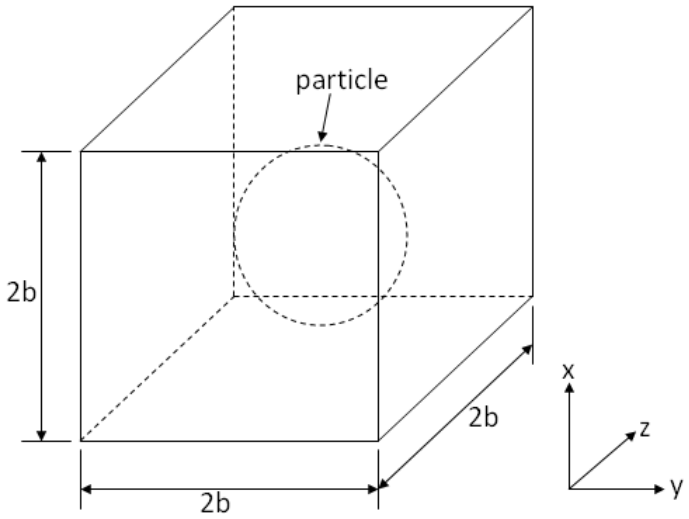

Figure 3.9: Voronoi cell for simple cubic packing

In order for a micromechanical analysis to be carried out the displacement boundary conditions must be prescribed on all six surfaces of the cube. Li and Wongsto arrive at the following expressions for the displacement boundary conditions on each pair of faces

$$\begin{aligned}
&\left(u\big|_{x=b} - u\big|_{x=-b}\right)\Big|_{y,z} = 2b\varepsilon_x^0 \\
&\left(v\big|_{x=b} - v\big|_{x=-b}\right)\Big|_{y,z} = 0 \\
&\left(w\big|_{x=b} - w\big|_{x=-b}\right)\Big|_{y,z} = 0
\end{aligned} \qquad \textbf{3-3}$$

$$\left(u\Big|_{y=b}-u\Big|_{y=-b}\right)\Big|_{x,z}=2b\gamma_{xy}^{0}$$
$$\left(v\Big|_{y=b}-v\Big|_{y=-b}\right)\Big|_{x,z}=2b\varepsilon_{y}^{0} \qquad \textbf{3-4}$$
$$\left(w\Big|_{y=b}-w\Big|_{y=-b}\right)\Big|_{x,z}=0$$

$$\left(u\Big|_{z=b}-u\Big|_{z=-b}\right)\Big|_{x,y}=2b\gamma_{xz}^{0}$$
$$\left(v\Big|_{z=b}-v\Big|_{z=-b}\right)\Big|_{x,y}=2b\gamma_{yz}^{0} \qquad \textbf{3-5}$$
$$\left(w\Big|_{z=b}-w\Big|_{z=-b}\right)\Big|_{x,y}=2b\varepsilon_{z}^{0}$$

The faces of the unit cell are indicated in the above terms by $\Big|_{x=b}$ and $\Big|_{x=-b}$, and $\Big|_{x,y}$ highlights the common coordinates between the two faces. Li and Wongsto now raise an important issue regarding the application of the boundary conditions; which is that the equations given above are not independent for the corresponding points on the edges of each face i.e. the above equations can be prescribed on the faces of the unit cell but not on the edges and vertices. This is due to edges being shared by two faces (or three faces for vertices). The task then is to obtain independent conditions between the edges. To do this, the edges must be constructed into sets where each set is independent of the other edge sets. This requires that there are four sets, each containing three edges. This was neatly shown by Li and Wongsto in the diagram shown in Figure 3.10. In the image a set of edges could include any three edges which lie in different directions (*x*, *y* and *z* directions) such as edges *I*, *V* and *IX*. Expressions are given relating the edges from one set with those of another (e.g. relating edge *I* with edges *II*, *III* and *IV*) which leads to a complete set of boundary conditions for the unit cell. The same process must also be carried out for the vertices. The equations given by Li and Wongsto[111] are then enough to define the displacement boundary conditions of the unit cell.

Further conditions must be placed on the unit cell in the form of traction boundary conditions. In this case the traction boundary conditions are deemed natural boundary conditions and are all zero i.e. traction should not be imposed as a boundary condition but may be included as an external load.

The final problem to overcome is the application of loads to the unit cell. In the approach outlined above there are two ways of doing this. Each of the boundary conditions used in the above approach utilise macroscopic strains which in the work by Li can be treated as independent degrees of freedom for the system[102, 112] i.e. the macroscopic strains introduce six extra degrees of freedom to the system. This being the case, the first method of applying load is to impose macroscopic strains as loads. Equally, macroscopic stresses can be applied by imposing concentrated forces to the degrees of freedom. The second application is detailed in the reference[111] using an energy equivalence approach.

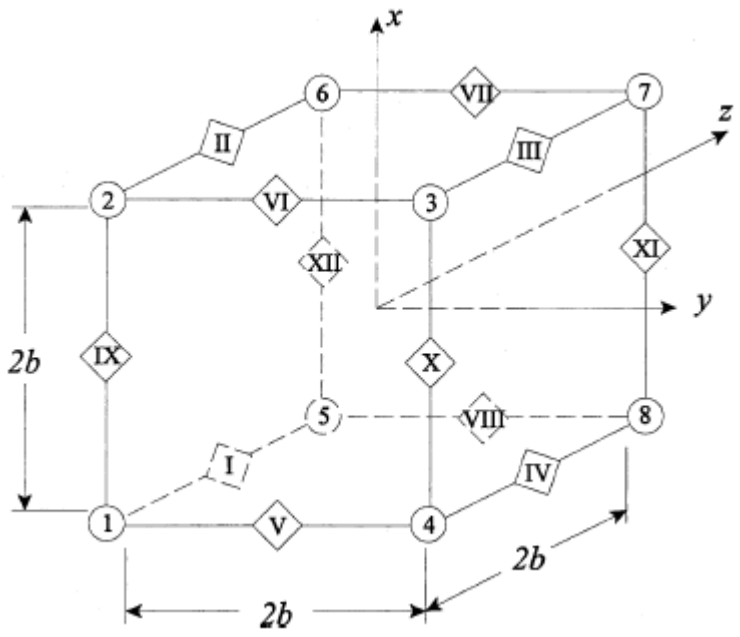

Figure 3.10: Cubic unit cell show edges (Roman numerals) and vertices (Hindu-Arabic numerals)[111]

A note must be given that when using a unit cell utilising translational symmetry in an FE approach care must be taken with regards to the meshing of the unit cell. The restriction is that the mesh must translate exactly from one face to its opposing face. Any disregard for this condition will lead to an incorrect result.

3.2.1.5.2 3-D Unit Cell Construction Using Reflectional Symmetry

In many applications it is desirable to make use of reflectional symmetry (as in Figure 3.7 and Figure 3.8) to simplify the problem to be analysed. In order to do this a new set of boundary and loading conditions must be prescribed to obtain a

solution. The problem has been approached by Weissenbek[108] (and references therein) for Particle reinforced materials resulting in an output similar to that of Li[101]. The problem is tackled clearly by Li and will be followed where appropriate in this study.

The first task is to assume a 3-D unit cell with reflectional symmetry. An example (developed from the 2-D unit cell in Figure 3.7) is shown in Figure 3.11. The sides of the final unit cell in Figure 3.11(b) have the dimensions b_x, b_y and b_z. A key issue when utilising reflectional symmetries is that loading cases must be considered separately as the boundary conditions may change depending on the desired load. Li[101] derived the boundary conditions using the symmetries as used in Figure 3.11.

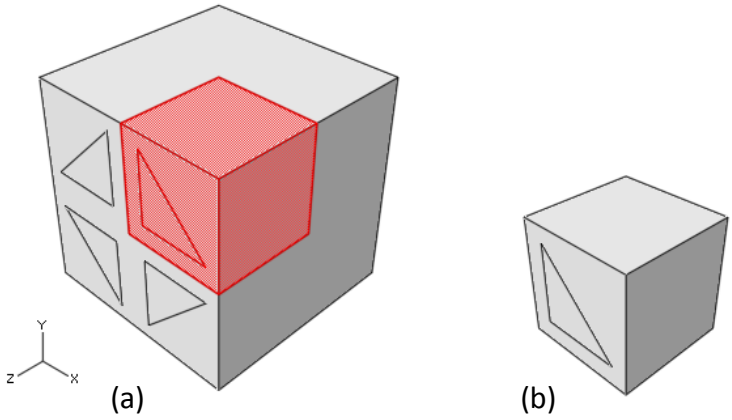

Figure 3.11: 3-D unit cell with reflectional symmetry

Li starts by considering just the *x*-faces of the unit cell and assumes that a stimulus σ_x^0 is symmetric under reflection in the *x*-plane. With these conditions the response *v*, *w* and σ_x are symmetric and *u*, τ_{xy} and τ_{xz} are anti-symmetric. Then considering the face $x=b_x$ the only condition then to apply is on the face of the unit cell lying normal to the *x*-axis at $x=b_x$. This introduces the term ε_x^0 and as with the unit cell created with translational symmetries ε_x^0 is an extra degree of freedom introduced to the model and load can be prescribed through this point. The other conditions are free conditions or natural boundary conditions for shear which should not be imposed. The same approach given above can then be used for the *y* and *z*-faces introducing further degrees of freedom ε_y^0 and ε_z^0. The result is that six

boundary conditions exist on the three pairs of sides of the unit cell under a macroscopic stress σ_x^0

$$
\begin{aligned}
&u\big|_{x=0} = 0 \\
&u\big|_{x=b_x} = b_x \varepsilon_x^0 \\
&v\big|_{y=0} = 0 \\
&v\big|_{y=b_y} = b_y \varepsilon_y^0 \\
&w\big|_{z=0} = 0 \\
&w\big|_{z=b_z} = b_z \varepsilon_z^0
\end{aligned}
\qquad \textbf{3-6}
$$

The extra degree of freedom ε_x^0 is subjected to a concentrated force to produce σ_x^0. This is the only force applied, such that the unit cell is subjected to a uniaxial stress state σ_x^0. The same approach was used by Li to produce boundary conditions for a unit cell subjected to uniaxial stress states σ_y^0 and σ_z^0.

Further boundary conditions must be prescribed for shear stress states. Following Li's example one may consider a shear stress τ_{yz}^0. In the reference[101], Li highlights the extra complexity involved in prescribing boundary conditions for shear stresses in unit cells containing reflectional symmetry. The issue arises from the fact that one shear stress will be symmetric, whilst the two remaining shear components are anti-symmetric.

The prescription of boundary conditions continues in a similar way to that of the direct stress components. Taking first the reflection about the *x*-plane, the shear component τ_{yz}^0 is symmetric. The responses *v*, *w* and σ_x are therefore symmetric and *u*, τ_{xy}^0 and τ_{xz}^0 are anti-symmetric. Ultimately Li arrives at:

$$
\begin{aligned}
&u\big|_{x=0} = 0 \\
&u\big|_{y=0} = w\big|_{y=0} = 0 \\
&u\big|_{z=0} = v\big|_{z=0} = 0 \\
&u\big|_{x=b_x} = 0 \\
&u\big|_{y=b_y} = w\big|_{y=b_y} = 0 \\
&u\big|_{z=b_z} = 0 \;\&\; v\big|_{z=b_z} = b_z \gamma_{yz}^0
\end{aligned}
\qquad \textbf{3-7}
$$

where γ_{yz}^{0} is introduced as an extra degree of freedom through which a load can be prescribed. The same approach can be used to obtain the boundary conditions for the two other shear loading cases.

The boundary conditions presented here are adequate for the work carried out in this study but there are some important restrictions in place. The unit cells using translational symmetry are broadly applicable in all cases in this study. However, it is important that during meshing the nodes on opposing sides are truly translational as any error here will give rise to an inaccurate result.

In order to simplify problems it is desirable to make use of reflectional symmetry. The work by Li[101] demonstrates that under reflectional symmetry different boundary conditions are required for axial and shear loading and this must be adhered to. Furthermore, the use of reflectional symmetry is restricted to UD and cross-ply laminates in the current study as angle-ply laminates do not contain the appropriate reflectional symmetry. It is also important to point out that the equations presented in this review are applicable only to cubic unit cells.

3.2.2 Analytical Approaches

The theories examined in this study are all micromechanics approaches. FRPs can be considered on different scales and be characterised as homogeneous, quasi-homogeneous or inhomogeneous. The characteristic changes depending on the scale considered for the material. At the macroscopic level FRPs are generally considered as quasi-homogeneous materials i.e. the material properties are independent of location within the material. This approach does not differentiate between the matrix and reinforcing constituents. This approach is rarely sufficient to predict properties of three-dimensional materials as the predicted material response does not demonstrate any differentiation between fibres and matrix. Micromechanics methods have generally been favoured for property prediction of three-dimensional materials. In this approach the constituents and the local strains and stresses are differentiated along with their interactions. A number of reviews of these micromechanics approaches exist in the literature encompassing various

approaches[97, 98, 113-115]. Some of the approaches in these references are not listed here.

3.2.2.1 Voigt and Reuss Approach

A common micromechanics approach used to obtain composite material properties is the bounding method. Two bounding methods will be used in this study to assess their suitability for predicting the effective elastic properties of Z-pinned UD and cross-ply carbon/epoxy laminates. The first bounding approach used is the simplest approach. The method is to assume that the material exhibits a macroscopic uniform stress or uniform strain response to loading. If one assumes a uniform stress state then the effective complimentary strain energy is given by

$$U_c^{eff} = \frac{1}{2}\int_V \sigma^T S \sigma dV \qquad \textbf{3-8}$$

Where *S* is the compliance matrix given by

$$[S] = \begin{bmatrix} 1/E_1 & -\nu_{21}/E_2 & -\nu_{31}/E_3 & 0 & 0 & 0 \\ -\nu_{12}/E_1 & 1/E_2 & -\nu_{32}/E_3 & 0 & 0 & 0 \\ -\nu_{13}/E_1 & -\nu_{23}/E_2 & 1/E_3 & 0 & 0 & 0 \\ 0 & 0 & 0 & 1/G_{23} & 0 & 0 \\ 0 & 0 & 0 & 0 & 1/G_{13} & 0 \\ 0 & 0 & 0 & 0 & 0 & 1/G_{12} \end{bmatrix} \qquad \textbf{3-9}$$

Reuss used the uniform stress assumption across all constituents in a composite material to obtain the complimentary strain energy[116]

$$U_c^{\text{Reuss}} = \frac{1}{2}\left(\int_{V_m} \sigma^T S^m \sigma dV + \int_{V_f} \sigma^T S^f \sigma dV \right) \qquad \textbf{3-10}$$

where *m* and *f* denote the matrix and fibre constituents respectively. If one assumes energy equivalence then

$$U_c^{eff} = U_c^{\text{Reuss}} \qquad \textbf{3-11}$$

it is then a simple task to find S^{eff}, where using energy equivalence

$$\frac{1}{2}\int_{V}\sigma_i S_{ij}^{eff}\sigma_j = \frac{1}{2}\int_{V_m}\sigma_i S_{ij}^{m}\sigma_j dV + \frac{1}{2}\int_{V_f}\sigma_i S_{ij}^{f}\sigma_j dV \qquad \textbf{3-12}$$

and cancelling out the uniform stress components

$$S_{ij}^{eff} = \left(S_{ij}^{m}V_f^{m} + S_{ij}^{f}V_f^{f}\right) \qquad \textbf{3-13}$$

This calculation yields a lower bound for the compliance matrix and hence the mechanical properties. In a similar manner the upper bound can be calculated by assuming a uniform strain as demonstrated by Voigt[117] where the effective stiffness matrix C^{eff} is given as

$$C_{ij}^{eff} = \left(C_{ij}^{m}V_f^{m} + C_{ij}^{f}V_f^{f}\right) \qquad \textbf{3-14}$$

where

$$\left[C\right] = \left[S\right]^{-1} \qquad \textbf{3-15}$$

It was demonstrated by Hill that the Reuss and Voigt values bound the actual overall moduli with no restriction placed on the geometry of the phases under consideration[118]. However, the approach is only applicable to elastic materials. The use of Voigt and Reuss' approach was presented by the author at the Composites 2009 conference in London along with supporting FE analysis[119].

The biggest issue with this simple bounds approach is that it assumes uniform stress or strain throughout the composite. However, in reality there is a complex and non-uniform response throughout all constituents within the material under different loading conditions. Various works have attempted to overcome this problem. One proposal is the bridging model by Huang[120, 121]. The key feature of this approach is to link the average stress states in the matrix and the fibre by a bridging matrix

$$\left\{d\sigma_i^{m}\right\} = \left[A_{ij}\right]\left\{d\sigma_j^{f}\right\} \qquad \textbf{3-16}$$

where the superscripts *m* and *f* refer to the matrix and fibre phases respectively. This seems like a logical approach but there are issues surrounding the formulation of the bridging matrix. The bridging matrix can be expressed as

$$\left[A_{ij}\right]=\begin{bmatrix}\left[a_{ij}\right] & 0\\ 0 & \left[b_{ij}\right]\end{bmatrix} \qquad \textbf{3-17}$$

where $[a_{ij}]$ and $[b_{ij}]$ are 3x3 sub-matrices. As seen in ref [121] the calculation of the terms in $[a_{ij}]$ and $[b_{ij}]$ are dependent on the parameters α_{ij} which are determined through experiments or numerical simulations. Huang does present an analytical approach to obtain the parameters α_{ij} allowing use of the bridging matrix without experimental analysis but this introduces a level of 'play' in the results. Recommendations are given for parameter values but these are not strict for every material to be analysed, leading to the possibility of a range of results. A comparison for results of E_{22} and G_{12} between the bridging model, Chamis' formulae[96] and experimental results is given showing a good agreement between both analytical approaches and the experimental data. However, no indication is given by Huang as to what values of the parameter α_{ij} are used. In terms of presented results these parameters may be used as a 'fiddling' factor, turning the use of the bridging model into an elaborate curve fitting exercise. Therefore, as a predictive tool the bridging model appears to be flawed.

The second approach followed in the present study is a bounding approach brought about from variational principles. This is followed due to the advantages that a bounds approach can give to engineers and designers alike. The bounds approach provides upper and lower limits for the elastic properties of the material under consideration. In terms of design this provides a built-in safety mechanism when predicting the stiffness of materials. Another distinct advantage is that although the problems may be complex in their derivation, they generally provide elegant mathematical solutions requiring only constituent data such as the constituent volume fractions and the constituent material properties.

3.2.2.2 Walpole's Bounds

The variational bounding approach to be used in this study is that set out by Walpole[122, 123]. The purpose of the work in this study is to assess the validity of this often used bounds approach to Z-pinned FRP materials. As a result the theory is examined in the literature survey to demonstrate its origins and formulation.

The problem of obtaining the effective moduli of composite materials is a long standing question and one which is yet to be categorically answered. The rule of mixtures approach leads to an immediate question which was tackled by Brown[124]. Suppose a material is made of two constituents, can the effective moduli of the composite be determined by knowing just the moduli of the constituents and their volumes? In the case of Brown the task was to assess this question for the effective magnetic permittivity of two phase materials but the question applies equally to the determination of elastic properties in multiphase materials. Brown found that the effective magnetic permittivity of two phase materials is not adequately defined by the moduli and volumes of the phases and Hashin and Shtrikman concluded that the same result could be expected for the prediction of elastic properties of composites[125]. As a result, Hashin and Shtrikman set about obtaining bounds for the effective elastic properties of composites containing isotropic inclusions by using variational principles[125]. The first effort by Hashin and Shtrikman applied to composites containing isotropic inclusions undergoing prescribed surface displacements but was later extended to cases with anisotropic phases and prescribed surface tractions[126, 127]. The first of these references provides proof of the problem whilst the second demonstrates the process of obtaining bounds for the elastic moduli of general isotropic multiphase materials. Although in reference[127] Hashin and Shtrikman apply their theory to composites containing polycrystals it is stated in [127] that the theory is applicable to composites of arbitrary phase geometry. The theory has also been used previously in the literature with respect to FRPs[128, 129] and hence there appear to be no restrictions beyond the known assumptions (indicated at the end of this section), on its application to fibre based systems.

Walpole's approach is very similar to Hashin and Shtrikman's approach with a key difference involving what Hashin termed the "subsidiary problem"[127]. In the following section Walpole's theory is outlined and a more in depth derivation of the theory is provided in Appendix 4 to aid the reader in fully grasping the approach. The derivation is provided in the Appendix as some parts of the derivation are skipped over in the original reference[122].

Walpole's bounds overcome the issues of assuming uniform stress or strain through the composite by imposing what is termed as the stress polarization tensor p_{ij}. This idea was introduced by Eshelby[130] and allows for a differentiation of the stresses between phases. Similarly, q_{ij} is the strain polarization tensor. The polarization tensors are combined with a comparison material, also used by Hill and Hashin and Shtrikman[126, 127, 131], in order to manipulate the boundary value problem.

Consider a volume V with n different homogeneous phases where a phase 'r' has a volume V_r. In Walpole's notation the tensor of elastic moduli of phase r is denoted as L_r with its inverse M_r. In the current text these are referred to as the stiffness matrix C_r and its inverse, the compliance matrix S_r respectively, as used in the Reuss[116] and Voigt[117] values in Chapter 3.2.2.1. The tensors, C_r and S_r are considered to be symmetric and positive definite as for real materials. A comparison material is then chosen with tensors C_0 and S_0 where the comparison material is chosen as being homogeneous and real such that each tensor is symmetric and positive definite.

Two boundary-value problems are stated. In the first a displacement is prescribed over the surface of the considered region. The composite material is replaced by the comparison material and a strain field ε is defined such that $\sigma^*=C_0\varepsilon+\tau$ (where σ^* is the approximated stress field) is self-equilibrated.

The second problem is similar but traction is prescribed over the surface of the considered region. A stress field σ is defined in the comparison material so that the strain field $\varepsilon^*=S_0\sigma-\eta$ (where ε^* is the approximated strain field) can be derived from a continuous displacement.

In the present analysis approximate fields are made by choosing polarizations and these are then inserted into the classic extremum principles to bound the overall energy; from this the overall moduli can also be bound. It is stated in ref[123] that piecewise-uniform polarization fields are the most general form from which the required averages can be calculated using the known information and the best values are noted as:

$$\begin{aligned} \tau &= \left(C_r - C_0\right)\overline{\varepsilon}_r, \\ \eta &= \left(S_0 - S_r\right)\overline{\sigma}_r \end{aligned} \qquad \textbf{3-18}$$

where $\overline{\varepsilon}_r$ and $\overline{\sigma}_r$ are the averages over V_r of ε and σ (The real strain and stress fields within the composite).

Appropriate manipulation of the boundary value problems sees the first problem result in

$$2U = \overline{\varepsilon} C \overline{\varepsilon} \le -\sum \int_{V_r} \varepsilon_r^{'} \left(C_0 - C_r\right) \varepsilon_r^{'} dV_r + \sum V_r \overline{\varepsilon} C_r \overline{\varepsilon}_r \le \sum V_r \overline{\varepsilon} C_r \overline{\varepsilon}_r = \overline{\varepsilon} \overline{C} \overline{\varepsilon} \quad \textbf{3-19}$$

if $\left(C_0 - C_r\right)$ *is semi positive definite*

This leads to the main theorems of Walpole's theory;

If C_0-C_r is (for all r) positive (negative) semi-definite then so is $\overline{C} - C$

If S_0-S_r is (for all r) positive (negative) semi-definite then so is $\overline{S} - S$ **3-20**

Following from the above theorems, the aim is to obtain the strain field ε, generated by the polarization stress τ. The strain field $\varepsilon^{\dagger}$ produced by the distribution of body forces is derived from the displacement

$$u_i^{\dagger}\left(r\right) = \int G_{ij} \left[\tau_{jk}\right] n_k dS + \int G_{ij} \tau_{jk,k} dV \qquad \textbf{3-21}$$

where the comma (,) denotes differentiation.

The surface force $\left[\tau_{ij}\right] n_j$ comes as a result of the equilibrium conditions on the discontinuity surfaces, where [ ] indicates the discontinuity across the interface in the outward normal direction to the inclusion surface n_i. This problem was

presented first by Eshelby[130] and was described as the 'subsidiary problem' by Hashin and Shtrikman[126].

The form of the displacement in 3-21 is adjusted by applying Gauss's formula (Divergence theorem) $\int_{\Omega} f_{i,i} d\Omega = \oint_{\partial\Omega} f_i n_i dS$, resulting in

$$u_i^{\dagger}(r) = -\int \frac{\partial G_{ij}}{\partial \xi_k} \tau_{jk} dV \qquad \textbf{3-22}$$

It is at this point that Walpole's theory deviates from the bounds approach put forward by Hashin and Shtrikman. Ultimately, the Hashin Shtrikman approach utilises Fourier methods in order to compute the bounds of the energy *U*. Walpole made use of the Green's function G_{ij} in his approach leading to a reduction in the mathematical limitation imposed by the limits of integration in the Fourier transformation[98].

To calculate the Green's function one must start with the displacements *u*, *v* and *w* as given by Love[132]. The final form of the displacement u_i as given by Love can be generalised as

$$u_i = \frac{1}{4\pi\mu}\frac{1}{r}F_i - \frac{\lambda+\mu}{8\pi\mu(\lambda+2\mu)}\frac{\partial^2 r}{\partial x_i \partial x_j}F_j \qquad \textbf{3-23}$$

The displacement given above is used to give the Green's function as used by Walpole

$$G_{il} = \frac{1}{4\pi\mu_0}\frac{\delta_{il}}{r} - \frac{(\lambda_0+\mu_0)}{8\pi\mu_0(\lambda_0+2\mu_0)}\frac{\partial^2 r}{\partial x_i \partial x_l} \qquad \textbf{3-24}$$

where κ_0 and μ_0 are the comparison material bulk and shear modulus respectively. It must be noted that the derivation of this Green's function is for isotropic materials only and as a result the comparison material is limited in this formulation to isotropic properties only.

To obtain the strain field $\varepsilon_{ij}^{\dagger}$ one must differentiate 3-22 and after suitable determination of the average fields in 3-19, Walpole arrives at

$$\overline{C} = \left(\sum c_r \left(C_0^* + C_r \right)^{-1} \right)^{-1} - C_0^* \qquad \textbf{3-25}$$

where C_0^* is referred to as the 'overall constraint tensor' by Walpole and is defined as

$$C_{0\ ijkl}^{\ *} = \kappa_o^* \delta_{ij}\delta_{kl} + \mu_0^* \left(\delta_{ik}\delta_{jl} + \delta_{il}\delta_{jk} - \frac{2}{3}\delta_{ij}\delta_{kl} \right) \qquad \textbf{3-26}$$

where μ_0^* and κ_0^* are the comparison material 'overall constraint' shear and bulk moduli respectively and δ_{ij} etc are Kronecker delta. The overall constraint tensor, shear and bulk modulus are in relation to the comparison material containing a void. Such that the comparison material, along with the polarisation stress or strain can be used to obtain the equivalent material elastic properties.

Dually it follows that

$$\overline{S} = \left(\sum c_r \left(S_0^* + S_r \right)^{-1} \right)^{-1} - S_o^* \qquad \textbf{3-27}$$

where $\overline{S} = \overline{C}^{-1}$.

Equations 3-25 and 3-27 are now sufficient to obtain bounds on the elastic properties of a composite material following the theorems set out by Walpole in equation 3-20:

Denote $\overline{C}$ as $\overline{C}^p$ when $\left(C_0 - C_r \right)$ is positive semi definite for all *r*. The theorem says that $\left(\overline{C}^p - C \right)$ is also positive semi definite, i.e. $\overline{\varepsilon}\overline{C}^p\overline{\varepsilon} \geq \overline{\varepsilon}C\overline{\varepsilon}$. **3-28**

Denote $\overline{C}$ as $\overline{C}^n$ when $\left(C_0 - C_r \right)$ is negative semi definite for all *r*. The theorem says that $\left(\overline{C}^p - C \right)$ is also negative semi definite, i.e. $\overline{\varepsilon}\overline{C}^n\overline{\varepsilon} \leq \overline{\varepsilon}C\overline{\varepsilon}$ **3-29**

Thus, $\overline{\varepsilon}\overline{C}^n\overline{\varepsilon} \leq \overline{\varepsilon}C\overline{\varepsilon} \leq \overline{\varepsilon}\overline{C}^p\overline{\varepsilon}$ **3-30**

It is also of note that when C_0* is set to zero or infinity then the result of Reuss and Voigt are returned. Walpole's theory will be employed to evaluate the bounds of effective elastic properties for Z-pinned laminates and to obtain the

tightest bounds it is important that L_0-L_r is chosen such that it is semi-positive/semi-negative definite and this must be true for every phase *r*.

As with any theory there are certain assumptions and restrictions in Walpole's theory which must be pointed out. The first assumptions are that the material under consideration is elastic and large enough that the effective properties are effectively independent of the tractions and displacements on the material surfaces. Furthermore the theory is restricted to the material being treated as macroscopically homogeneous and the material surfaces must be macroscopically uniform. It is stated by Walpole[122], and earlier by Hashin and Shtrikman[127] that the phase geometry may be arbitrary.

A key restrictive factor of the theory is the form of the Green's function used by Walpole. This is derived for an isotropic material and this limits the choice of a comparison material to an isotropic one. Clearly this means that the theory will perform best when only isotropic phases are analysed but it is still applicable to anisotropic phases[123]. In later references Walpole tackles the problem of anisotropic phases[123, 133] but the approach does not seem satisfactory with regards the implementation of the comparison material. This is because the derivation of the Green's function is retained and as a result should only be applicable to isotropic materials. A derivation incorporating an anisotropic material would allow better characterisation of composites with anisotropic materials but the resulting formulae needed to fully characterise a CFRP would be extremely complex.

3.3 Experimental Observations on Z-pinned Laminates

In order to assess the reliability of the analytical work to be demonstrated later in the thesis it is important that experimental observations be utilised. This is a cornerstone of assessing analytical work, as demonstrated by the World Wide Failure Exercise. For this reason a brief account on experimental observations for Z-pinned composites is given. However, providing this account is not easy since whilst there is a fair amount of experimental literature available on stitched composites, the same cannot be said of Z-pinned laminates. The general conclusion

for stitched composites is that the interlaminar delamination strength is vastly improved with the application of stitching whilst the effect on the in-plane properties appears to have divided opinion, as summarised by Mouritz *et al*[134]. Many accounts in the literature appear to contradict each other with some accounts suggesting a degradation of the in-plane materials whilst other studies demonstrate no change or a slight improvement of the in-plane properties.

It would be easy to apply all of the findings for stitched composites to Z-pinned laminates but this would be very naïve. Some of the features reported to increase the degradation of in-plane properties in stitched composites simply do not apply to Z-pinned laminates. One cited problem is the damage of in-plane fibres during the stitching process. This is less likely to occur in Z-pinned laminates due to the manufacture process. In stitching, the up and down movement of the threading needle is likely to snag and break the in-plane fibres; however, in the application of Z-pins there is only one slow movement of the Z-pin into the laminate which is likely to reduce the chances of in-plane fibre breakage. The impact of damaged in-plane fibres on the mechanical properties has been disputed by Herszberg and Bannister[135] who proposed that rather than fibre breakage, fibre spreading is a likely cause of a degradation of in-plane properties. This is said to occur in the thickness and transverse directions in stitched composites but in reality, fibre spreading in the thickness direction is more likely to be limited in Z-pinned composites. This is because the Z-pin is applied during a pressurised curing process which will constrain the in-plane fibres from moving whereas stitches are applied to cloths of fibres and then impregnated with matrix material. It is likely that the stitching process will incur more fibre waviness and laminate thickness variation. In-plane fibre movement must still occur in Z-pinned laminates due to the displacement of fibres with the insertion of Z-pins.

A further issue regarding the application of experimental observations of stitched composites to Z-pinned materials is the effect on the laminate surface of stitch loops. These stitch fibres run across the top and bottom of the laminate and are said to reduce the in-plane properties due to kinking of the outer plies. Farley demonstrated that removal of these surface loops (creating through-thickness

reinforcement similar to tufting) improved the in-plane compressive strength of Kevlar and carbon fibre laminates by 7-35%[136]. Clearly these surface loops are not present in Z-pinned laminates and this is a further area where experimental results for stitched composites cannot be applied to Z-pinned structures.

As discussed above it is difficult, if not impossible, to use experimental data of stitched composite to characterise the trends in material properties of a composite upon the application of Z-pins. Furthermore, searches of the literature demonstrate that there is very little in the way of experimental studies on Z-pinned composites. Partridge and Cartie produced a study regarding the delamination resistance of Z-pinned laminates[137] as this is one of the primary parameters that is targeted for improvement with Z-pin reinforcement. They concluded that any application of Z-pins resulted in resin rich pockets filling the area in which laminate fibres were pushed apart. They also presented results showing that under Mode I loading the Z-pins were pulled out of the resin envelope and the friction associated with this was a major mechanism for energy absorption. They also acknowledged that under shear loading the failure mechanism is highly complex with the Z-pin undergoing bending deformation prior to shear failure.

Steeves and Fleck provided an account on the 'knockdown' in in-plane properties of T300/914C and IMS/924C carbon/epoxy laminates[94]. They reported that although the in-plane tensile and compressive strengths were reduced by 27% and at least 30% respectively, the in plane stiffness was unaffected. This is demonstrated by the stress strain curves presented in Figure 3.12. They determined that the drop in compressive strength values came as a direct result of the fibre misalignment in the fibres adjacent to the Z-pins. The worst fibre misalignments occurred where fibres weaved through the field of Z-pins. When a single row of pins was used and no weaving was present the compressive strength was concluded to be the same as the equivalent unpinned laminate.

Steeves and Fleck also used a unit cell analysis to predict the strength of Z-pinned laminates[94]. These authors created two-dimensional FE models using T300/914C laminates with models using 6-noded triangular plane-strain elements.

Fibre curvature due to the Z-pins was modelled with misalignment angles taken from visual studies of Z-pinned laminates. The resin rich zone and the Z-pin were modelled as voids within the material with the justification that the stiffness of the matrix material is much lower than that of the laminate. The model predicts that microbuckle failure occurs from the Z-pin as was observed in the experimental analysis. The predicted strength values for Z-pins applied along the *x*-axis direction were in good agreement with experimental results. However, the predicted strengths for laminates with Z-pin patterns located at 23° and 45° to the *x*-axis were much higher than the experimental results. This was put down to the determination of fibre misalignment for the unit cell.

A further experimental study was carried out by Troulis[93]. It was found that the laminate thickness in the region of a Z-pin was around 8-10% greater than the average thickness of the composite. It is unclear as to whether this is due to the Z-pin protruding from the surface, in-plane fibre misalignment or matrix material being displaced from inside the laminate to the surface. However, it was confirmed that Z-pinning inflicts minimal damage to the in-plane fibres. During testing of delamination resistance it was noted the resistance was a function of the laminate thickness, Z-pin insertion depth, Z-pin density and Z-pin diameter and that an increase in any of these parameters lead to an increase in delamination resistance. An examination of in-plane properties was also given showing reductions in E_1 and E_2 of 12% and 14% respectively for IM7/M21 laminates. However, a fair amount of scatter was noted, particularly regarding the prediction of E_2. Furthermore, in-plane shear testing demonstrated that there was little change in S_{12}, regardless of the level of Z-pin diameter and areal density. Troulis states that the reduction in fibre volume fraction either side of the Z-pin (in the resin rich zones) was a key factor in the degradation of in-plane properties but there was no discussion on the increase in fibre volume fraction due to the bunching of fibres in the transverse direction as mentioned by Mouritz *et al*[134].

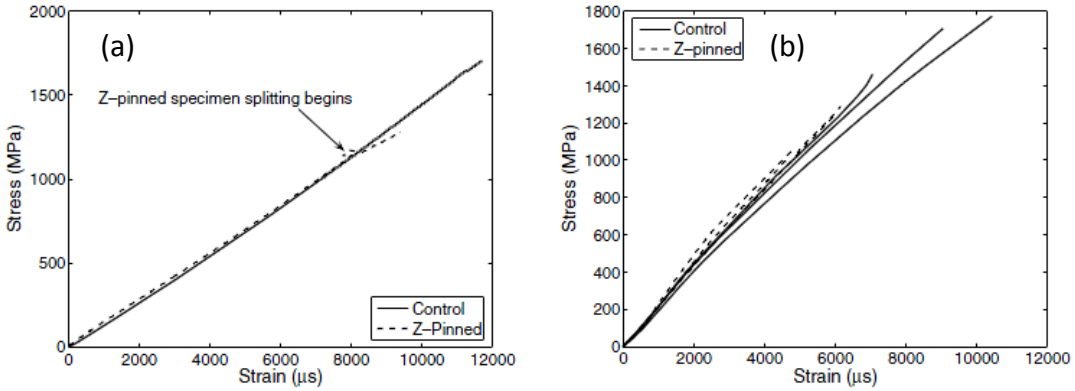

Figure 3.12: Stress strain curves for pinned(Z-pin) and unpinned(control) specimens of UD IMS/924C obtained by Steeves and Fleck; (a) In-plane tension test, (b) In-plane compression test[94]

A clear issue with the available experimental data is that it is very contradictory regarding the in-plane stress strain response with Steeves and Fleck reporting slight improvements in in-plane elastic properties whereas Troulis shows degradation of these properties. However, there is an agreement that Z-pinning improves the through-thickness response.

A very good account of the current state of through-thickness reinforced composites analysis is given by Mouritz and Cox[138]. This work covers 3D woven, stitched and Z-pinned composites. In the current work the focus is on Z-pinned laminates however, the work by Mouritz and Cox is extremely useful in highlighting the similarities and differences of the effects of different Z reinforcement methods.

Mouritz and Cox comment that there is *uncertainty and conflicting data concerning the degree to which through-thickness reinforcement degrades in-plane mechanical properties*[138]. Furthermore, it is highlighted that the link between through-thickness reinforcement specification (reinforcement spacing, density etc) and the effect of in-plane properties has rarely been presented. However Mouritz and Cox do acknowledge that the in-plane mechanical properties of through-thickness reinforced laminates are controlled by the fibre architecture, defects and fibre volume fraction. Commonly 3D woven laminates have a [0/90] lay-up whilst stitched and pinned laminates can have any desired lay-up. Mouritz and Cox also suggest that through-thickness reinforcement takes up 0.5-10% of the mid-plane area and the typical diameter of stitches and pins is 0.1-1.0mm.

Mouritz and Cox give a good discussion on the introduction of defects to the laminate during the insertion of Z direction reinforcement[138]. 3D weaving often applies the reinforcement through the warp and weft toes and can penetrate the thickness of the laminate without damaging fibres. However, stitches and pins are usually forced into dense packs of fibres and as a result damage can be caused. As a result of this, stitches are normally only applied to dry pre-forms as the tacky resin in pre-pregs sticks to the needle and causes damage as the needle runs in and out of the laminate. However it is extremely difficult to use Z-pins with dry pre-forms as the pins do not maintain their position within the dry fibres, although the damage caused by inserting Z-pins into pre-pregs is not as severe as stitching as there is only one movement, minimising the build up of resin on the Z-pin.

A further issue regarding the Z-pin manufacture process is that Z-pins are usually installed manually. This results in less consistent properties throughout the laminate making analysis even more difficult. 3D weaving and stitching on the other hand are usually machine controlled processes which generally allows for a more uniform laminate.

One similarity between all three methods of through-thickness reinforcement is that distortion of the in-plane fibres is always found. This has to be the case due to the replacement of in-plane fibres with through-thickness reinforcement. Fibre misalignment is said to be between 5-20°. This range is significant and further issues can arise from the fact that this range can be witnessed in a single laminate (rather than from specimen to specimen). There is great difficulty in reporting this misalignment due to the lengthy time it takes to analyse the area around even one reinforcement fibre. To analyse a whole series of laminates would take an incredible amount of effort. One method discussed by Mouritz and Cox to ease the job is X-Ray tomography. However, the whole job is made easier in common pinned laminates due to the pre-pregs used. Pre-pregs usually have uniformly spaced fibres and as a result the in-plane fibre misalignment due to pinning tends to be more uniform than in 3D woven and stitched laminates.

Mouritz and Cox also present a small discussion on the issue of in-plane fibre volume fraction in the region of through-thickness reinforcement fibres[138]. However, as with the vast majority of work discussed in this literature review they comment that fibre volumes could both increase or decrease. However, they do state that the Z-pinned laminates suffer more greatly from a decrease in the in-plane fibre volume fraction due to the laminate thickness usually increasing. Again, as recorded elsewhere it is noted that experimental characterisation of defects is limited and potentially unreliable.

The discussion of results available in the literature given by Mouritz and Cox is limited to cases where the equivalent 2D data was also given i.e. experimental data for unreinforced laminates. The authors explain that the most important in-plane stiffness is the modulus E_1 in the most dominant fibre direction. In stitched and 3D woven laminates it is shown that there is only a small impact in E_1 regardless of the level of through-thickness reinforcement. In some cases, particularly in stitched laminates there is a rise in E_1. For stitched laminates this is true under tension, compression and under bending. The effect on E_1 seen in pinned laminates is largely dependent on the lay-up considered. UD laminates suffer from a drop in E_1 with an increase in Z-pin volume fraction. Mouritz and Cox present normalized E_1 values by dividing the measured E_1 with Z-pins present by the E_1 value of the unreinforced laminate. The drop in recorded E_1 under tension in UD laminates with a 4% Z-pin volume fraction is around 25%. However, this value drops to around 10% in [0/90] cross ply laminates and no significant drop was found in [0/+45/-45/90] quasi-isotropic laminates.

The rise in E_1 witnessed in stitched composites is said to be due to the increase in in-plane fibre volume fraction which occurs when the stitches are applied whilst the dry pre-form is under tension. Mourtitz and Cox propose that the greatest increase in E_1 that could be expected is around 10%. Any further increase is met by scepticism from the authors. Any reduction in E_1 is said to be due to a reduction in the number of fibres. This predominantly occurs as the in-plane fibre content reduces due to thickening of the laminate. The link between the reduction of in-plane fibres and the reduction of E_1 has been demonstrated for pinned

composites but not for stitched or 3D woven laminates[138]. The authors also note that fibre breakage and resin rich zones will not have a big impact on the elasticity of the system.

It is shown in the reference that the tensile strength of 3D woven and stitched laminates can either increase or decrease depending on the study. Furthermore, these results are largely statistically insignificant. That even a robust review paper is unable to show statistical significance in results demonstrates that further attention needs to be paid to parameters such as the manufacture method and constituent material features. This would allow for results to be categorised and grouped to allow for appropriate comparison.

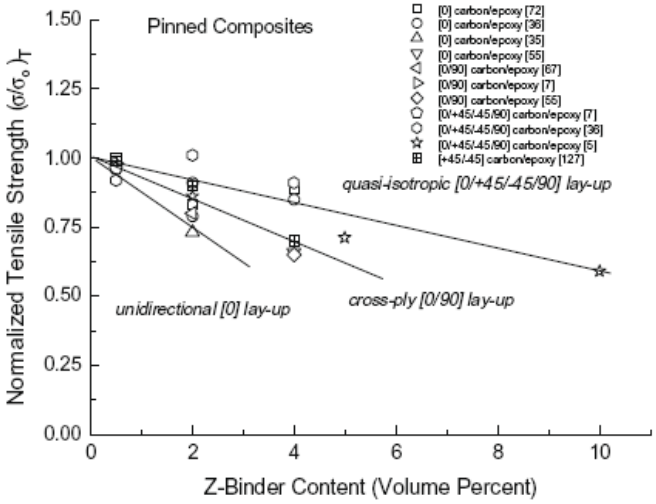

Figure 3.13: Effect of Z-pin content on the normalized tensile strength of pinned composites[138]

The authors appear more sure about pinned composites by stating that the tensile strength of such laminates will always decrease with increasing Z-pin volume. However, looking at the graph presented in Figure 3.13 it is clear that there is still an issue with validity. The normalized strength of a pinned composite of UD lay-up is shown to be approximately 0.6 at a Z-pin volume fraction of 3% via the line of fit that is presented by Mouritz and Cox. However, looking at data for Z-pin volume fractions of 4%, there are data points for UD lay-ups showing normalized tensile strengths of 0.9-0.95. This raises doubt over their initial line of best fit presented, again highlighting the ambiguity of the effect of implementing

through-thickness reinforcement. The decrease in strengths were explained to be down to fibre misalignment, fibre breakage and the forces induced at the edge of the resin rich zones due to the applied tensile force.

The general result for the compressive strength of 3D woven, stitched and pinned laminates is the same as for the tensile strength. Compressive strengths are shown to increase and decrease for different examples of 3D woven and stitched composites whilst pinned composites always showed a decrease in strength.

Possible reasons mooted for any compressive strength increase are that the through-thickness reinforcement increases the delamination resistance and hence the compressive strength is increased. Strength decreases are most likely formed when the in-plane fibres are diverted from their normal path and the diversion acts as a site for kink formation. Fibre kinking then occurs at lower loads than normal, hence reducing the compressive strength.

Mouritz and Cox conclude by stating that the in-plane static properties are affected for 3D woven, stitched and pinned composites and all in different ways[138]. In the context of the current work they say that the in-plane properties of pinned composites are never increased. The data that they present backs this claim but the extent of the knockdown in properties appears to be overstated as demonstrated by the graph in Figure 3.13 where the line of best fit indicated is not close to the entire range of data presented. Furthermore, the authors can only make enlightened predictions on the mechanisms acting on the through-thickness reinforced composites examined. This again highlights the issue of a lack of reliable test data and the contradictory stance of the data that are currently available.

3.4 Conclusions

In Chapter 3.1 various methods of through-thickness reinforcement were presented. There are two basic types of through-thickness reinforcement with one being complex three-dimensional fibre architecture such as braided, knitted and woven composites. The second type is that of applying through-thickness reinforcement to pre-cured laminates (stitching, tufting and Z-pinning). Generally these are run vertically through the thickness of the laminate but can be angled

and in the case of stitches the fibres can loop over each other. In the present work the second type of reinforcement is examined.

There are a number of approaches taken for finite element modelling of through-thickness reinforced composites. In the present application the work of Dickinson *et al*, Steeves and Fleck and Grassi *et al* is relevant due to their focus on Z-pinned laminates. The general approach has been to model the 'base' composite on the macroscopic level whilst modelling the Z-pin and incorporating resin rich zones and fibre bending due to the presence of through-thickness reinforcement. Work by Lomov *et al* was discussed and whilst the intention of the work was to predict the properties of three dimensional composites with highly complex fibre architecture the principles are applicable to Z-pinned composites. In the approach the fibres and matrix are all modelled separately with the fibre orientation adjusted along the fibre length. This is a mesoscopic approach and could provide a more detailed result than the simpler models used by Dickinson *et al* and Grassi *et al*.

An important feature of all of the FE modelling approaches is the use of unit cells (RVEs) in order to simplify the problem to be analysed. The use of unit cells is very important in order to reduce the size of the problem such that small details such as the Z-pin geometry can be incorporated. However, extreme care must be taken as unit cell analysis requires the accurate application of boundary conditions in order to provide a correct result. Furthermore, a major assumption in unit cell analysis is that the unit cell is repeated exactly, making it difficult to model irregular material features such as voids.

Various theories exist to analyse the effective elastic properties of FRP composites. The basic energy approach using Voigt's and Reuss' assumptions were demonstrated and will be used later in the thesis. These formulations assume uniform strain and uniform stress respectively throughout all of the constituents. In reality the strain and stress in each constituent i.e. the fibres and matrix, will vary greatly due to the differing material properties between the phases in certain load cases. Huang overcame this problem by introducing a 'bridging' matrix that links the stresses in each constituent. However, there are certain issues regarding the

calculation of the bridging matrix where ideally, experiments should be carried out to obtain certain parameter values. Another classic approach uses variational principles to produce bounds on the overall elastic properties. These are advantageous as they require only the constituent material properties and volume fractions as input data. A derivation of Walpole's theory was given to show some key steps and proofs that were overlooked in the original references. The theory borrows ideas from Hashin and Shtrikman, Eshelby and Hill. To overcome the problem of differing stress responses between constituents a polarization tensor is used. Allied to this is the introduction of a suitable comparison material. Ultimately the derivation arrives at an equation (given above as eq 3-25)

$$\bar{C} = \left(\sum c_r \left(C_0^* + C_r \right)^{-1} \right)^{-1} - C_0^* \qquad \textbf{3-25}$$

which can be used to obtain the effective stiffness matrix for the material under consideration. Although the derivation is reasonably lengthy the final formulation is user friendly. To obtain bounds of the effective elastic moduli one must set the comparison material to be semi-positive and semi-negative definite.

Regarding experimental work it is important that the correct observations are made. Widely available experimental results for stitched composites are not desirable for analysing materials predictions of Z-pinned composites due to subtle differences in manufacture and final materials. However, one common feature between experimental observations for stitched and Z-pinned composites is that different works are often contradictory. This mostly manifests itself with regard to in-plane properties of through-thickness reinforced composites and the justification of the results. Ultimately this makes justification of any analytical results a very difficult process as the chances are they will agree with some experimental trends but contradict others.

4 Useful Techniques for Investigating Through-Thickness Behaviour of Carbon Fibre Laminates

Before discussing the experimental study and their outcomes it is important to outline the tools and techniques used in obtaining and analysing the results. The tools and techniques, including statistical techniques, FE tools and testing tools are discussed in this chapter.

4.1 Finite Elements

In order to assess the test specimens and composite types to be presented thorough validations and investigations were carried out employing finite element analysis (FEA). The FE package used and key considerations are outlined here.

4.1.1 The Finite Element Package

The FE package used for all work was Abaqus CAE, versions 6.6 to 6.9. This is a popular commercial FE code which can be used for a wide variety of modelling. In the majority of cases described in the following chapters the FE package was used to create models using 3-D solid elements. In all cases 8-noded solid 3-D hexahedral elements were used and all cases were assumed to be linear elastic. In order for a unit cell model to be created properly it should include the model geometry, material data, section assignments and load and boundary conditions as well as the type of analysis to be carried out. The tasks required to complete a model are catered for in a series of modules included in Abaqus/CAE. An outline of the modules is given below as they are included in Abaqus.

Part: The part module allows the user to create the initial part(s) in a sketcher or by importing geometry from another program such as Pro Engineer Wildfire. The model type (deformable, discrete region, analytical region), feature shape (solid, shell, wire, point) and feature type (extrusion, revolution, sweep) are defined in this step. The part module also allows the part geometry to be modified or deleted and provide a means to partition the model which can be useful for the meshing process.

Property: The property module allows the user to create materials and sections. Material inputs cover a wide variety of choices allowing various types of analysis (e.g. elastic, plastic, thermal, electrical). Once a material is created a section should then be created using the material and then this should be applied as a section of the model. Multiple materials and sections can be created. This module also allows datum points, axes, planes and coordinate systems to be created. In the case of anisotropic material sections it is important that a local coordinate system is defined. In more recent versions of Abaqus/CAE (version 6.7 onwards) there is also a composite lay-up process in the property module. This allows the user to assign layers to the part in a semi-automatic manner to model composites with homogeneous layers.

Assembly: In the assembly module the user can translate the various parts within a global coordinate system such that there is one complete assembly made up of various instances. Even if only one part is used an assembly must be made as load and boundary conditions are applied to the assembly, not the part. The assembly can also be partitioned like the part.

When creating an instance the user will be asked to define whether the instance is dependent or independent. A dependent instance means that the part is meshed whilst an independent instance means that the mesh is applied to the assembly. By default the instance type is dependent.

Step: The step module includes the set-up of a change in the model and a sequence of steps can be created. Commonly there may only be one load step where various loads are available (static, dynamic, heat transfer, thermo etc). The step module also allows the user to submit output requests.

Interaction: The interaction module allows the user to set up interaction definitions between various areas of the model. This allows for example, equation, rigid body or tie constraints to be imposed as well as interactions such as contact conditions. These interactions are step-dependent and as a result the active step must be indicated.

Load: The load module allows the user to define loads (concentrated force, moment, pressure etc), boundary conditions, fields and load cases. Again, these are step-dependent so the active step must be indicated.

Mesh: This module allows the user to assign a mesh on the part or assembly. This allows the user to change the element type, mesh density and local mesh features as well as visualising the mesh. There is also a mechanism for verifying the mesh.

Job: The job module is used to analyse the created model. In the creation of a job the user can define the amount of memory applied to the analysis etc. Once a job is created it can be used to write an input file, data checked or submitted. Once submitted, an input file is created and carried out whilst the user has the option to monitor the progress of the job.

Visualisation: The visualisation module allows the user to view the job results in graphical form. Various data can be obtained from the graphical representation as well as the data requested as outputs in the step module.

All of the above modules will be required to create and carry out and analyse a finite element model using Abaqus/CAE.

4.1.2 Finite Element Sanity Checks

Whilst constructing each model, sanity checks were carried out in order to clarify that the FE work was valid. These checks were conducted in various ways. The first check is for a multi-material model, such as a model of a composite where the fibre and matrix are modelled separately (as used in Chapter 8). In these instances the case is first run using the material properties of a homogeneous isotropic material for all the constituents. Running the model with these material properties under a range of loading conditions allows for an investigation of the constituent interfaces and of the applied boundary conditions. Application of inappropriate boundary conditions will result in an incorrect stress/strain response which will be highlighted in a model where each constituent has the same isotropic properties (where no variation of the stress/strain response should be present).

Another important issue with FEA is the mesh sensitivity of the cases being studied. The suitability of the mesh can be determined by carrying out a convergence check for the mesh density. A typical convergence check can be carried out using:

$$\left|\frac{\sigma^{j}-\sigma^{i}}{\sigma^{j}}\right|<\alpha \qquad \textbf{4-1}$$

This should be carried out at a region of high stress variation where errors are likely to occur. The stresses, σ_i and σ_j are taken at the location of stress variations for models with *i* and *j* elements. α is a user defined variable which is a positive number. Adjusting this value sets the level of convergence. For the work presented here α was set to 0.02 (2%). This was deemed suitable as it would be below the expected experimental variation.

4.2 Testing Machines

For experimental characterisation of the through-thickness behaviour of composite laminates it is important that materials are tested under pure shear, tensile and compressive conditions. Universal testing machines are commonly used to carry out tests as they can be used for a wide range of cases. They can be used for all the pure tensile and compression tests presented in the literature and can also be used for a wide range of the shear test methods available.

In the current study, compression tests were carried out using two test machines; a 200KN load cell Instron 4507 test machine and an Amsler hydraulic compression test machine. The Instron was controlled by a local control unit attached to the equipment and the Amsler was controlled by a PC. In both cases the applied load was displacement controlled with a cross head speed of 0.5mm/min. Strain data was collected from the strain gauges at a rate of 30 measurements per minute with all data being saved to a USB flash drive. Before specimen testing a compliance test was carried out on each loading device to obtain the values of machine deformation which could then be taken into account during result analysis.

4.3 Strain Measurement

For any mechanical materials testing, the deformation or strain measurement is highly important. In general there are two main methods of strain measurement to have been used in the literature on through-thickness testing of composites. These are resistance strain gauging and the optical technique, Moiré interferometry. In the current study resistance strain gauging is used and a brief overview of the technique is given below.

Resistance strain gauging is the favoured method of measuring strains in the literature. In this case a foil strain gauge is adhered to the material under consideration. Each strain gauge has a certain parameter called a gauge factor *K*, which has a basic relationship with the resistance of the gauge and the strain it is being subjected to.

$$K = \frac{\Delta R}{R\varepsilon} \qquad \textbf{4-2}$$

where *R* is the resistance of the gauge and *ε* is the strain. This relationship means that the strain can be observed from the change in resistance when the gauge factor is known. Unfortunately, in most applications the strains are too small to give noticeable changes in the resistance. As a result the Wheatstone bridge is commonly used. This converts the small changes in resistance into a voltage which can be amplified and the strain taken from this. An example of a quarter bridge operation is shown in Figure 4.1

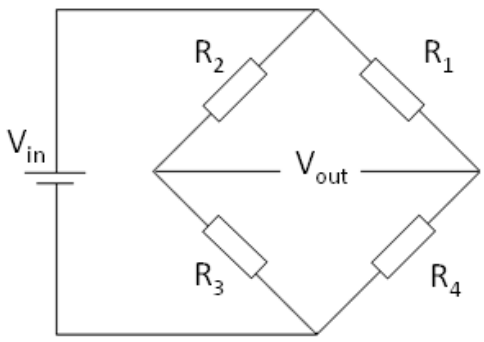

Figure 4.1: Wheatstone bridge

The principle of the Wheatstone bridge is that when all the resistances are the same i.e. R_1=R_2=R_3=R_4 then the bridge is balanced and the output voltage V_{out} is equal to zero. Therefore there is no strain on the system. When using a Wheatstone bridge for a single strain gauge one of the resistors is replaced with a strain gauge. This acts as a variable resistor when the gauge is subjected to strain which will unbalance the system. When the system is unbalanced the output voltage is no longer zero and can be used to obtain the strain:

$$V_{out} = \frac{K\varepsilon N V_{in}}{4} \qquad \textbf{4-3}$$

where V_{in} is the voltage applied to the bridge and N is the number of active sections of the bridge. In the case of a quarter bridge there is one active section (the strain gauge) so N is equal to 1.

One issue with standard foil strain gauges is that they cannot be used to measure large strains as they are limited by a lack of ductility. This can be combated by using post yield gauges. These are made using a ductile metallic grid with a highly ductile polymer backing.

The strain gauges used in the tests were predominantly post yield gauges. Two tests were carried out using standard foil gauges. Before the gauges were installed the surfaces of the specimens were polished and cleaned. Cleaning is required to ensure that no grease or debris lies on the specimen surface which could affect the adherence of the strain gauge. Subsequent to cleaning the surface of the specimen, marks are made to align the gauges. Next a cyanoacrylate adhesive was used to attach the strain gauge to the specimen surface. All the gauges used were 2mm in length and had a resistance of 120Ω. Each gauge was used alone and formed part of a quarter bridge. Three wires were soldered to each gauge to connect it to the quarter bridge.

4.4 Data Processing

In order to obtain stress/strain data the load and strain information were supplied from the testing machine and strain gauges respectively to a PC in Microsoft Excel format. The data were then transferred to a USB flash drive and

processed using Excel. The stress value was calculated for each specimen by measuring the cross sectional area of the specimen gauge length using a micrometer and then the stress, σ can be calculated using

$$\sigma = \frac{Load}{Area} \qquad \textbf{4-4}$$

The strength value was taken where the load value on the stress strain curve dropped suddenly, indicating that there was a large decrease in the load carrying capability of the test specimen.

Initial Young's modulus and Poisson's ratio were calculated using a linear regression technique. Rather than drawing a line of best fit by eye the method of least squares determines the line of best fit by calculation. For a linear relationship which is expected for the initial strains of specimens under through-thickness compression the straight line can be defined as having the relationship:

$$y = a + bx \qquad \textbf{4-5}$$

This equation relates to n set of plotted data points (x_1, y_1), (x_2, y_2)…(x_n, y_n) such that the sum of the squares of the distances between the straight line to the given set of data points is a minimum. The sum of the squares of the distances between the straight line and the data points is given as:

$$S = \sum_{i=1}^{n} \left(y_i - a - bx_i \right)^2 \qquad \textbf{4-6}$$

a and b in equation 4-6 must be determined such that S is a minimum and for this to be the case:

$$\frac{\partial S}{\partial a} = -2\sum_{i=1}^{n} \left(y_i - a - bx_i \right) = 0 \quad \text{and} \quad \frac{\partial S}{\partial b} = -2\sum_{i=1}^{n} x_i \left(y_i - a - bx_i \right) = 0 \qquad \textbf{4-7}$$

Rearranging the equations in 4-7 gives the values of a and b as:

$$a = \frac{\sum_{i=1}^{n} y_i - b\sum_{i=1}^{n} x_i}{n} \quad \text{and} \quad b = \frac{n\sum_{i=1}^{n} x_i y_i - \sum_{i=1}^{n} x_i \sum_{i=1}^{n} y_i}{n\sum_{i=1}^{n} x_i^2 - \left(\sum_{i=1}^{n} x_i \right)^2} \qquad \textbf{4-8}$$

The linearity of the data can only be expected for data in the low strain region as beyond this the material may exhibit non-linear behaviour. Care must also be taken to avoid readings from very low strains as there is a risk of incorrect strain values being recorded in this region. In all the experimental analysis carried out the initial elastic properties were calculated between strains of 0.5% to 3%. The data in this region were found to be linear and without any initial loading effects.

4.5 Statistical Analysis

It is a useful exercise to observe the scatter of experimental results. This information indicates how repeatable any experiment was. A simple calculation of the scatter is the coefficient of variation, given by:

$$C_v = \frac{\sigma_{sd}}{\mu_m} \qquad \textbf{4-9}$$

where σ_{sd} is the standard deviation and μ_m is the population mean. This can only be used for data where the mean is non zero and where the mean is close to zero (as in data for the Poisson's ratios) the C_v can be greatly affected by small changes in the mean value.

In order to calculate the coefficient of variation, the mean μ_m of the data is given by:

$$\mu_m = \frac{\sum_{i=1}^{n} x_i}{n} \qquad \textbf{4-10}$$

Following this the standard deviation σ_{sd} for the data is given by:

$$\sigma_{sd} = \sqrt{\frac{1}{n}\sum_{i=1}^{n}\left(x_i - \mu_m\right)^2} \qquad \textbf{4-11}$$

The coefficient of variation has been used widely in the literature to give an indication of the repeatability of tests.

4.6 Through-Thickness Compression Test Specimen; Material Manufacture and Preparation

The aim of this chapter is to provide some directions for the manufacture and preparation of the test specimens examined in this thesis. The approaches presented are given from the experience of the author and should provide the reader with knowledge of the best methods and order of manufacture for each specimen.

4.6.1 Laminate Manufacture

As detailed in chapter 2.7, three specimens were chosen for investigation under through-thickness compressive loading. These specimens are the waisted specimen, parallel sided specimen and hollow cylinder specimen. All three specimens were manufactured using the same $[45/-45/90/0]_{ns}$ quasi-isotropic, AS4/8552 carbon/epoxy laminates. Each of the blocks had a fibre volume fraction of approximately 60%. The pre-preg material was manufactured by Hexcel and the specimens were cut from two large blocks of the laminate material. The material was manufactured by QinetiQ without the assistance of the author but the method of manufacture used is detailed below. It should be noted that the curing cycle depicted in Figure 4.4 is for guidance only and details of the exact cycle used were unavailable to the author.

For thick laminates such as those to be tested here the best method of manufacture is to use an autoclave process as shown in Figure 4.2. This process is widely used to create high-performance composites for use in aerospace, marine and military applications. Importantly the process is capable of good consolidation of thick composite lay-ups and can produce laminates with high fibre volume fractions.

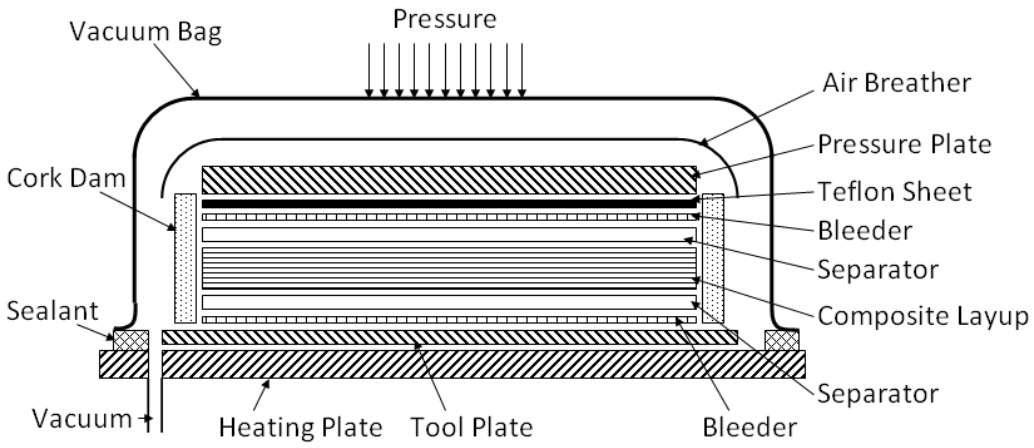

Figure 4.2: Autoclave molding layup assembly

Pre-preg material was used to construct the laminates investigated in this study. UD pre-preg sheets with a cured thickness of 0.25mm were first cut to shape and then laid up to form $[45/-45/90/0]_{ns}$ laminates with cured thicknesses of 28mm and 40mm. The bleeder layer shown in Figure 4.2 is used to absorb any excess resin that is present through curing. A typical curing cycle is presented in Figure 4.3. This process begins at room temperature and is heated at a rate of 2-4°C/min to a temperature of 110-125°C under a full vacuum. This allows the resin to become mobile and removes any foreign particles. This condition is maintained for one hour and then a pressure of around 0.7MPa is applied and the vacuum removed. The temperature is again increased at a rate of 2-4°C/min up to a temperature of 175°C and held for 2 hours. The part is then left to cool down to room temperature. This should be a highly controlled process to avoid residual stresses and material defects.

The two composite laminate blocks were received from *Q*ineti*Q* with no further processing. The blocks were then marked out to create smaller sections from which seven waisted specimens, seven cylindrical specimens and eight parallel sided specimens could be manufactured.

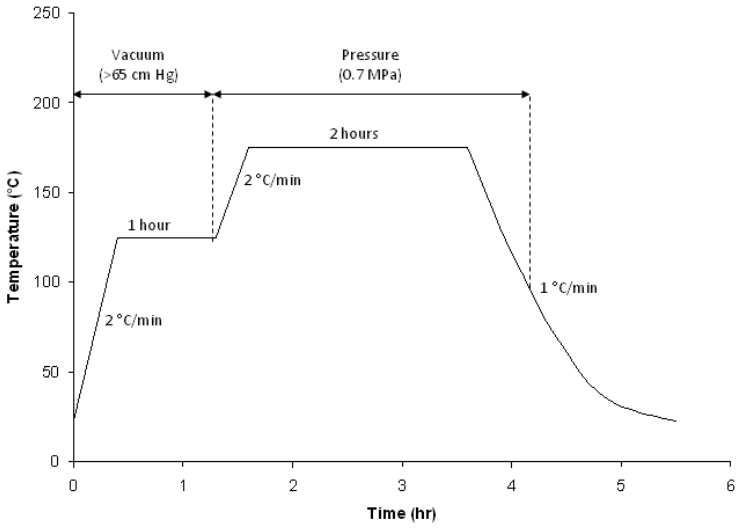

Figure 4.3: Typical curing cycle for carbon/epoxy laminates[33]

4.6.2 Laminate Cutting

4.6.2.1 Laser Cutting

Due to the abrasive nature of the material and the thickness of the laminates a decision had to be made on cutting the composite. The first method attempted was laser cutting in a bid to keep the cost of cutting as low as possible (the costs were low as the equipment was readily available to the author). The laser used was a Powerlase 400 W Q-switched DPSS (diode pumped Nd:YAG) laser. This method has been demonstrated in the literature by Lau *et al*[139].

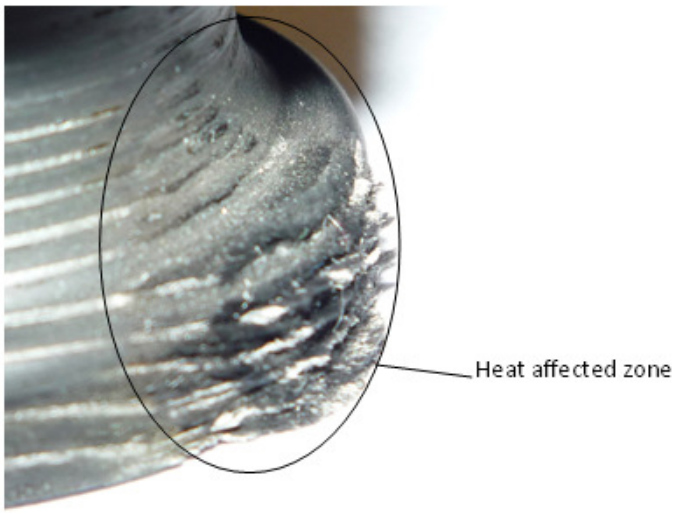

Figure 4.4: Carbon fibre showing heat affected zone from laser cutting

The laser is applied as a pulse to limit heat generation within the composite. With laser cutting, heat generation is a huge problem as it can severely damage the matrix material. Not only does this make the material unusable, it also produces toxic gases and as a result laser cutting must always be carried out in a thoroughly ventilated area. Ultimately it was found that the material was too thick to cut using lasers. The heat distribution through the thickness of the material was uneven and at every attempt the matrix material melted leaving loose carbon fibres as shown in Figure 4.4. As a result lasers were abandoned as a cutting tool.

4.6.2.2 Abrasive Cutting

The approach used after laser cutting was an abrasive method, favoured in the machining and cutting of carbon fibre. A diamond edged cutting wheel was used in a Struers Labotom-3 cut-off machine. The material was clamped into the machine to ensure that it did not slip during processing and water coolant was applied directly to the cutting wheel to ensure that the material was not subjected to excessive heat. This abrasive method proved to be effective at cutting the carbon/epoxy laminates to size but the biggest draw-back of this approach was the cost of tooling due to the requirement of a new diamond edged cutting wheel.

4.7 Specimen Machining

When the two large blocks had been cut into smaller sections they were machined in various ways to produce the waisted, cylindrical and parallel sided specimens.

4.7.1 Parallel Sided Specimens

The thickness of the parallel sided specimens was reduced using the cutting wheel and was then polished using finishing sandpaper with a grade of 320. Care was taken to ensure that the laminate remained symmetric about the mid-plane of the specimen i.e. the two central layers of the specimen were 0°. A micrometer was used to check the finished specimens and all dimensions were found to have a tolerance of ±0.1mm. Care was also taken to ensure that the ends of the specimen were parallel to each other by grinding the specimens and measuring the height of the specimen at various locations around the cross-section. Each face was also

visually checked for any ply waviness and to ensure that each face was perpendicular to any connected faces.

4.7.2 Waisted Specimens

The waisted specimen proved to be the most difficult to manufacture. During the machining process two of the seven specimens fractured and were no longer useable. One of the reasons for the difficulty in manufacture is the abrasiveness of the carbon/epoxy material. This led the machine tools to wear out quickly and when the tools became blunt they damaged the specimens.

The specimens were machined using a computer numerical controlled (CNC) machine in order to obtain controlled dimensions. The grinding of the waisted section was done individually on each side and the process was aided by water cooling to avoid heat build up which could damage the specimens.

The cutting tool used did not provide an adequate surface finish so the specimens were polished in two stages with sand paper. The first stage used a sand paper with a grade of 160 and the second stage used the same 320 fine grade sand paper that was used to polish the parallel sided specimens. Again, as with the parallel sided examples the waisted specimens were checked to make sure that the end surfaces were parallel to each other and the specimen mid-plane and perpendicular to the four sides of the gauge length. Dimension tolerances were found to have a maximum of ±0.02mm which was found in the height of the gauge length.

4.7.3 Cylindrical Specimens

The cylindrical specimens had a degree of difficulty about their construction but were easier to machine than the waisted specimen. The section of material was first drilled through the centre. This did cause a lot of wear to the drill tool and when the tool became blunt it was changed. This hole was then used as a datum to create the external profile of the specimen. The external profile was machined using a lathe and the dimensional tolerances were found to be ±0.1mm. The wall thickness could not be measured through the centre of the gauge length until after testing due to the shoulder of material around the top and bottom of the

specimens. This may be a source of measurement error but is unlikely to be severe. The machining process left a good surface finish and as with the parallel sided and waisted specimens the surface was polished with the 320 grade sandpaper. An attempt was also made to polish the inner surface of the specimen which proved difficult but again, the finish left by the machining of this feature was good. The ends' surfaces were checked to make sure they were parallel to each other and perpendicular to the gauge length and no significant errors were found.

5 Finite Element Study

Before the specimens were manufactured a thorough finite-element analysis was conducted in order to validate the geometries being used. The initial use of FEA was to validate the specimen geometry. A study is needed to demonstrate the through-thickness stress response throughout the gauge length and also to highlight the presence of unwanted features such as end effects and stress concentrations. In order for through-thickness compression tests to be valid, the stress state through the gauge length should be as uniform as possible. Each of the specimens was studied separately and the final specimen geometries are presented.

The UD lamina material properties were unavailable for the test material and so a system with similar constituents was used in the finite element analysis. The system chosen was AS4/3501-6 and the UD lamina properties are shown in Table 5-1 where transverse isotropy of the UD lamina is assumed.

Property	E_1 (GPa)	E_2 (GPa)	E_3 (GPa)	G_{12} (GPa)	G_{13} (GPa)	G_{23} (GPa)	v_{12}	v_{13}	v_{23}
AS4/3501-6	126	11	11	6.6	6.6	3.9	0.28	0.28	0.4

Table 5-1: AS4/3501-6 UD lamina mechanical properties[140]

5.1 Parallel Sided Specimen

One of the key issues arising from the literature is the end effects present in the parallel sided specimen. There is some disagreement between groups as to the optimum height to width ratio for parallel sided specimens that demands further investigation. ASTM D 695 recommends that for compressive testing of rigid plastics that the height is twice the width of the specimen[141]. This ratio was used by Lodeiro *et al*, Mespoulet *et al* and Park and Lee in experimental studies[47-49]. Shorter specimens commonly with the depth, width and height having the same dimensions have been used by Park and Lee, Kim *et al* and Guo *et al*[46, 49, 50]. The FE study carried out here analyses both the tall and short specimens to observe the difference in end effects.

For this size test it was assumed that the ends of the specimen were constrained by friction so that they were unable to move. This condition provides a

worst case scenario outcome such that a conservative approach is taken. In reality the frictional effects will be much lower and in the experiments conducted in this study the specimen ends were greased to reduce friction as much as possible.

Three specimen heights were investigated using UD and quasi-isotropic laminates to observe any effect with the change in this dimension. This investigation was designed to look at the impact of specimen height on end effects and the uniformity of the macroscopic stress response throughout the specimen. Three heights; 12mm, 18mm and 24mm were investigated, each with the same square cross-section. The width and depth of each specimen were kept constant at 12mm for each dimension. In the case of the UD specimens examined a one eighth model was sufficient as use was made of symmetry. Due to the ±45° fibres in the quasi-isotropic laminate affecting the use of symmetry a half model was created using the symmetry in the *xy* plane of the specimens.

The 12mm and 18mm models were constructed using 4 elements per layer. In order to reduce the size of the 24mm model only the top 24 plies were modelled with 4 elements per layer with the lower layers containing 2 elements per layer. This is justified because the area of interest and high stress variation is at the top of the model where load is applied.

5.1.1 Parallel Sided Specimen Height Investigation

5.1.1.1 UD [0] Models

In the study of the parallel sided specimens nodal displacements on the top surface of the model were used to simulate a loading plate lying parallel to the top of the specimen. This is the ideal scenario and was used to observe the effect of specimen lay-up and height on the model response.

The end stress response of the UD laminates was similar for all heights examined. The σ_x, σ_y, σ_z, τ_{xy}, τ_{xz} and τ_{yz} stress contour plots are provided in Figure 5.3. A stress concentration was found along the top and bottom of the model running parallel to the fibre direction. This is caused by the friction between the model and the loading plates where the loaded ends are constrained. The centre of

the model is free to deform and this causes a variation in the stresses at the model ends (which are constrained). The maximum σ_z stress concentrations in all three UD models were roughly 2.4. In all models the stress concentration had dissipated after ten layers (2.5mm). Therefore, even in the 12mm model there is still a uniform stress in the gauge length of 7mm. This is demonstrated in Figure 5.1 where the normalised σ_z stresses along the edges *A-A'* and *B-B'* are shown with respect to the number of layers (*N*) in the model. The points of reference are displayed in Figure 5.2 and the normalisation was carried out by dividing the through-thickness stress values σ_z along *A-A'* and *B-B'*, by the average through-thickness stress σ_z^{ave}. This average stress was taken across the *xy* plane over the bottom of the FE model (which is equivalent to taking the average stress across the *xy* plane along the mid-plane of the specimen) in Figure 5.2. The graphs in Figure 5.1 demonstrate the similarity of response with respect to the height of the model. It was observed that the taller model demonstrated a slightly more uniform through-thickness stress response. This was due to the extra height allowing the dissipation of stresses.

The σ_z stress contour plots are shown in Figure 5.3. These show visually the variation of stresses, highlighting the stress concentrations at the ends of the specimen. Another area of concern is the stress response through the centre of the specimen along the *z*-axis. This is the area where a uniform stress response is expected as it should be the least affected area in terms of end effects. The difference between σ_z^{max} and the average value, σ_z^{avg} (average stress taken across the *xy* plane through the specimen mid-plane) through the centre of each model is 7%, 4% and 3.6% for the 12, 18 and 24mm models respectively. This again highlights the more uniform stress response of the tallest model. The findings suggest that for UD materials a taller specimen is desirable as it provides a small but noticeable gain in the uniformity of the stress response.

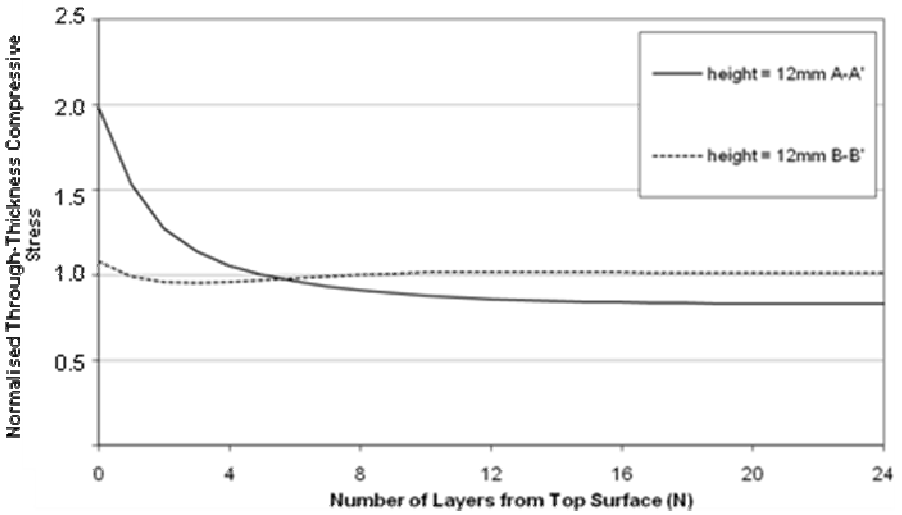

(a)

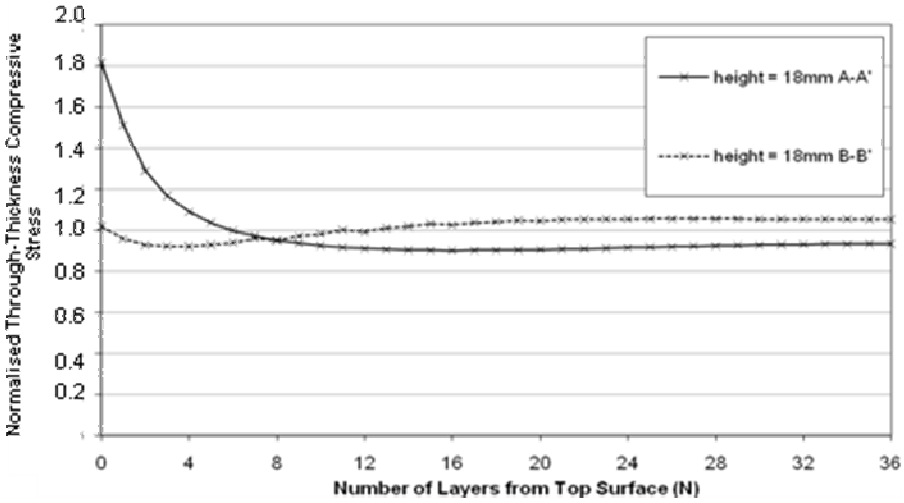

(b)

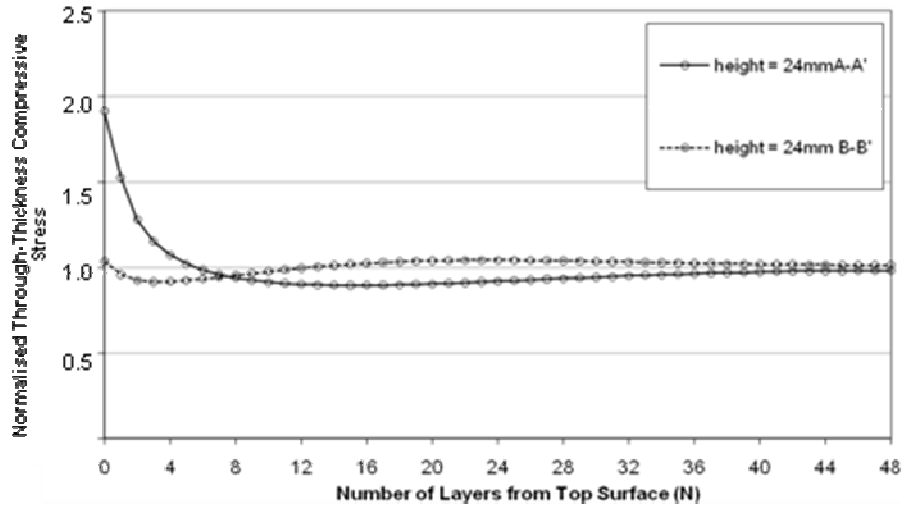

(c)

Figure 5.1: Variation of normalised through-thickness stress σ_z along A-A' and B-B' for: (a) 12mm, (b) 18mm and (c) 24mm parallel sided specimens

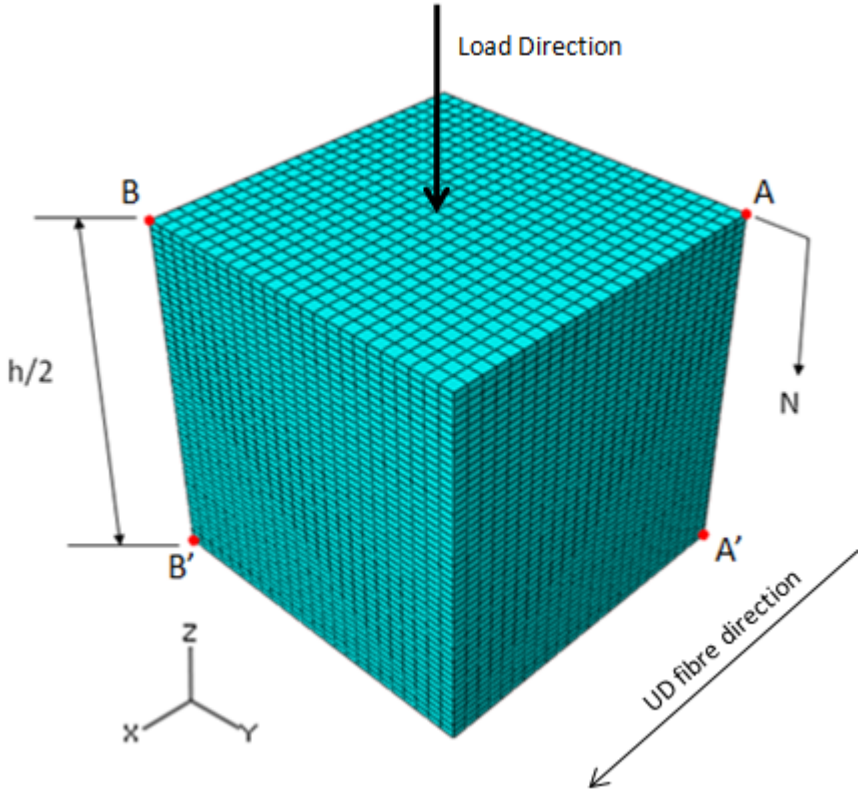

Figure 5.2: 1/8th FE model used for analysing 12mm tall UD parallel sided specimen (reflectional symmetry on the three hidden faces)

Also of note is the magnitude of the different stress components. This is important in relation to through-thickness testing as it is important that the primary stress acting on the specimen is the through-thickness stress σ_z. The range of σ_x stresses in all three models is small and the magnitudes are lower than the through-thickness compressive stress where the maximum compressive σ_x (-0.667Mpa) is around 3 times smaller than the maximum compressive σ_z (2.14MPa) when the model is subjected to a 1MPa load. A similar story is found for σ_y where the maximum compressive stress σ_y (0.606MPa) is around 3 times smaller than the maximum compressive stress σ_z (2.14MPa). Of potential concern is the tensile σ_y stress that is found. In the current models a maximum σ_y tensile stress of 0.022MPa is found in the tallest model. However, this is approximately 50 times smaller in magnitude than the average through-thickness stress through the models (1MPa) and as a result it is not deemed to have an effect on the failure of the specimens. The transverse compressive strength of the AS4/3501-6 material used in these models is 200MPa[140] whilst the transverse tensile strength is 48MPa. Therefore

the maximum induced tensile σ_y would have to be closer to 0.4 – 0.5MPa (compared to a maximum through-thickness stress σ_z of 2.14MPa) to be a cause for concern.

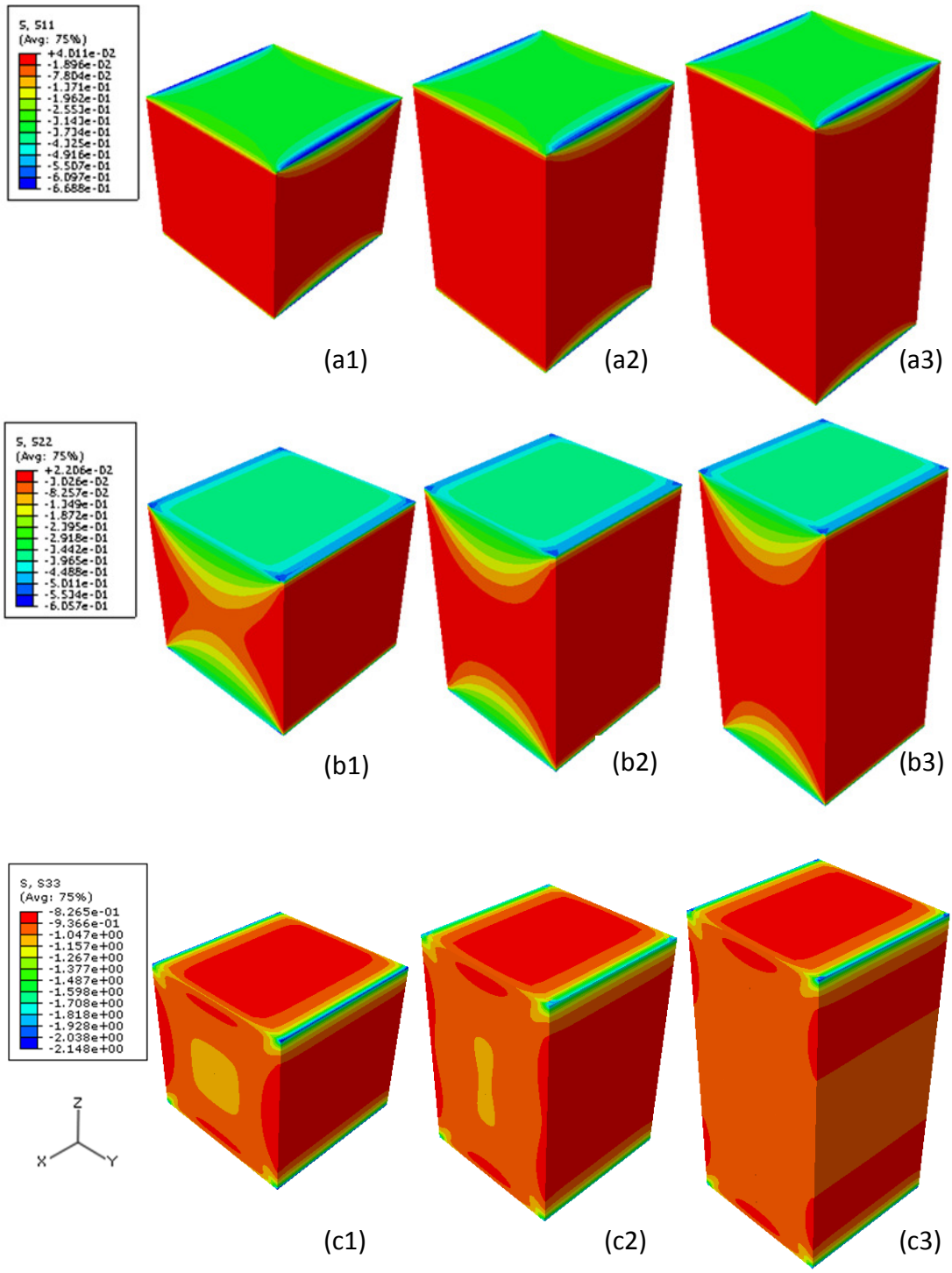

Figure 5.3: Stress contour plots σ_x, σ_y and σ_z for [0] UD parallel sided blocks under a 1MPa through-thickness compressive load; (a) σx, (b) σy, (c) σz, (1)h=12mm, (2) h=18mm, (3) h=24mm (images shown are created using reflection of the 1/8th model to create a full specimen image)

Similar findings are found for the induced shear stresses where the maximum values are substantially lower than the through-thickness stress values obtained as can be seen in the keys of Figure 5.3 and Figure 5.4. Again, this demonstrates that the specimens should fail due to the through-thickness stress σ_z.

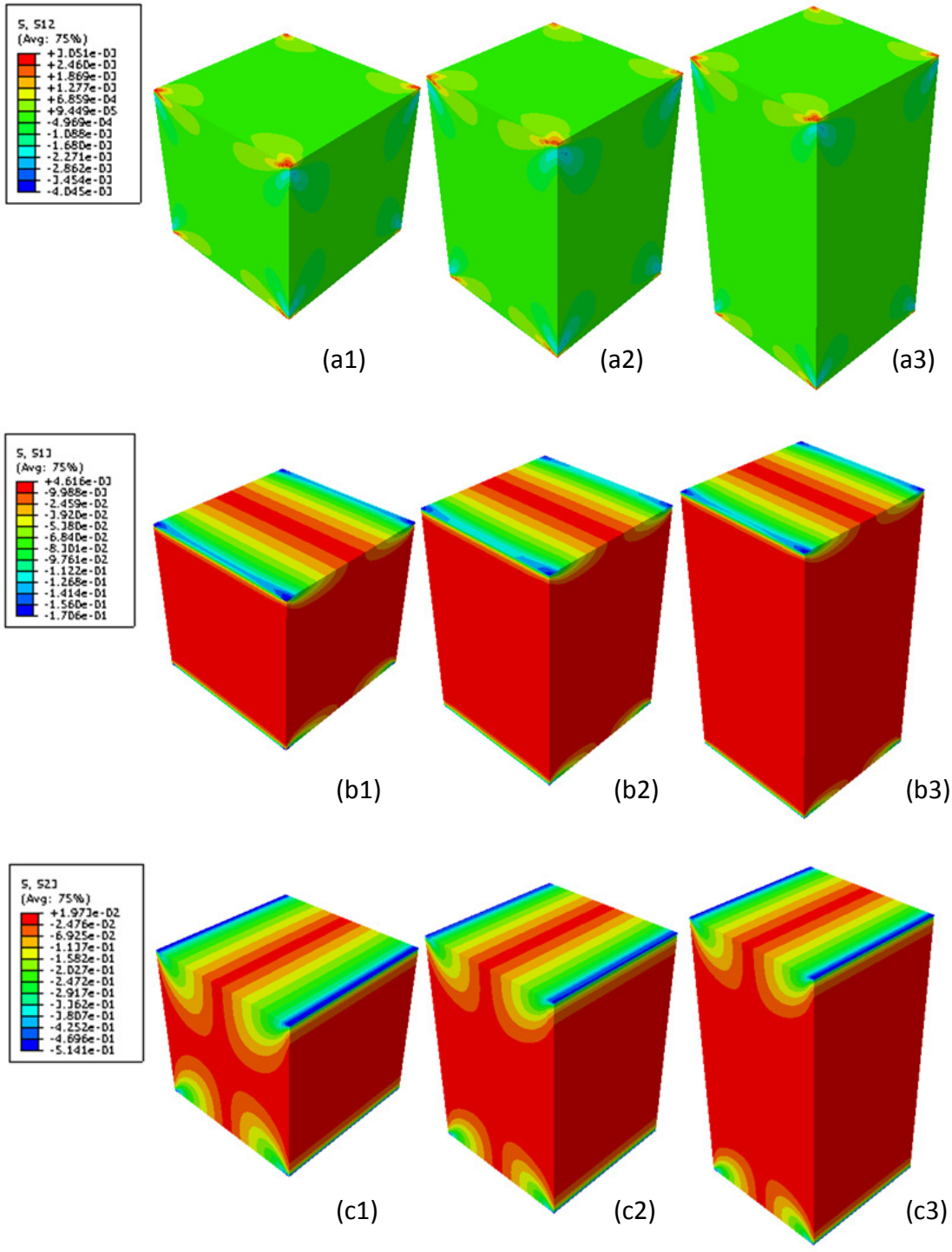

Figure 5.4: Stress contour plots τ_{xy}, τ_{xz} and τ_{yz} for [0] UD parallel sided blocks under a 1MPa through-thickness compressive load; (a) τ_{xy}, (b) τ_{xz}, (c) τ_{yz}, (1) h=12mm, (2) h=18mm, (3) h=24mm (images shown are created using reflection of the 1/8th model to create a full specimen image)

5.1.1.2 Quasi-Isotropic $[\pm 45/90/0]_s$ Models

The quasi-isotropic models utilised symmetry in the *xy* plane such that only half the specimen was modelled. It was found that a change in the specimen height had very little impact on the stress response of the quasi-isotropic material. The normalised through-thickness σ_z stress response for the three quasi-isotropic models is displayed in Figure 5.5 with the reference points shown in Figure 5.8. However, a large difference between the UD and quasi-isotropic results was observed. The maximum stress concentrations found at the top and bottom of the models were again present but were found to have a value of approximately 1.8 which is substantially lower than the value of 2.4 found in the UD models. It was also found that the end stress concentrations had fully dissipated after 5 plies (1.25mm). Both of these findings are due to the quasi-isotropic nature of the $[\pm 45/90/0]_s$ laminate. The high stress concentrations in the UD laminate were present along the edge lying parallel to the fibre direction. This was caused because the material is less stiff in the transverse direction (compared to the fibre direction), which leads to the material deforming transverse to the fibre direction. This results in a large variation in the stresses. In the quasi-isotropic material the fibre reinforcement increases the stiffness to the same degree in both the *x* and *y* direction. As a result the amount of material deformation is reduced and a reduction in the stress concentration is noted. The dissipation of stress concentrations in the quasi-isotropic laminate leads to a uniform stress area of approximately 9.5mm in the 12mm tall model.

The results in Figure 5.5 and the σ_z stress contour plots for the three quasi-isotropic models shown in Figure 5.6 highlight the presence of free-edge effects. These edge effects are only present on the free surfaces of quasi-isotropic models due to the differing ply orientations. The problem of free-edge effects is discussed in Chapter 6 of the thesis. In the current chapter it is important to point out that these free edge stresses are in fact stress concentrations. These appear to have an impact on the stress concentrations caused by friction between the specimen and the loading plate. The top two layers in these models are the +45˚ and -45˚ layers and their differing displacements under load cause free edge stresses. These edge

stresses are magnified at the end of the specimen due to the introduction of friction causing further stress. In fact in this case the stress concentration at the corners is around 1.5. This compares to a value of 1.2 along the centre of the specimen edge and highlights the impact of free-edge stress concentrations along with the role of geometric stress concentrations.

As a result of the edge effects it is hard to assess the stress uniformity on the edges of the models and as a result the models were also run using transversely isotropic material properties. These values were obtained by creating unit cell models of the quasi-isotropic laminates using boundary conditions provided in Chapter 3.2.1.5.1. The material properties obtained are provided in Table 5-2. These properties are used in subsequent results labelled 'TI' to provide maximum stress concentrations as the free-edge effects can introduce large stress singularities inflating the stress concentration value.

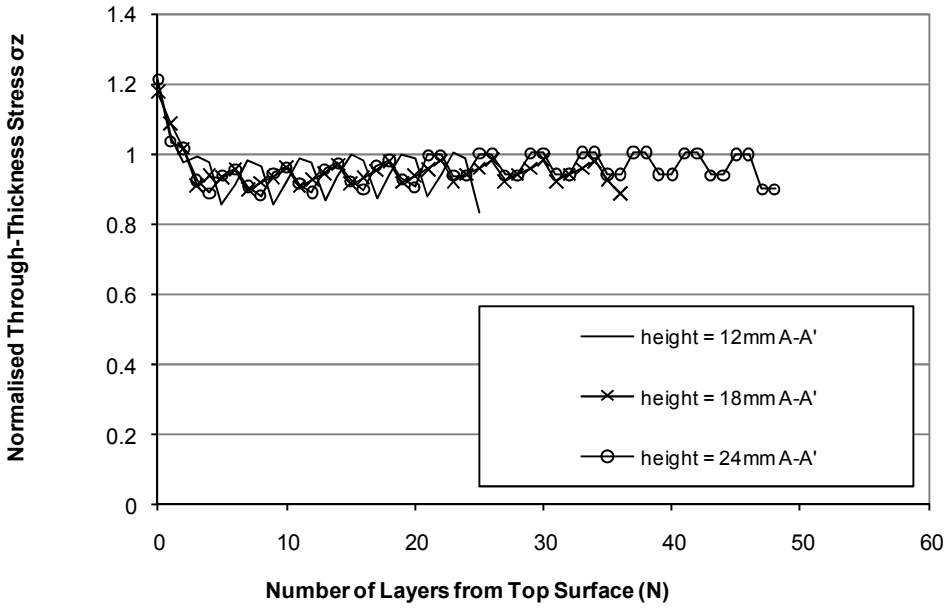

Figure 5.5: Variation of through-thickness stress σ_z along A-A' for $[\pm 45/90/0]_s$ quasi-isotropic 12mm, 18mm and 24mm parallel sided specimens

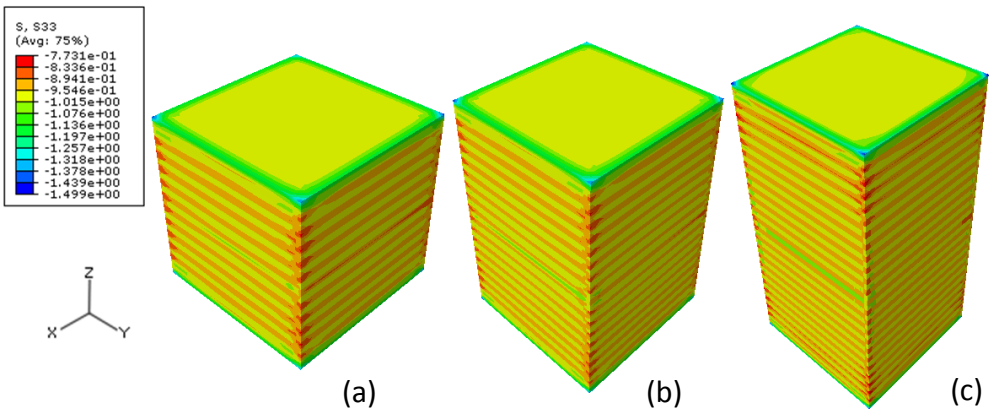

Figure 5.6: Through-thickness stress σ_z contour plot for $[\pm 45/90/0]_s$ quasi-isotropic parallel sided blocks under a 1MPa through-thickness compressive load; (a) h=12mm, (b) h=18mm, (c) h=24mm

Property	E_1 (GPa)	E_2 (GPa)	E_3 (GPa)	G_{12} (GPa)	G_{13} (GPa)	G_{23} (GPa)	ν_{12}	ν_{13}	ν_{23}
Quasi-Isotropic AS4/3501-6	46.5	46.5	12.4	12.9	4.98	4.98	0.18	0.33	0.33

Table 5-2: Transversely isotropic material properties used for through-thickness specimen FE modelling

The edge stress results from the TI models (see Figure 5.7) are free from edge effects and show that the resultant through-thickness stress σ_z is the same regardless of the specimen height. This result demonstrates that for the testing of quasi-isotropic laminates a cubic model (height of 12mm in this case) will produce a uniform stress response in the region of the strain gauges. This also shows that free edge effects have little impact on the geometric stress along the centre of the model edge in this case, as the stress concentration values for the quasi-isotropic models is very similar to that found in the TI models (around 1.2). This is likely because the top layers are the +45˚ and -45˚ layers which confines the free edge stresses to the corner of the models i.e. not impacting on the central edge. If the layers were 0˚ or 90˚ layers then it is likely that the stress concentrations would increase in the central region to around 1.5. In all cases the free edge effects mask the stress distribution around the surfaces of the models, highlighting that for FE validation of quasi-isotropic specimens one must be aware of the impact of free-edge effects on the FE data.

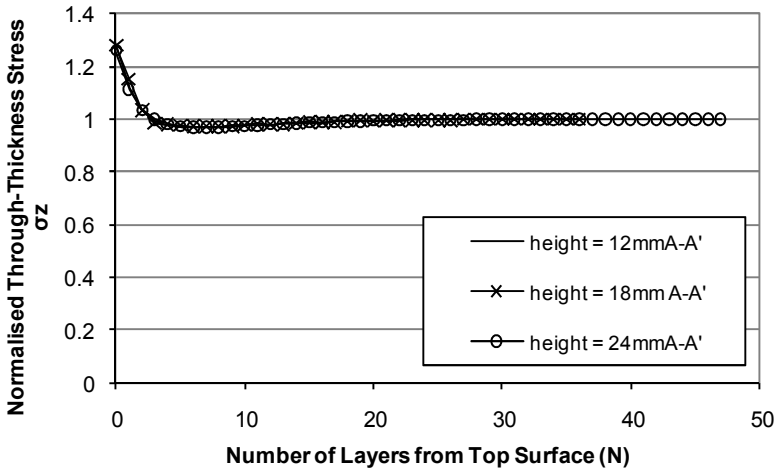

Figure 5.7: Variation of through-thickness stress σ_z along A-A' for $[\pm 45/90/0]_s$ quasi-isotropic 12mm, 18mm and 24mm parallel sided specimens using TI material properties

Through the centre of the quasi-isotropic laminates the stress response appears to be substantially more uniform than in the UD laminates. This is demonstrated by the difference between σ_z^{max} and σ_z^{avg} through the centre of the models. These were 1.4%, 1.1% and 1% for the 12mm, 18mm and 24mm quasi-isotropic models respectively, compared to 7%, 4% and 3.6% for the UD models. These values are only true away from the free-edges due to the presence of free-edge effects.

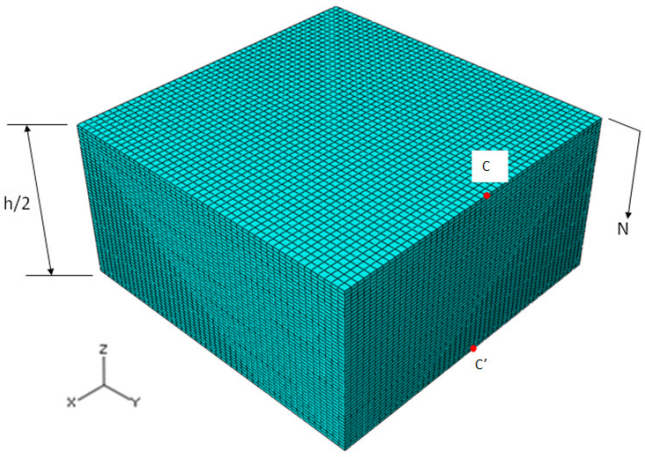

Figure 5.8: Half FE model used for analysing 12mm tall $[\pm 45/90/0]_s$ quasi-isotropic parallel sided specimen (Reflectional symmetry on the bottom surface)

The most important feature of the results is that for quasi-isotropic laminates the through-thickness stress response σ_z is similar for all three specimen heights. In the UD models it was noted that taller specimens provided a noticeably more uniform through-thickness stress σ_z response. However, the results for the quasi-isotropic laminate examined suggest that a thinner, more material efficient specimen can be utilised without compromising the result. The FE results also demonstrate that σ_z will be the dominant resultant stress in the specimens.

5.1.2 Final Parallel Sided Specimen Geometry

The focus of the FE study for parallel sided specimens was to assess the effects of a change in height dimension under through-thickness loading for UD and quasi-isotropic specimens. Under loading it was observed that a stress concentration existed when through-thickness compression was applied; this had a maximum value of 2.4 ($\sigma_z^{max}/\sigma_z^{ave}$) for the three geometries examined and dissipated through the first ten layers on the top and bottom of the laminate. These values reduced to 1.8 and five layers respectively for the $[\pm45/90/0]_s$ quasi-isotropic models. It was also noted that in the UD models the taller specimen provided a more uniform stress response with through-thickness stress σ_z values showing smaller deviations from the average central through-thickness stress. In the quasi-isotropic laminates the stress response is more uniform compared to the UD laminates, regardless of specimen thickness (this is when using transversely isotropic material properties. In standard quasi-isotropic form the free edge effects will present high stress variations on the faces of the model). The three quasi-isotropic laminates were all very similar in terms of stress response. Therefore, for the quasi-isotropic material any size specimen of the three examined can be used as the stress responses are similar. As a result a cubic specimen was chosen for examination of the quasi-isotropic laminates in this study. The final cross-section dimensions for the cubic specimen are given in Figure 5.9. The cross section dimensions are 12x12mm and owing to the cubic nature of the final specimen the thickness is also 12mm.

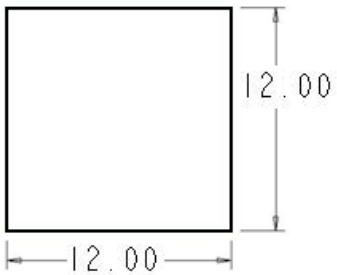

Figure 5.9: Final parallel sided specimen dimensions

5.2 Waisted Specimen

The waisted specimen has been used previously with varying dimensions. In the present study the height of the specimen was limited by thickness of the material which was 40mm. The specimen must also contain some 'shoulder' material which is used to grip the specimen whilst it is being machined. In the specimens manufactured for this study the shoulder thickness was set to be 4mm which was deemed sufficient for holding the specimens during manufacture whilst also giving an appropriate overall thickness to contain the gauge length and fillet sections. Ferguson *et al* highlighted that for UD materials a rectangular cross-section through the gauge length will reduce the stress variation present through the gauge area. This result is examined with respect to quasi-isotropic laminates and a further investigation is given to the effect of changing the fillet radius dimension on the induced stress concentrations.

5.2.1 Cross-Sectional Dimension Effect

Work by Ferguson *et al* showed that using a rectangular cross-section instead of a square cross-section could lead to a 35% reduction in the recorded stress variation through the gauge length. As a result of this, the effect has been studied here using FE analysis. One of the key issues when comparing the rectangular and square cross section models is the selection of dimensions. For comparison the dimensions selected for the rectangular cross-section are the same as those used by Ferguson *et al*[54] and are shown in Figure 5.10. The difficulty in comparing the rectangular geometry to the square geometry comes with regard to the cross-section dimensions and the fillet radii used. In the rectangular model the cross-section dimensions are 16x10mm. The dimensions chosen for the square

cross-section are 12x12mm. The fillet radius dimensions for the rectangular cross-section model were 12mm and 9mm for the long and short sides respectively. It was anticipated that the smaller fillet radius dimension would be the cause of the major stress concentration and as a result the fillet radius value selected for the square cross-section model was 9mm. The maximum stress concentration was calculated by dividing the maximum through-thickness compressive stress by the average through-thickness stress through the mid-plane of the FE model

$$\frac{\sigma_z^{\max}}{\sigma_z^{ave}} \qquad \textbf{5-1}$$

In all models symmetry was utilised allowing half the specimen to be modelled. The bottom of the model was constrained so it could not displace in the *z* direction but was free to deform in the other directions. Load was applied as nodal displacements across the top surface of the models.

The FE analysis carried out here gave a reduction in through-thickness stress variation across the mid-plane of UD models of around 20%. This was calculated as the percentage difference between the maximum and minimum through-thickness stress σ_z across the mid-plane of the models. This compares to a value of 35% given by Ferguson *et al*. There could be various reasons for the difference in result, the primary reason being that in the reference no dimensions are given for the square cross-section model so it is likely that in this case they are different, hence leading to the difference in results. Other possible causes are the mesh refinement and the material properties used. In this work the models contain four elements per layer in the region of the fillet radius and two elements per layer elsewhere. The figures presented by Ferguson *et al* suggest that their models used only one element per layer.

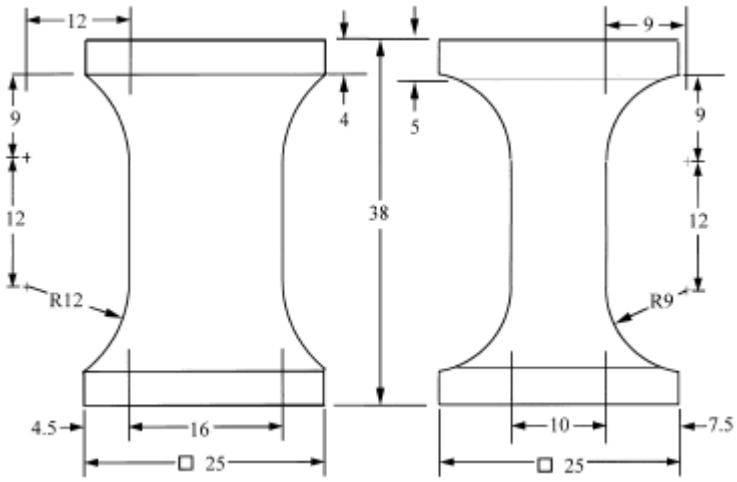

Figure 5.10: Geometry of the waisted (DERA) specimen used by Ferguson *et al* [54](measurements in mm)

The stress variation in the quasi-isotropic laminates (the transversely isotropic model) is lower than the UD laminates for both the square and rectangular cross-section models. It is also of note that for the quasi-isotropic cases the reduction in stress variation across the gauge length is around 3%. This is a marked difference to the 20% witnessed in the UD laminates. The recommendation then is that for quasi-isotropic laminates either a rectangular or square cross-section waisted specimen can be used without affecting the result.

As a further study, the maximum stress concentration was examined. This result is important as previous work has cited stress concentrations as a major factor in failure and hence reducing these effects is of great importance. The stress concentration results for rectangular and square models using UD and quasi-isotropic (TI) laminates are shown in Figure 5.11. The results demonstrate that the maximum through-thickness stress concentration does not vary much between rectangular and square cross-section waisted models. The difference is around 0.91% in the UD models and reduces to 0.21% in the TI models. These results are statistically insignificant, again supporting the use of either a rectangular or square cross-section specimen for quasi-isotropic materials. It should be noted that in models where layers were modelled separately i.e. free edge stresses were allowed to be present, the maximum stress concentration was between 1.3-1.32. Therefore the free-edge stresses appear to have little impact on the maximum geometric

stress concentration in these models. However, free edge stresses may play and important role in failure or affect strain readings across the gauge length of the test specimens.

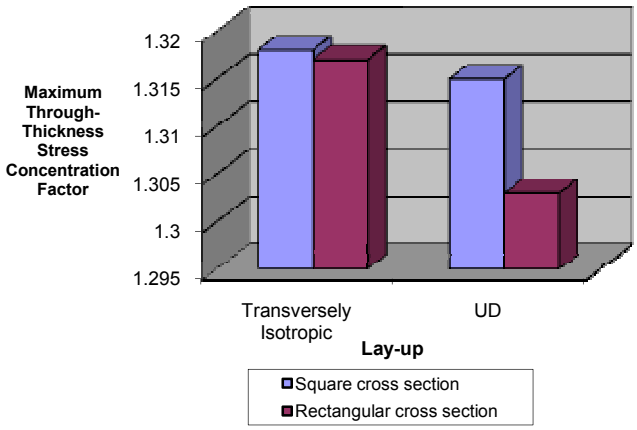

Figure 5.11: Maximum through-thickness stress concentration factors for rectangular and square cross-section waisted specimens

5.2.2 Fillet Radius Dimension Effect

Another key dimension related to the waisted specimen in the literature is the fillet radius, used at the joint between the gauge length and the shoulder section. The highlighted issue in this region is the induced through-thickness stress concentration. The FE study carried out here assumes a circular fillet radius rather than elliptical examples. All the cases examined have a square cross section measuring 12x12mm and the gauge length was constrained to be a minimum of 12mm in height. This was chosen to maximise the gauge length whilst also allowing for relatively large fillet radii. Furthermore, this dimension for the gauge length is equal to the cubic specimen geometry which will allow for a direct comparison and aid in assessing the value of the waisted geometry. The ends of the specimen were constrained to a maximum value of 25x25mm to ensure the maximum number of specimens could be extracted from the quantity of material available.

For the investigation various radius dimensions were considered. The first model used no connecting fillet radius. Then the radius value was increased up to a maximum value of 11.25mm. This was chosen as an upper limit to the fillet radius

dimension due to the imposed constraints of requiring some shoulder material and a 12mm gauge length, as stated above. The graph of fillet radius against the maximum stress concentration is shown in Figure 5.13. The results for UD and $[45/-45/90/0]_{ns}$ quasi-isotropic laminates (using modelling of separate layers (QI) and a TI model) are shown and all three models display a reduction in the stress concentration factor when the fillet radius dimension is increased. There is a slight difference in result between the UD and quasi-isotropic models; when fillet radii values are small the stress concentrations are greater in the UD models and when fillet radii values rise above around 6mm the stress concentrations become greater in the quasi-isotropic models. The TI model shows good agreement with the UD models at fillet radii values above 6mm. The higher stress concentrations in the quasi-isotropic models are caused by free-edge effects. In all cases the highest stress concentration value was witnessed at the corners of the specimens at the end of the gauge length/start of the fillet radius as demonstrated by the dark blue colour in this region in Figure 5.12. The quasi-isotropic material shows a lower stress concentration at small fillet radius values due to the extra reinforcement offered by the varying fibre orientations. This reduction is even greater in the TI models where the absence of free-edge effects is thought to produce the true maximum stress concentration factor for the specimen. The TI model shows a similar stress concentration to the UD models at higher fillet radii values. In the quasi-isotropic models large free-edge stress are found in the corners of the ±45° layers which are magnified at the fillet radii. This causes the larger stress concentrations in the quasi-isotropic models compared to the TI models and this result is studied further in Chapter 6.4.2.

As a result of the stress concentration values the recommendation is that for quasi-isotropic laminates like those to be tested here and UD laminates the fillet radius value should be at least 6mm. Beyond this the decrease in stress concentration is small compared to the increase in fillet radius values but to minimise the stress concentration one should look to include as large a fillet radius as possible.

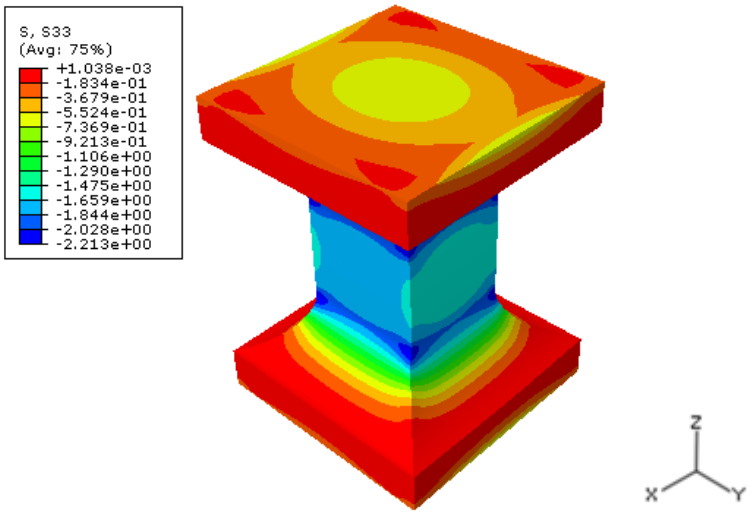

Figure 5.12: Through-thickness stress σ_z contour plot of UD waisted specimen containing fillet radii of 9mm, subjected to a through-thickness compressive load

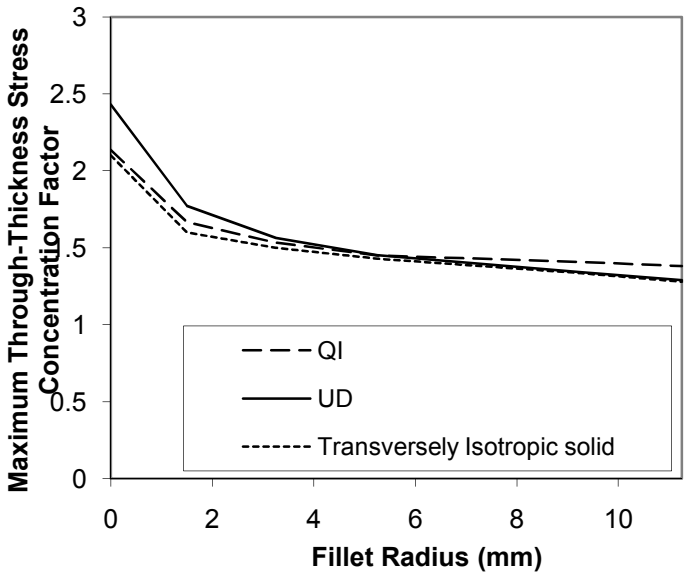

Figure 5.13: Maximum through-thickness stress concentration factor with respect to fillet radius dimension for waisted specimen

A further note arising from Figure 5.13 is the confirmation that free edge effects do not greatly increase the maximum geometric stress concentrations. This is shown by the fact that the maximum stress concentration given by the TI model is almost identical to that given by the quasi isotropic model where free edge effects are able to form. However, in reality, free edge effects are stress singularities and could be infinitely large which the models cannot show. Therefore this result must be taken with caution.

As with the cubic specimens the stresses σ_x, σ_y, τ_{xy}, τ_{xz} and τ_{yz} were also examined. These are shown in Figure 5.14 and as with the cubic specimens they demonstrate that the magnitudes of these stresses, although not negligible, are small enough that one can be confident that the specimen will fail due to the through-thickness stress σ_z.

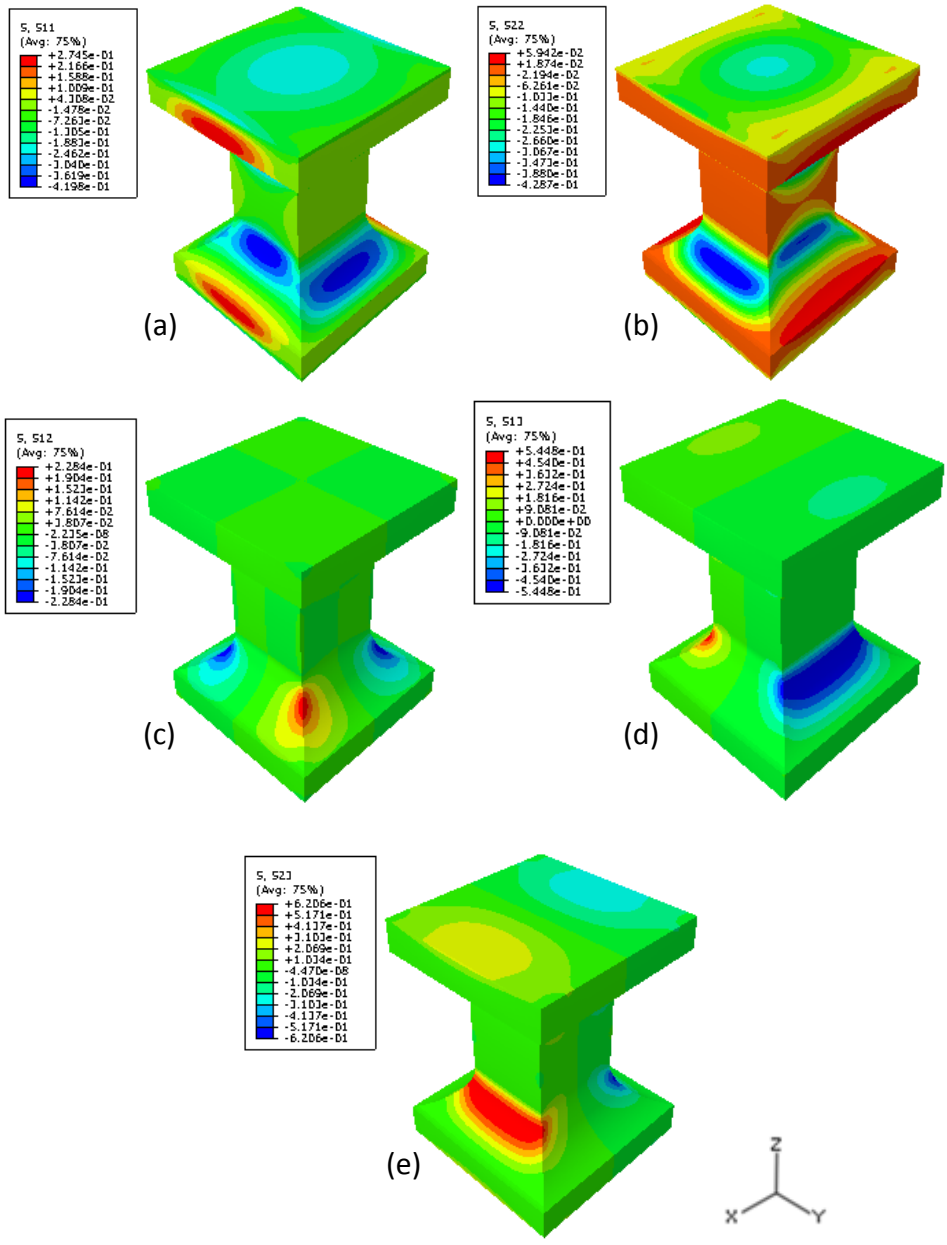

Figure 5.14: Stress contour plots of UD waisted specimen containing fillet radii of 9mm, subjected to a through-thickness compressive load: (a) σ_x,(b) σ_y, (c) τ_{xy}, (d) τ_{xz} and (e) τ_{yz}

5.2.3 Other Waisted Specimen Dimensions

The work presented here shows a gauge length with a minimum dimension in any one direction of 10mm (In the rectangular FE model). Previous works have utilised gauge areas with smaller dimensions but as mentioned by Ferguson *et al*, a larger gauge area reduces the risk of local effects such as voids and other material defects. Furthermore the choice of a relatively large gauge area should help to reduce the impact of free-edge effects as discussed in Chapter 6.

The shoulder material was set to 4mm. This is included to help ensure that there is an even dissipation of end effects which along with the fillet radii should ensure that the gauge length is free from any fluctuation in the stress response. The shoulder material also acts as an excess so material can be removed where required to ensure that the end surfaces of the specimens are parallel with each other. Furthermore, this shoulder material is required to grip the specimen during machining of the waisted profile.

5.2.4 Final Waisted Specimen Dimensions

The final waisted specimen dimensions are provided in Figure 5.15. It has a square cross section (12x12mm) rather than a rectangular form. The FE results showed that for quasi-isotropic specimens like those tested here that there was little difference between the rectangular and square cross-section specimens. The minimum dimension in Ferguson's rectangular specimen was 10mm. In the current study the minimum dimension is 12mm which should reduce any risk of buckling under loading. Furthermore, the use of a square cross-section increases the minimum fillet radius value which will reduce the maximum stress concentrations.

The square cross-section of the waisted specimens uses measurements that are identical to the final parallel sided specimen. This allows a complete comparison between the parallel sided and waisted specimens, helping to identify the exact effects of the waisting on the stress, strain and strength results. This should provide desirable information on the characteristics of both the waisted and cubic specimens.

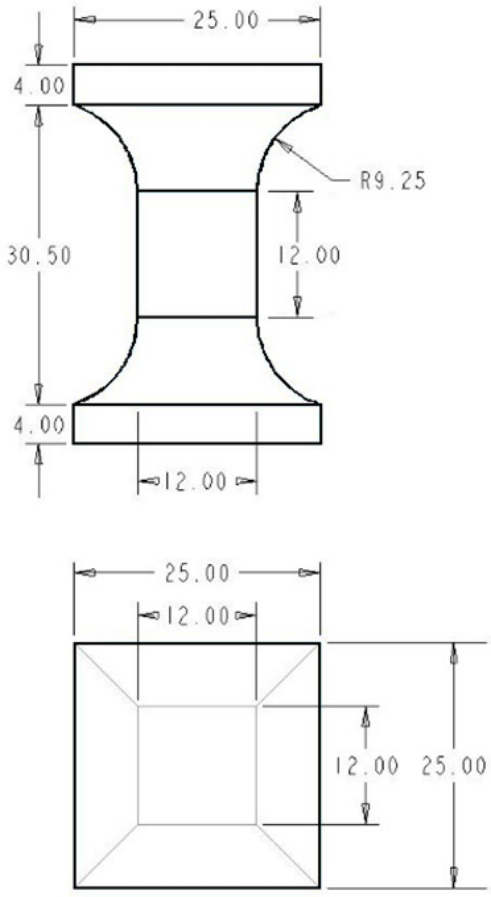

Figure 5.15: Final waisted specimen geometry

A further issue was covered regarding the fillet radius dimension. It was observed that in general, the higher the radius, the lower the maximum stress concentration and more uniform the stress response through the gauge length. As a result a fillet radius of 9.25mm was used. This allowed a 12mm gauge length and 4mm end tab thicknesses required to grip the specimens during manufacture. The FE analysis was constructed with fillet radii up to 11.25mm but these subtracted from the end tab material without significantly reducing the maximum stress concentration so the decision was taken to use fillet radii of 9.25mm.

5.3 Cylindrical Specimen

The cylindrical specimen to be used is similar to the specimen proposed by DeTeresa *et al* [55]. This was chosen to enable a review of the DeTeresa specimens when subjected to pure through-thickness compression. The cylindrical specimen

has a smaller thickness than the waisted specimen; it is constrained to a final height of 25.4mm, as used by DeTeresa *et al* and also has a wall thickness of 2.5mm.

5.3.1 End Section Shape Effect

In order to apply torque (to induce shear stresses) in the DeTeresa *et al* example the end sections had to be square. A proposal put forward by the author of this study is that the end section could be cylindrical, similar to the gauge length. To this end it is important to assess the specimen response depending on the end section geometry.

The square ended cylinder specimen was created using the dimensions given by DeTeresa *et al*[55]. A second model was created with cylindrical end sections in order to assess the stress variations and stress concentrations present in both specimens. Both models had fillet radius values of 6.35mm, a gauge length of 6.35mm and inner and outer diameters through the gauge length of 15.9 and 21mm respectively.

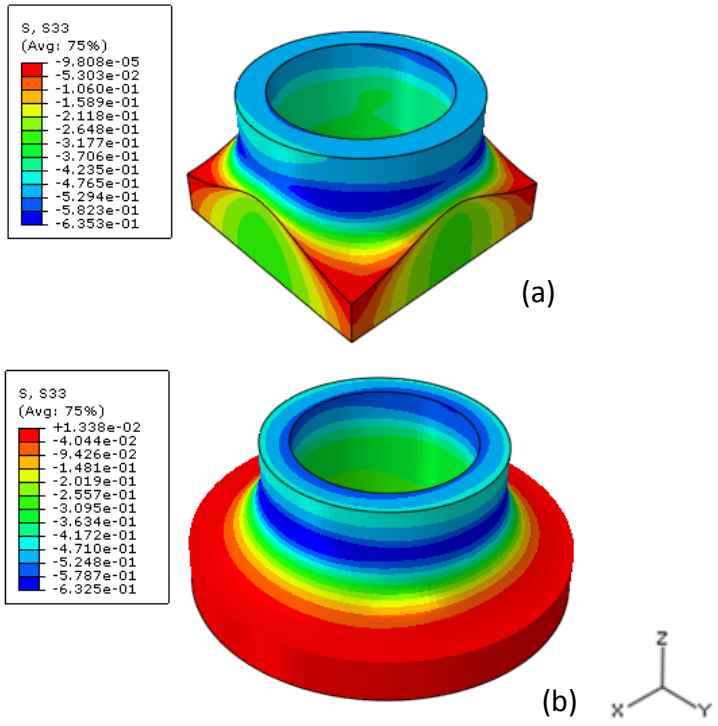

Figure 5.16: Through-thickness stress contour plots of UD cylindrical models subjected to a through-thickness compressive load; (a) square end, (b) cylindrical end

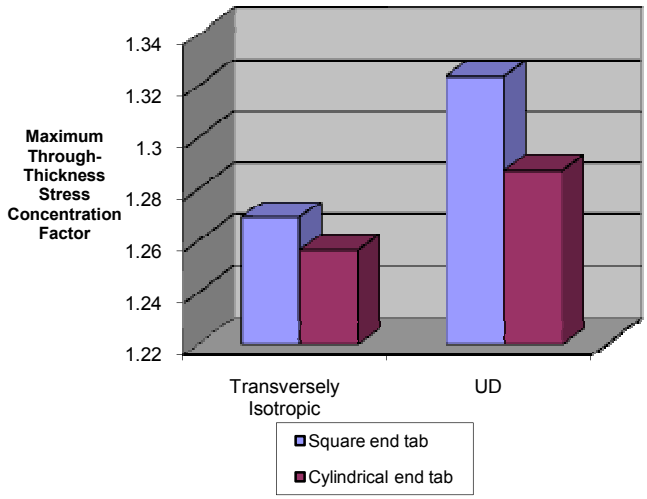

Figure 5.17: Maximum through-thickness stress concentration factors for square and cylindrical end tabbed cylindrical specimens

Stress contour plots of both specimens are shown in Figure 5.16. The stress results show that the cylindrical ended specimen provides a slightly more uniform stress response through the gauge length. The key reason for this is that in the square ended specimen the fillet radius is intersected by the edge of the end tab on the square faces. The non-uniform response extends from the fillet radii through the specimen walls; this is completely avoided in the cylindrical end tabbed specimen. A further issue concerns the stress concentration factors. The maximum stress concentrations for both types of end tab are presented in Figure 5.17. These results highlight that the stress concentrations are lower in the quasi-isotropic models which agrees with the results obtained for the waisted specimens. Moreover, the results show that the maximum stress concentration factor is lower in the cylindrical end tab specimen compared to the square end tab specimen. The differences aren't extreme, differing from 1.265 to 1.25 in the TI model, but are noticeably larger than the differences observed between the square and rectangular cross-section waisted specimens.

The recommendation for the cylindrical specimen is that the cylindrical end tab is used. The FE analysis shows that it produces a more uniform stress response

and reduces the maximum stress concentration compared to the square end tabbed specimen for both UD and quasi-isotropic lay-ups.

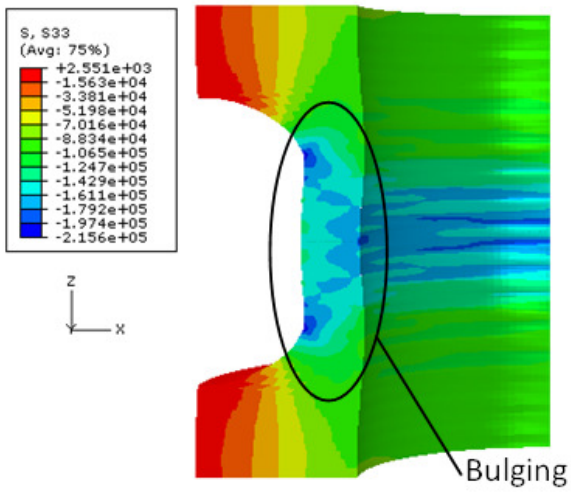

Figure 5.18: Cylindrical FE model section displaying bulging of the gauge length wall (Deformation scale factor = $2x10^4$)

A further feature of the results is shown in Figure 5.18. It is clearly seen in the image that the cylinder walls do not deform uniformly. Instead, through the centre of the gauge length the walls bulge outwards. Although this effect is not deemed to be large it should none the less be acknowledged when analysing the experimental results. Any bending is likely to promote fracture of the specimen and could also affect the strain results.

5.3.2 Fillet Radius Dimension Effect

The fillet radius dimension was studied for the waisted specimen and is also an area of concern for the cylindrical specimens. Due to the smaller overall thickness of the cylindrical specimens the radius dimensions are smaller than those examined in the waisted specimens with the maximum radius used being 6mm. The gauge length of the specimens was constrained with the wall thickness being 2.5mm thick. This figure was used by DeTeresa and is used here to allow a comparison with the DeTeresa specimen. For pure through-thickness compression testing this is not the ideal dimension due to the prevalence of free edge effects (shown in Chapter 6) but it is followed here as the DeTeresa specimen was used for combined shear and through-thickness compression testing. Part of the purpose of the current work is to assess what happens to this specimen during pure

compression and whether this impacts on the ability of the specimen to obtain results for combined shear and through-thickness compression tests.

The graph of fillet radius against maximum stress concentration factor is given in Figure 5.19. As with the waisted specimens the maximum stress concentration reduces with an increase in fillet radius. However, at all fillet radius values the stress concentration factors in both UD and quasi-isotropic cylindrical models are markedly lower than the stress concentration values recorded in the waisted specimens. In the waisted specimens it was noted that at low fillet radius values the maximum stress concentration was lower in the quasi-isotropic models. The same is true for the cylindrical specimens and again this is due to the reinforcement provided by the varying fibre orientations. However, the results between the waisted and cylindrical models differ at higher fillet radius values. In the waisted specimen the quasi-isotropic models gave the highest through-thickness stress concentrations due to free-edge effects at the corners in the +45 and -45 layers. The build up of free-edge stresses is constrained in the cylindrical specimens due to the lack of sharp corners. As a consequence the stress concentration in the quasi-isotropic model remains lower than that in the UD models. Furthermore, in both materials it appears as though the stress concentration value does not alter significantly for fillet radius values above 4.5mm.

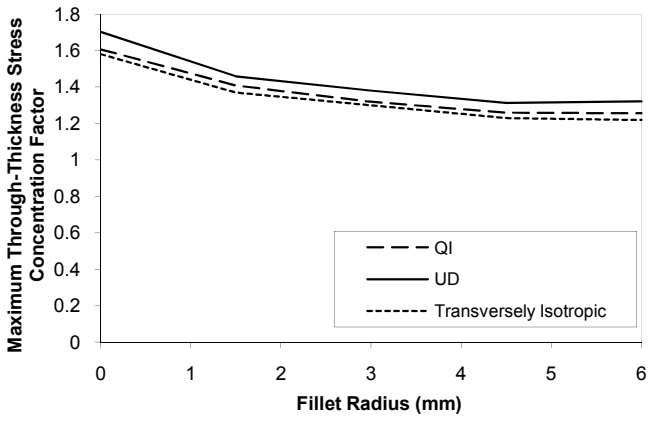

Figure 5.19: Maximum through-thickness stress concentration factor with respect to fillet radius dimension for cylindrical specimen

As with the cubic and waisted specimens it appears that the free edge effects do not increase the geometric stress concentrations significantly in the quasi-isotropic models. Again though, the free edge effects do impact on the uniformity of the stress result and could act as failure initiation sites.

From the stress concentration results it is recommended that for UD and quasi-isotropic materials the fillet radius value is set to at least 4.5mm for cylindrical specimens with an overall height of 25.4mm and 4mm shoulder tabs.

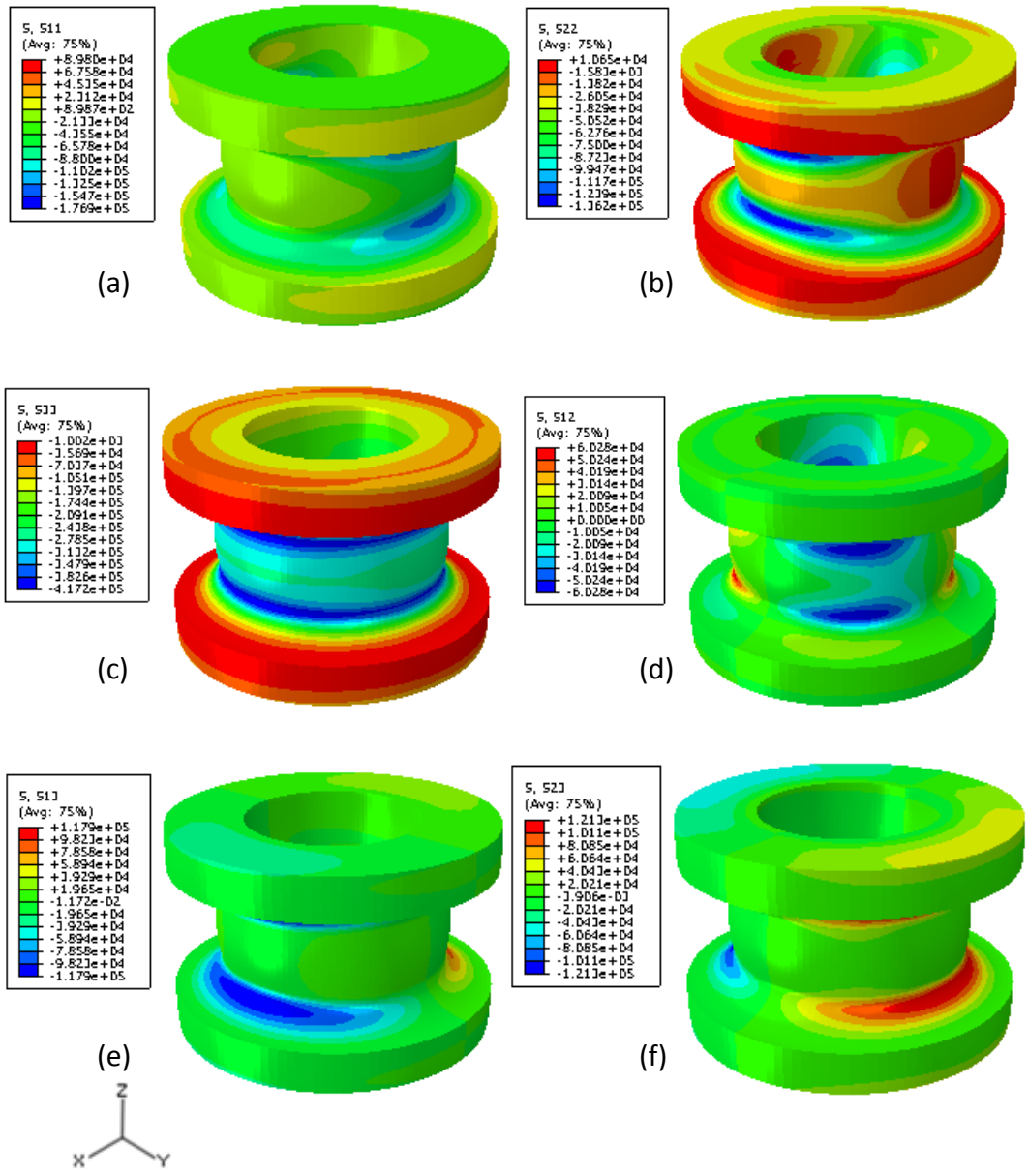

Figure 5.20: Stress contour plots for UD cylindrical specimen with 4.5mm fillet radius subject to through thickness compressive load: a) σ_x, b) σ_y, c) σ_z, d) τ_{xy}, e)τ_{xz} f) τ_{yz}

A look at the σ_x, σ_y, σ_z, τ_{xy}, τ_{xz} and τ_{yz} stress distributions shown in Figure 5.20 shows that similar to the cubic and waisted specimens, the dominant stress is σ_z. As mentioned previously, this is important as one must be sure that the specimen geometry is not introducing any unwanted stress resultants.

5.3.3 Other Cylindrical Specimen Dimensions.

As with the waisted specimen the cylindrical specimen contains 4mm of shoulder material at each end of the specimen. Again this is to help with the dissipation of stresses caused by end effects and to provide excess material which can be utilised to ensure that the end surfaces lie parallel with each other.

5.3.4 Final Cylinder Specimen Geometry

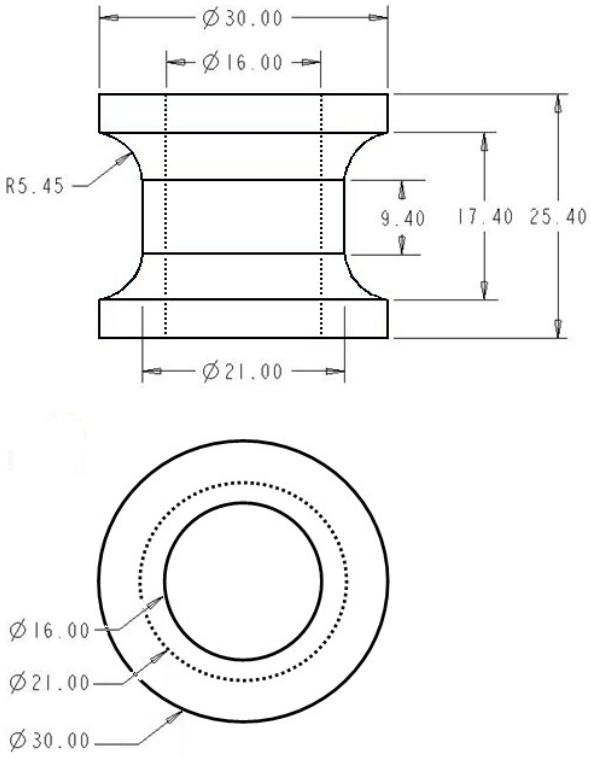

Figure 5.21: Final cylinder specimen geometry

The final cylinder specimen geometry had a cylindrical end tab as shown in Figure 5.21. The FE analysis showed that this provided a more uniform stress response and reduced the maximum stress concentrations compared to the square end tabs used by DeTeresa *et al*. The fillet radius was chosen to be 5.45mm. Beyond around 5mm the maximum stress concentration did not reduce

significantly with an increasing fillet radius. 5.45mm was chosen as it resulted in a gauge length of 9.4mm which was large enough to obtain a uniform stress response as well as allowing for 4mm thick end tabs. The inner and outer gauge diameter dimensions were set to 16 and 21mm respectively. These are similar to the DeTeresa dimensions.

5.4 Conclusion

A thorough finite element study has been carried out to finalise each specimen design. The results show that quasi-isotropic laminates produce more uniform stress responses than the UD laminates in all three specimens.

It has been shown that the parallel sided specimen can be tested in cubic form when characterising quasi-isotropic laminates due to the good uniformity of the stress response for these specimens. As a result the final parallel sided specimen chosen has a cubic geometry measuring 12x12x12mm.

In the waisted specimens a square cross-sectional gauge length will be used. The FE results show that for quasi-isotropic laminates there is little difference in the stress response between the rectangular and square cross-section specimens. Furthermore the square cross-section allows for a maximisation of the fillet radii on all sides where a large fillet radius is desirable to reduce through-thickness stress concentrations. The final waisted specimen has a gauge area measuring 12x12x12mm which should give a reliable specimen and provide a clear identification of the effects of the fillet radii compared to the cubic specimen.

It has been demonstrated that the cylindrical specimen provides a more uniform stress response when cylindrical end tabs are used. This finding is followed in the final cylindrical geometry used here. It is also important to maximise the fillet radius to reduce through-thickness stress concentrations at the ends of the gauge length. The wall thickness used here will be the same as the DeTeresa specimen in order to assess the response of the specimen to pure through-thickness compression.

6 Investigation of Free-edge Effects Produced by Through-Thickness Loading

6.1 Free-edge-Effects

In laminates, such as the quasi-isotropic laminate investigated in this study a fluctuation of stresses is present at the free-edges under loading. These 'free-edge effects' are caused by the differing Poisson's contractions at the edge of each ply when the laminate is subjected to loading. The schematic diagram in Figure 6.1 shows the movement of four plies within a quasi-isotropic laminate when subjected to through-thickness compression. It is clear that if the interfaces between the plies were frictionless then there would be a step change in the surface between the different layers. The surface continuity is kept because the plies are connected, giving rise to interface shear stresses. The surface continuity gives rise to the ridge and valley surface observed. These stresses quickly dissipate towards the centre of the laminate where a uniform set of stresses is observed between all the plies in the laminate.

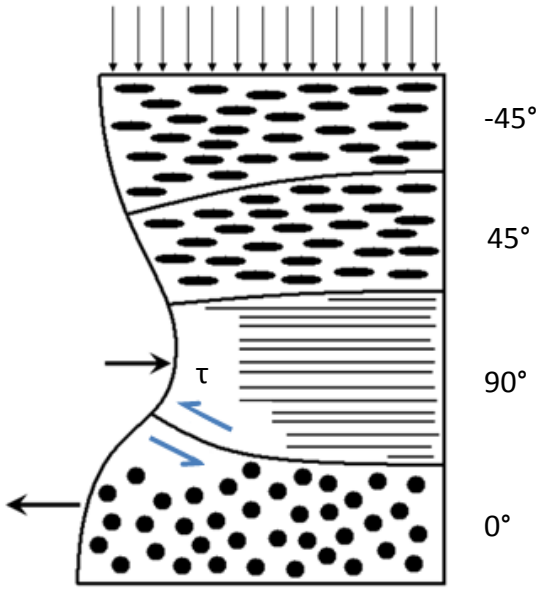

Figure 6.1: Schematic diagram of the edge deformation of plies in a quasi-isotropic laminate subjected to through-thickness compression

It is clear that the specimens used in this study will be subject to free-edge effects and the following work aims to demonstrate the severity of these edge

effects with respect to the gauge length of each of the through-thickness specimens examined in this study.

6.2 Finite Element Models

During the initial finite element study presented in Chapter 5 it was observed that edge effects would be present in all three specimens. The models used in Chapter 5 were adequate to observe the macroscopic stress distribution throughout the whole model but were not refined enough to accurately capture the local stress variations found at the free-edges. The first problem to overcome then was how to improve the accuracy of the model without creating a model that is too complex to run on a modern personal computer (PC). There are two ways to increase the accuracy of a finite element model: the first is to increase the mesh density and the second is to increase the order of the elements used. The initial waisted and cylindrical models created and used in Chapter 5 were as complex as could be run on the PC available to the author. With this being the case it was clear that refinement could not be obtained by adding more or higher order elements to the existing FE models.

The models used in the previous study showed that the stress distribution through the gauge length of each specimen was uniform. Therefore, the edge effects are also expected to show some uniformity. It is expected that the edge effects present in layers with the same fibre orientation will be similar to each other and as a result only eight layers are modelled. Two model geometries were investigated for edge effects. The first was a square cross sectional model with width and depth dimensions the same as the gauge area cross-section of the waisted and cubic specimens and the same ply thickness of 0.25mm. The second model was a hollow cylindrical disc with the same dimensions as used in the gauge length of the cylindrical specimens and again, a ply thickness of 0.25mm was used as in the physical specimens. The models used are shown in Figure 6.2.

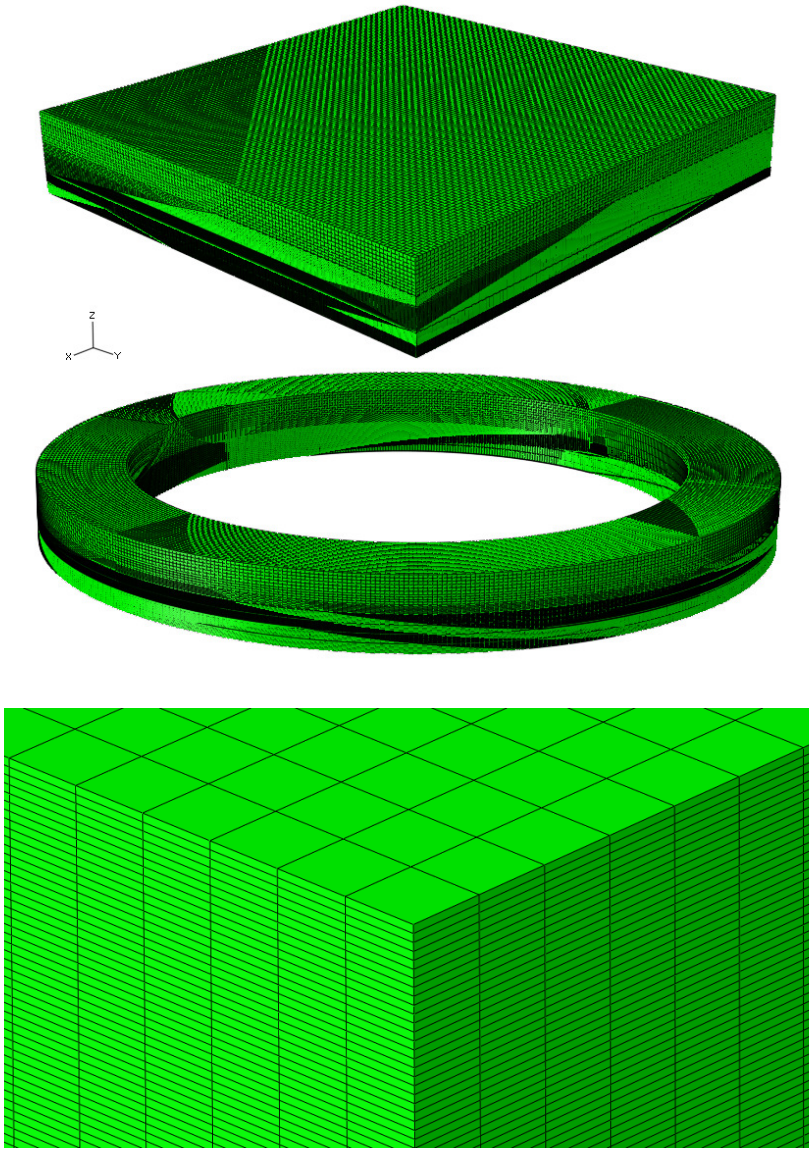

Square Cross-Section

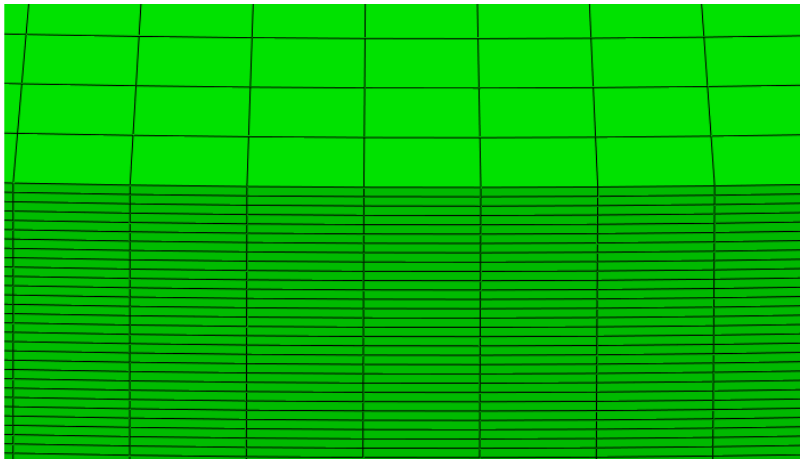

Cylindrical Cross-Section

Figure 6.2: Meshed square and cylindrical cross section 'slice' models, used to observe the free-edge effects present during through-thickness compressive loading. Models contain 8 plies

Each model was created using C3D8R hexahedral solid elements. The decision to use C3D8R elements as opposed to C3D20R elements was taken due to the PC requirements of such a large model. In this instance, using C3D8R elements allowed the use of many more elements whilst still being able to run on the available computing equipment available. The bottom of each model was constrained in the *z* direction using reflectional symmetry and load was applied through nodal displacements prescribed across the top surface of each model. This condition comes as a result of the findings in Chapter 5, where the central layers of the FE models remain predominantly plane after loading. The five central most layers in both models had 24 elements in the thickness direction, reducing to 18 and 12 elements per layer in the three outer layers of the model. This compares to the four elements per layer used by Park and Lee as discussed in Chapter 2.6. The amount of elements was decided upon after a convergence check but was also the highest amount of elements permitted on the machine used (PC with a 64bit processor and 8GB of RAM plus 1GB of assigned virtual memory). In total the square cross sectioned slice contained 1,756,800 elements and the cylindrical slice model contained 1,641,600 elements.

Stress	0° layer (MPa)	90° layer (MPa)	45° layer (MPa)	-45° layer (MPa)
Square Cross Section FE				
σ_1	0.335209	0.335285	0.333233	0.337876
σ_2	-0.330757	-0.330733	-0.330581	-0.330866
τ_{12}	0.00101111	0.00173768	-0.0000746	-0.000104
Cylindrical Cross Section FE				
σ_1	0.34887	0.361798	0.377221	0.34873
σ_2	-0.330947	-0.327808	-0.332662	-0.334982
τ_{12}	-0.00566823	0.0232537	-0.0157703	-0.0166882

Table 6-1: Resultant stresses from through-thickness compressive loading from; square cross section FE and cylindrical cross section FE

The results shown in Table 6-1 display the in-plane stress resultants of the square and cylindrical cross-section FE models. These stress values were taken from the central node in each layer of the finite element model and demonstrate that away from the free-edges the FE models predict a uniform state of stress.

6.3 Results and Discussion

The work carried out used FEA to obtain the free-edge stress response of quasi-isotropic laminates under through-thickness loading. In order to analyse the data it is important to understand what is being discussed. In this chapter the model reference and data point locations are detailed for clarification.

Both the square and cylindrical models are shown in Figure 6.3 where '*a*' is the characteristic width and '*b*' is the model height used for analysis. The models used are as described in Chapter 6.3 and a key point is that whilst each model was eight plies thick the analysis focuses on the four central most layers. The results should then apply to the four central layers of an infinitely tall symmetrical quasi-isotropic laminate.

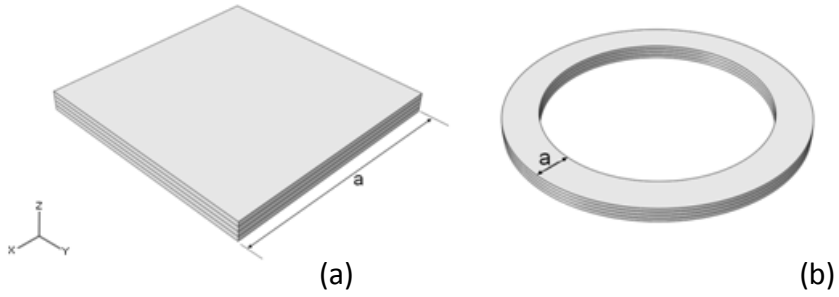

Figure 6.3: Square and cylindrical slice models showing the width dimension; (a) square model a=12mm and b=1mm, (b) cylindrical model a=2.5mm and b=1mm

The lines of data points are shown in Figure 6.4. Two main areas were considered: concerning interlaminar stresses and stresses acting along the edge of the model. To obtain the interlaminar stresses, results were taken along the top and bottom surface of each layer using data points such as those signified by 'Interlaminar (-45 top)' in Figure 6.4. The edge stresses were taken on the model surfaces from the four remaining indicated locations as shown in Figure 6.4. One line is positioned on the surface lying perpendicular to the *x* direction (referred to

as the *X*-face) and the other lying parallel to the *x* direction (referred to as the *Y*-face). Further results obtained at 45° and 135° to the *X*-face.

Figure 6.6 and Figure 6.7 show the through-thickness σ_3 stress contour plots for both cylindrical and square cross-section models. Figure 6.8 and Figure 6.9 show the interlaminar stresses in the cylindrical and square models respectively whilst Figure 6.10 and Figure 6.11 show the edge stress variations for both the square and cylindrical cross section models. The figures show a clear variation in the stresses close to the edges of both models. The graphs showing the variation of stresses across the edge of the models highlight the difference in stresses between the layers.

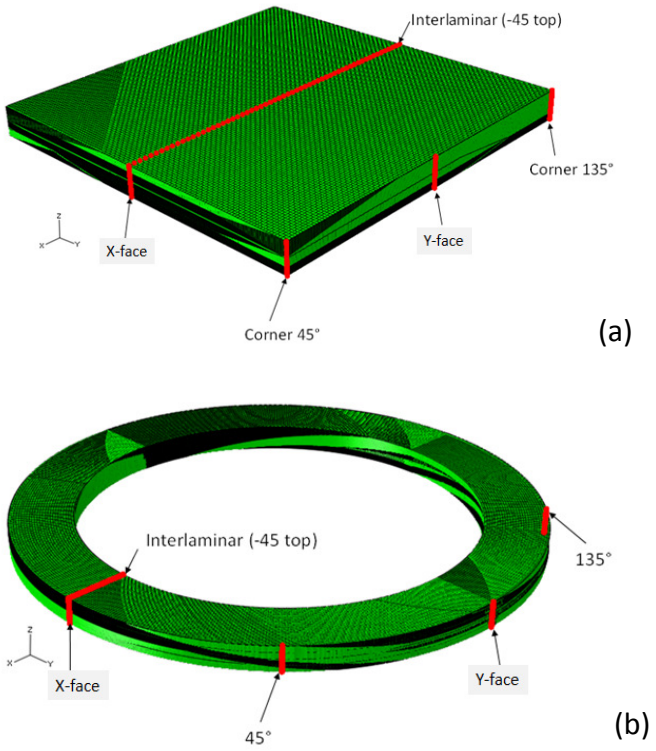

Figure 6.4: Indication of data points used to obtain stress distributions for investigations of the edge effects of: (a) square cross-section model, (b) cylindrical cross section model

The formation of free-edge effects is highlighted by the finite element result shown in Figure 6.5. The image shows the local deformations at the corners of the specimen along the *X*-face of the square model i.e. the fibres in the bottom 0° layer run in the *x* direction of the model. The reason these exist is due to the material properties and the lamina orientation. Each lamina has differing material properties in the fibre and transverse directions. In the case of the lamina used

here E_1 is just over ten times greater in magnitude than E_2 as presented in Table 5-1. When the 0° layer is subjected to through-thickness compression the layer will deform more in the *y* direction due to the lack of fibre reinforcement in this axis. With a 90° layer placed above this the top surface of the 0° layer becomes constrained. In the global sense the 90° layer is stiffer in the *y* direction than the 0° layer and as a result when the 0° layer expands in the *y* direction the top surface is prevented from deforming due to a tensile force imposed by the adjoining 90° layer as demonstrated by the schematic diagram in Figure 6.1. The images in Figure 6.1 and Figure 6.5 also highlight the 'ridge and valley' deformation caused by the differences in material properties, also highlighted by Guo *et al*[46]. The differences in elastic properties also cause edge effects between the 45° and -45° layers. Furthermore, the local deformations also result in shear stresses building up at the edges of the laminate as the material remains intact.

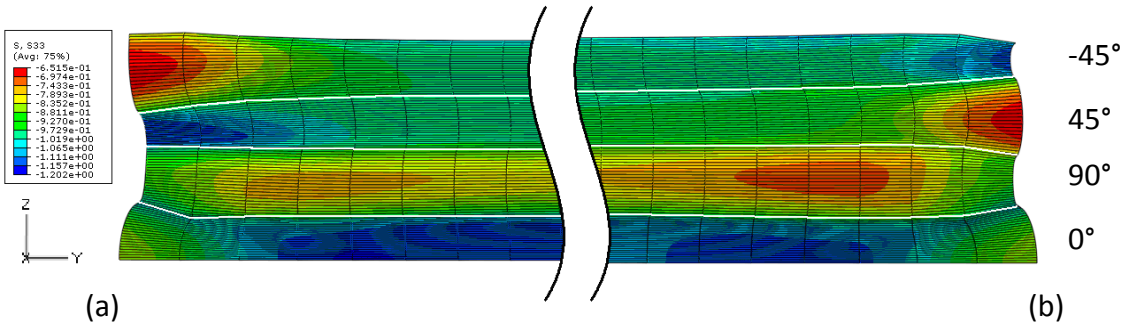

Figure 6.5: Edge deformations in the four central layers ([45/-45/90/0]) from an 8 layer square cross-section model; (a) corner 45°, (b) corner 135°

6.3.1 Interlaminar, *X*-face and *Y*-face Edge Stresses

The models used here show that through the centre of the gauge length the through-thickness stress σ_3 is greater in magnitude than both of the in-plane direct stresses, σ_1 and σ_2. This is an important condition of the specimens to ensure that failure is through the desired through-thickness means. The through-thickness stress, σ_3 response of the square and cylindrical cross-section models is presented in Figure 6.6 and Figure 6.7 respectively. These images visually highlight that there is a variation in the stresses close to the edges of the model whilst there is a more uniform stress response through the centre. The free-edge effects are also noticeably different for each layer of the composite as indicated by the difference in colour on the edges of each layer.

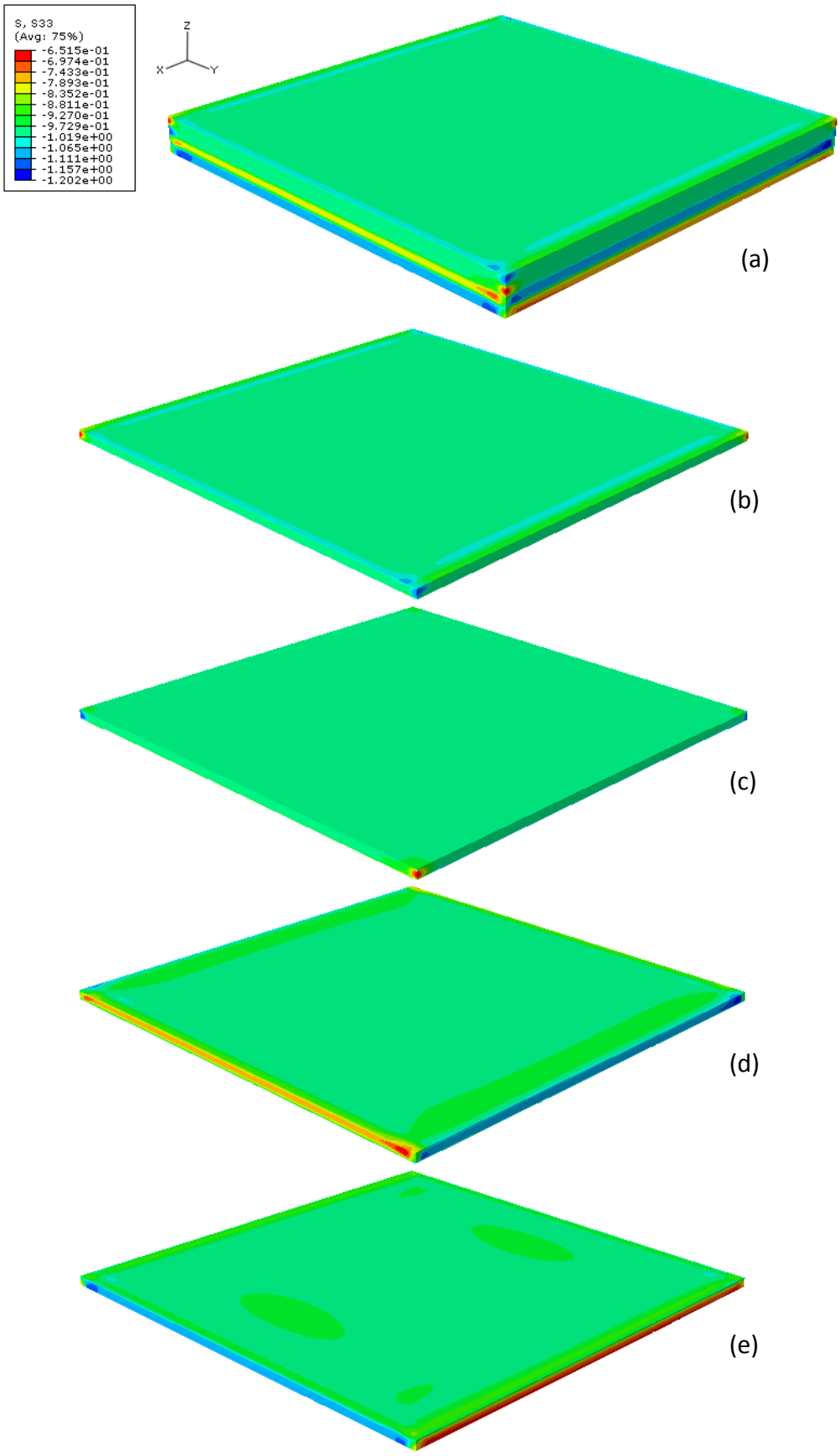

Figure 6.6: Through-thickness σ_3 stress contour plots for square cross-section slice; (a) Four centremost layers of the model, (b) -45° layer, (c) 45° layer, (d) 90° layer, (e) 0° layer

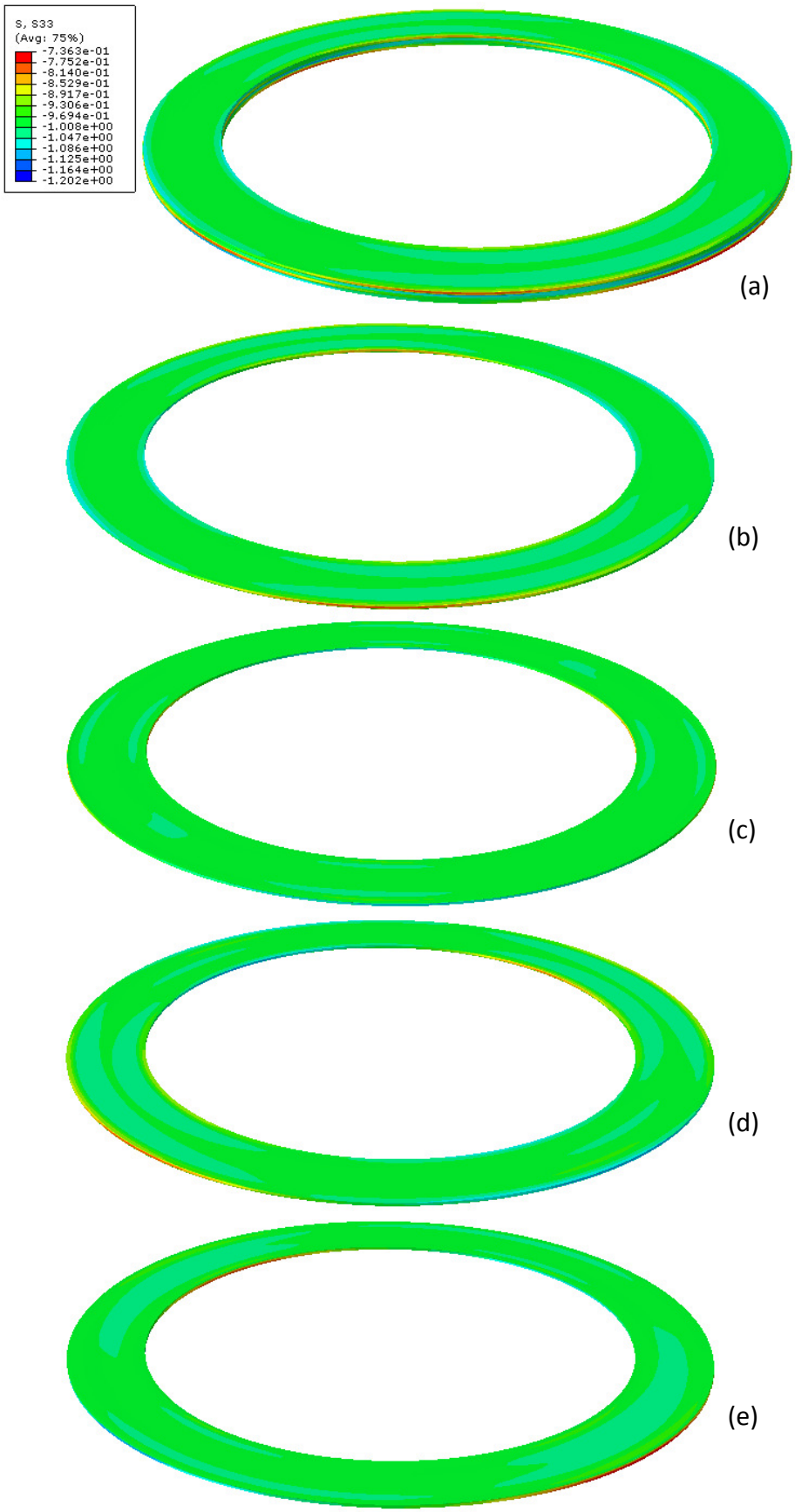

Figure 6.7: Through-thickness σ_3 stress contour plots for cylindrical cross-section slice; (a) Four centremost layers of the model, (b) -45° layer, (c) 45° layer, (d) 90° layer, (e) 0° layer

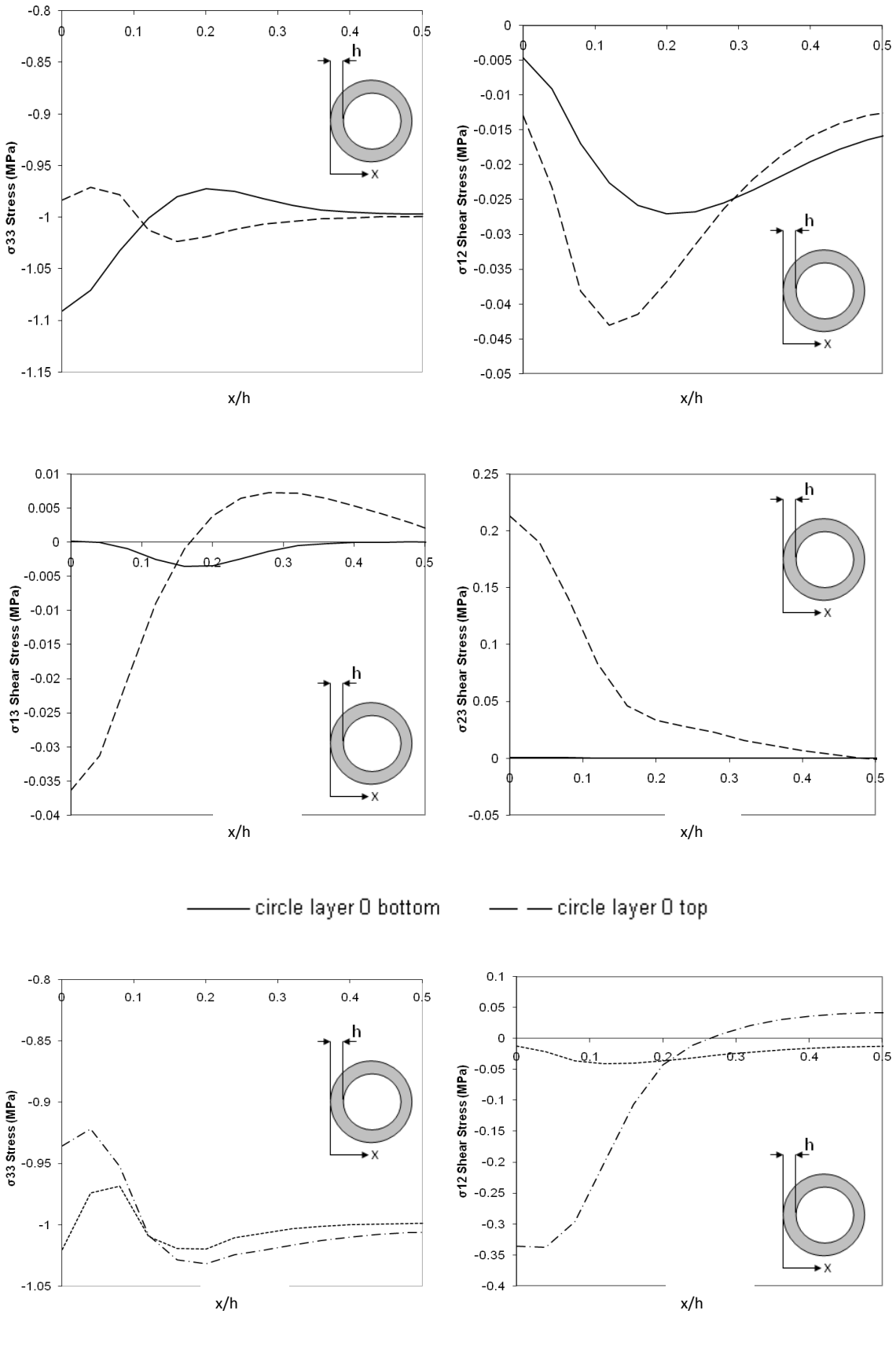
σ33 Stress (MPa)
x/h
σ12 Shear Stress (MPa)
x/h
σ13 Shear Stress (MPa)
x/h
σ23 Shear Stress (MPa)
x/h
h
x
circle layer 0 bottom
circle layer 0 top
σ33 Stress (MPa)
x/h
σ12 Shear Stress (MPa)
x/h
circle layer 90 bottom
circle layer 90 top

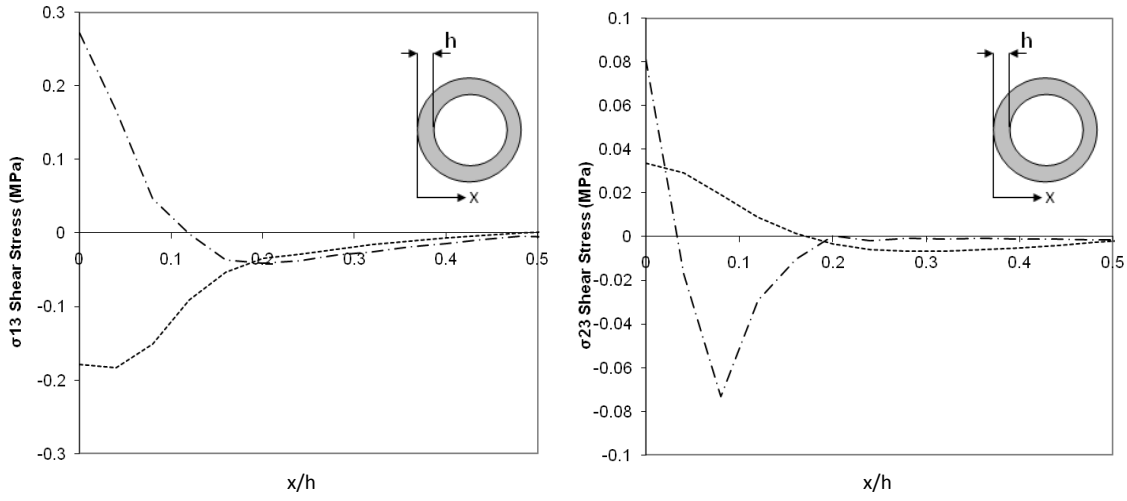

------- circle layer 90 bottom — - — circle layer 90 top

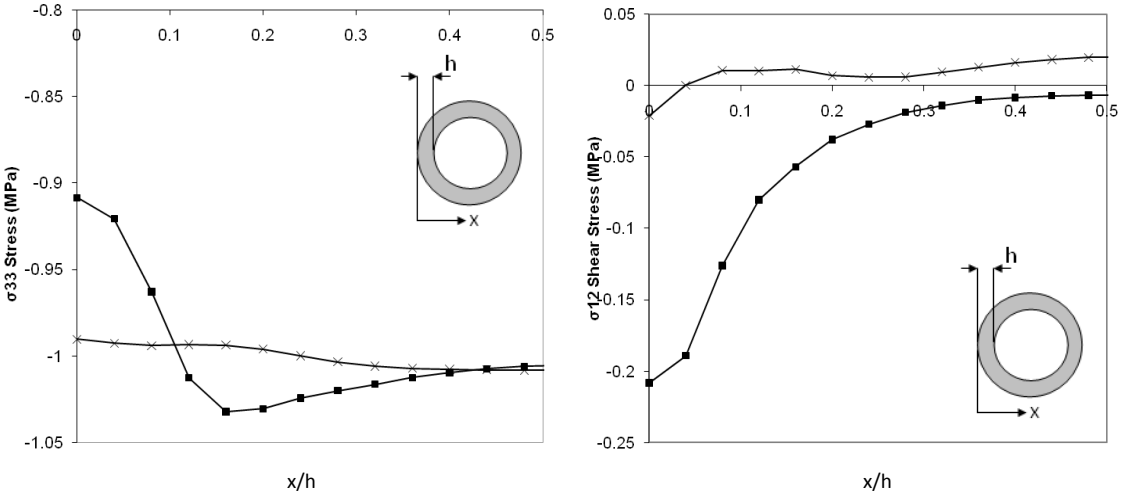

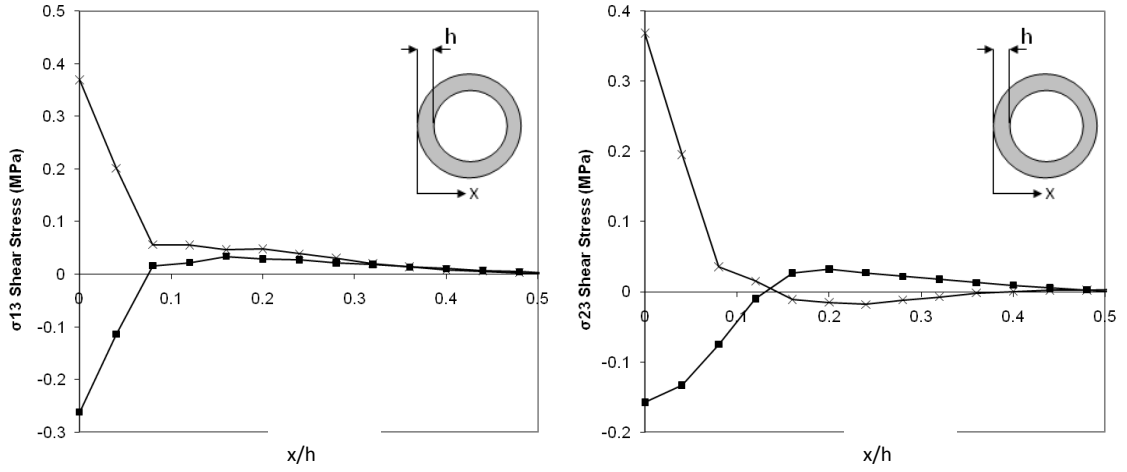

—■— circle layer 45 bottom —×— circle layer 45 top

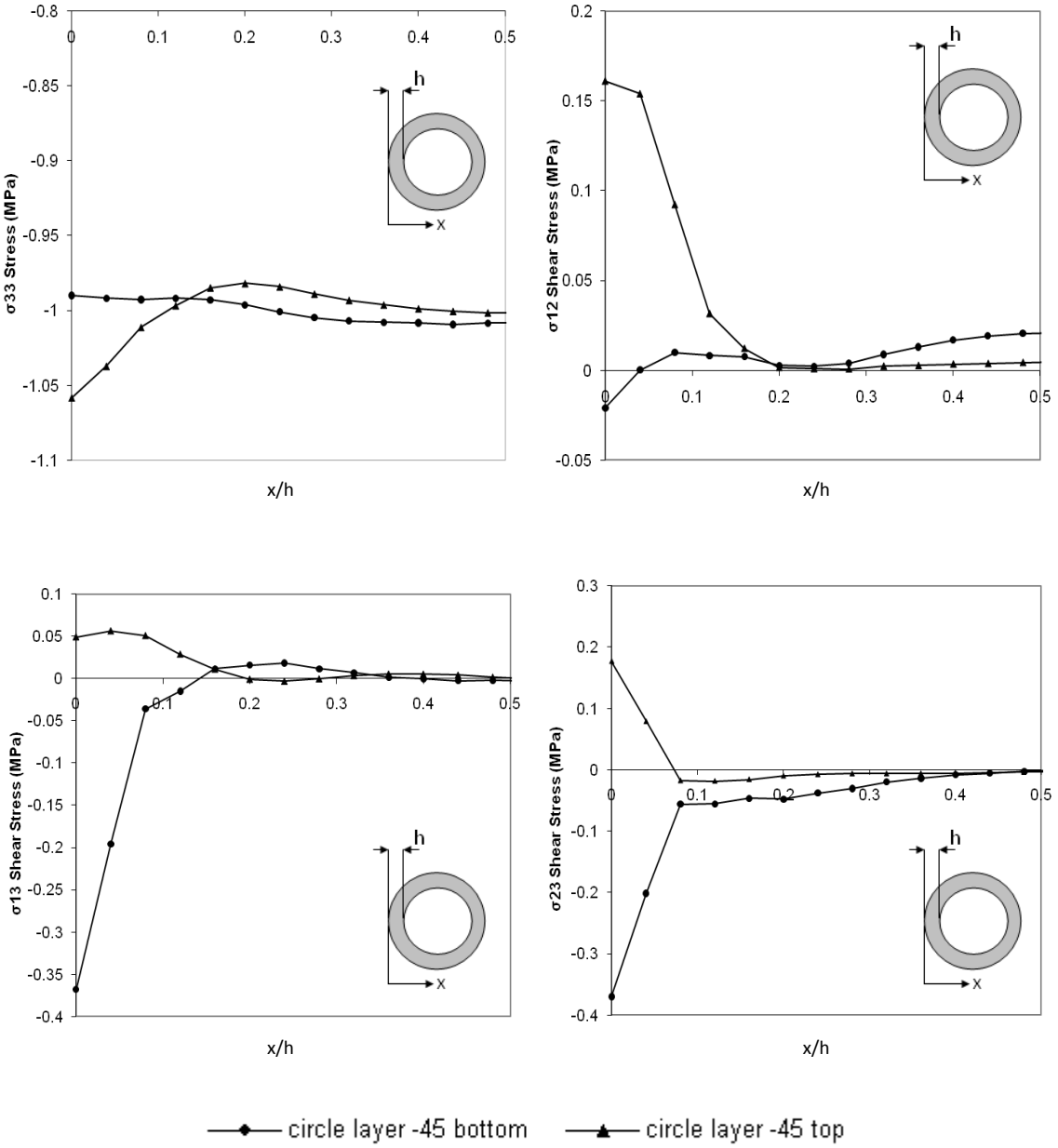

Figure 6.8: Stress distributions for cylindrical models (all stresses in MPa)

The edge stress results from the *x*-face and y-face are in agreement for both models as demonstrated by the graphs in Figure 6.10. In the case of the through-thickness stress σ_3 there is an increase of around 8.5%. This increase was witnessed only in the 0° and 90° plies due to their differing material properties with respect to one another. Very little σ_3 variation was found in the ±45° plies from the *X* and *Y*-face data points since in those directions the through-thickness response is the same in both layers. This is because at those points the ±45° plies have essentially the same material properties with respect to the *x* and *y* directions.

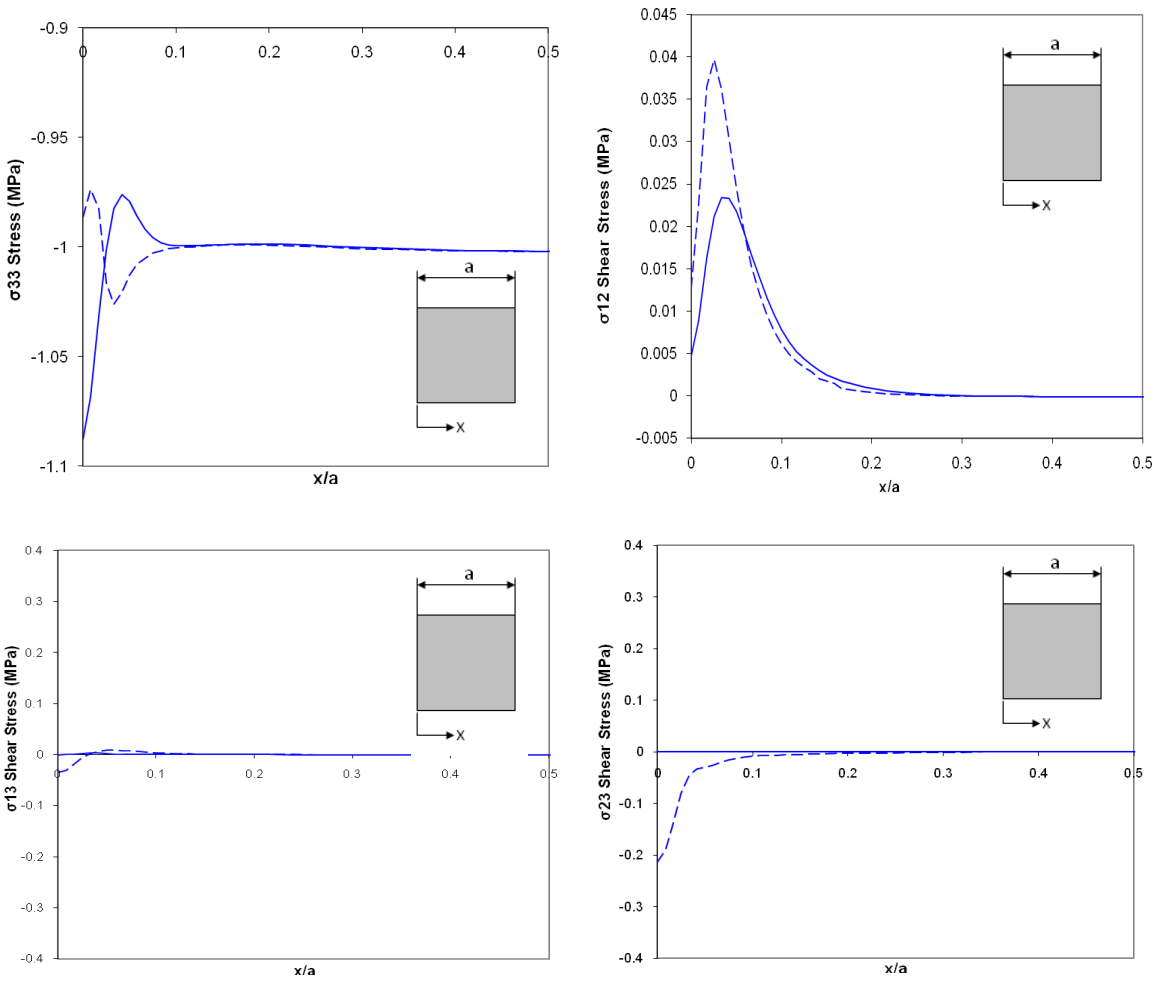
σ33 Stress (MPa)
x/a
σ12 Shear Stress (MPa)
σ13 Shear Stress (MPa)
σ23 Shear Stress (MPa)
a
x
square layer 0 bottom
square layer 0 top

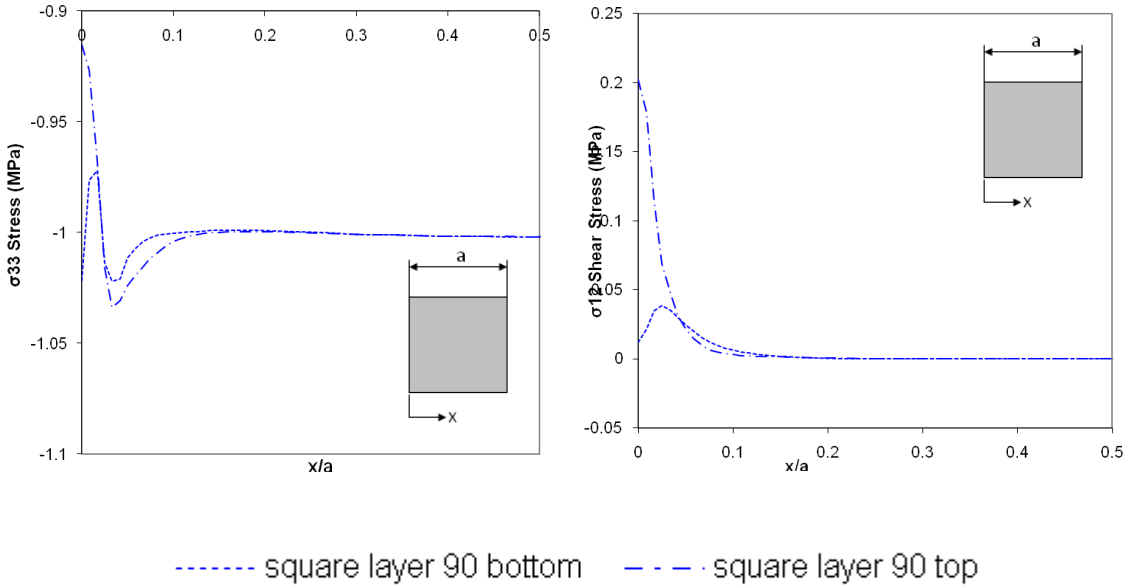
σ33 Stress (MPa)
x/a
σ12 Shear Stress (MPa)
a
x
square layer 90 bottom
square layer 90 top

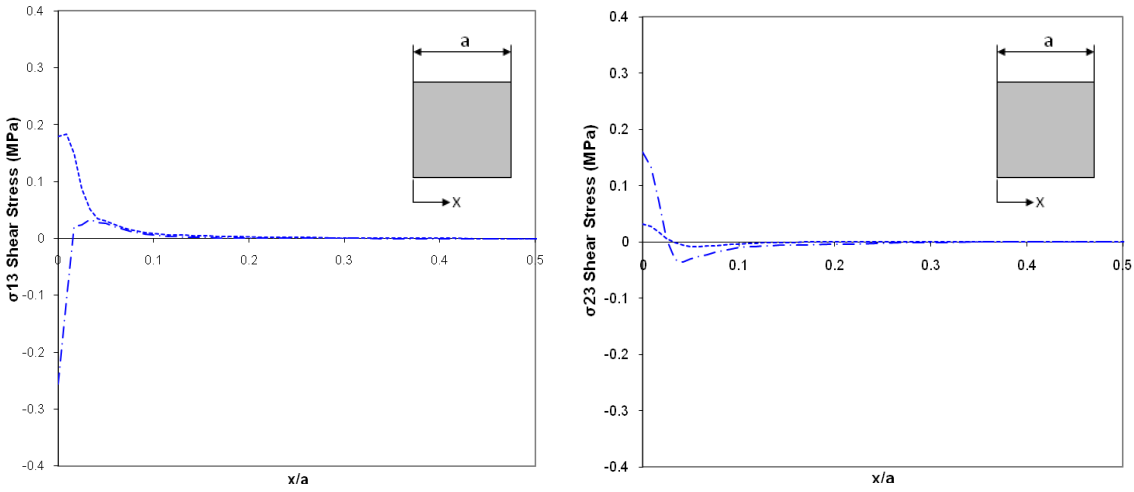
σ13 Shear Stress (MPa)
σ23 Shear Stress (MPa)
x/a
a
x
square layer 90 bottom
square layer 90 top

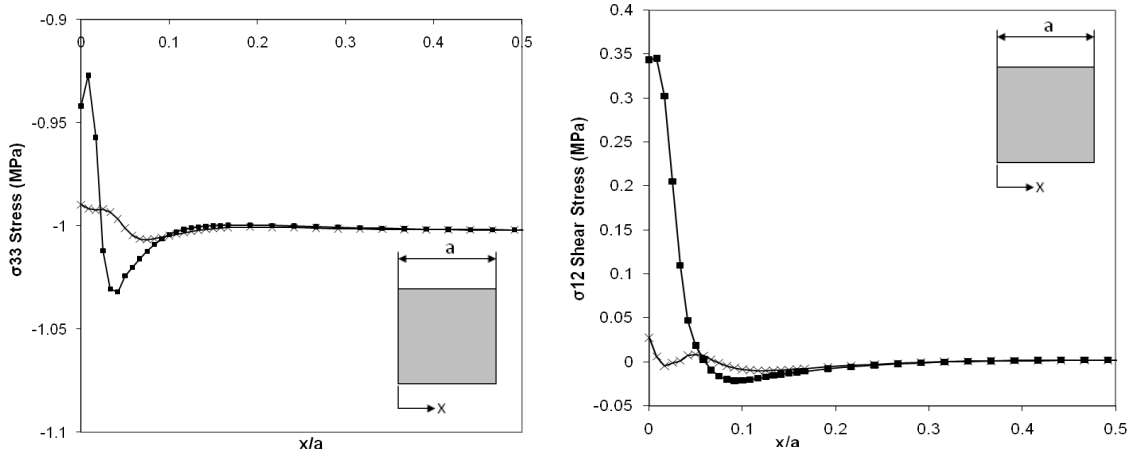
σ33 Stress (MPa)
σ12 Shear Stress (MPa)
x/a
a
x

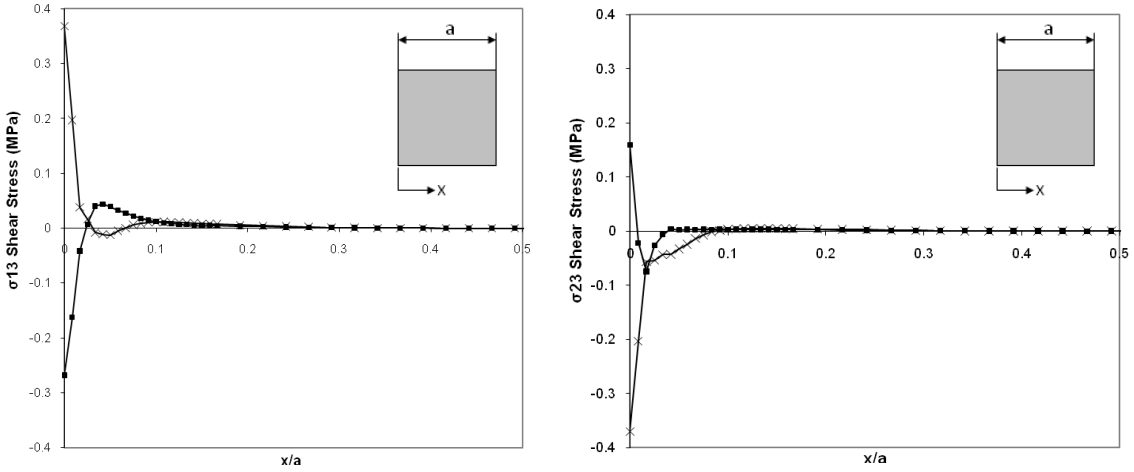
σ13 Shear Stress (MPa)
σ23 Shear Stress (MPa)
x/a
a
x
square layer 45 bottom
square layer 45 top

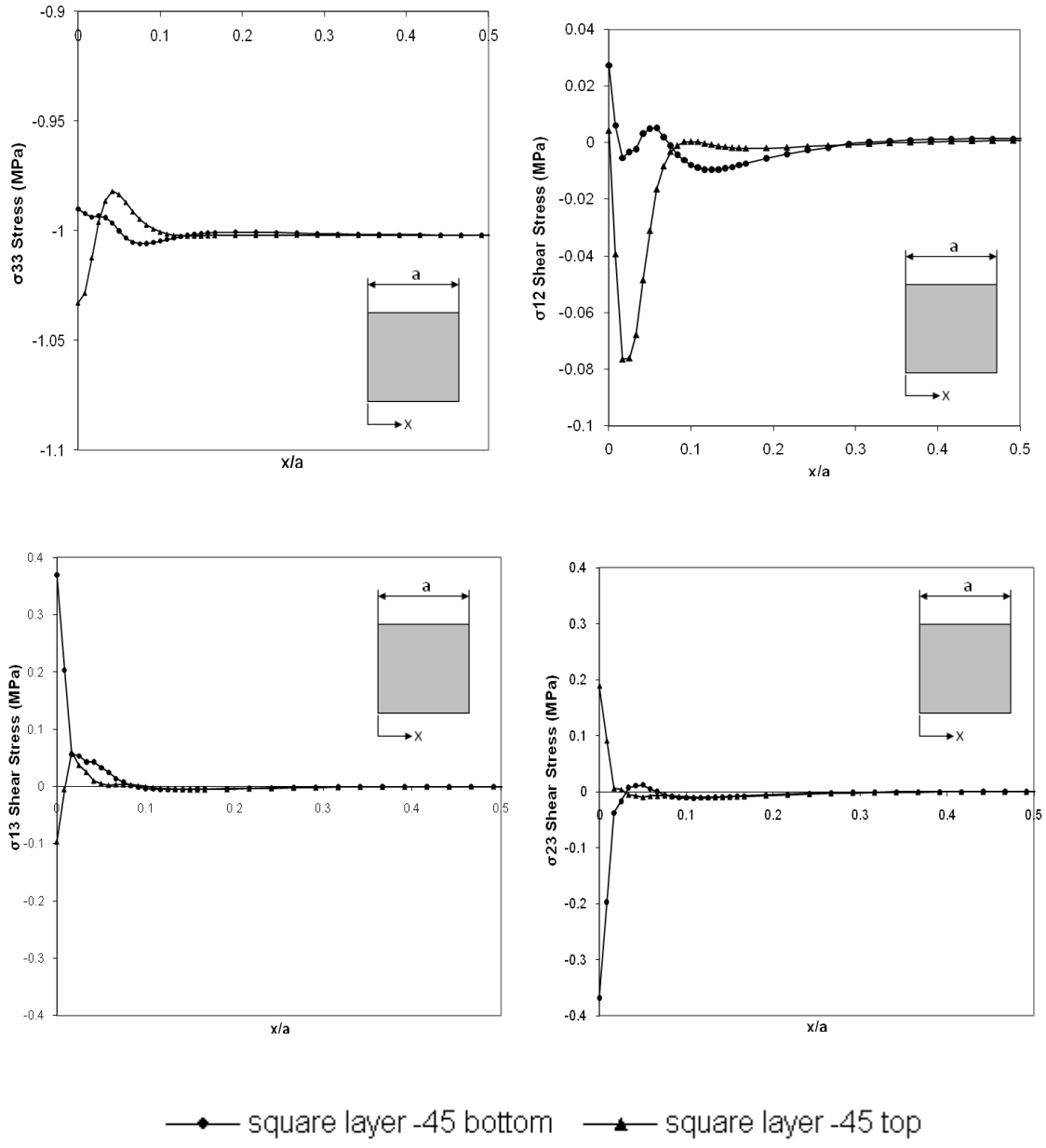

Figure 6.9: Stress distributions for square models (all stresses in MPa)

Through the centre of the square model no shear stresses were present. Close to the edges however, shear stresses begin to develop. These shear stresses develop due to the differing Poisson's contractions present between each layer. As mentioned previously, if the interface between the layers was frictionless then there would be a step change in the position of the edge of the layer. In reality the layers are connected and as a result the edge of the material forms a ridge and valley appearance. The forces induced by the connections between layers result in shear stresses developing as shown schematically in Figure 6.1. In both models the

shear stress τ_{12} reaches a value which has a magnitude of around 34% of the average σ_3 through-thickness stress at the edge interface between the 90° and 45° layers. The shear stresses τ_{13} and τ_{23} had magnitudes which reached 37% of the average σ_3 through-thickness stress at the edge of the -45° and 45° layers respectively. These values are substantial, especially because in general the shear strength of composite materials is much lower than the compressive strength. In the case of AS4/3501-6 used in these models the in-plane shear strength S_{12} is 79MPa; this is 40% of the value of transverse compressive strength of 200MPa for a UD lamina. Therefore, the shear stress values found in the square model could contribute towards material failure by promoting crack initiation.

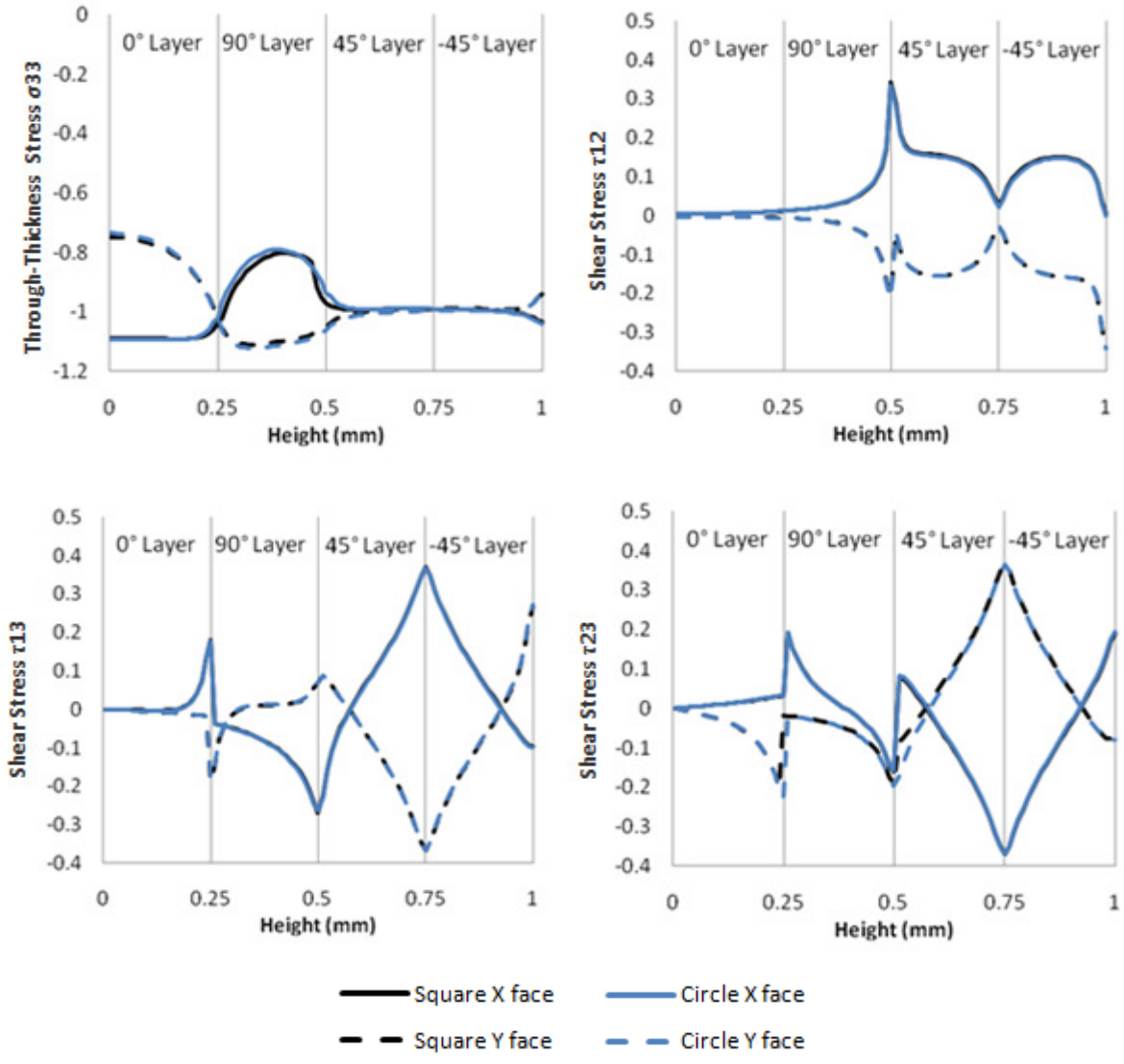

Figure 6.10: Stress variation across the edge of the square and cylindrical cross-section models from the *X*-face and *Y*-face data sets (all stresses in MPa)

The graphs in Figure 6.9 highlight that in the square cross-section model the edge effects have almost fully dissipated after 1.5mm from each edge into the centre of the model. This is approximately six times the lamina thickness. In the case of the cylindrical specimens the graphs in Figure 6.8 show that the edge effects never truly dissipate through the depth of the cylinder walls. This is due to the cylinder walls having a thickness of just 2.5mm. According to the result from the square cross-section model a total of 3mm in depth is required for the edge effects to reduce and this is not the case in the cylindrical model. The highest magnitude of stresses is still seen at the edges of the model but the stresses in the centre of the model remain higher than those in the square cross-section model. These edge effects appear throughout the model in each layer and as a result they must have an effect on the strength of the specimen.

In general both models produced identical edge stress values across the *X* and *Y*-faces which shows that in these locations the model geometry does not affect the stress results. The level of shear stresses caused by edge effects is of particular concern to the results presented by DeTeresa *et al* for combined through-thickness compression and shear loading. The interlaminar stress graphs in Figure 6.8 demonstrate that the edge effects are rife through the gauge length of the cylindrical specimen (which has the same wall thickness as the DeTeresa specimen). Through the centre of the specimen the shear stress due to through-thickness loading should be zero, but this is not the case in the cylindrical FE model and the result is that free-edge effects will have an impact on the shear stresses calling into question the results obtained by DeTeresa *et al*.

6.3.2 45° and 135° Direction/Corner Edge Stresses

The 45° and 135° data sets provided some interesting results between the square and cylindrical models. The stress variations across the edges of the models in these locations are given in Figure 6.11. Unlike the axial and normal data set results the 45° and 135° data set results show a difference in stress response between the two models. The stress result variations between the two models were caused by the difference in geometry between the two models at these locations. Figure 6.4 shows that in the square model the 45° and 135° data sets lie

at the corners of the model. In the cylindrical model these data points are taken from a 'face' which causes the edge stress results to be similar to the results taken from the *X* and *Y*-faces.

It was observed that the deviation in through-thickness stress σ_3 from the average was higher in the square cross-section model with the variation occurring in the ±45° layers. At this location in the square model there is little material around the data points (due to the 90° corner) which means that there is less resistance to local edge deformations through the composite compared to the cylindrical specimens. The high material deformation at this point is seen in the top two layers in Figure 6.5. The high stresses here will increase the severity of the stress concentrations in the waisted specimens and will promote premature failure. The rise in σ_3 in the cylindrical specimen at these data points is the same as seen in the 0° and 90° layers from the *X* and *Y*-face data points. The presence of these high edge effects also support the TI models used in Chapter 5 to characterise the stress concentrations as these edge effects will be severely mesh dependent. This can be observed by the amount of edge stress variation witnessed in the models in this chapter compared to those presented in Chapter 5.

The development of shear stresses at the 45° and 135° data sets shows an inversion of the σ_3 results in the square and cylindrical specimens. There, the square model produced larger stresses but generally, the largest shear stresses are found in the cylindrical specimens along the 45° and 135° data sets. The exception is τ_{12} where there are large spikes in the shear stress between the 90° and 45° layers and the -45° and 0° layers. These in-plane shear stresses were caused by the severe edge deformations in the square model in the ±45° layers. The material remains intact which results in the large in-plane shear stresses.

The largest through-thickness shear stresses τ_{13} and τ_{23}, were found between the 0° and 90° layers in the cylindrical specimens. The results are similar to those found in the *X* and *Y*-face data sets but the affected plies are different reflecting the choice of 45° and 135° data sets. The maximum through-thickness shear stresses are lower in the square model as the deformation in the 0° and 90°

plies is lower at the corners than it is in the centre of the *X* and *Y*-faces. The lower deformation means that the reaction forces needed to hold the plies together are lower, resulting in lower out-of-plane shear stresses. There is a rise in τ_{13} and τ_{23} at the 45° and 135° data sets in the square models compared to the cylindrical model in the ±45° layers. This is due to the high local deformation of these plies at the corners of the square model however, these shear stresses are still lower than the maximum values found in the 0° and 90° plies in the cylindrical model.

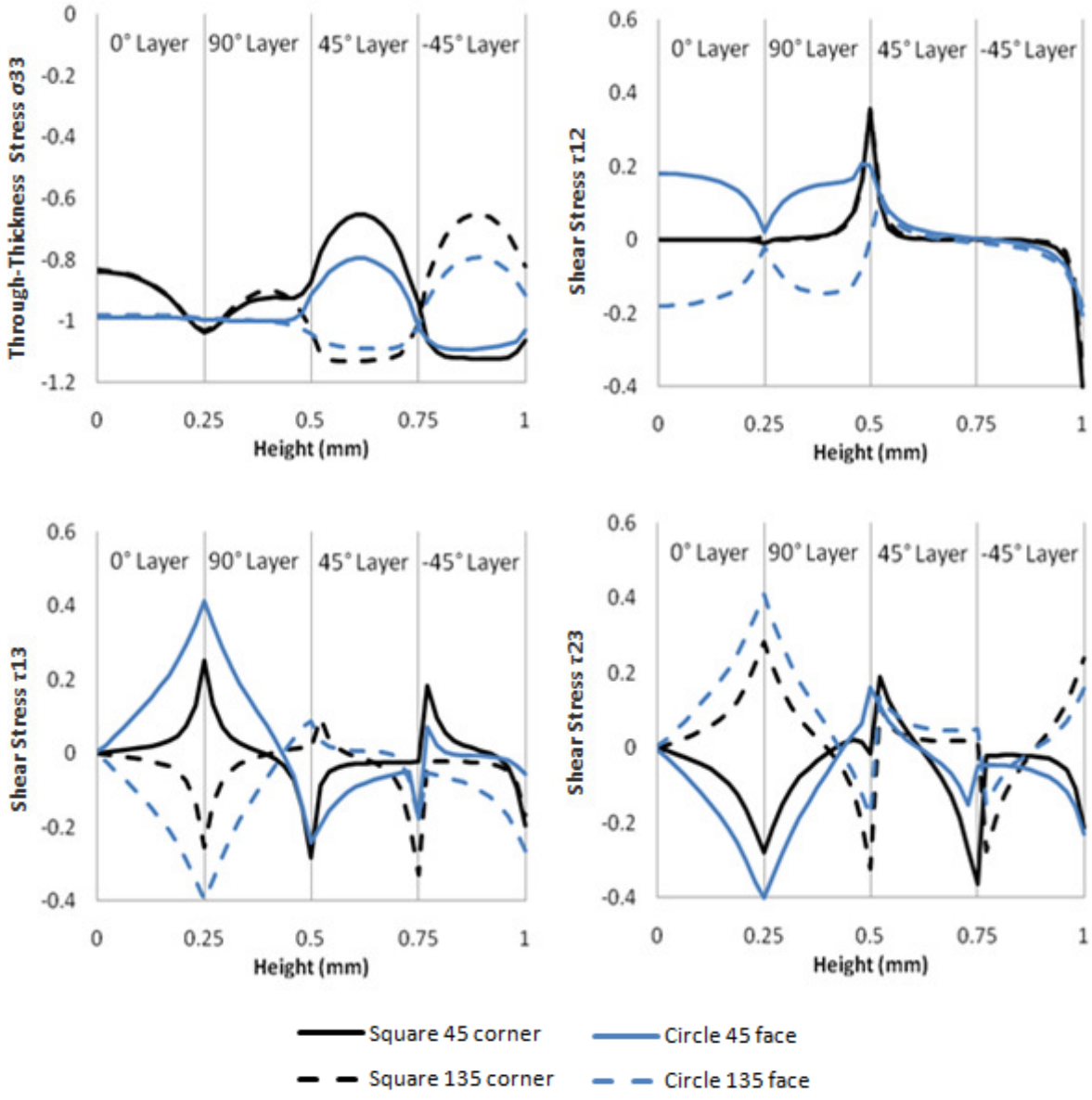

Figure 6.11: Stress variation across the edge of the square and cylindrical cross-section models from the 45° corner/face and the 135° corner/face data sets (all stresses in MPa)

The effect of through-thickness compression on shear strength was presented by DeTeresa *et al*[55]. They utilised a cylindrical specimen with a cross section very similar to that shown in the current study. The general finding for carbon fibre composites was that as a greater constant through-thickness compressive force is applied a higher shear strength value is obtained up to the through-thickness compressive strength of the specimen. It is valuable then, to discuss the impact of free edge effects on the state of shear stress within a quasi-isotropic laminate under through-thickness loading.

The cylindrical model shows that free-edge effects run through the wall under through-thickness loading as indicated by the graphs in Figure 6.8. In the work by DeTeresa the shear stress is calculated using the equations:

$$\tau_e = \frac{2T}{\pi r_o^3 \left(1-\left(r_i^4 / r_o^4\right)\right)}$$
$$\tau_p = \frac{2T}{2\pi\left(r_o^3 - r_i^3\right)} \qquad \textbf{6-1}$$

Neither of these equations take into account any pre-existing state of shear stress. Furthermore, DeTeresa does not mention the subject of free-edge stresses except to say that it was assumed that edge effects could be ignored and that the through-thickness stress was uniform through the gauge length; the FE results shown here in Figure 6.7 show that this is far from reality. As discussed previously, the shear stress can reach 35%-40% of the through-thickness stress. Taking an example from DeTeresa[55], a specimen constructed from IM7/8551-7 with a quasi-isotropic lay-up is subject to a constant through-thickness compressive load of 138MPa. At this load level the specimen failed at a shear stress τ_{12} equal to 91.9MPa. However, this result does not take into account free-edge stress and as a result it can be assumed that this value is conservative. The graph of τ_{12} shear stress in Figure 6.8 shows that in the cylindrical specimen the shear stress through the centre of the model has a value approximately 4% of the through-thickness stress in the same location. Using this value means that the true shear stress in the DeTeresa specimen could have been 95.5MPa. The presence of free-edge effects in the cylindrical specimen is now

quite important for fully understanding the load carrying capability of the specimen. This is represented graphically in Figure 6.12 where at higher levels of applied through-thickness compression the specimen is seen to cope with higher shear stresses than reported by DeTeresa. In other words, the material is capable of taking a higher shear stress but this is limited by the specimen geometry. The question could then be asked, why not make a solid cylinder, or a specimen with thicker walls so that the impact of free-edge effects is dissolved. However, this would change the specimen entirely and it would no longer be viable for shear testing due to the requirement of a thin walled cylinder.

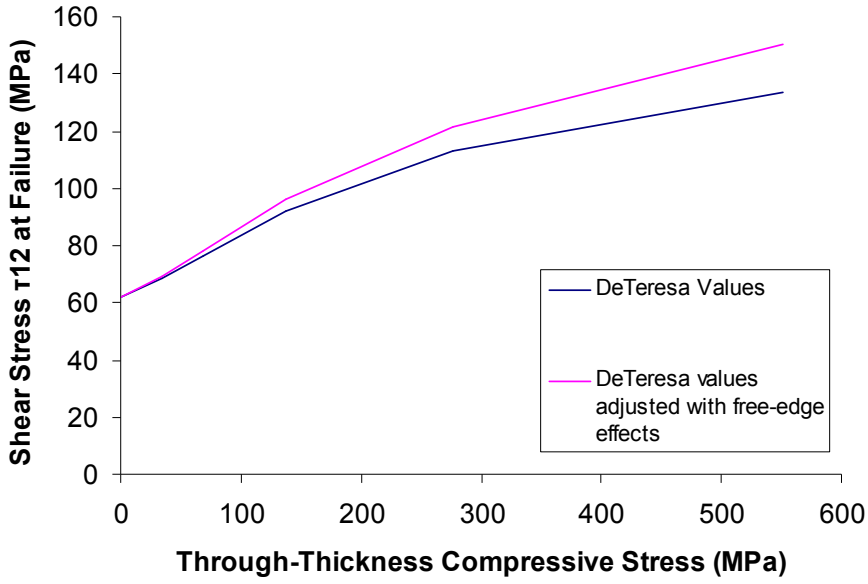

Figure 6.12: Graph showing shear stress failure values for quasi-isotropic IM7/8551-7 DeTeresa specimens, with and without account of free-edge effects.

In this instance the role of free-edge effects is very important and can have a significant impact on the accuracy of test results. This is proven by the loose calculation above. Of course this example should be taken with caution, as for other lay-ups the effects would be very different. In a UD lay-up for example, there should be no sign of free-edge effects and consequently the method used by DeTeresa would be sufficient.

6.4 Conclusion

The interlaminar stress graphs presented in Figure 6.8 and Figure 6.9 confirm that edge effects will be present in the gauge lengths of all three specimens when subjected to through-thickness loading. The free-edge effects appear to fully dissipate after 1.5mm from the free-edges. This raises alarm for the cylindrical specimens as the wall thickness is only 2.5mm. Therefore the free-edge effects extend through the centre of the models. It is predicted that this will lead to premature failure of the specimens tested in this study. Furthermore, the edge effects appear to significantly increase the shear stresses which are likely to have affected the results presented by DeTeresa *et al* when testing cylindrical specimens under combined through-thickness compression and shear. It has been shown that in reality the DeTeresa specimens were likely subject to higher shear stresses than reported.

Along the *X* and *Y*-faces the stress variations for both the square and cylindrical cross-section models are near enough identical. However, at the 45° and 135° corners/faces the edge stresses differ between each model. The results show a higher σ_3 in the square model due to severe local deformations in the ±45° layers. It is concluded that this will further increase the stress concentrations in the waisted specimens when quasi-isotropic laminates are used, aiding premature fracture.

7 Through-Thickness Compressive Tests

The aim of this chapter is to provide an assessment of three specimen geometries subjected to through-thickness compressive loading. The through-thickness moduli, Poisson's ratios and strength are provided with comments on the mode of failure and trends in the results. The chapter is concluded by making a statement on the effectiveness of the three specimens and the implications of the current work on results previously presented in the literature.

7.1 Pre-Test Procedure

7.1.1 Test Specimens

After specimen manufacture, seventeen specimens remained from the twenty two proposed. This was broken down into five waisted specimens, five cylindrical specimens and seven cubed specimens. One of the cylindrical specimens was deemed unusable due to heat damage from the attempts at laser cutting. A further cylindrical specimen suffered catastrophic delamination during the drilling process used to create the central hole. All other cylindrical specimens were inspected visually and did not appear to suffer from any delamination. Two of the waisted specimens fractured during the process of machining the waisted profile. This occurred when the machine tools became blunt and particular attention must be paid to this characteristic. The machine cost of producing the waisted specimens is substantially higher that the cylindrical and cube specimens. One of the eight cube specimens was cut from material close to the edge of the original block of material. In this region the plies did not remain straight and as a result the specimen was not used. This decision was taken as it was deemed that the result was likely to be adversely affected by the differing laminate properties.

7.1.2 Loading Devices

The loading devices are detailed in Chapter 4.2. The cube and cylindrical specimens were tested using the Instron 3507 200kN load cell machine and the waisted specimens were tested using the Amsler hydraulic compression test machine. One waisted specimen had initially been tested using the Instron but the

strength of the material exceeded the load capability of the device and as a result the Amsler machine (with a load capacity of 3000kN) was used to test the waisted specimens. A schematic diagram is presented in Figure 7.1 which is representative of both loading machines. Both devices have a ball joint on one of the plates to reduce the risk of uneven loading.

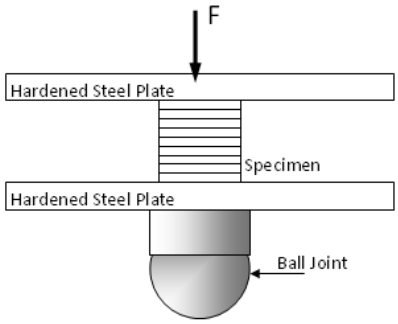

Figure 7.1: Schematic diagram of loading equipment

In both machines the application of load was displacement controlled and the cross-head displacement was set at 0.5mm/min. There is an argument for using a specially designed test jig but work by Park and Lee showed that use of a purpose built self-aligning fixture made the results less repeatable[49]. In the current set-up the self aligning mechanisms built in to the loading machines were deemed adequate for the tests to be carried out.

7.1.3 Specimen Loading

As described above, no special loading jig was used to apply compression to the specimens. The specimens were simply rested onto the bottom plate of the loading device and then the top plate was slowly offered up to the top of the test specimen. In order to align the specimen in the centre of the loading plates a grid was drawn on to the loading plate with location markers set for each specimen. A visual check of the contact between the loading plate and specimen was carried out and the machine load reading was monitored to ensure that the specimen was not pre-stressed.

An issue highlighted by the finite element study was the effect of friction on the specimen. This is a particular problem on the cube specimens due to their size

and lack of ‘shoulder’ material in which stress concentrations can dissipate. In an effort to reduce any friction between the loading plate and the specimens, grease was applied to both ends of all the test pieces prior to loading.

7.1.4 Strain Measurement

Three different methods of strain measurement were used. Six initial tests were carried out using four cube specimens and two cylindrical specimens. Two cube specimens were tested without any strain gauges attached. The strain information was taken from the machine displacement information. Prior to testing these specimens, a machine displacement check was carried out. This baseline test was used to observe any systematic displacement that is present in the machine as well as the displacement that occurs during loading. This machine displacement was then subtracted from the displacement reading taken during testing to provide the load displacement curve. With knowledge of the load and exact specimen geometry taken from micrometer measurements the stress strain curves were produced.

The two cylindrical specimens and two remaining cube specimens for the initial tests used standard foil strain gauges. These were applied to the specimens as detailed in Chapter 4.3. These tests were carried out to determine whether standard strain gauges were suitable for the compressive tests being carried out. The strain gauges failed at a stress of 48% of the specimen strength on average for the cylindrical specimens and at 40% for the cube specimens. Subsequent to these tests the decision was taken to use single post yield gauges with a gauge length of 2mm. These post yield gauges are specifically designed for high strain applications.

The waisted and cylindrical specimens both had four strain gauges per specimen i.e. two gauges aligned parallel to the loading direction (axial) and two gauges loaded transverse to the loading direction (transverse). Strains on the cube specimen were measured from two strain gauges: one gauge in the axial direction and one gauge in the hoop direction. The gauge layouts for each specimen are shown in Figure 7.2. The strain gauges on the waisted specimens were ‘paired’ together, such that the axial gauges were positioned on opposing faces and the

hoop gauges were placed on the remaining two opposing faces. The gauges on the cylindrical specimen were lined up in a similar manner. By placing the gauges opposite each other, any bending of the specimen should be highlighted in the strain results. The results can then be averaged to eliminate the effects of bending on the strain results. The two gauges on the cube specimen were placed on two faces that were perpendicular to each other. Only two strain gauges were used on the cubes since due to the dimensional tolerances and the small height of the specimens, it was deemed that bending would not adversely affect the strain reading.

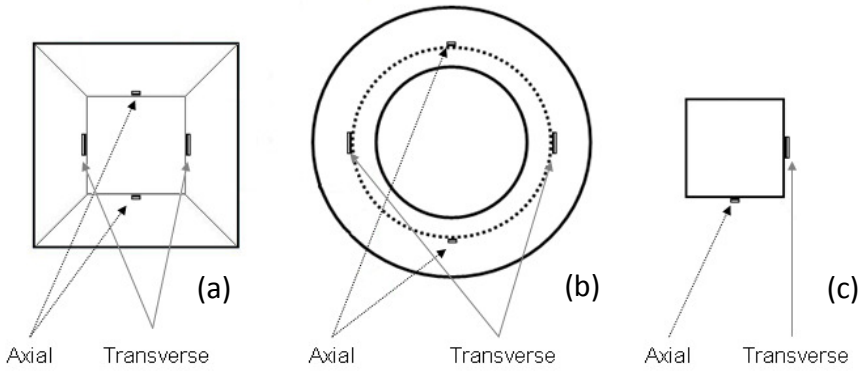

Figure 7.2: Strain gauge locations on: (a) waisted specimen, (b) cylindrical specimen, (c) cubic specimen

7.2 Results and Discussion

Characteristic stress strain curves for each type of specimen are shown in Figure 7.3. Further raw data for each specimen is presented in Appendix 3. It was observed that all three specimens provided a non-linear stress strain response. This is discussed further in Chapter 7.2.4. The stress strain response was linear in the majority of cases up to axial strains between 3% and 4%. Where the stress strain response is non-linear at axial strains lower than 3% the formation of the curves (in Appendix 3) suggests that the non-linearity is due to strain gauge failure except in Cylinder 2 where the curves suggest that uneven loading was present at the onset of loading.

The stress strain results for each gauge pair on the waisted and cylindrical specimens were in good agreement demonstrating that bending was not present. The results of the tests are shown in Table 7-3.

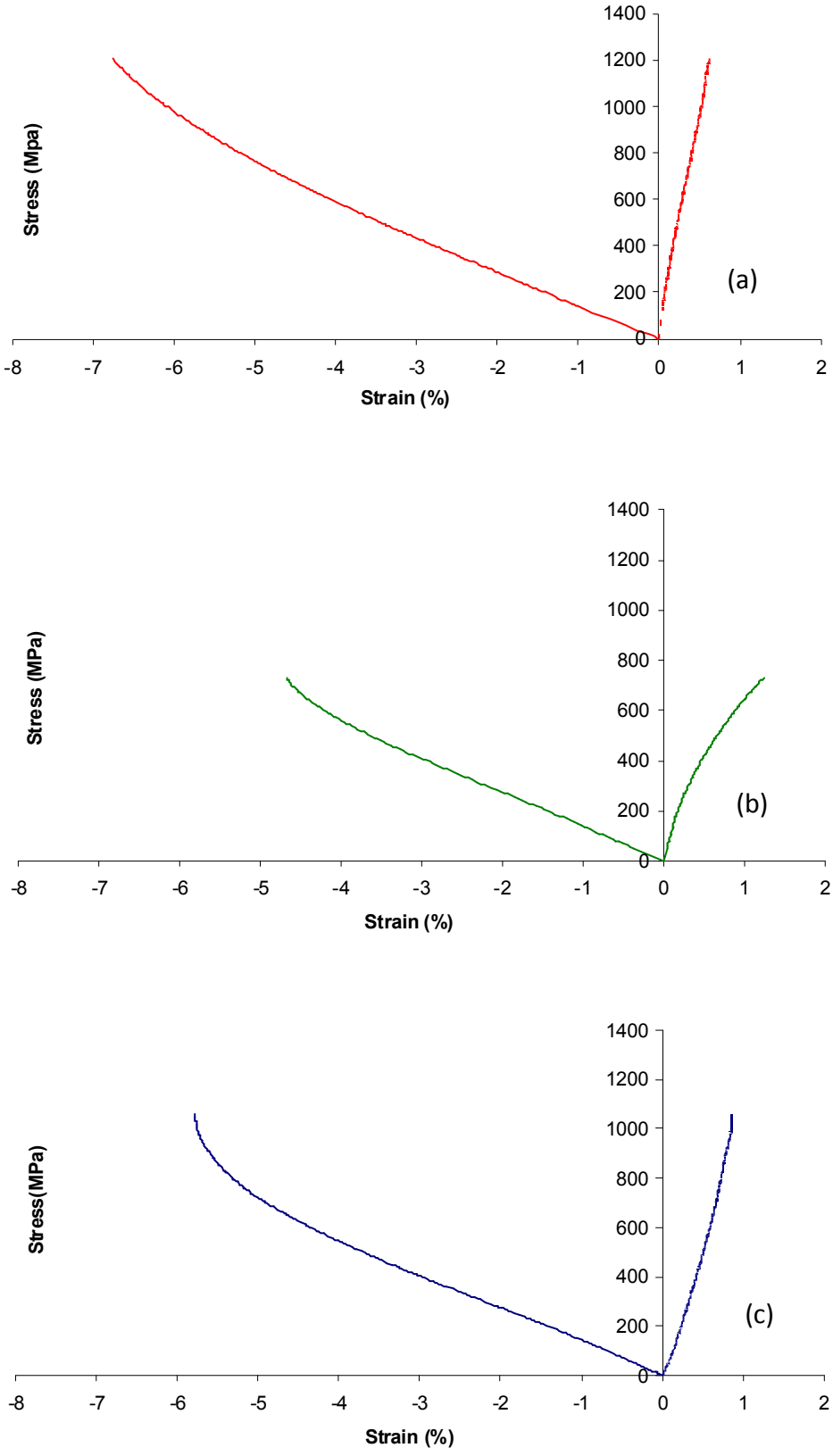

Figure 7.3: Characteristic through-thickness stress *vs* strain curves for; (a) waisted specimen, (b) cylindrical specimen, (c) cube specimen

7.2.1 Young's Modulus

The individual specimen and average Young's modulus values are presented in Table 7-1 and characteristic curves of the through-thickness compressive stress *vs* Young's modulus, E_z are shown in Figure 7.4. As a result of the non-linearity at high strains the Young's modulus of each specimen was calculated between strains of 0.5% to 3% (The non-linear results are discussed in Chapter 7.2.4). This region of the stress strain curve was found to be linear for all three specimens and was free from initial loading effects. Through-thickness Young's modulus values were calculated using the equation:

$$E_z = \frac{\sigma_z}{\varepsilon_z} \qquad \textbf{7-1}$$

Specimen Type	Specimen Cross-Sectional Area (mm^2)	Young's Modulus, E_z (Gpa)	C_v (%)
Waisted 1	148.89	12.6	
Waisted 2	144.01	14.1	
Waisted 3	142.39	13.4	
Waisted 4	144.24	15.8	
Waisted 5	143.92	14.1	
Waisted Average		*14.0*	*7.5*
Cube 1*	144.02	10.3	
Cube 2*	147.12	10.2	
Cube 3	143.90	13.8	
Cube 4	146.02	10.2	
Cube 5	143.99	14.4	
Cube 6	142.01	13.5	
Cube 7	144.27	11.3	
Cube Average		*11.9 (12.64)*	*14.6(12.39)*
Cylinder 1	143.28	11.9	
Cylinder 2	145.97	16.6	
Cylinder 3	145.30	14.2	
Cylinder 4	144.92	13.2	
Cylinder 5	146.12	11.2	
Cylinder Average		*13.4*	*14.1*

Table 7-1: Through-thickness Young's modulus, E_z results

* Results obtained from machine displacement values

() Values in brackets show results without including cube 1 and 2

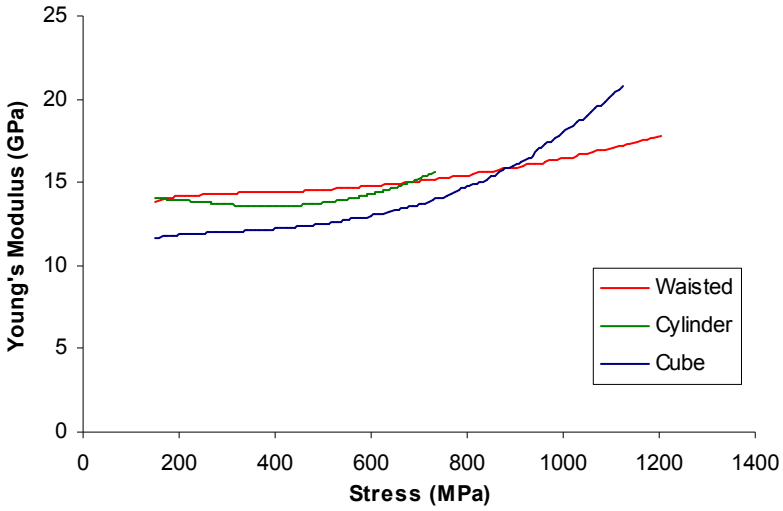

Figure 7.4: Characteristic through-thickness stress *vs* Young's modulus curves

7.2.1.1 Waisted Specimen

The Young's modulus of each specimen was calculated by taking the stress strain data and carrying out the linear regression technique described in Chapter 4.4 for each axial strain gauge. The curves were then averaged and the resultant stress strain curve was used to obtain the initial Young's modulus.

The initial Young's modulus of the waisted specimen was the highest on average of the three specimens. The C_v value was also the lowest of the three specimens at 7.5% indicating that good repeatability of results is attainable using the waisted specimen.

7.2.1.2 Cylindrical Specimen

The cylindrical specimens provided a slightly lower through-thickness modulus on average compared to the waisted specimens. It was found that the axial strains in the cylindrical specimens were larger than those obtained in the waisted specimen due to bending of the cylinder walls creating extra strain. Some wall bending had been expected as a result of the finite element study in Chapter 5.3. The scatter of results was also larger than that of the waisted specimens with a C_v value of 14.1%

7.2.1.3 Cube Specimen

The cube specimen strains were obtained in three ways as described in Chapter 7.1.4. The strains obtained from the machine displacement information were noticeably greater than those obtained from strain gauges. This is because both the specimen and the loading machine are subject to strains when the test takes place. A test was initially carried out to observe the base machine displacement such that it could be subtracted from the test result but it is believed that this process was still prone to errors and the result is an increased strain reading. When this result is used in equation 7-1 the result is a lower modulus value. When the results of cubes 1 and 2 are used the average E_z value is 11.90Gpa and the C_v value is 14.6%. If the results of cubes 1 and 2 are not used in the averaging progress the average E_z value increases to 12.64Gpa and the C_v value decreased to 12.39%. Furthermore, cubes 3 and 4 were tested using standard foil strain gauges. Neglecting these results, the measured average of E_z increases again, now up to 13.10GPa with a fall in the C_v value to 9.94%. These values are more in line with what was expected following the results of the waisted and cylindrical specimens and highlight problems relating to the method of strain data collection. The result of these findings is that post yield gauges are recommended in order to obtain the most reliable through-thickness compressive data.

During testing it was noted that the wires connected to the strain gauges made contact with the loading plates. This predominantly only happened at larger strains but may have contributed to inaccurate strain readings during testing; hence reducing the through-thickness modulus values obtained.

7.2.2 Poisson's Ratio

The through-thickness Poisson's ratios were calculated for each specimen. Due to the quasi-isotropic laminate used it is assumed that v_{xz} and v_{yz} are equal. To this end, only one value is given for each specimen. The result averaging process used to obtain the through-thickness Poisson's ratio was the same as that described in Chapter 7.2.1.1.

The Poisson's ratio results for all the specimens are shown in Table 7-2 and the ratios were calculated following the equation:

$$\nu_{zy} = \frac{\varepsilon_{trans}}{\varepsilon_{axial}} = \frac{\varepsilon_y}{\varepsilon_z} \qquad \textbf{7-2}$$

7.2.2.1 Waisted Specimen

The waisted specimen results proved to have the least variation of the three specimens examined with a C_v value of just 7%. No value could be obtained for the third waisted specimen as both transverse strain gauges failed. The average through-thickness Poisson's ratio obtained by the waisted specimens was 0.064 which is in general agreement with Roy and Kim who obtained values between 0.05 and 0.07[51].

7.2.2.2 Cylindrical Specimen

The cylindrical specimens provided through-thickness Poisson's ratios which were around 69% and 40% greater than those provided by the waisted and cube specimens respectively. There are two parameters used to obtain the Poisson's ratio: the axial strains and the transverse strains. The axial strains in the cylindrical specimen were in reasonable agreement with those obtained from the waisted and cube specimens, being marginally larger on average. However, the transverse strains found in the cylindrical specimens were noticably larger than those found in the waisted and cube specimens as shown in Figure 7.5. As a result, the through-thickness Poisson's ratio obtained from the cylindrical specimens is substantially larger than those from the other two specimen types. The large transverse strain readings were attributed to bulging of the specimen walls under loading. This was observed in the finite element study, although difficult to observe during testing. The strain gauges were placed along the mid-plane of the specimen gauge length which coincided with the location of the maximum bending. This bulging of the specimens inflated the transverse strain readings substantially as they collect strains along the gauge length mid-plane where bending is at a maximum. The axial gauges crossed over the mid-plane and hence were affected by the bending but not

to the same extent as the transverse gauges. These strain results were the cause of the large Poisson's ratio results.

Specimen Type	Poisson's ratio, $\nu_{zx}=\nu_{zy}$	C_v (%)
Waisted 1	0.065	
Waisted 2	0.068	
Waisted 3	N/A†	
Waisted 4	0.055	
Waisted 5	0.068	
Waisted Average	*0.064*	*7.0*
Cube 1*	N/A	
Cube 2*	N/A	
Cube 3	0.110	
Cube 4	0.065	
Cube 5	0.073	
Cube 6	0.047	
Cube 7	0.090	
Cube Average	*0.077*	*27.9*
Cylinder 1	0.078	
Cylinder 2	0.126	
Cylinder 3	0.162	
Cylinder 4	0.1	
Cylinder 5	0.074	
Cylinder Average	*0.108*	*30.3*

Table 7-2: Through-thickness Poisson's ratio results

* Results obtained from machine displacement values

† Transverse strain gauge failure

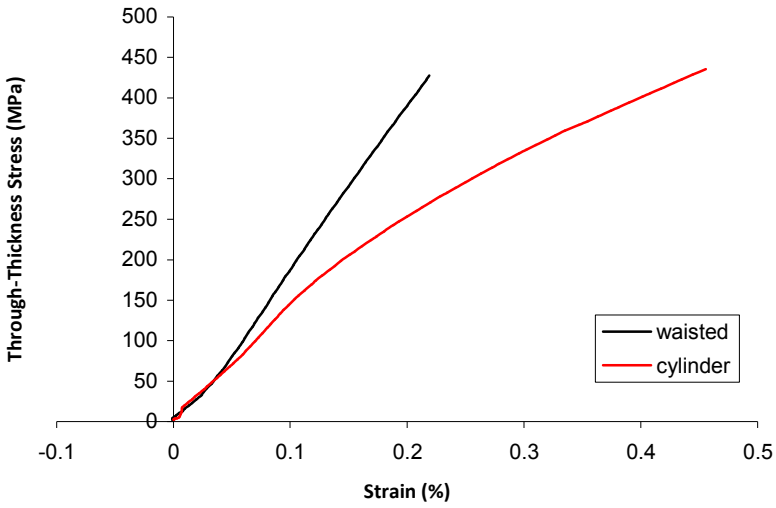

Figure 7.5: Characteristic stress *vs* transverse strain curve for waisted and cylindrical specimens

The cylindrical specimens also had the largest C_v values for the Poisson's ratio results. However, in a statistical sense this result is not too meaningful as the coefficient of variation is subject to large changes with only small variations when values are close to zero and as a result C_v values are commonly high for through-thickness Poisson's ratio results.

7.2.2.3 Cube Specimen

The first two cube specimens could not be used to obtain results as there is no way to measure the transverse strain when merely the machine displacement information is used to obtain the strain data. The scatter of results was higher than the waisted specimens and the average Poisson's ratio was also higher. However, the average result was skewed by one result which was much larger than the others. This result could have come about from specimen bending and as only one gauge was used for each direction no averaging was available to cancel the effects of bending. However, due to the universal joints in the loading machine it is likely that bending was not an issue. Statistically the result is still comparable with that obtained by the waisted specimens.

7.2.3 Specimen Failure

The failure stress results can be observed in Table 7-3 with a breakdown of the result for each individual specimen as well as the specimen average result. The stress at failure was calculated from the load strain data. When there was a sudden drop in load, failure was deemed to have occurred. In all specimens failure occurred suddenly without warning and was accompanied by a loud explosive noise common with brittle fracture.

7.2.3.1 Waisted Specimen

The failure stress in the waisted specimens was the highest of the three specimen types investigated with an average compressive strength of 1371.2MPa. The finite element analysis demonstrated that the waisted specimen was free from end effects in the gauge length which would affect the strength value unlike the cube specimens. Failure was sudden and was accompanied by a loud noise and debris firing from the specimen in various directions. As a result some of the small

specimen fragments were lost during testing. Another feature common with the waisted specimen was that failure occurred at one end of the gauge length at the start of the fillet radius. The reason for this is highlighted by the initial finite element models created. These showed that stress concentrations would be present close to the junction between the fillet radii and the start of the gauge length. The waisted specimens failed either at the top or bottom of the gauge length and as a result there appears to have been no issue regarding the application of load or a specimen property which could have caused the specimens to systematically fail in the same location i.e. to always fail at the bottom of the gauge length or to always fail at the top of the gauge length. An example of a typical failed waisted specimen is shown in Figure 7.6. Failure was limited to a few plies and showed no constant fracture angle. This is unlike the results shown by Ferguson *et al* for UD and [0/90] woven laminates. In those UD and [0/90] woven laminates, the failure surface was characterised by having an inclined fracture plane with the plane lying normal to the fibres. This is as a result of induced shear stresses causing the matrix material to fracture. However, in the case of quasi-isotropic material the fibre orientations prevent this from causing catastrophic failure. Each of the specimens did show small regions of fracture at inclined angles. These are incredibly difficult to measure accurately but are around 45°. These inclined regions of the fracture surface indicate that shear failure is evident in the fracture of these specimens. The reason that these cracks do not propagate through the specimens is that the fibres are much stronger than the matrix material, hence when a crack develops normal to the fibres in one layer, it is prevented from propagating through the next layer as the fibre orientation changes.

As well as the fracture surface features, the high strength of these specimens is also dependent on the fibre orientations. UD carbon/epoxy waisted specimens tested by Ferguson *et al* in standard and miniature form, and Mespoulet *et al* had average through-thickness compressive strengths of 297, 283 and 321MPa respectively. These UD material strengths are much lower than the 1371.2Mpa found here and this is due to the fibre orientations. Again this is due to

the crack propagation being prevented by the fibres. Visual investigation of the specimens showed signs of fibre breakage along the fracture surface which suggests that specimen failure was only permitted after fibre fracture. This was also observed by Kim *et al* for quasi-isotropic laminates.

Specimen Type	**Compressive Strength (Mpa)**	**C_v (%)**
Waisted 1	1435	
Waisted 2	1336	
Waisted 3	1206	
Waisted 4	1507	
Waisted 5	1372	
Waisted Average	*1371.2*	*7.4*
Cube 1	1292	
Cube 2	1139	
Cube 3	1125	
Cube 4	1200	
Cube 5	1226	
Cube 6	1117	
Cube 7	1187	
Cube Average	*1183.71*	*4.9*
Cylinder 1	797	
Cylinder 2	811	
Cylinder 3	775	
Cylinder 4	779	
Cylinder 5	842	
Cylinder Average	*800.8*	*3.0*

Table 7-3: Through-thickness compression strength results

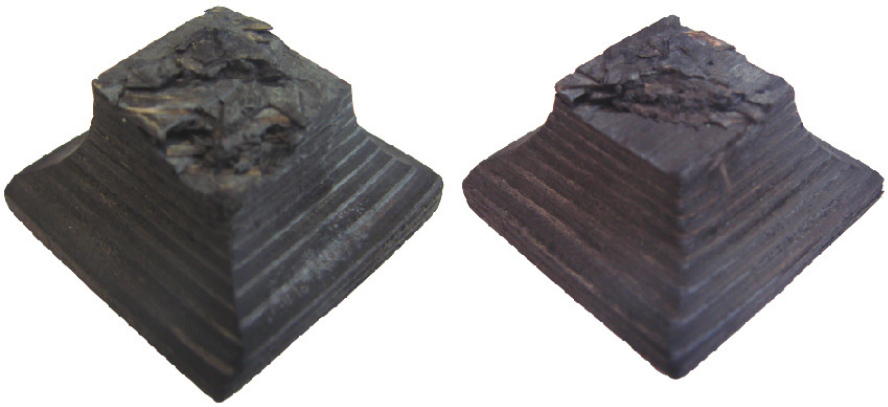

Figure 7.6: Typical failed waisted specimen

7.2.3.2 Cylindrical Specimens

The cylindrical specimens had the lowest strength of the three specimen types examined with an average value of 800.8Mpa. One of the reasons for this low failure stress could be the specimen geometry. Although the cross sectional area of the cylindrical specimen gauge length is very similar to the waisted and cube specimens, the depth of the gauge length is much smaller. The waisted and cube specimens have a depth of 12mm whereas the wall thickness of the cylinder is just 2.5mm. This difference means that the cylindrical specimen strengths are more likely to be influenced by voids or material defects. In this example they may act as sites for stress concentrations through the gauge length.

Figure 7.7: Typical failed cylindrical specimen

As with the waisted specimen, the finite element analysis of the cylindrical specimen demonstrated that stress concentrations would be present in the region where the fillet radius and gauge length join. In the waisted specimen this caused failure to occur clearly at the end of the gauge length. In the cylindrical specimens, however, failure was seen around the mid-plane of the gauge length indicating that the fillet radius stress concentrations were not a major factor in failure. A typical failed cylindrical specimen is shown in Figure 7.7. Another likely cause of the comparatively low failure stress of the cylindrical specimen was the presence of free-edge effects. This issue was examined in Chapter 6 where FEA results showed that large free-edge effects would be present throughout the gauge length walls. A further issue with the relatively thin specimen walls is that cracks are only required

to propagate a small distance meaning that small cracks are more likely to lead to failure compared to the waisted and cubic specimens.

The fracture surface on each of the cylindrical specimens shows some fibre breakage but it is not as evident as in the waisted specimens. Generally the fracture surface runs between plies. Attempts were made to capture the fracture of these specimens on video using a digital camera recording at 30fps. At this frame rate the camera struggled to capture the fracture indicating that fracture was a very sudden event. Two of the videos demonstrated a common feature. When fracture occurred, a small piece of material broke off from the specimen. It is likely that a weak part of the specimen fractures and as this happens a crack propagates through the specimen following the path of least resistance. Generally the crack follows a path between plies and where it skips between plies the crack generally runs in the fibre direction rather than causing fibre breakage.

7.2.3.3 Cube Specimens

The cube specimens had an average strength of 1183.71Mpa. This was considerably higher than the cylindrical specimen but lower than the waisted specimen. The cube specimen had an identical geometry to the gauge length but the failure seen was significantly different. The fractured cube specimens were characterised by having a large section of the specimen remaining accompanied by a number of small pieces of debris as captured in Figure 7.8. The cube specimens exhibited more angled fracture planes than the waisted specimens indicating that shear stresses contributed to failure.

The low failure stress of the cube specimens was attributed to stress concentrations induced by the contact between the specimens and the loading plates. This was highlighted in the finite element study in Chapter 5.1 and is unavoidable in these specimens. Not only does this reduce the strength of the material but it also controls the fracture initiation point. As the cube specimen fails leaving a large section remaining intact it is clear that failure initiates close to the end of the specimen. This was also found by Lodeiro *et al*[47] and Park and Lee[49]. The common feature between failure in the cubic and waisted specimens was

presence of flat and inclined fracture planes. Again it appears as though final failure is only permitted after fibre breakage. Furthermore the inclined fracture planes suggest that matrix shear is the initial form of failure i.e. matrix cracks begin to form but are prevented from propagating through the specimen by the in-plane fibres. Therefore final failure occurs upon fracture of the in-plane fibres.

Figure 7.8: Typical failed cube specimen

The average strength value of 1184MPa obtained for the cubic specimens compares well to the 1050-1150Mpa strengths reported by Roy and Kim. These values were reported for $[0/90/\pm45]_{50s}$ AS4/3501-6 carbon/epoxy specimens with a cross-sectional area of 35.94mm^2.

7.2.4 Non-Linear Stress Strain Response

The graphs in Figure 7.3 show a varying amount of non-linearity in the through-thickness stress strain response for all three specimens. One potential reason for this is that as the specimen is subject to high through-thickness stresses the material on the edge of the specimen deteriorates. When this happens, the transfer of load is confined to the central region of the specimen and the strain on the damaged edges increases at a lesser rate. The damage created may not be enough to cause catastrophic failure due to the compressive nature of the test causing crack closure; hence the non-linearity is observed. However, it is likely that this action only accounts for a small part of the non-linearity reported.

Another possible material cause of the non-linear response is that at lower load levels the weaker matrix material takes up the strain. As the load level

increases the material stays intact but the matrix cannot take up further strain and the fibres will begin to undergo deformation. However, the stiffness of the fibres is greater than that of the matrix and as a result some hardening behaviour may be witnessed. This is not witnessed in UD specimens (as tested by Ferguson *et al*[54]) because the material fails at much lower strains.

A further source of non-linearity appeared to be a failure of the adhesive used to attach the strain gauges to the specimens. At strain values above 4% the stress strain curves became non-linear and in a number of the cube specimens the stress strain curve characteristics were common with strain gauge bonding failure. The problem was exacerbated in the cubic specimens by their low height. The low height meant there was a lack of clearance between the strain gauge wires and the load plates. As high loads were reached and the clearance decreased, in some cases the wires made contact with the loading plates. This contact forced the strain gauge to peel away from the specimen causing the reduction in strain at high stresses as seen for the cube specimen in Figure 7.3 (c).

7.3 Finite Element Modelling of Test Specimens at Failure Loads

In Chapter 7.2 the failure stresses for the waisted, cubic and cylindrical specimens were discussed. These values are now used in conjunction with the FE models utilised in Chapter 5 to help assess the stress state in each specimen at failure. The aim is to shed some light on the possible causes of failure for the three specimens under through-thickness compressive loading.

The waisted specimens tested had an average through-thickness failure stress of 1371.2MPa. In the current model a load has been applied which results in an average through-thickness stress across the midline of the gauge length of 1370.0MPa. This allows for the analysis of the in-plane stresses at failure load. Stress contour plots for each specimen subject to loads at failure magnitude are presented in Figure 7.9, Figure 7.10 and Figure 7.11. It is clear, as in the initial finite element modelling that the through-thickness stress σ_z is much greater than the other stress components σ_x, σ_y, τ_{xy}, τ_{xz}, τ_{yz}.

It is immediately obvious that the stresses in the fibre direction of each ply i.e. σ_x are not high enough to cause fibre failure in the axial direction. The maximum and minimum σ_x stresses in the waisted specimen at failure are 740.8MPa and -518.7MPa. These values are less than half the lamina failure stresses[140] and as a result these stresses should be considered but they clearly do not determine failure alone. A full list of maximum stress component values can be found in Table 7-4.

A similar story is found for tensile σ_y stresses where the maximum value is 26.01MPa as opposed to a ply strength of 48MPa (ply strength values for the AS4/3501-6 material used in the models is provided in Table 7-5 and is taken from ref [141]). However, a much more significant result is given for the transverse compressive σ_y stress. Here the maximum value is -616.0MPa which is three times greater than the -200MPa in-plane transverse compressive strength of a UD lamina. This value is less than half the average through-thickness compressive stress but is still significant. It is likely, under compressive loading that small cracks develop in individual lamina but they are prevented from propagating due to the layers either side of the crack. In UD laminates it is seen that failure stresses under through-thickness compressive loading are similar to the transverse compressive strengths of the UD lamina. This is because there are no “supporting” layers either side of the cracked layer and the crack can easily propagate through the laminate.

It is evident then, that in quasi-isotropic laminates (and likely all angle ply laminates) that cracks develop but their propagation is hindered by the angled fibres in the layers above and below the cracked layer. However, this may not tell the whole story as the shear stresses evident in Figure 7.9 (τ_{xy} = 150MPa) are also higher than the shear strength of an individual UD layer (79MPa). These high shear stress are found only at the free edges of the laminate and the maximum values coincide with the areas of high geometric stress concentrations. These shear stresses could cause further cracks but their growth will be inhibited by crack closing forces produced by the through-thickness compressive load.

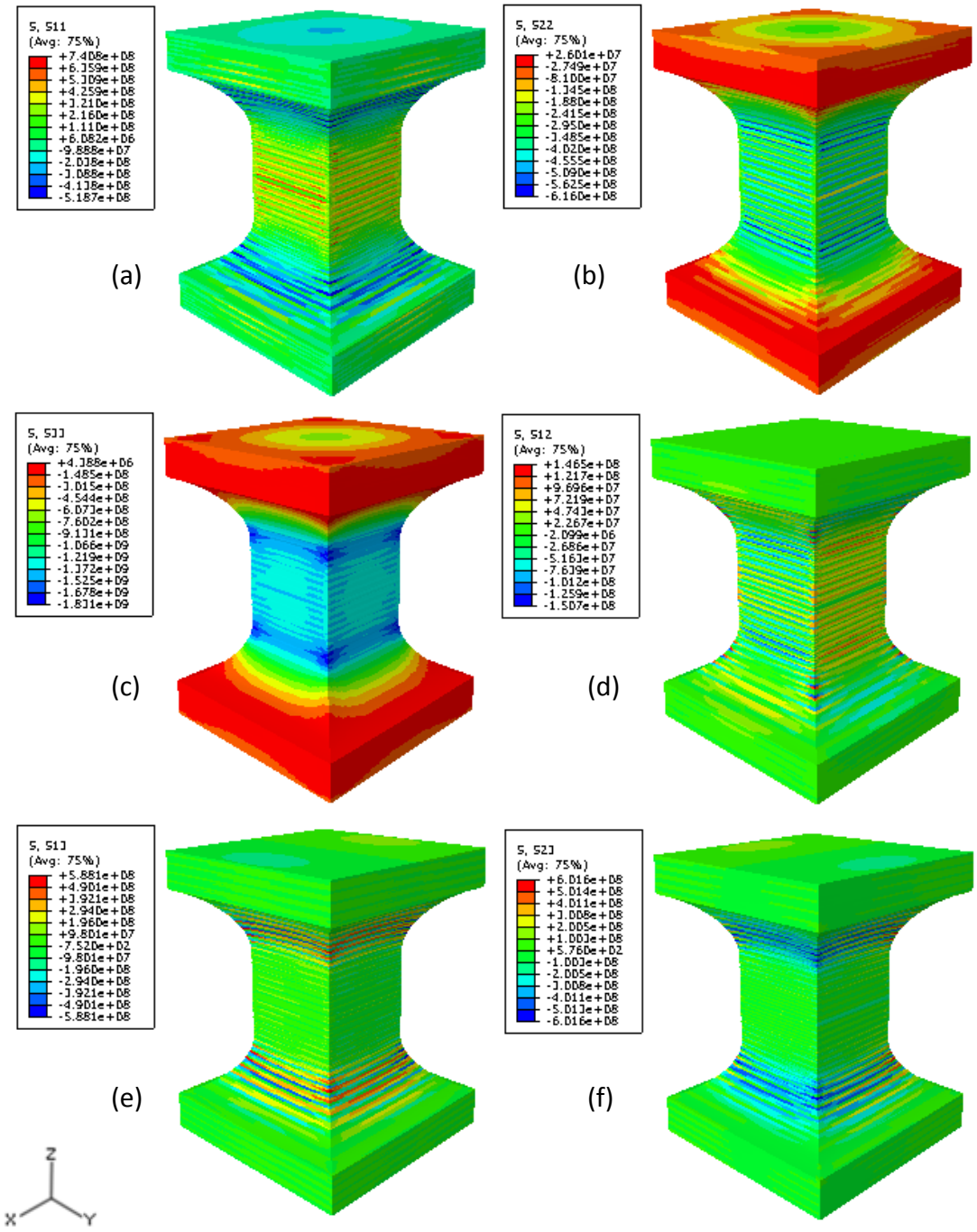

Figure 7.9: Stress contour plots of waisted specimen at failure load: a) σ_x, b) σ_y, c) σ_z, d) τ_{xy}, e)τ_{xz} f) τ_{yz}

It is clear then that the failure mechanism for quasi-isotropic laminates under through-thickness compression is highly complex. It was shown in the failed specimens in Figure 7.6 that fibre failure occurs along with cracks propagating between plies in the laminate.

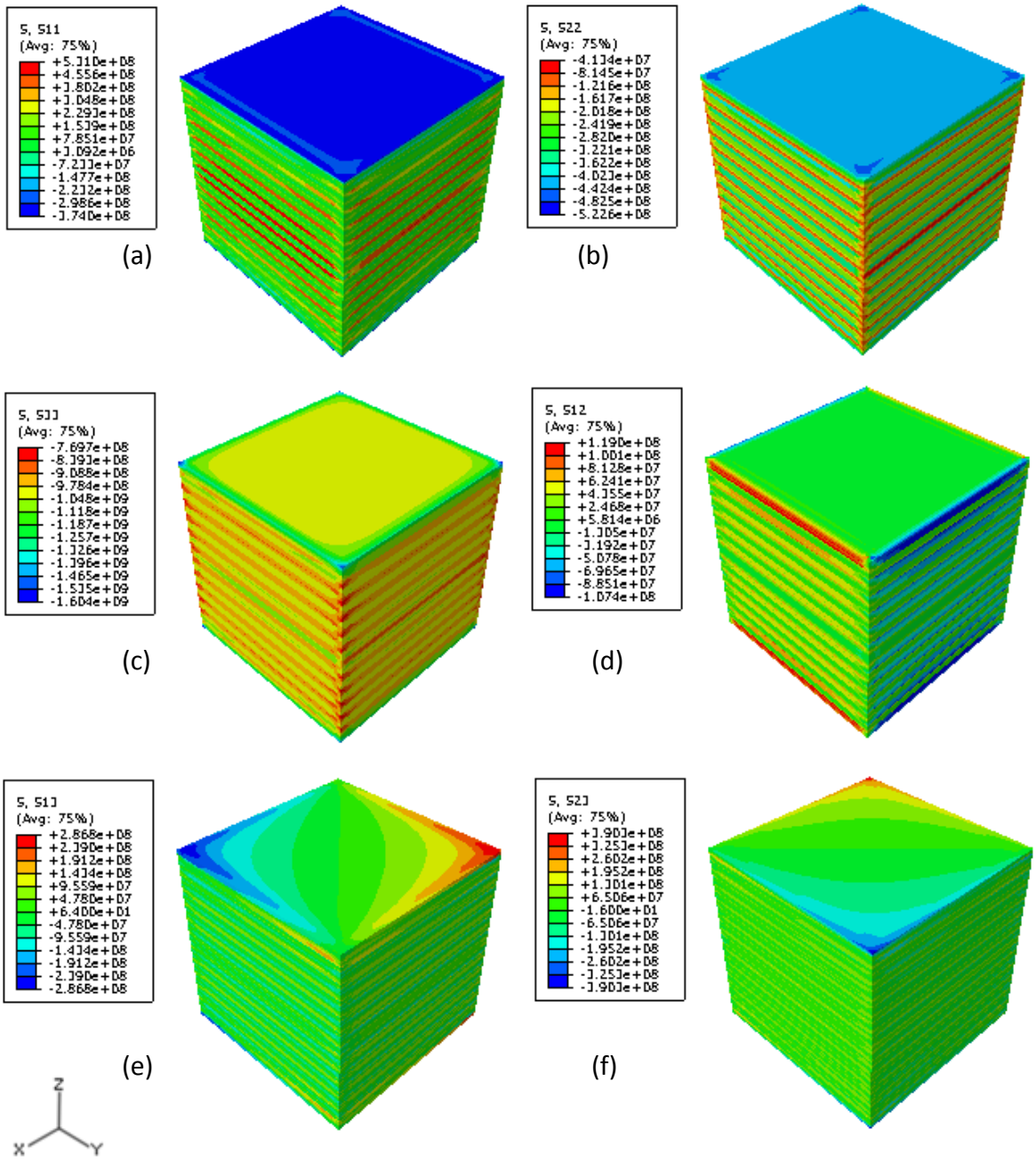

Figure 7.10: Stress contour plots of cubic specimen at failure load: a) σ_x, b) σ_y, c) σ_z, d) τ_{xy}, e)τ_{xz} f) τ_{yz}

A possible mechanism for failure is that cracks are produced throughout the laminate in many regions but the specimen remains intact due to closing forces provided by the compressive load and also due to angled plies surrounding the cracked area preventing crack propagation. It is then conceivable that a weak fibre bundle could break and the resulting forces of this break could force a crack to propagate through the laminate and cause catastrophic failure. This theory would also help to explain the variation in results as the weakness of fibres is likely to differ between specimens.

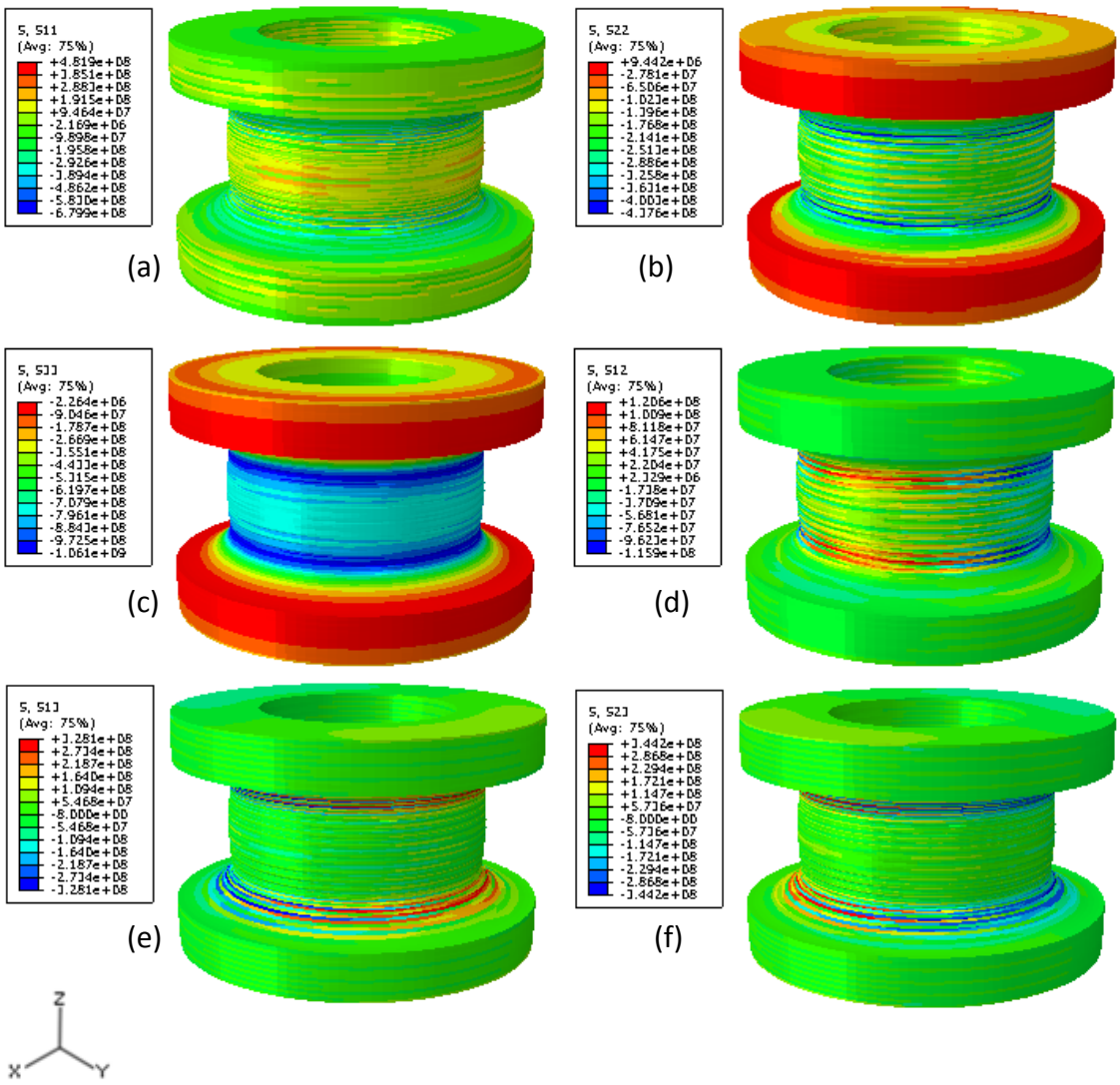

Figure 7.11: Stress contour plots of cylindrical specimen at failure load: a) σ_x, b) σ_y, c) σ_z, d) τ_{xy}, e)τ_{xz} f) τ_{yz}

Similar stress results were found for the cubic and cylindrical specimens, albeit lower in magnitude. However, UD lamina strengths are still exceeded for shear and transverse compressive stresses. The lower strengths of these specimens is more than likely caused by differences in the specimen geometry. It is witnessed in Figure 7.10 that high stress concentrations are present throughout the top layers of the cubic specimen. As a result it is likely that failure will occur here when a weak fibre breaks and final failure would then be instantaneous. In the cylindrical specimens stress concentrations are present but the likely reason for such a low strength compared to the waisted specimens is that the thin cylinder walls allow the free edge effects to be evident throughout the specimen. Therefore shear

stresses and high free edge stress concentrations are rife and the result is that failure occurs at a lower through-thickness stress.

Specimen Type	Stress	Maximum (MPa)	Minimum (MPa)
Waisted	σ_x	740.8	-518.7
	σ_y	26.0	-616.0
	σ_z	4.4	-1831.0
	τ_{xy}	146.5	-150.7
	τ_{xz}	588.1	-588.1
	τ_{yz}	601.6	-601.6
Cubic	σ_x	531.0	-374.0
	σ_y	-41.3	-522.6
	σ_z	-769.7	-1604.0
	τ_{xy}	119.0	-107.4
	τ_{xz}	286.8	-286.8
	τ_{yz}	390.3	-390.3
Cylindrical	σ_x	481.9	-679.9
	σ_y	9.4	-437.6
	σ_z	-2.3	-1061.0
	τ_{xy}	120.6	-115.9
	τ_{xz}	328.1	-328.1
	τ_{yz}	344.2	-344.2

Table 7-4: Maximum and minimum individual stress component values from waisted, cubic and cylindrical FE models at failure loads (positive values indicate tension, negative values indicate compression)

Parameter	Strength Value (MPa)
Longitudinal Tensile Strength $\sigma_x^u{}_t$	1950
Longitudinal Compressive Strength $\sigma_x^u{}_c$	1480
Transverse Tensile Strength $\sigma_y^u{}_t$	48
Transverse Compressive Strength $\sigma_y^u{}_c$	200
In-Plane Shear Strength S_{xy}	79

Table 7-5: Ply strength properties for AS4/3501-6 [141]

7.4 Conclusions

Through-thickness compressive tests were carried out on waisted, cylindrical and cubic $[-45/45/90/0]_s$ quasi-isotropic carbon/epoxy laminates. Young's modulus values were broadly similar for all three specimen types with the

cube specimens having the lowest average Young's modulus. The average result from the cube specimens was affected by two tests where the strain readings were calculated from the machine displacement values. These results produced higher than average strains and hence reduced the Young's modulus.

The Poisson's ratio results for the waisted and cube specimens showed fair agreement but the values obtained from the cylindrical specimens were much higher on average. This was due to high transverse stress readings caused by bending of the specimen walls.

All of the specimens failed suddenly without warning and failure was accompanied by a loud bang. The waisted specimens provided the highest strength value and final failure happened in most cases between the gauge length and fillet radius. The cube specimens provided a lower strength value than the waisted specimen and failure occurred at the ends of the specimens. This occurred due to stress concentrations induced by contact between the specimens and the loading plates. The cylindrical specimens were the weakest of the three specimen types. This was linked to the relatively thin specimen walls which heighten the effects of voids and material irregularities. Furthermore, the thin walls mean that cracks generally have a small distance to travel to propagate through the gauge length. Another issue linked to the thin walls was free-edge effects which were concluded to have contributed to failure after FE analysis (Chapter 6) showed that the free-edge effects would propagate through the gauge area.

As stated the actual failure mechanism of quasi-isotropic laminates under through-thickness compression is highly complex. Furthermore, the failed specimens highlight that for final failure to occur both matrix cracking and fibre breakage must be evident. In the current study the conclusion is that cracks develop within the laminates under compression but are prevented from propagating due to closing forces and the reinforcement offered by layers surrounding the crack. A weak fibre bundle will fracture at high loads and the force of this process causes surrounding cracks to propagate through the material resulting in catastrophic failure. This process cannot be confirmed in the current

study but appears to be a reasonable theory given the evidence provided in the FE stress analysis and failed specimens.

All three specimen types exhibited a non-linear through-thickness stress strain response. It was concluded that this was due to a mixture of material response and strain gauge peeling. Characteristics of strain gauge peeling were witnessed in some of the cubic specimen stress strain curves. Moreover, due to the high strength values of the specimens it is thought that as the material undergoes high strains the fibres start to take up more of the applied load. The result of these factors is that at high load levels the material appears to become stiffer.

8 Property Prediction of Z-Pinned Carbon/Epoxy Laminates

The aim of this chapter is to demonstrate the effectiveness of material property prediction for Z-pinned composites via FE modelling and mathematical bounding approaches. The FE approaches used are a meso-scale unit cell and a semi-homogeneous model following the process set out by Dickinson *et al*[85]. The bounding methods used are the often used and simple to apply Voigt and Reuss bounds and Walpole's bounds[122, 123]. These bounding approaches are used to assess their applicability to analysing Z-pinned composites. A direct comparison of all the approaches is presented with conclusions drawn on the benefits and issues regarding each approach.

8.1 FE Modelling Approach

The literature survey in Chapter 3 showed that for Z-pinned composites there is one common modelling approach used by Dickinson *et al* and Grassi *et al*[85, 86]. In the approach, the base composite is considered as a homogeneous material with no distinction made between fibres and matrix. The models also include a resin rich zone and zones for curved in-plane fibres. This creates a relatively simple unit cell incorporating certain features typical to Z-pinned composites. However, current commercial FE packages and computing power allow for more detailed analyses to be conducted.

The literature survey also examined meso-scale modelling used by Lomov[95] (with further 3-D modelling techniques given by Bogdanovich[100]). The meso-scale approach distinguishes between the fibre and matrix which is desirable in the case of through-thickness reinforced composites for including features such as resin rich zones and the change in fibre volume fraction V_f^f in the presence of through-thickness reinforcement.

The approach used in the current work follows a meso-scale approach for use with Z-pinned composites. Models will be shown using [0] UD and $[0/90]_s$ cross-ply laminates containing through-thickness reinforced in the form of Z-pins and stitches orientated along the *z*-axis.

8.1.1 Construction of Z-pinned Meso-Scale Unit Cells

Upon the decision to model through-thickness reinforced composites on the meso-scale it is important to create appropriate unit cells. The first issue is to define the geometry of the material and its symmetry types and locations. The steps to obtaining a unit cell for a UD composite containing Z-pin reinforcement are shown in Figure 8.1. Note that the unit cell in Figure 8.1(c) can be reduced further through reflectional symmetry in the *z*-plane.

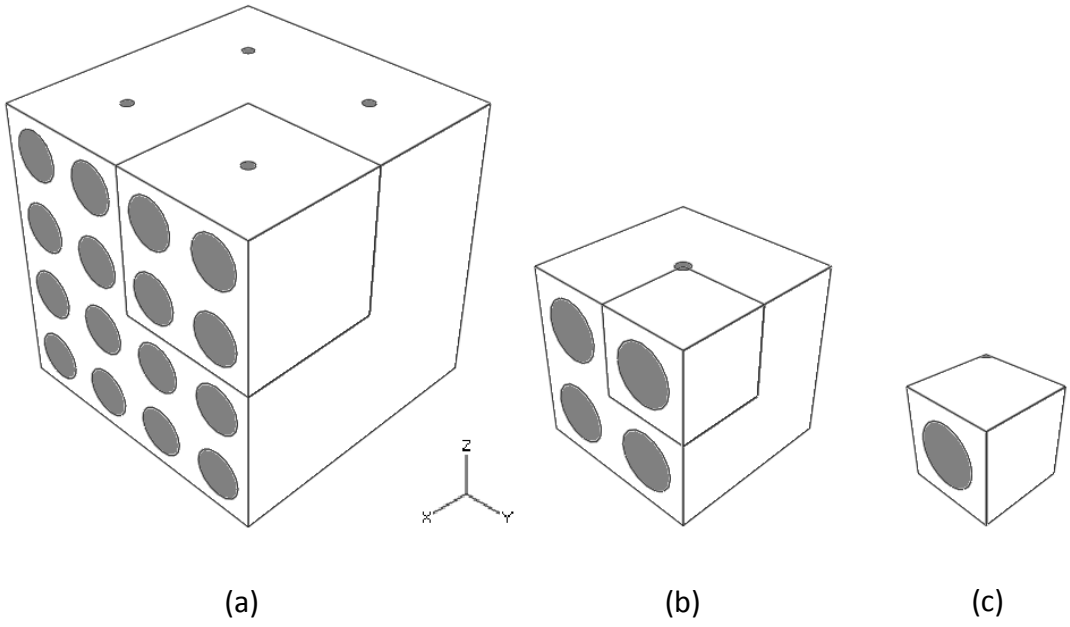

(a) (b) (c)

Figure 8.1: Steps to produce an efficient unit cell for a UD composite containing through-thickness reinforcement; (a) initial material, (b) smallest unit cell using translational symmetry only, (c) unit cell using reflectional symmetry

The unit cell in Figure 8.1(b) is the smallest unit cell available using only translational symmetries. This can be further reduced by making use of reflectional symmetries as shown in Figure 8.1(c). Note that care must be taken to ensure that the symmetry conditions imposed are correct e.g. the Z-pin placement within the unit cell. Furthermore, the unit cell in Figure 8.1(c) can be reduced further through reflectional symmetry in the *z*-plane through the mid section of the fibre. The type of symmetry used is a vital piece of information for the prescription of the appropriate boundary conditions as detailed in Chapter 3.2.1.5.

The same process can be used for calculating unit cells for cross-ply laminates as well. Note that if the composite contains angled fibres (e.g. [±45/90/0]

quasi-isotropic laminates) or angled through-thickness reinforcement (the reinforcement is inclined at an angle from the *z*-axis) then reflectional symmetry is not permitted as the angle fibres do not hold reflectional properties.

The unit cell models presented in this thesis were created entirely using Abaqus/CAE. A summary of the modules required to create a model were presented in Chapter 4.1.1. The process of the unit cell creation in Abaqus/CAE is now provided.

The models used are created as 3-D solid extrudes. In the [0] UD composite containing Z-pin reinforcement, the dimensions of the overall unit cell were set to be 1x1x1mm. The next process is to use the partition tool to partition the faces of the cube with the fibre and the Z-pin. These face partitions can then be used to partition the unit cell by extrusion. Material properties are then prescribed for the fibre, matrix and Z-pin constituents. At this point the unit cell was partitioned to enable a structured hexahedral mesh to be applied. This would be required for any unit cell which houses angled fibres. These unit cells would use only translational symmetry where it is vital that the mesh is mirrored exactly on opposite sides of the model. This is a requirement of linking the displacements of opposite sides of the unit cell. In the current work the models were created using Abaqus where although it is straightforward to produce a uniform mesh across the model there is no easy method of arranging the node numbers. As a result the created input file needs manual manipulation to sort the node numbers properly. To avoid this problem models were created using reflectional symmetry which removes this problem.

Following on from the geometry, material and mesh creation the load and boundary conditions must be prescribed. In order to do this one must first create six nodes to act as six extra degrees of freedom; one for each individual load case. This was done by creating six individual reference points in the assembly module and creating a set for each reference point in order to use these degrees of freedom in the equation constraints. Since reflectional symmetry has been used the first three boundary conditions are imposed directly to the unit cell. Symmetric

conditions are applied; XSymm on one *x*-face, YSymm on one *y*-face and ZSymm on one *z*-face such that all three faces are connected by one vertex. Equation conditions such as those given in equations 3-6 and 3-7 can be applied on the remaining faces, edges and vertices depending on the loading conditions.

Once the equation constraints are prescribed, macrostress loads can be applied by applying a concentrated force to the appropriate reference point (degree of freedom). The model is now ready to be run after the appropriate sanity checks which are discussed in Chapter 8.3.1.

8.1.2 Features of the Meso-Scale Unit Cell Approach for Z-pinned Composites

Although the geometry and final unit cells are slightly more complex than those proposed by Dickinson *et al* and Grassi *et al*[85, 86] there are certain advantages to the meso-scale unit cells proposed. As the fibres and matrix are modelled separately there is no need to include a resin-rich zone. The separate modelling of fibres, Z-pins and matrix also leads to another useful inclusion. In the region of the Z-pin, the in-plane fibre volume fraction may increase due to the bunching up of fibres as shown in Figure 3.3. In the semi-homogeneous models used by Dickinson *et al* and Grassi *et al* this fibre bunching is neglected and instead fibre spreading is assumed which should lead to lower predictions for the in-plane stiffness.

In the current unit cell models the in-plane fibre diameter is kept constant through the depth of the unit cell as shown in Figure 8.2. This means that away from the through-thickness reinforcement the fibre radius can be selected to give the desired volume fraction for the base UD composite. This is calculated from the following

$$V_f = \frac{Volume_{fibre}}{Volume_{total}} \qquad \textbf{8-1}$$

In equation 8-1 the calculation shows that the fibre volume fraction is calculated by dividing the fibre volume by the total volume of the unit cell. As this is for the constitutive lamina this includes only the fibres and matrix i.e. it does not include

any through-thickness reinforcement that is not part of the UD lamina. Therefore, in the region of the Z-pin the total area of the fibre and matrix is reduced; this is shown in Figure 8.2. The figure shows a top down view of a UD unit cell containing a Z-pin. Away from the through-thickness reinforcement the width of the matrix and fibre is *a*. At the other side of the unit cell the width of the matrix and in-plane fibre is *b*, where one can observe that *b*<*a*. Using this with equation 8-1 and assuming that the depth and length of the unit cell are constant one can write

$$V_f = \frac{Volume_{fibre}}{b \times (depth \times length)} > \frac{Volume_{fibre}}{a \times (depth \times length)} \qquad \textbf{8-2}$$

The result is that in the region of the Z-pin in the unit cell the fibre volume fraction is increased naturally due to the imposed geometry.

An advantage of the meso-scale unit cell approach is that the effective properties can be obtained with just the knowledge of the constituent material properties. These are generally widely available and require no lamina testing. Furthermore, it allows for an easy change of parameters such as the fibre volume fraction without having to obtain further experimental data.

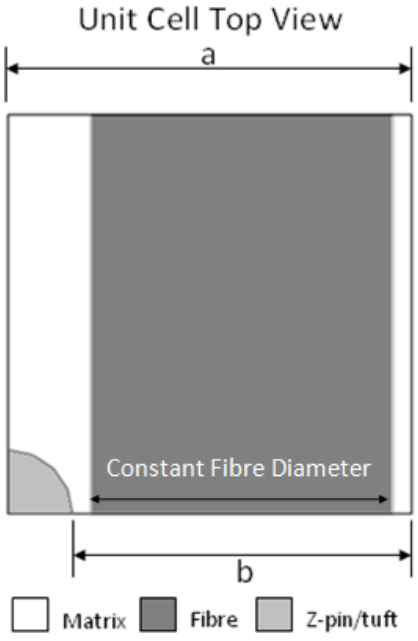

Figure 8.2: Top view of unit cell containing through-thickness reinforcement

Although not a distinct advantage it should be noted that the creation of the unit cells proposed here is no more complex than those created by Dickinson *et al* and Grassi *et al*. Three sets of material properties are required here (matrix, fibre and Z-pin), the same as required for the Dickinson/Grassi models (matrix, UD lamina and Z-pin). The geometry is relatively simple and in the current approach sharp angles are kept to a minimum. These can act as sites for mesh effects, where the mesh used can give rise to inaccurate stress/strain responses and were present in the Dickinson and Grassi models around the resin rich zone.

8.1.3 Assumptions Used in the Current Meso-Scale Unit Cell Approach

As with the vast majority of modelling and analytical techniques certain assumptions have been used in the creation of the unit cells presented here. Firstly, and most importantly, it has been assume in the models used that many fibres in the UD lamina can be modelled as one large fibre in the unit cell. This means that some of the detail in stress response will be lost but significantly reduces the computing power required to carry out the analysis. However, the selection of a single fibre bundle should not greatly affect the result and is a common modelling assumption. An example of fibre bundling modelling is given in Figure 8.3, where Lomov *et al* bundled fibres together to create models of stitched composites[95].

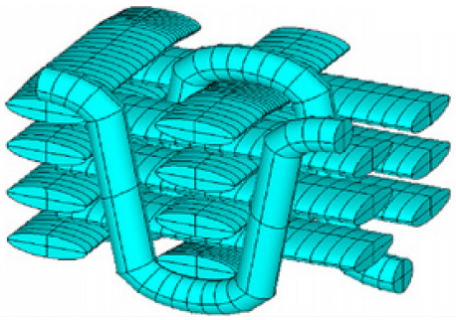

Figure 8.3: Model using fibre 'bundles' as utilised by Lomov *et al* [95]

The Z-pin is also assumed to be cylindrical. This is particularly important when Z-pins are being analysed as they commonly have a cylindrical cross-section. Furthermore it is assumed that the fibres remain straight throughout the model. This means that the models neglect in-plane fibre misalignment; this approach is used to retain simplicity within the model. It was observed in the Dickinson models

in the literature[85], that actually, the modelling of in-plane fibre curvature had very little effect on the predicted effective properties. Hence, its absence in the meso-scale FE models appears to be satisfactory.

One issue with constant fibre geometry is the constraint on the fibre volume fraction. In a square the largest circle that can be included is approximately 78.5% of the area of the square. As the Z-pin diameter is increased the available space for the fibre is reduced from a square to a rectangle and as a result the permitted fibre area decreases. Using the example in the figure below where *a* is the Z-pin radius and *f* is the fibre diameter and setting *p* to be 0.2 and *f* to 0.8 the maximum fibre volume fraction (assuming a circular fibre cross-section) is now 50%.

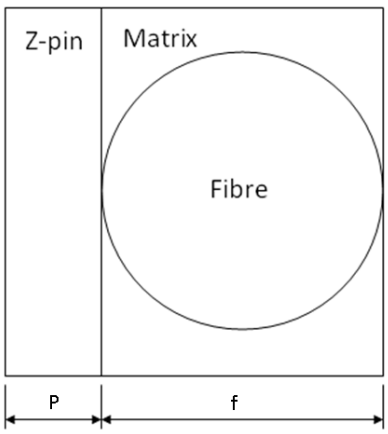

Figure 8.4: Demonstration of reduction in fibre volume in Z-pinned meso-scale unit cell

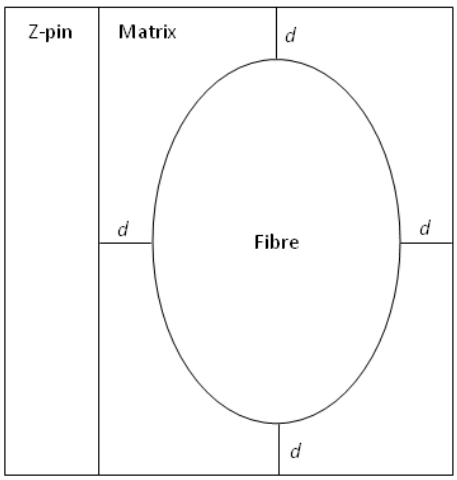

Figure 8.5: Demonstration of in-plane fibre geometry and distance from unit cell edge

The result of using a single fibre model is that, in the current study, the fibre is allowed to take the form of a cylinder, an ellipse and a lozenge in order that the 60% fibre volume fraction can be maintained regardless of the Z-pin diameter. The shape was chosen such that the distance between the fibre and the top, bottom and sides of the unit cell were the same. This is shown schematically in Figure 8.5 where an elliptical fibre is used. The distance from the 'extreme' points of the fibre to the edge of the unit cell are given by *d*.

By the nature of the unit cell approach it is assumed that the unit cell represents a general section of the material and that the unit cell is repeated throughout the composite[102]. This means that effects such as voids etc are difficult to include i.e. if they are included in the unit cell then it is assumed that the defect is periodic throughout the material. As with other models presented in this thesis, C3D8R elements were used allowing for a fine mesh without requiring more computing power than was available.

8.2 Bounding Approaches

Two bounding approaches are used to obtain the through-thickness properties of Z-pinned composites. These are the classic Voigt and Reuss bounds[116, 117] (as presented by the author[119]) and the bounding approach proposed by Walpole[122, 123] as discussed in Chapter 3. MathCAD files were created for each approach used. These files allow the user to input the material data, volume fractions and orientations and then the elastic properties for the material are returned.

The two approaches were examined in the literature survey in Chapter 3 but need some further clarification before being used for Z-pin reinforced composites. The issues of clarification are simply how one includes all three elements of the material under consideration i.e. the matrix, the fibres and the through-thickness reinforcement.

8.2.1 Reuss' and Voigt's Bounds

The application of Reuss' and Voigt's bounds to the calculation of effective properties of Z-pinned composites is relatively simple. The final equations for

bounding the elastic properties were presented in Chapter 3.2.2 in equations 3-13 and 3-14. In order to analyse Z-pinned composites the final equations are found to adjust to

$$S_{ij}^{eff} = \left(S_{ij}^{m} V_f^{m} + S_{ij}^{f} V_f^{f} + S_{ij}^{z} V_f^{z} \right) \quad \textbf{8-3}$$

$$C_{ij}^{eff} = \left(C_{ij}^{m} V_f^{m} + C_{ij}^{f} V_f^{f} + C_{ij}^{z} V_f^{z} \right) \quad \textbf{8-4}$$

where *m*, *f* and *z* refer to the matrix, fibre and Z-pin phases respectively. From the compliance and stiffness matrices the Young's moduli, shear moduli and Poisson's ratios can be obtained.

8.2.2 Walpole's Bounds

As with Reuss' and Voigt's bounds the application of Walpole's bounds to through-thickness reinforced composites is simple. Expanding equation 2-96 one arrives at

$$C_{ij}^{eff} = \left(V_f^{m} \left(C_o^{*} + C_{ij}^{m} \right)^{-1} + V_f^{f} \left(C_o^{*} + C_{ij}^{f} \right)^{-1} + V_f^{z} \left(C_o^{*} + C_{ij}^{z} \right)^{-1} \right)^{-1} - C_0^{*} \quad \textbf{8-5}$$

Note that in the above equation some of the terms have been adjusted for continuity with the Reuss and Voigt calculations. In the original Walpole notation the volume fractions are defined as c_r and are here referred to as V_f^m etc. Furthermore, in the original equation the effective stiffness matrix was referred to as $\overline{C}$ but is here referred to as C_{ij}^{eff}.

8.2.3 Coordinate Transformation

It is important when using these bounding approaches for through-thickness reinforced composites and for angle-ply laminates that the fibres/Z-pins are treated appropriately. The compliance/stiffness matrices must be transformed correctly in order that the reinforcement orientation is accounted for.

The through-thickness reinforcement must be transformed to lie parallel to the *z*-axis. With regard to the mathematical formulae used, one can include a

mechanism in order to angle the through-thickness reinforcement at an angle away from the *z*-axis. We start by setting the matrix

$$\lambda = \begin{bmatrix} 0 & 1 & 0 \\ -\sin\theta & 0 & \cos\theta \\ \cos\theta & 0 & \sin\theta \end{bmatrix} \qquad \textbf{8-6}$$

where θ is the angle of the through-thickness reinforcement from the *z*-axis about the *x*-axis. For a Z-pin lying parallel to the *z*-axis θ is 0°. The transformation matrix is then set as

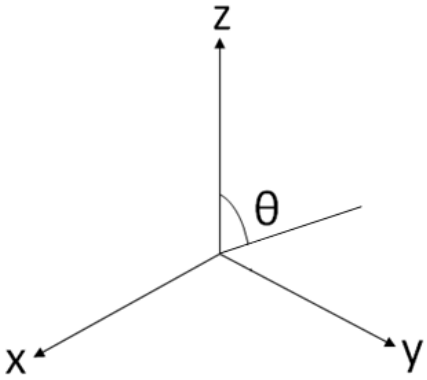

Figure 8.6: Diagram showing the angle of the through-thickness reinforcement θ from the z-axis about the x-axis.

$$T_z = \begin{bmatrix} l_1^2 & l_2^2 & l_3^2 & 2l_2l_3 & 2l_1l_3 & 2l_1l_2 \\ m_1^2 & m_2^2 & m_3^2 & 2m_2m_3 & 2m_1m_3 & 2m_1m_2 \\ n_1^2 & n_2^2 & n_3^2 & 2n_2n_3 & 2n_1n_3 & 2n_1n_2 \\ m_1n_1 & m_2n_2 & m_3n_3 & m_2n_3+m_3n_2 & m_1n_3+m_3n_1 & m_1n_2+m_2n_1 \\ l_1n_1 & l_2n_2 & l_3n_3 & l_2n_3+l_3n_2 & l_1n_3+l_3n_1 & l_1n_2+l_2n_1 \\ l_1m_1 & l_2m_2 & l_3m_3 & l_2m_3+l_3m_2 & l_1m_3+l_3m_1 & l_1m_2+l_2m_1 \end{bmatrix} \qquad \textbf{8-7}$$

where

$$\begin{pmatrix} l_1 \\ m_1 \\ n_1 \end{pmatrix} = \begin{pmatrix} \lambda_{11} \\ \lambda_{21} \\ \lambda_{31} \end{pmatrix} \qquad \begin{pmatrix} l_2 \\ m_2 \\ n_2 \end{pmatrix} = \begin{pmatrix} \lambda_{12} \\ \lambda_{22} \\ \lambda_{32} \end{pmatrix} \qquad \begin{pmatrix} l_3 \\ m_3 \\ n_3 \end{pmatrix} = \begin{pmatrix} \lambda_{13} \\ \lambda_{23} \\ \lambda_{33} \end{pmatrix} \qquad \textbf{8-8}$$

To then transform the compliance matrix of the Z-pin one must use the equation

$$S_z^\theta = \left(T_z^T\right)^{-1} S_z T_z^{-1} \qquad \textbf{8-9}$$

where T_z is the transformation matrix and S_z is the Z-pin compliance matrix with the fibre axis in the *x* direction. Furthermore, S_z^{θ} is the transformed Z-pin compliance matrix to be used in the final bounds equations 8-3, 8-4 and 8-5.

Further to the transformation of the through-thickness reinforcement one must also transform the in-plane fibres if any angle-ply laminates are to be analysed. For this we require the transformation matrix

$$T_f = \begin{bmatrix} (\cos\varphi)^2 & (\sin\varphi)^2 & 0 & 0 & 0 & -2\cos\varphi\sin\varphi \\ (\sin\varphi)^2 & (\cos\varphi)^2 & 0 & 0 & 0 & 2\cos\varphi\sin\varphi \\ 0 & 0 & 1 & 0 & 0 & 0 \\ 0 & 0 & 0 & \cos\varphi & \sin\varphi & 0 \\ 0 & 0 & 0 & -\sin\varphi & \cos\varphi & 0 \\ \cos\varphi\sin\varphi & -\cos\varphi\sin\varphi & 0 & 0 & 0 & (\cos\varphi)^2 - (\sin\varphi)^2 \end{bmatrix} \quad \textbf{8-10}$$

where T_f signifies a fibre transformation and φ is the angle of the fibre from x about the z-axis.

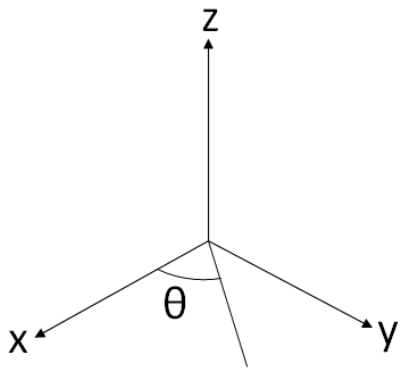

Figure 8.7: Diagram showing the angle of the through-thickness reinforcement φ from the x-axis about the z-axis.

The equation shown in 8-9 is then utilised

$$S_f^{\theta} = T_f^{-T} S_f T_f^{-1} \quad \textbf{8-11}$$

which results in a transformation of the compliance matrix for the fibre about the *z*-axis. The stiffness matrix can equally be obtained from

$$C_f^{\theta} = T_f C_f T_f^{T} \quad \textbf{8-12}$$

8.3 Results and Discussion

In the following section the results produced from both the FE and bounds approaches will be shown for UD and cross-ply laminates with and without Z-pin reinforcement. Attempts are made to provide a comparison between the current meso-scale FE models and the bounds approaches with the semi-homogeneous FE approach given by Dickinson *et al* and Grassi *et al*[85, 86].

Prior to the analysis of any FE results it is important to be sure that there are no basic problems. In order to do this one should conduct basic sanity tests.

8.3.1 Meso-Scale FE Modelling Approach

8.3.1.1 Meso-Scale FE Model Sanity Check

The basic sanity check used for all of the models demonstrated in this work is the application of homogeneous isotropic material properties to the models. This is done by giving each of the constituent geometries the same isotropic material properties and as a result the FE computation should provide material properties that are the same as the input data. Any errors here would signify a problem with the unit cell. Furthermore, the stress contour plots can be examined; these should be completely uniform with no stress variations for applied uniform loads.

Young's Modulus (GPa)	Poisson's ratio	Shear modulus (GPa)
200	0.3	76.92

Table 8-1: Isotropic material data used as input data for finite element sanity checks

Property	Reference (Input Values)	[0] V_z=0%	[0] V_z=1%	[0] V_z=5%	$[0/90]_s$ V_z=0%	$[0/90]_s$ V_z=1%	$[0/90]_s$ V_z=5%
E_x (GPa)	*200*	200	200	200	200	200	200
E_y (GPa)	*200*	200	200	200	200	200	200
E_z (GPa)	*200*	200	200	200	200	200	200
ν_{xy}	*0.3*	0.3	0.3	0.3	0.3	0.3	0.3
ν_{xz}	*0.3*	0.3	0.3	0.3	0.3	0.3	0.3
ν_{yz}	*0.3*	0.3	0.3	0.3	0.3	0.3	0.3
G_{xy} (GPa)	*76.92*	76.92	76.92	76.92	76.92	76.92	76.92
G_{xz} (GPa)	*76.92*	76.92	76.92	76.92	76.92	76.92	76.92
G_{yz} (GPa)	*76.92*	76.92	76.92	76.92	76.92	76.92	76.92

Table 8-2: Elastic properties obtained from UD and cross-ply unit cell models with through-thickness reinforcement volume fractions (V_f^z) set to 0%, 1% and 5%

The isotropic input data for the sanity checks are given in Table 8-1. The results for unit cells up to a through-thickness reinforcement volume fraction of 5% are given in Table 8-2.

The von Mises stress contour plots shown in Figure 8.8 show the results of the sanity checks for the UD unit cell containing through-thickness reinforcement with a volume fraction (V_f^z) of 2%. It is clear in the images that the stress response is completely uniform. Equally the strain field was found to be uniform. Furthermore, the effective properties shown in Table 8-2 are identical to the input data given to the matrix, fibre and through-thickness reinforcement. The results demonstrate that there are no obvious errors with the unit cell geometry or the application of boundary conditions and loads.

8.3.1.2 Predicting UD Data with Meso-Scale Unit Cell

In order to clarify the current modelling technique it is important that it be used to obtain known material data. For this purpose the models were used to analyse a UD composite for which there are experimental data. The input data have been taken from work by Sun and Vaidya (Originally given in ref[142]). The reference also refers to experimental data for the same material allowing one to observe the effectiveness of the unit cells used. The input data are given in Table 8-3 where the fibre is assumed to be transversely isotropic and G_{23} can be found from the relationship

$$G_{23} = \frac{E_2}{2(1+\nu_{23})} \qquad \textbf{8-13}$$

Furthermore, the matrix material is assumed to be homogeneous and isotropic.

	E_1 (GPa)	E_2 (GPa)	G_{12} (GPa)	G_{23} (GPa)	ν_{12}	ν_{23}
AS4	235	14	28	5.6	0.2	0.25
3501-6	4.8	4.8	1.8	1.8	0.34	0.34

Table 8-3: Fibre and matrix input data AS4 fibres and 3501-6 epoxy materials[90]

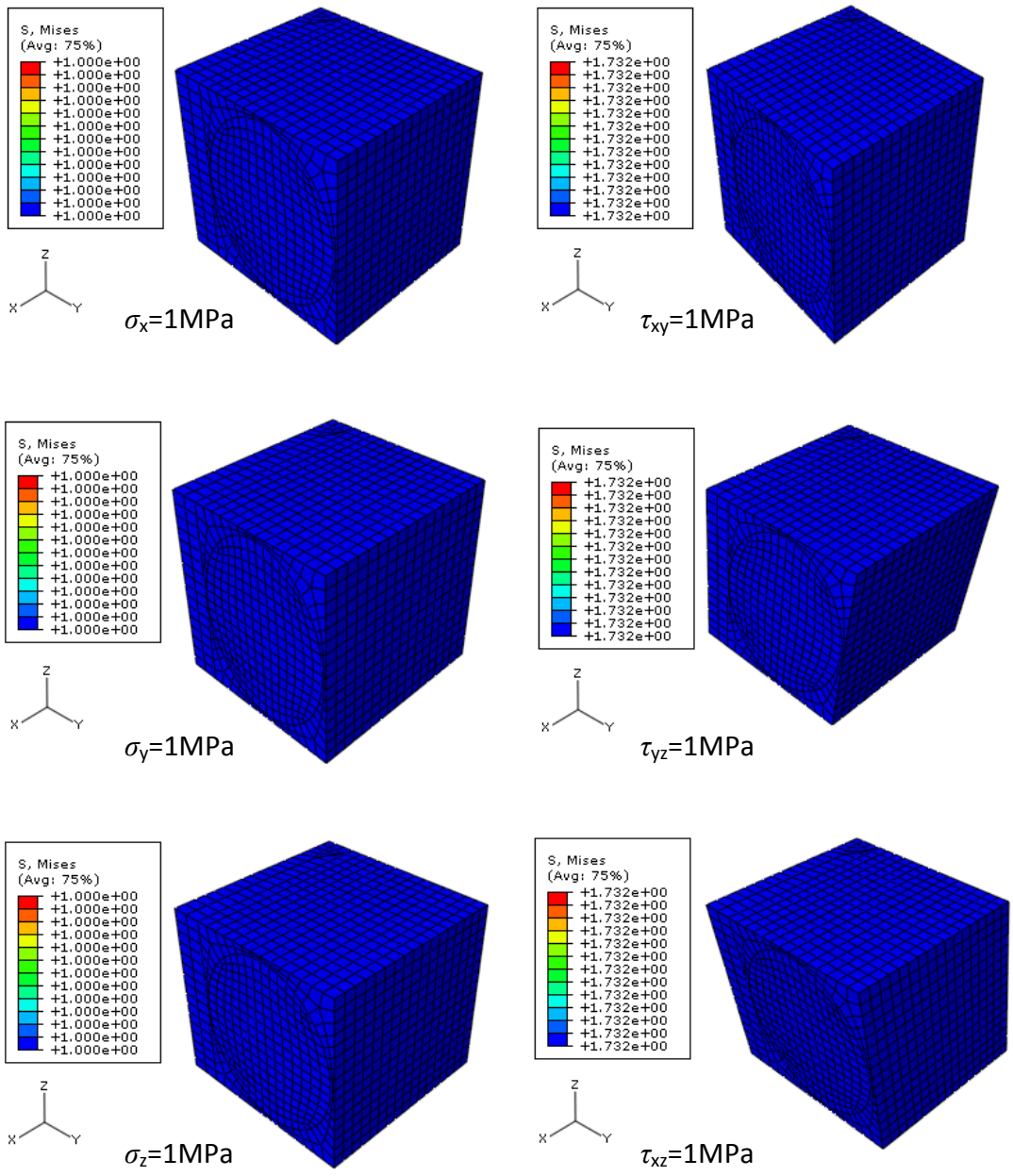

Figure 8.8: Von Mises stress contour plots for six major load cases of UD unit cell containing 2% Z-pin volume fraction using homogeneous material properties and assuming a unit cell utilising reflectional symmetry (sanity check)

The UD material properties provided from the experimental data[143, 144] and the predicted values from the current unit cell analysis are given in Table 8-4. Unit cells were created assuming both square and hexagonal packing arrangements with a fibre volume fraction, V_f^f of 0.6. The unit cells used are presented in Figure 8.9. The unit cell results shown demonstrate similar differences between square

and hexagonal fibre arrangements as shown by Sun and Vaidya who used a similar unit cell[90].

	E_x (GPa)	E_y (GPa)	E_z (GPa)	v_{xy}	v_{yz}	v_{xz}	G_{xy} (GPa)	G_{yz} (GPa)	G_{xz} (GPa)
Experimental[143]	142.0	10.30	10.30*	-	-	-	7.60	3.80	7.60*
Experimental[144]	139.0	9.85	9.85*	0.3	-	0.3*	5.25	-	5.25*
Unit Cell (Square packing)	142.5	9.61	9.61	0.26	0.35	0.26	6.04	3.10	6.04
Unit Cell (Hex packing)	142.5	8.76	8.76	0.25	0.41	0.25	6.07	3.56	6.07

Table 8-4: Elastic properties obtained from experiments[143, 144] and FE unit cell analysis for UD composite

The FE results show a generally good agreement with the experimental results, particularly for the square packed model. The area of greatest difference between the experimental results and the FE results appears to be the shear modulus predictions. However, there is a large scatter between the experimental results and as the FE predictions lie within the reported experimental data there are few concerns with the current FE approach. As the square model produced properties closest to the experimental data this arrangement will be used in the subsequent meso-scale FE models.

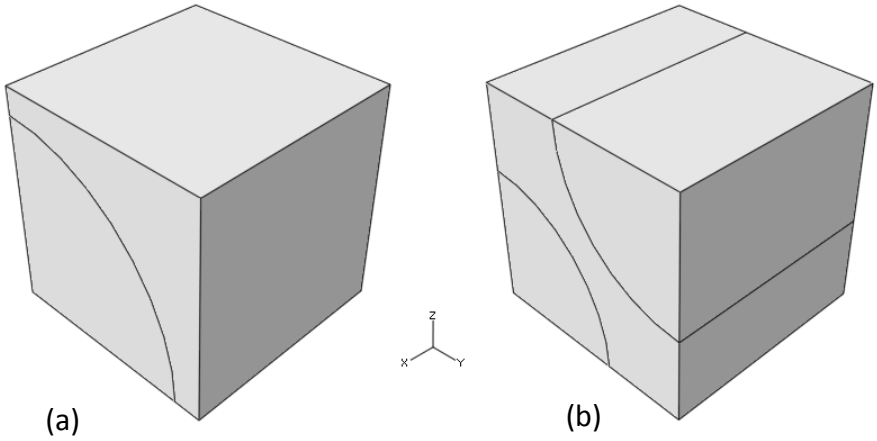

Figure 8.9: UD unit cells (V_f^f=0.6); (a) Square Packing, (b) Hexagonal Packing

8.3.2 Use of the Dickinson FE Approach

In order to compare the current work with the approach by Dickinson *et al* the author has recreated the 'Dickinson' unit cells using the approach set out in ref[85] discussed in Chapter 3.2.1.1. The Dickinson unit cells created here are subjected to sanity checks as used in the previous chapter as well as the input data used by Dickinson *et al*. The results are then compared to those in the literature[85, 86] in order that further use of the model for comparison is demonstrated to be reliable.

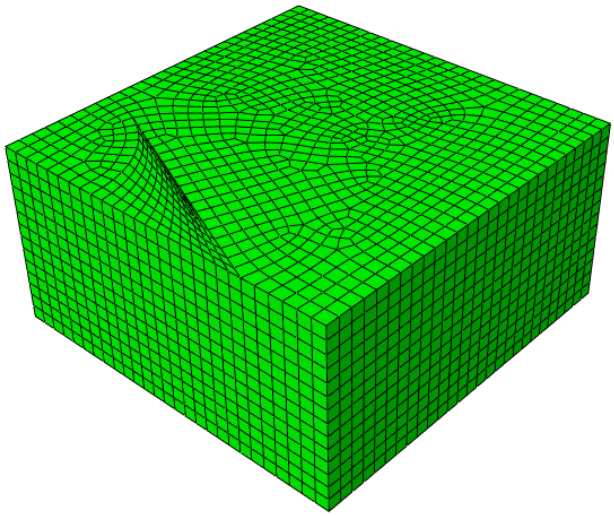

Figure 8.10: Recreation of Dickinson FE model

The unit cell created here is a 3-D model following the dimensions given by Dickinson et al[85] and making use of reflectional symmetries as used in the previous section. This means that the loading and boundary conditions applied to the current 'Dickinson' model are the same as those used for the meso-scale unit cell. A typical Dickinson model is shown in Figure 8.10 where C3D8R elements have been used as throughout the thesis.

8.3.2.1 Sanity Checks

The material input data for the sanity checks of the 'Dickinson' model are the same as those used in the previous section, shown in Table 8-1. Again through-thickness reinforcement values were set at 0%, 1% and 2% with [0] UD and $[0/90]_s$ cross-ply laminates being examined. The results were identical to those given in Table 8-2 showing no errors and recreating the input data. The stress contour plots

also demonstrated a fully uniform response, repeating the results for the meso-scale unit cell given in Figure 8.8.

8.3.2.2 Recreation of Dickinson *et al* and Grassi *et al* Results

An attempt has been made to recreate the results presented by Dickinson *et al* and Grassi *et al*[85, 86]. The reason is that if the results can be recreated, a direct comparison for various lay-ups and material properties can be given. The models examined here are [0] UD and $[0/90]_s$ without through-thickness reinforcement and [0] UD and $[0/90]_s$ with a Z-pin of 2% volume fraction. The input data are given in Table 8-5.

Materials	E_1 (GPa)	E_2 (GPa)	E_3 (GPa)	v_{12}	v_{23}	v_{13}	G_{12} (GPa)	G_{23} (GPa)	G_{13} (GPa)	V_f^f
Lamina (AS4/3501-6)	136.40	8.90	8.90	0.25	0.38	0.25	5.95	3.21	5.95	0.6
Z-pin (T300/9310)	144.00	7.31	7.31	0.25	0.39	0.25	4.45	2.65	4.45	-
Epoxy (3501-6)	4.44	-	-	0.34	-	-	1.65	-	-	-

Table 8-5: Material input data for Dickinson model recreation[85]

The recreation results of the unreinforced and reinforced cases are given in Table 8-6, Table 8-7, Table 8-8 and Table 8-9. It is observed that the current recreation is slightly better at predicting the properties of a UD composite as the returned material properties are the same as the input data whereas the Dickinson and Grassi results show a slight variation in the transverse stiffness values E_y and E_z.

The results predicted in this study using the Dickinson approach match well with the data provided by Dickinson and Grassi[85, 86]. This result provides confidence in the boundary conditions utilised throughout this study as well as the ability to produce results in line with the approach set out by Dickinson *et al*[85]. This allows for a comparison of the Dickinson approach to the meso-scale FE approach and the bounding approaches used in this study.

	E_x (GPa)	E_y (GPa)	E_z (GPa)	v_{xy}	v_{yz}	v_{xz}	G_{xy} (GPa)	G_{yz} (GPa)	G_{xz} (GPa)
Dickinson *et al*[85]	136.4	8.85	8.85	0.25	0.38	0.25	5.95	3.21	5.95
Grassi *et al*[86]	136.4	8.86	8.81	0.25	0.37	0.25	5.95	3.20	5.95
Dickinson Recreation (Current Study)	136.4	8.90	8.90	0.25	0.38	0.25	5.95	3.21	5.95

Table 8-6: Material properties for [0] UD laminate with no through-thickness reinforcement

	E_x (GPa)	E_y (GPa)	E_z (GPa)	v_{xy}	v_{yz}	v_{xz}	G_{xy} (GPa)	G_{yz} (GPa)	G_{xz} (GPa)
Dickinson *et al*[85]	72.80	72.80	10.05	0.03	0.36	0.36	5.9	4.16	4.16
Grassi *et al*[86]	72.80	72.80	10.05	0.03	0.34	0.34	5.94	4.15	4.15
Dickinson Recreation (Current Study)	72.88	72.88	10.11	0.03	0.35	0.35	5.95	4.17	4.17

Table 8-7: Material properties for $[0/90]_s$ cross-ply laminate with no through-thickness reinforcement

	E_x (GPa)	E_y (GPa)	E_z (GPa)	v_{xy}	v_{yz}	v_{xz}	G_{xy} (GPa)	G_{yz} (GPa)	G_{xz} (GPa)
Dickinson *et al*[85]	123.1	8.85	11.17	0.31	0.31	0.2	5.80	3.17	5.70
Grassi *et al*[86]	121.8	8.60	11.92	0.33	0.27	0.24	5.81	3.13	5.67
Dickinson Recreation (Current Study)	124.4	8.95	11.26	0.31	0.30	0.19	5.77	3.17	5.43

Table 8-8: Material properties for [0] UD laminate with 2% Z-pin density

	E_x (GPa)	E_y (GPa)	E_z (GPa)	v_{xy}	v_{yz}	v_{xz}	G_{xy} (GPa)	G_{yz} (GPa)	G_{xz} (GPa)
Dickinson *et al*[85]	67.48	67.48	12.30	0.04	0.29	0.29	5.87	4.00	4.00
Grassi *et al*[86]	67.30	67.30	12.31	0.05	0.30	0.30	5.82	3.98	3.98
Dickinson Recreation (Current Study)	67.14	67.14	12.44	0.04	0.28	0.28	5.88	4.00	4.00

Table 8-9: Material properties for $[0/90]_s$ cross-ply laminate with 2% Z-pin density

8.3.3 Bounding Approach Checks

As is the case with the FE analysis to be utilised it is important that the bounding approaches being used are checked for basic errors. In the current study this is done by carrying out a sanity check using homogeneous, isotropic material properties similar to the FE sanity check. This should result in the bounds producing the same results as each other. This clarifies that the theories are capable (as predicted) of producing results for isotropic materials. Beyond the basic sanity check the bounding approaches are also used to predict the material properties of a UD composite and compared to experimental data to ensure that the approaches do bound the material data.

8.3.3.1 Bounding Approach Sanity Check

The sanity checks carried out on the Voigt, Reuss and Walpole theories are shown below. In all cases the material properties were chosen to be homogeneous and were the same as those given in Table 8-1. The results are displayed in Table 8-10 and demonstrate that when the same homogeneous input data are used for each constituent, Voigt's, Reuss' and Walpole's theories all return the input data. This demonstrates that each theory is free from basic errors regarding the prediction of homogeneous material properties.

	E_x (GPa)	E_y (GPa)	E_z (GPa)	v_{xy}	v_{yz}	v_{xz}	G_{xy} (GPa)	G_{yz} (GPa)	G_{xz} (GPa)
Reference	200	200	200	0.3	0.3	0.3	76.92	76.92	76.92
Voigt	200	200	200	0.3	0.3	0.3	76.92	76.92	76.92
Reuss	200	200	200	0.3	0.3	0.3	76.92	76.92	76.92
Walpole Upper	200	200	200	0.3	0.3	0.3	76.92	76.92	76.92
Walpole Lower	200	200	200	0.3	0.3	0.3	76.92	76.92	76.92

Table 8-10: Elastic properties obtained from Voigt, Reuss and Walpole approaches using homogeneous material properties; results identical regardless of constituent volume fraction

8.3.3.2 Predicting UD Data with Bounding Approaches

The bounding theories were used to predict UD elastic properties. This was to confirm that the theories do in fact produce bounds on the material properties where the true values lie between the produced bounds. This is a clear

requirement of any bounding theory. The input data is the same as that given in Table 8-3.

The results of the bounding approaches and experimental data by Daniel and Lee[143], and Sun and Zhou[144] are given in Table 8-11. The results demonstrate that both approaches are capable of bounding the experimental values for AS4/3501-6 with the exception of the E_x prediction from Walpole's upper bound. This is because when a UD laminate is loaded in the fibre direction, the strain response is uniform as demonstrated by the FE prediction in Figure 8.11. Walpole's bound still imposes the restriction that the strains in the matrix and fibre will be different (this is imposed by the polarization strain in equation 3-18) which highlights a restriction of the theory that is not presented by Walpole. This is that the tightest bounds are applicable only to materials where the inclusion is surrounded by matrix material. This can include the transverse direction of a UD composite. The problem can be overcome quite simply. In directions where fibre reinforcement is on the surface of the repeating volume under consideration one may choose a comparison material with infinite (or very large) properties. This will return the Voigt (uniform strain) prediction. This will be followed in the remaining predictions carried out in this study.

	E_x (GPa)	E_y (GPa)	E_z (GPa)	ν_{xy}	ν_{yz}	ν_{xz}	G_{xy} (GPa)	G_{yz} (GPa)	G_{xz} (GPa)
Experimental[142]	142.0	10.30	10.30*	-	-	-	7.60	3.80	7.60*
Experimental[144]	139.0	9.85	9.85*	0.3	-	0.3*	5.25	-	5.25*
Voigt	143.0	10.70	10.70	0.24	0.31	0.24	17.52	4.08	17.52
Reuss	11.64	7.93	7.93	0.34	0.31	0.34	4.09	3.03	4.09
Walpole Upper	105.7	10.6	10.6	0.26	0.31	0.26	16.05	4.04	16.05
Walpole Lower	18.2	8.96	8.96	0.32	0.31	0.32	6.02	3.42	6.02

* Value assumed from transverse isotropy

Table 8-11: Elastic properties obtained from experiments[143, 144] and Voigt's, Reuss' and Walpole's approaches for UD composite

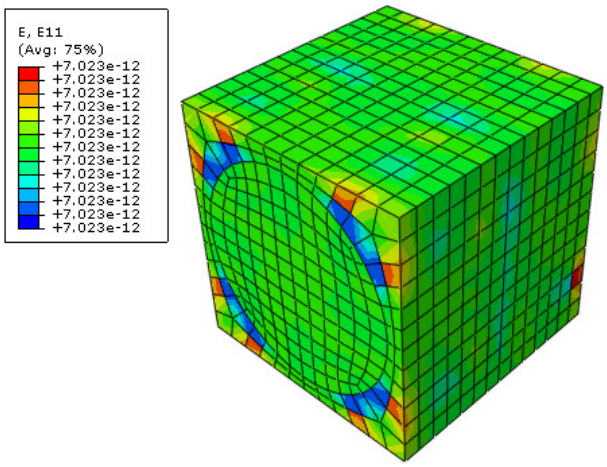

Figure 8.11: Strain contour plot ε_1 from UD meso-scale FE model

It was observed that both bounding methods follow the same trends; for example both lower bound approaches vastly underestimate E_x. This is because the stress assumption in both theories is inadequate. Furthermore it is seen in Table 8-11 that Walpole's theory produces tighter bounds in all instances as expected due to the use of the polarisation tensors differentiating the stress and strain response between constituents (except for the restriction pointed out above).

8.3.4 Comparison of Dickinson FE Approach, Meso-Scale FE Models and Bounding Approaches

Having subjected the FE and bounding approaches to sturdy sanity checks it is now possible to compare them for their applicability to Z-pinned composites. In order to do this the various analysis methods will be used to predict the mechanical properties of [0] UD and $[0/90]_s$ cross ply AS4/3501-6 laminates. Z-pin reinforcement materials will be T300/9310 and steel, with analysis ranging from no reinforcement to Z-pin reinforcement with a volume fraction of 5%. The in-plane fibre volume fraction in all cases was 60% and square fibre packing was assumed.

In order to compare the Dickinson approach with the current meso-scale approach and the bounding methods one requires both homogenised and constituent material data for the carbon composite to be analysed. In order to do this the meso-scale model was used to analyse a UD unit cell using the input data shown in Table 8-3 and assuming V_f^f=60%. The homogenised data extracted from this model was then used in the Dickinson style FE model. This was deemed

appropriate due to the good agreement found between experimental and meso-scale FE results shown in Table 8-4. The Z-pin material data were taken from the reference of Grassi *et al*[86] and the final set of input data is summarised in Table 8-12. This shows both the constituent and homogenised material input data.

	E_x (GPa)	E_y (GPa)	E_z (GPa)	N_{xy}	N_{yz}	N_{xz}	G_{xy} (GPa)	G_{yz} (GPa)	G_{xz} (GPa)
AS4	235.0	14.0	14.0	0.2	0.25	0.2	28.0	5.6	28.0
3501-6	4.8	-	-	0.34	-	-	1.8	-	-
AS4/3501-6 UD Lamina	142.5	9.61	9.61	0.26	0.35	0.26	6.04	3.10	6.04
T300/9310 Z-Pin	144.0	7.31	7.31	0.25	0.39	0.25	4.45	2.65	4.45
Steel Z-pin	200	-	-	0.3	-	-	7.69	-	-

Table 8-12: Summary of input data used in FE modelling and bounding methods

8.3.4.1 Young's Moduli

Young's moduli predictions for the UD and $[0/90]_s$ cross-ply laminates are presented in Figure 8.12 and Figure 8.13 respectively. The graphs on the left of each figure show the Young's modulus predictions with T300/9310 carbon fibre Z-pins and the graphs on the right of each figure show the predictions with steel Z-pins.

The E_x graphs show the upper bound of Walpole's theory and Voigt's bound to be coincident. As discussed above, using the tightest bounds on Walpole's theory (by having C_0-C_r just semi-positive definite for all constituents '*r*') this is not the case. The reason for this is that the tightest upper bound imposes a condition that the strains between the fibre and matrix are non-uniform. However, in reality a uniform strain assumption is accurate as shown in Figure 8.11. Therefore the tightest Walpole upper bound underestimates the stiffness of the composite in the fibre direction. As a result here for E_x the comparison material properties are tended to infinity in order that an identical result to Voigt's is produced i.e. a uniform strain assumption.

The uniform strain assumption remains close to the actual strain response in the presence of Z-pins because the axial modulus of the carbon fibre is greater than the transverse modulus of both the T300 and steel Z-pins. Therefore the overall strain response is dominated by the in-plane fibre resulting in an almost uniform strain. This result was observed in the meso-scale FE model where the modulus E_x was increased by a very small amount in the presence of a steel Z-pin, due to its higher transverse modulus compared to the relatively low transverse modulus of the T300 Z-pin. The bounding methods show a noticeable increase in E_x with an increasing volume fraction of the steel Z-pin. This occurs because the bounding methods merely use information regarding the quantity of each constituent. Therefore the addition of stiff material into the bounding calculations increases the stiffness of the overall system.

The Dickinson model result shows a drop in E_x of approximately 16% between the unpinned UD model and the model containing a Z-pin with 5% volume fraction. A similar result is found in the cross-ply laminates with a drop in E_x and E_y of around 18%. The reason for this is the use of a homogenised material used to model the UD composite part. This technique provides the same result as the meso-scale FE model when no Z-pin is present but as through-thickness reinforcement is added it takes away from the homogeneous composite material. As discussed in the literature review in Chapter 3, the Dickinson model does not account for the displacement of in-plane fibres and any associated increase in fibre volume fraction in the region of the Z-pin as reported in some works. As the Z-pin volume fraction is increased, the relative in-plane fibre volume fraction decreases in the Dickinson model and as a result, so does the stiffness. This does not agree with experimental results provided by Steeves and Fleck[94] where the value of E_x remained more or less constant with the application of Z-pins but is in reasonable agreement with the results of Troulis[93]. The review by Mouritz and Cox[138] agrees with the finding of Troulis showing a knockdown in E_x. The use of a constant fibre geometry and separate modelling of fibres and matrix in the present meso-scale model means that the meso model agrees with the results of Steeves and Fleck.

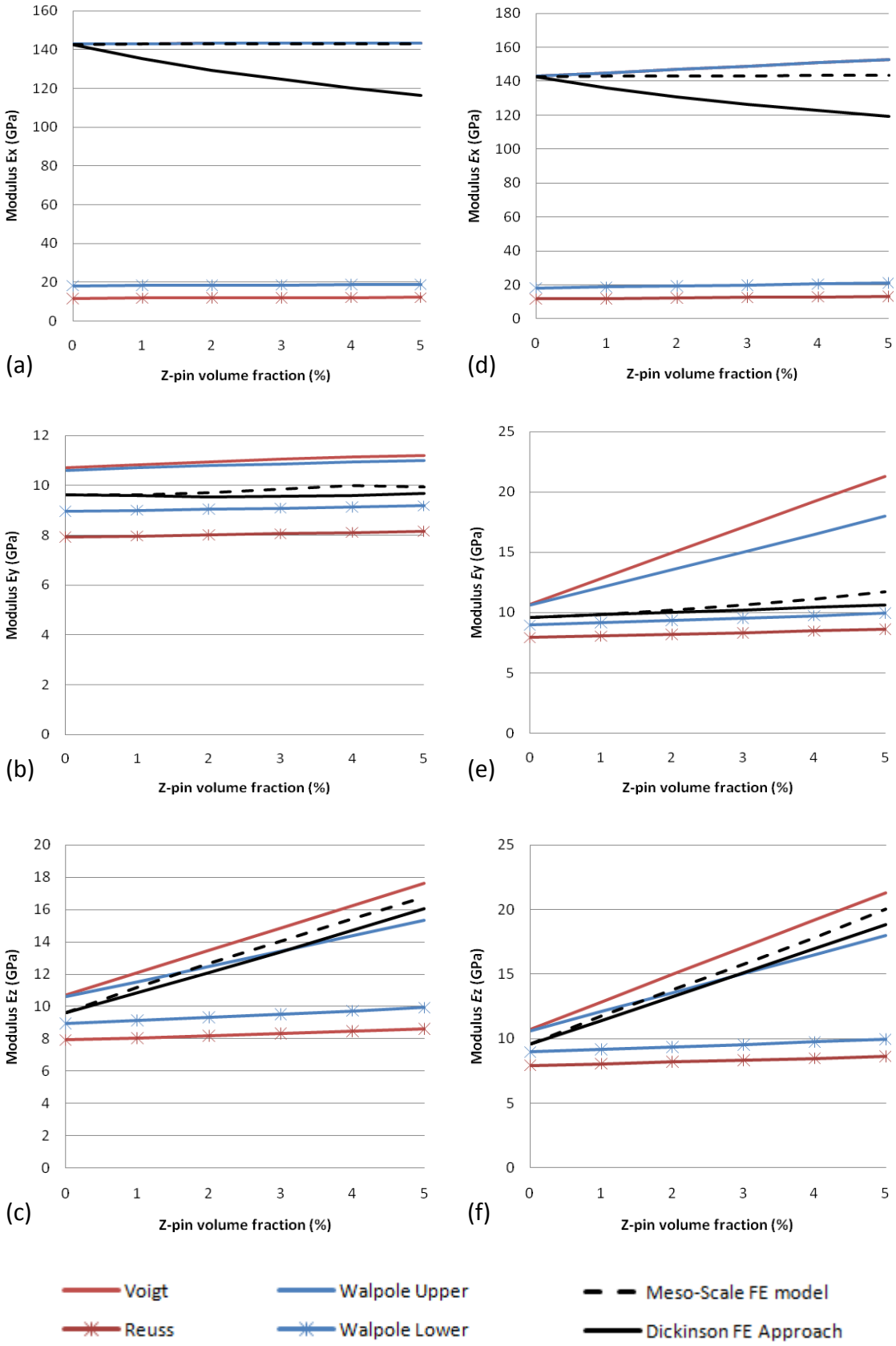

Figure 8.12: Young's moduli predictions for [0] UD AS4/3501-6 containing Z-pin reinforcement; (a) E_x with T300/9310 Z-pin, (b) E_y with T300/9310 Z-pin, (c) E_z with T300/9310 Z-pin, (d) E_x with steel Z-pin, (e) E_y with steel Z-pin, (f) E_z with steel Z-pin

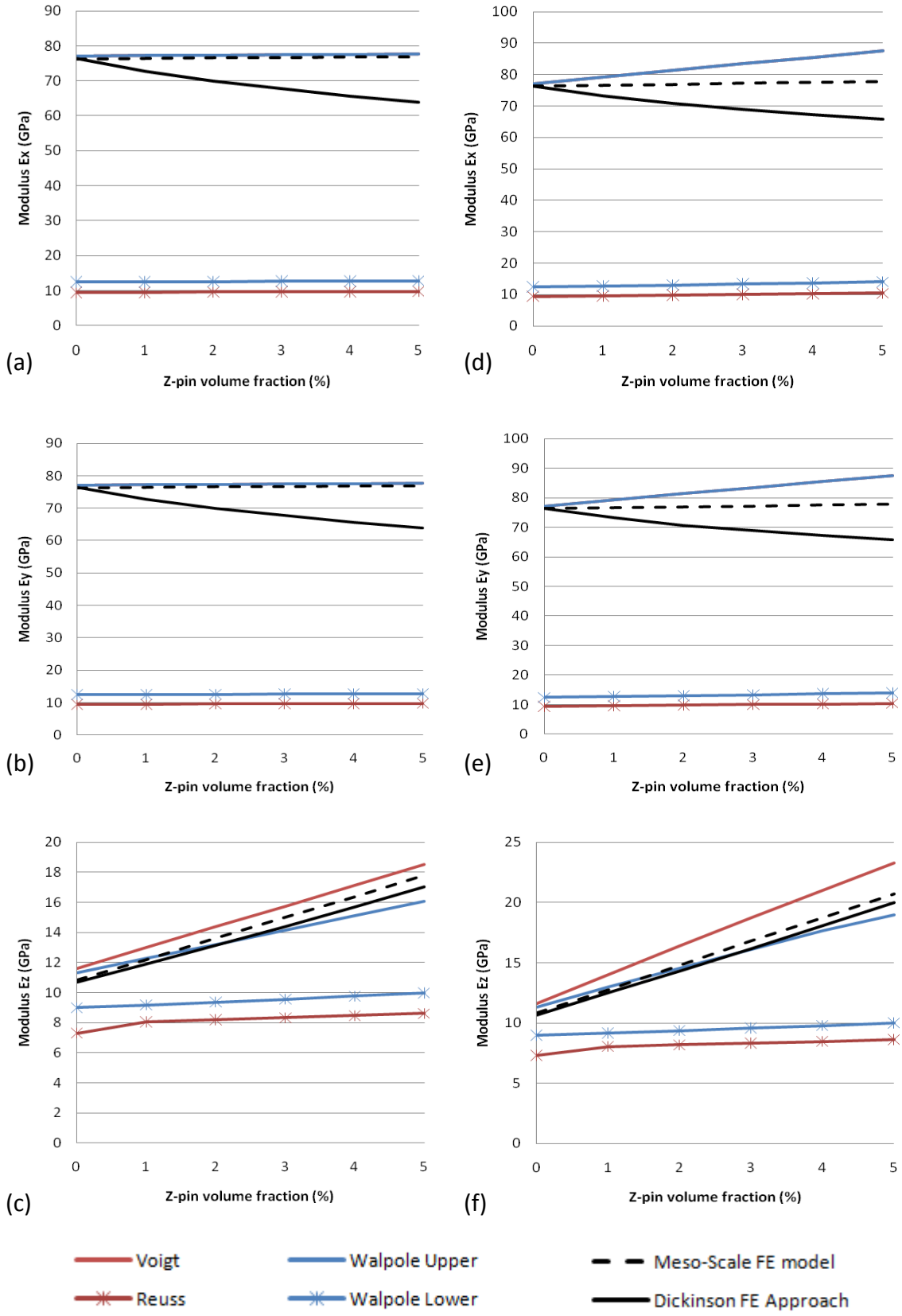

Figure 8.13: Young's moduli predictions for $[0/90]_s$ cross-ply AS4/3501-6 containing Z-pin reinforcement; (a) E_x with T300/9310 Z-pin, (b) E_y with T300/9310 Z-pin, (c) E_z with T300/9310 Z-pin, (d) E_x with steel Z-pin, (e) E_y with steel Z-pin, (f) E_z with steel Z-pin

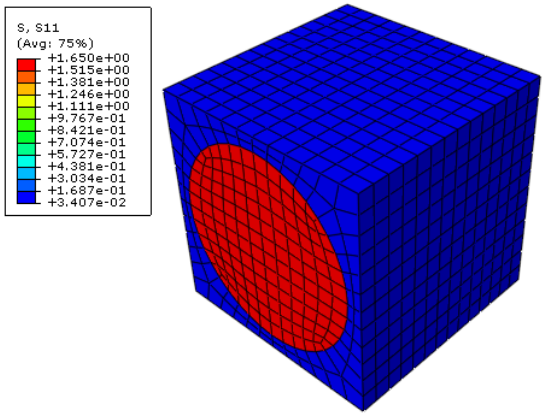

Figure 8.14: Stress contour plot σ_1 from UD meso-scale FE model

Similar results are found in the cross-ply laminates and also extend to the results for E_y due to the transverse isotropy of the laminates. The results for E_x and E_y from the FE and bounding approaches were identical in the cross-ply laminates, all demonstrating transverse isotropy and also reduced overall E_x values compared to the UD laminates. This occurs due to the overall reduction in number of fibres in the *x* direction within the laminate.

The Reuss and Walpole lower bound predictions massively underestimate E_x. These bounds make assumptions on the *x* direction stress response of the composite when subject to an axial load which in reality differ largely between the fibres and the matrix as witnessed in Figure 8.14. Here the stress in the fibre is very high whilst the stress in the matrix is very low in comparison. Of note is that the Dickinson FE model cannot show this detail due to the use of homogenised material.

The E_y predictions for the UD composite shown in Figure 8.12 (b) and (e) demonstrate that the Voigt, Reuss and Walpole values comfortably bound both sets of FE data for all Z-pin volume fractions. The reason for this is that in this transverse direction the stress and strain responses are both non-uniform. Therefore the uniform stress and strain assumption of Reuss' and Voigt's approaches are inadequate to produce a correct E_y value. Walpole's bounds provide a better prediction as the polarization tensors used impose a variation of the stress and strain between the matrix, fibre and Z-pins which narrows the bounds. The results of the FE models are in reasonable agreement with each other

with the meso-scale model providing slightly higher E_y results in the presence of increasing Z-pin volume fractions. This is caused by the UD composite fibre volume fraction in the presence of through-thickness reinforcement which is reduced in the Dickinson model. In the meso-scale model the fibre volume fraction increases with respect to the matrix material which increases the value of E_y when through-thickness reinforcement volumes are increased. The values of E_y are greater with the steel Z-pin compared to the carbon fibre Z-pin due to the higher transverse modulus in the steel material.

The FE predictions both demonstrate substantial increases in E_z with increasing Z-pin volume fractions. This comes as no surprise bearing in mind that the Z-pins are stiff in their axial direction and this is placed in parallel to the *z* direction of the composite. Moreover, the meso-scale approach demonstrates a greater increase in E_z again due to the fibre volume fraction in the presence of the through-thickness reinforcement.

The upper bound of Walpole's prediction for E_z shown in Figure 8.12 (c) and (f) and Figure 8.13 (c) an (f) demonstrates the issue encountered with the E_x prediction which resulted in using a comparison material with infinite material properties. For the unpinned UD composite the bound produced is good i.e. it bounds the real E_z value as the assumptions used comply with the situation. However, when the Z-pin volume fraction reaches around 2% a uniform strain assumption becomes more valid and Walpole's theory no longer bounds E_z due to the same issues as with E_x i.e. there is a restriction on Walpole's theory that if any reinforcement breaks the surface of interest then the strain polarization is incorrect as the in the real situation the strains will become uniform between the constituents. This is of course based on the assumption that in the region of the Z-pin the in-plane fibres are not damaged or significantly displaced causing a drop in the number of in-plane fibres within the selected body of material. Ultimately this means that whenever reinforcement is added in a particular direction then Voigt's (or Walpole's theory using a comparison material with the elastic constants set to infinity) theory should be used to provide the upper bound for the Young's modulus in that direction. This result is similar to the meso-scale model because

the uniform strain approach is a good assumption. Where fibres do not run in the direction (for example the *y* and *z* directions in a UD composite) then Walpole's theory provides a reasonably accurate response.

Ultimately, the prediction of the Young's moduli through FE modelling appears to be influenced largely on the assumption of fibre volume fraction in the region of the Z-pin. In the meso-scale model the in-plane fibres are assumed to bunch up as they are displaced by the Z-pin. In the Dickinson model the fibres are assumed to be 'removed' from the model which leads to a reduction in the fibre volume fraction in the region of the Z-pin. These two approaches then present two extreme assumptions and as has been demonstrated, these assumptions manifest themselves in the moduli predictions. The conclusion is that the two FE approaches provide a realistic range of Young's moduli predictions with two extreme assumptions.

8.3.4.2 Poisson's Ratios

The Poisson's ratio results for the UD and cross-ply laminates are displayed in Figure 8.15 and Figure 8.16. The bounds produced for the Poisson's ratios are generally quite good and the upper bounds are commonly closer to the FE results.

In the FE models, both ε_x and ε_y increase with an increasing Z-pin volume fraction because the stiffness of the Z-pin in the *x* and *y* directions is less than that of the material it replaces. It is noted that the rate of increase in deformation is greatest in the *y* direction and owing to the relationship that

$$\nu_{xy} = \frac{\varepsilon_y}{\varepsilon_x} \qquad \textbf{8-14}$$

as the Z-pin volume is increased ν_{xy} also increases. This is greater in the Dickinson model due to the increasing matrix volume fraction and decreasing in-plane fibre volume fraction in the model when the Z-pin volume is increased. The effect is lesser in the meso-scale model as the fibre volume fraction does not decrease. In the presence of steel Z-pins the effect is reduced due to the large transverse stiffness of the material compared to the carbon fibre Z-pins.

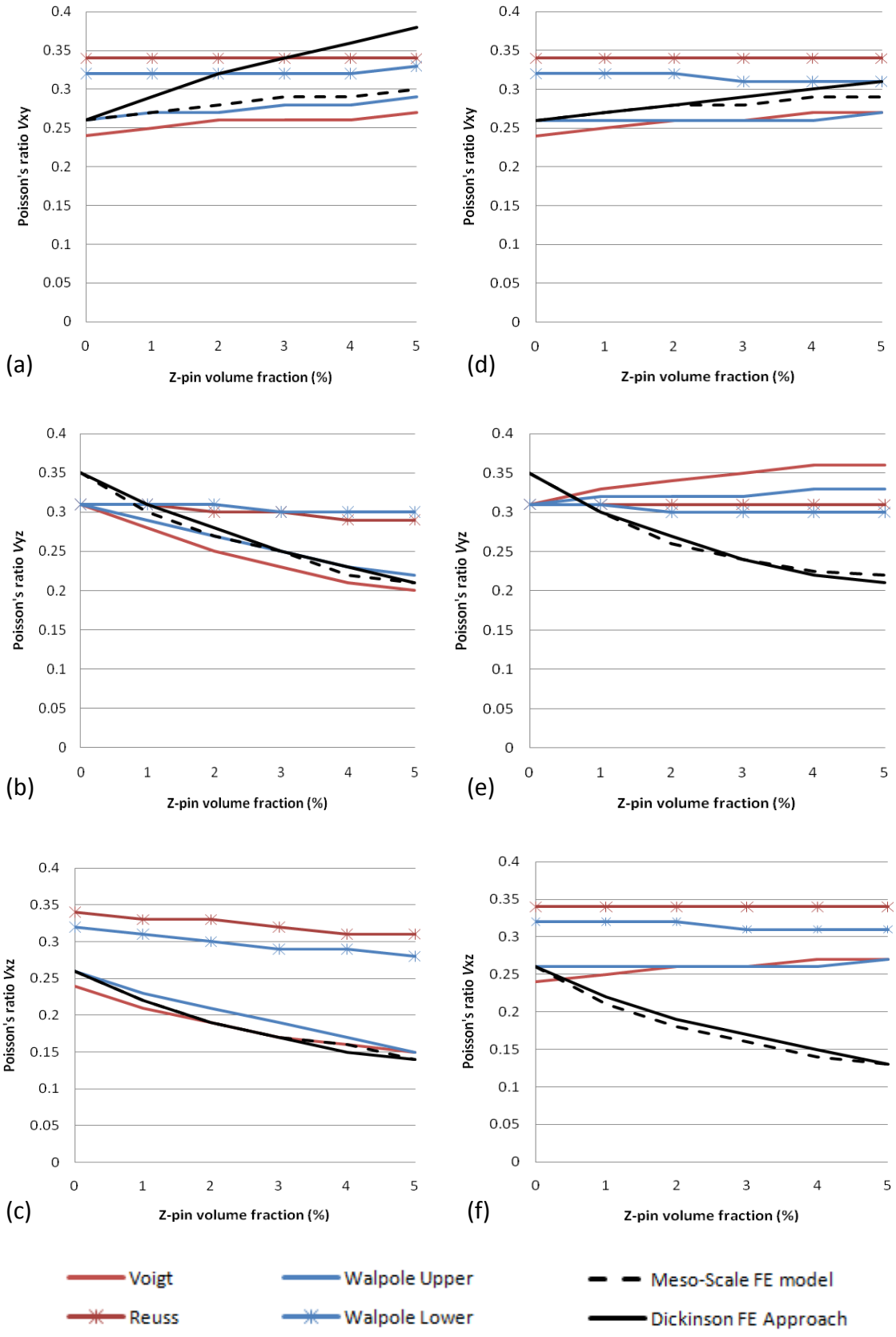

Figure 8.15: Poisson's ratio predictions for [0] UD AS4/3501-6 containing Z-pin reinforcement; (a) v_{xy} with T300/9310 Z-pin, (b) v_{yz} with T300/9310 Z-pin, (c) v_{xz} with T300/9310 Z-pin, (d) v_{xy} with steel Z-pin, (e) v_{yz} with steel Z-pin, (f) v_{xz} with steel Z-pin

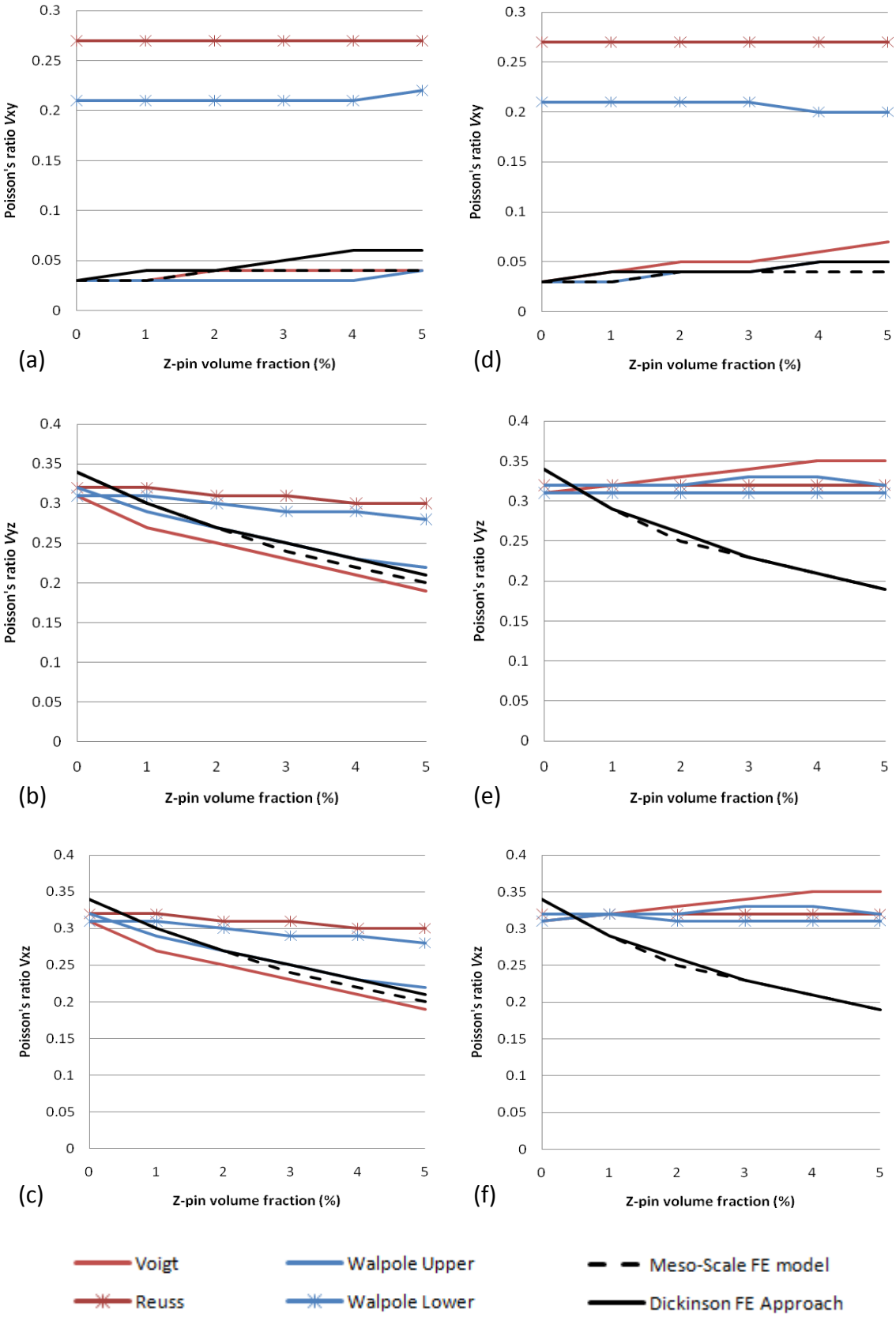

Figure 8.16: Poisson's ratio predictions for $[0/90]_s$ cross-ply AS4/3501-6 containing Z-pin reinforcement; (a) v_{xy} with T300/9310 Z-pin, (b) v_{yz} with T300/9310 Z-pin, (c) v_{xz} with T300/9310 Z-pin, (d) v_{xy} with steel Z-pin, (e) v_{yz} with steel Z-pin, (f) v_{xz} with steel Z-pin

The value of v_{xy} in the cross-ply laminates is much lower than in the UD laminates because the in-plane fibres in the *y* direction dramatically reduce the Poisson's contraction in this axis. There is a small rise in the predicted value of v_{xy} from both FE models and they more or less agree with each other due to the stiffening effect of the *y* direction fibres although the greater rises are seen in the Dickinson models for the same reasons as in the UD laminates.

In both the UD and cross-ply laminates the upper bounds (rather than the lower bounds) are closest to the FE result (particularly the meso-scale FE model). This is owing to the strain assumption used in these bounds where the actual strain result is more uniform than the stress result. The bounding methods also predict that there will be an increase in v_{xy} when the Z-pin volume fraction is increased.

The results for v_{yz} and v_{xz} are similar for the approaches utilised here. The FE models predict large drops in both of these Poisson's ratios with increasing Z-pin volume fractions. This happens because, as seen with the E_z results, the application of Z-pins increases the stiffness of the material in the *z* direction. As a result, the Poisson's contraction in the *z* direction due to a load in the *x* or *y* direction reduces with increasing Z-pin volumes. This leads to the reductions in v_{yz} and v_{xz} shown in Figure 8.15 (b), (c), (d) and (f) and Figure 8.16 (b), (c), (d) and (f).

The bounding method results for v_{yz} and v_{xz} vary a lot depending on the lay-up and Z-pin material. When the carbon fibre (T300) Z-pin material is used, the Voigt bound and Walpole upper bound provide responses which are close to the values obtained from the FE predictions for both v_{yz} and v_{xz} in both lay-ups. As was found in the E_x predictions, when the composite is loaded in the *x* direction the uniform strain assumption is very close to the actual strain response and as a result v_{yz} and v_{xz} in the UD and cross-ply laminates is predicted well by the Voigt and Walpole upper bounds. The predictions for v_{yz} are slightly worse in the UD laminate, as due to a transverse load the strain response in the transverse direction, is less uniform than in the fibre direction due to an applied load in the fibre direction.

When the Z-pin is assumed to be made from steel the bounding predictions are unreliable due to the isotropic nature of the Z-pin. As was observed in the Young's moduli predictions, the upper bounds overestimate the stiffness in the *x* and *y* directions compared to the FE results due to the large transverse moduli of the steel reinforcement. A similar result is found for the Poisson's ratios and the values obtained overestimate the impact of the steel Z-pins.

The general conclusion then is that the upper bound methods produce a reasonably accurate prediction for v_{xy}, v_{xz} and v_{yz} when Z-pin materials have relatively low transverse modulus, as in the carbon fibre Z-pin material. When the Z-pin material has a high transverse modulus, as in the steel Z-pins the bounding methods overestimate the material stiffness resulting in an overestimation of v_{xz} and v_{yz}. Both FE approaches are in reasonable agreement regarding v_{xz} and v_{yz} but the Dickinson approach provides a larger estimation of v_{xy}, particularly in the UD laminates which is down to the assumption on the fibre volume fraction in the region of the Z-pin. Again, the FE models should provide an extreme range of values due to the in-plane fibre volume fraction assumptions.

8.3.4.3 Shear Moduli

As with the Young's moduli results the Z-pin material does not have much effect on the trend of results but does impact on the magnitude of the results as shown in Figure 8.17 and Figure 8.18. Both FE models exhibit a slight reduction in G_{xy} with the application of through-thickness reinforcement. This is likely to have been caused by increased stresses and strains in the region of the Z-pin resulting in a lower shear stiffness compared to the unreinforced composite. It is also possible that the choice of model geometry plays a role in the reduction. In the case of the meso-scale FE model the proximity of the in-plane fibre to the Z-pin can affect the local stress and strain response by introducing stress concentrations which would result in differences in the shear moduli. Upon the application of through-thickness reinforcement this results in a lowering of the shear modulus G_{xy}. Any possible further reduction is opposed by the benefit in shear stiffness gained by the application of further Z-pin material. It is difficult to ascertain whether this response is physically meaningful due to a lack of experimental observations to

clarify the mechanisms involved in the material response. Similar results are observed in both the UD and cross-ply laminates.

The lower bound predictions for G_{xy} are in general agreement with the FE predictions owing to a reasonably uniform stress response. However, there is a small degree of variation in the stresses and this results in Walpole's lower bound being closer to the FE predictions. However, Walpole's lower prediction does overestimate the G_{xy} compared to the FE results but given the lack of experimental data available it is not clear whether the results are accurate or not. However, the lack of variation in G_{xy} does agree with the findings by Troulis which would suggest that the results are meaningful.

The unit cell predictions for G_{yz} show a variation of around 10% and 13% at the highest Z-pin volume for carbon/epoxy and steel Z-pin materials respectively. This is dominated by the fibre volume fraction in the region of the through-thickness reinforcement. The bounding methods also predict an increase in the shear moduli of similar magnitudes to the meso-scale FE model and this comes as a result of the formulation of the bounds. As with the meso-scale FE model, the fibre volume is kept constant, thereby assuming that fibre spreading does not occur. In theory a rise in G_{yz} can be anticipated in the UD composites as G_{yz} is dominated by the transverse properties of the in-plane fibres and the matrix. These are low compared to the axial stiffness of the Z-pin and hence when Z-pin material is applied there should be an associated rise in G_{yz}. The variation in G_{yz} between unpinned and pinned laminates is predicted to be similar in the cross-ply laminates but due to the stiffening nature of the in-plane fibres oriented in the *y* direction the magnitude of G_{yz} is increased.

As with G_{xy} the lower bound predictions provide results close to the FE models for G_{yz}. Again this implies that under shear loading the stress response is relatively uniform as the Reuss bound appears to provide the closest prediction to the FE results. In the cross-ply laminates the results for G_{yz} and G_{xz} are identical due to the stacking sequence.

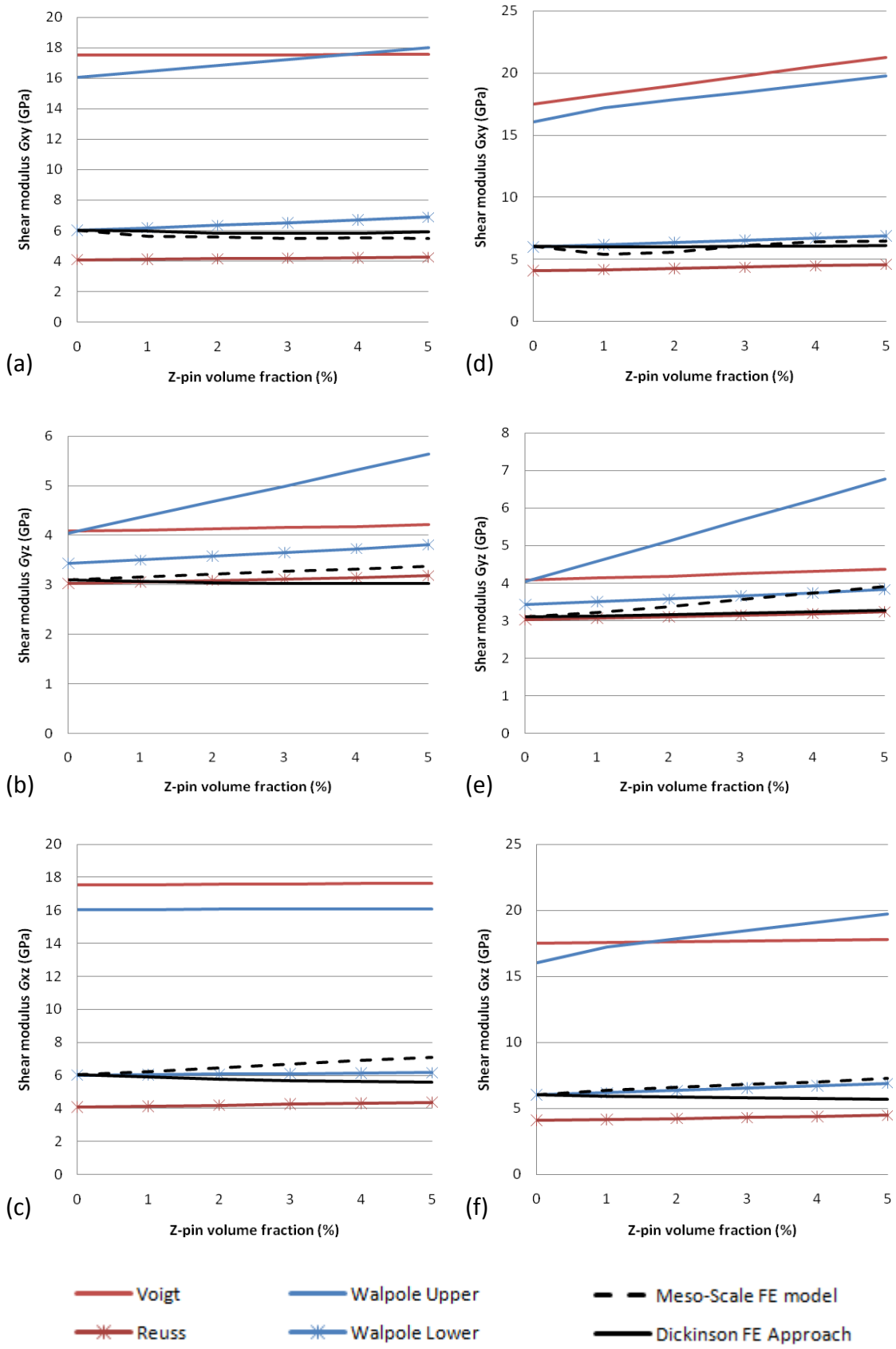

Figure 8.17: Shear modulus predictions for [0] UD AS4/3501-6 containing Z-pin reinforcement; (a) G_{xy} with T300/9310 Z-pin, (b) G_{yz} with T300/9310 Z-pin, (c) G_{xz} with T300/9310 Z-pin, (d) G_{xy} with steel Z-pin, (e) G_{yz} with steel Z-pin, (f) G_{xz} with steel Z-pin

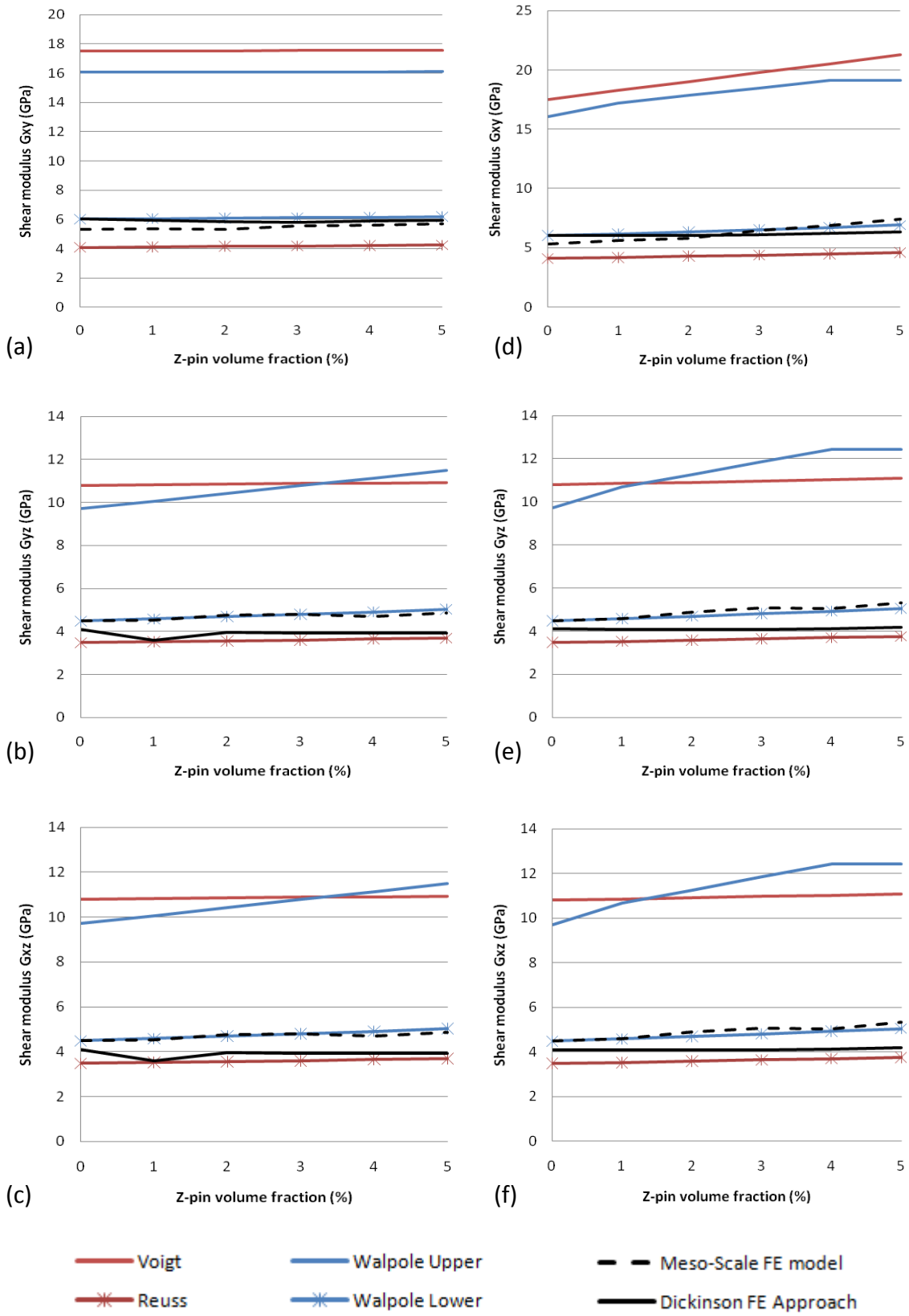

Figure 8.18: Shear modulus predictions for $[0/90]_s$ cross-ply AS4/3501-6 containing Z-pin reinforcement; (a) G_{xy} with T300/9310 Z-pin, (b) G_{yz} with T300/9310 Z-pin, (c) G_{xz} with T300/9310 Z-pin, (d) G_{xy} with steel Z-pin, (e) G_{yz} with steel Z-pin, (f) G_{xz} with steel Z-pin

The FE predictions of G_{xz} in the UD laminates show differing responses between the Dickinson and meso-scale FE approaches. This is again explained by the V_f^f assumption in the region of the Z-pin. The meso-scale model presents a rise in G_{xz} of 15% whilst the Dickinson approach shows a reduction of around 6% between unpinned and pinned laminates with a V_f^z of 5%. In the Dickinson model the reduction of in-plane fibres causes the decrease in G_{xz}, although the decrease is only small due to the introduction of stiff Z-pin material. In the meso-scale model the G_{xz} value of the UD laminate is supplemented by the introduction of Z-pin material and hence the rise in G_{xz} is presented.

The bounding methods again show that the lower bounds are closer to the FE predictions for the shear response and both show a small increase in the value of G_{xz}. As with G_{xy}, Walpole's lower bound provides a response closest to the FE predictions.

8.3.4.4 General Discussion

The results presented here highlight the importance of the assumption used, regarding the movement of in-plane fibres due to the presence of Z-pins. It is believed that the two FE approaches used in this study, namely the approach presented by Dickinson *et al*[85] and the current meso-scale FE model, provide predictions using two extreme assumptions on the movement of in-plane fibres. The two FE models presented therefore provide a relative range of the elastic properties within which the true values of any Z-pinned laminate should exist. Unfortunately, due to the lack of experimental data and characterisation it is difficult to say how accurate either FE approach is. In fact, the meso-scale FE model generally predicted results showing features observed by Steeves and Fleck for the Young's moduli and Troulis for the shear moduli. Conversely, the Dickinson approach showed trends in the Young's moduli that agreed with the findings of Troulis and Mouritz and Cox. This highlights the difficulty in analysing the present results.

The graphs presented in Figure 8.12 to Figure 8.18 show that the bounds provided by the Voigt and Reuss formulae and Walpole's theoryare quite wide. In

fact they can be very wide. Therefore, these approaches cannot be recommended to provide tight bounds on the effective material properties of Z-pinned laminates. However, it is noticeable that at least one of the formulae produces a good fit with the FE predictions in the vast majority of cases. Summaries showing the closest bounding prediction to the FE predictions for each laminate/Z-pin type are given in Table 8-13, Table 8-14 and Table 8-15 these show results for the Young's moduli, Poisson's ratios and shear moduli respectively. The bounding methods presented are generally closer to the meso-scale FE model which occurs as the bounding methods presented have used the same assumptions as the meso-scale FE model, i.e. when the Z-pin is applied it takes away from the matrix material and not the fibre material.

It remains a difficult task to assess the suitability of these bounding approaches to Z-pinned composites due to a lack of comparable experimental data however they have been assessed with relation to the FE results which are believed to provide a realistic range of elastic property values. The closest bounding predictions are all within 10% of the meso-scale FE values which is quite reasonable bearing in mind the simplicity of the formulae and input data used. The closest bounding predictions are all within 18% of the Dickinson models. As mentioned, this is due to the in-plane fibre volume fraction assumption in the region of the Z-pin. Mouritz and Cox showed that the in-plane fibres are subject to spreading in pinned composites leading to a degradation of in-plane properties. This goes against the current meso model assumptions where the in-plane fibres remain in place. However, this approach appears to be valid for stitched composites as discussed by Mouritz and Cox.

It was noted that when there is reinforcement in the direction of the Young's modulus to be predicted a uniform strain assumption is fairly close to the response of the FE models. Consequently in these cases i.e. E_x and E_z for Z-pinned laminates the Voigt bound provides the best prediction. In the transverse direction (E_y in the UD laminates) none of the predictions excel but with the current materials Walpole's lower bound is the closest. The Young's modulus predictions also highlight a key restriction of Walpole's theory. This is that when reinforcement

geometries extend to the surface of the representative volume under consideration the theory fails in predicting the modulus that coincides with the reinforcement orientation. This occurs because when the volume is loaded in the fibre (reinforcement) direction the theory imposes a difference of strains between the fibres and matrix. As discussed and shown in Figure 8.11 the real strain response is more or less uniform so the basic rule of the theory is incorrect. This can be overcome by setting the comparison material properties to infinity, which leads Walpole's theory to return the same result as the Voigt prediction i.e. a uniform strain solution. This happens because it makes the comparison material excessively stiff meaning the response becomes that of uniform strain.

The Poisson's ratio predictions were reasonable except for the out of plane predictions in the steel pinned laminates. These results were poor due to the high transverse properties of the steel reinforcement so no prediction is included in the summary table.

Besides the out-of-plane Poisson's ratios the predictions were again reasonable with Walpole's upper bound and the Voigt prediction providing the best results. These predictions were both very similar, as were the FE predictions.

The shear modulus predictions were all within 15% of the meso models on average and within 22% of the Dickinson models. Again, the bound predictions were, in general, in better agreement with the meso-scale FE models. Furthermore it seems that bounds predictions can be selected such that the shear moduli of Z-pinned composites can be estimated reasonably well; particularly in the cross-ply laminates. It is noticeable that the shear response of the FE models is not quite a uniform stress response which means that Walpole's lower bound is closer than the Reuss' bound in most cases.

	E_x	Ave % difference Meso model	Ave % difference Dickinson FE	E_y	Ave % difference Meso model	Ave % difference Dickinson FE	E_z	Ave % difference Meso model	Ave % difference Dickinson FE
UD T300	Voigt	0.26	12.4	Walpole Low	-7.28	-5.52	Walpole Up	-1.41	2.22
UD Steel	Voigt	3.42	14.7	Walpole Low	-9.97	-6.60	Walpole Up	-1.81	1.83
CP T300	Voigt	1.01	11.9	Voigt	1.01	11.9	Walpole Up	-3.47	-0.18
CP Steel	Voigt	6.85	17.6	Voigt	6.85	17.6	Walpole Up	-2.27	0.66

Table 8-13: Summary of analytical predictions closest to FE results as well percentage difference between the closest analytical and numerical results for Young's modulus predictions

	v_{xy}	Ave % difference Meso model	Ave % difference Dickinson FE	v_{yz}	Ave % difference Meso model	Ave % difference Dickinson FE	v_{xz}	Ave % difference Meso model	Ave % difference Dickinson FE
UD T300	Walpole Up	-2.30	-14.4	Walpole Up	-0.91	-2.78	Voigt	-0.85	0.26
UD Steel	Voigt	-7.20	-9.25	None	-	-	None	-	-
CP T300	Voigt	0	-18.6	Walpole Up	1.58	-0.74	Voigt	-6.66	-8.74
CP Steel	Walpole Up	8.33	-4.17	None	-	-	None	-	-

Table 8-14: Summary of analytical predictions closest to FE results as well percentage difference between the closest analytical and numerical results for Poisson's ratio predictions

	G_{xy}	Ave % difference Meso model	Ave % difference Dickinson FE	G_{yz}	Ave % difference Meso model	Ave % difference Dickinson FE	G_{xz}	Ave % difference Meso model	Ave % difference Dickinson FE
UD T300	Walpole Low	14.6	9.35	Reuss	-4.09	1.88	Walpole Low	-7.15	5.83
UD Steel	Walpole Low	7.64	6.47	Reuss	-9.76	-1.68	Walpole Low	-3.40	10.5
CP T300	Walpole Low	11.4	3.04	Walpole Low	1.34	21.9	Walpole Low	1.34	21.9
CP Steel	Walpole Low	4.18	5.38	Walpole Low	-2.84	15.8	Walpole Low	-2.84	15.8

Table 8-15: Summary of analytical predictions closest to FE results as well percentage difference between the closest analytical and numerical results for shear modulus prediction

	Voigt	Reuss	Walpole Upper	Walpole Lower
Number of closest agreements to FE results	10	2	8	12

Table 8-16: Number of predictions closest to FE results for each analytical method

Table 8-16 shows the number of times that each of the four formulae (Voigt, Reuss, Walpole upper and Walpole lower) was the closest to the FE predictions. This highlights the variability of the stress and strain response of the Z-pinned laminates. Furthermore, this demonstrates that with a suitable knowledge of the material characteristics, one can predict the material properties of Z-pinned laminates to within approximately 10% in the majority of cases (compared to the material predictions using the current FE analyses). Owing to a lack of experimental data and observations in the literature this is a reasonable figure. Moreover, without further knowledge of the physical characterisation of Z-pinned laminates it will be hard if not impossible to create a more suitable mathematical prediction tool to estimate the elastic properties of Z-pinned composites.

From the comparison of FE and bounding method results a Z-pinned laminate is best characterised in a mathematical form in the following way:

- Predictions for the Young's modulus in the direction of fibre reinforcement should be made using the uniform strain approach of Voigt's formula
- Predictions for the Young's modulus in a direction without reinforcement should be made using Walpole's lower bound
- Predictions for the Poisson's ratios should be made using either Walpole's upper bound or Voigt's formula
- Predictions for the Shear moduli should be taken from Walpole's lower bound prediction

It is important to stress that these points are only applicable to Z-pinned laminates similar to those studied here. It is clear that Z-pin materials or laminates with differing properties could give rise to significantly different results.

8.3.4.5 Notes on Walpole's Theory

Some observations were made during the study on Walpole's theory which have as yet, not been expanded upon; these observations concern the selection of the comparison material. As has been discussed in this chapter there is a serious restriction on the application of Walpole's upper bound to the prediction of Young's modulus values in the direction of fibre/Z-pin reinforcement. It has been demonstrated that this can be overcome by the application of a comparison material with material properties tending to infinity.

Along with the above restriction it was also noted there appears to be no systematic method of selecting the comparison material such that the C_0-C_r is semi-positive definite. In general, for a carbon/epoxy laminate the matrix material is weaker than the fibres (and Z-pins where appropriate) and the result is that when the comparison material is set to be the same as the matrix material C_0-C_m will be semi-negative definite whilst C_0-C_f will be fully negative definite. This creates the lower bound and would appear to be the best bound available. To create the upper bound, C_0-C_r must be semi-positive definite but as the comparison material is isotropic it is impossible to characterise the fibre with the comparison material. The solution to the best upper bound is then restricted to a trial and error process in order to obtain the most suitable comparison material.

A further observation is regarding the comparison material itself. The well known Green's function used by Walpole was (from 3-24)

$$G_{il} = \frac{1}{4\pi\mu_0}\frac{\delta_{il}}{r} - \frac{\left(\lambda_0 + \mu_0\right)}{8\pi\mu_0\left(\lambda_0 + 2\mu_0\right)}\frac{\partial^2 r}{\partial x_i \partial x_l}$$

The above Green's function applies only to isotropic materials by definition and hence the Green's function cannot be calculated with an anisotropic comparison material. In order to do this one would require a higher order Green's function which holds an extremely complex derivation which must also be developed to obtain the strains for the problem in question. To the author's knowledge this derivation has not been suitably published for this application and hence cannot be expanded on at this time.

A final observation is that the selection of comparison material yields bound on the elastic moduli of the composites under consideration. Therefore, selection of the correct comparison material should lead to an accurate prediction of the effective properties for the composite i.e. there is one set of comparison material properties which will lead to a prediction of the effective properties of the composite which is correct. There are no indications that this is possible; in fact it is highly unlikely but it would be interesting to study if there are any patterns regarding the selection of comparison materials to predict test data.

8.4 Conclusions

In Chapter 8.3 it was demonstrated that predictions provided by the FE modelling approaches were highly dependent on the fibre volume fraction assumption in the region of the Z-pin. In terms of general trends the meso-scale FE model provided higher results for the Young's moduli due to the assumption that there is no spreading of the in-plane fibres in the presence of a Z-pin. The Dickinson model takes an extreme assumption in the opposite direction by assuming that the Z-pin and associated resin rich zone completely displace the in-plane fibres in that region. Similar differences are found for the shear moduli but in general the FE models present similar results for the Poisson's ratios with the exception of v_{xy} for laminates with carbon/epoxy Z-pins. The reduction of the in-plane fibre volume fraction in the Dickinson model leads to a large increase in v_{xy}, whilst the meso-scale FE model showed a significantly smaller increase.

It has been demonstrated that in the broad sense the bounding methods produce wide bounds on the effective properties of Z-pinned laminates. Therefore they are not recommended for obtaining bounds on the effective properties. However, it is also noted that for each of the effective properties except v_{xz} and v_{yz} at least one of the bounds produces a prediction within 15% of the meso-scale FE predictions. Moreover, the selected predicted values are commonly within 10% of the FE predictions. This occurs because the stress or strain assumptions used by the bounding methods are close to reality under specific loading conditions. However, it is not feasible to use the presented bounding methods to obtain a reliable

prediction of the material properties of through-thickness reinforced laminates due to the amount of prior material and theoretical knowledge required.

9 Conclusions and Recommendations for Future Work

9.1 Conclusions

Through-thickness properties of FRPs are of greater concern than ever as composite materials are used in ever more complex design situations, including primary structures. This study has provided new information on the through-thickness characteristics of carbon/epoxy laminates in the following ways:

- Production of a comprehensive review of existing through-thickness test methods and results
- Implementation of a through-thickness compression test regime to provide data for the Second World Wide Failure Exercise (WWFE-II) to benchmark failure theories against predictions on composites under triaxial loading states
- Finite element validation of three specimens used to observe through-thickness compressive behaviour of quasi-isotropic laminates
- Study of the free-edge effects present under through-thickness loading of quasi-isotropic laminates of square and hollow cylinder cross-section
- Direct comparison of three specimen geometries, highlighting the geometry dependence of the through-thickness compressive strength of quasi-isotropic carbon/epoxy laminates
- Investigation of the effective elastic properties of through-thickness reinforced (Z-pinned) carbon/epoxy laminates
- Comparison of an existing unit cell FE approach and meso-scale unit cell created by the author to predict the effective properties of Z-pinned UD and cross-ply laminates highlighting the importance of the assumption on the in-plane fibre volume fraction in the region of the Z-pin
- Study into the effectiveness of using Voigt and Reuss bounds and Walpole's bounds to predict the effective elastic properties of Z-pinned materials

9.1.1 Through-Thickness Testing

The literature review on through-thickness testing methods highlighted three specimens that had been used previously for through-thickness compressive testing: waisted, parallel sided and hollow cylindrical specimens. In all three cases there was either limited or no design analysis of the specimens and as a result all three were modelled using finite elements to assess their response to through-thickness loading. The cubic specimen measured 12x12x12mm. The waisted specimen gauge length was 12x12x12mm and was connected to end tabs with a cross section of 25x25mm via fillets with a radius of 9.25mm. The waisted specimen had an overall height of 38.5mm. The cylindrical specimen had a gauge length of 9.4mm with inner and outer diameters of the cylinder being 16mm and 21mm respectively through the gauge length. The end tabs were connected to the gauge length via fillets with a radius of 5.45mm and the outer diameter of the end tabs was 30mm with an overall specimen height of 25.4mm.

Tests were carried out on the three specimen geometries using the same $[45/-45/90/0]_s$ quasi-isotropic AS4/8552 laminates. Initial tests highlighted the need to use post yield strain gauges due to the high strains produced by large through-thickness compressive loads. Results for the initial Young's modulus showed that the waisted specimen provided the highest values with an average E_z of 14GPa. The cylindrical specimens provided an average E_z of 13.4GPa which was in statistical agreement with the waisted specimens. The cubic specimens had an average E_z value of 11.9GPa which was deemed low compared to the other two specimen geometries. However, it was noted that the strains of the cubic specimens were measured by three means: machine load displacement curves, standard foil strain gauges and post yield gauges. When results from just the post yield gauges were analysed, it was found that the average E_z value increased to 13.1GPa which was in statistical agreement with the waisted and cylindrical specimens.

The Poisson's ratio (v_{zx}=v_{zy}) predictions for the waisted and cubic specimens were 0.064 and 0.077 respectively and owing to the C_v values the difference was deemed to be statistically insignificant. The cylindrical specimens produced a much

higher average for the Poisson's ratios at 0.108. It was concluded that this was due to warping of the cylinder walls under loading, artificially increasing the transverse strains. Therefore it must be stated that the current cylindrical specimen should not be used to obtain the Poisson's ratios.

The measured strength values highlighted the geometry dependence of this property. The waisted specimens had an average strength of 1371.1GPa which is substantially greater than the averages of 1183.7 and 800.8GPa given by the cubic and cylindrical specimens respectively. The waisted specimen regularly failed at the end of the gauge length indicating that the stress concentrations in this area contribute to failure. The cube specimens typically failed at one end of the specimen indicating that failure occurred due to the high stress concentrations imposed by the contact between the specimen and loading plates. The cylindrical specimens commonly failed within the gauge length. The low failure stress of the cylindrical specimens was likely caused by the presence of free-edge effects throughout the gauge length. Furthermore, it was observed that because the cylinder walls are relatively thin, the matrix cracks generally only have a small distance to propagate which could have increased their effect.

Finite element studies of square and cylindrical cross-section slices from the specimens highlighted that in the gauge length walls of the cylindrical specimens edge-effects would be rife. This casts doubt over the ability of the specimen to produce reliable results and calls in to question results of DeTeresa *et al*[55] who used a similar cylindrical specimen to produce results for specimens subjected to combined through-thickness compression and torsion.

Free-edge effects were also found to be large at the corners of the ±45˚ layers in the square cross-section model. It is believed that these free-edge effects contributed to the stress concentrations found at the corners of the waisted specimens between the gauge length and fillet radii.

The non-linearity of the stress strain response at high loads in the cubic specimens came as a result of strain gauge peeling. This in turn, came as a result of a lack of clearance for the wires extending from the strain gauges within the load set-up. The recommendation is that the cube specimen is suitable for obtaining

initial through-thickness properties but care must be taken with the wire management to ensure that strain gauge peeling does not occur or is at least limited.

9.1.2 Effective Property Prediction of Z-pinned Laminates

The effective properties of Z-pinned UD and cross-ply AS4/3501-6 laminates were predicted by four different means. The first predictions were obtained from an FE approach following the guideline of Dickinson *et al*[85]. The second approach was an FE unit cell model using a meso-scale approach while the third and fourth predictions were taken from bounding methods. These were Voigt and Reuss bounds and Walpole's bounds.

The two FE approaches hold significant and different assumptions which give rise to different results in the property predictions. There appears to be some doubt in the literature as to what happens to the in-plane fibres when through-thickness reinforcement is applied. Some works have suggested that the in-plane fibres are displaced and as a result the in-plane fibre volume fraction reduces in the region of the Z-pin while others suggest that the in-plane fibres bunch together and so the fibre volume fraction increases in the region of the Z-pin. The Dickinson approach utilises the former assumption and this is highlighted in the prediction of E_x. The Dickinson approach predicts a significant reduction of E_x when the Z-pin volume is increased. This comes as a result of the reduction in the number of in-plane fibres assumed by the model. The meso-scale FE model takes the opposite assumption and the fibre geometry is maintained through the model such that there is a proportional increase in the fibre volume fraction V_f^f as the Z-pin volume is increased. The result is that the prediction of E_x remains more or less constant, regardless of the Z-pin volume. As a result of the differences it appears as though the two FE models together provide a range of values, within which the true values of the effective properties is likely to lie. From the experimental observations reported in the literature survey in Chapter 3 it would seem that the in-plane fibre volume fraction in the region of the Z-pin varies greatly from group to group so it is not possible to conclude which, if either, of the FE results is most accurate. This

feature will be largely dependent on the manufacture of the laminate which will undoubtedly vary, even when manufacture is conducted by one group.

The predictions presented for the bounding methods are generally closer to the meso-scale model as they also use the assumption that the in-plane fibres are bunched together. In the majority of cases, the bound sets i.e. the Voigt and Reuss bounds and the Walpole bounds, produce a wide set of bounds. This is most evident in the prediction of E_x where the difference between the Voigt and Reuss bounds is around 130GPa and the difference between Walpole's upper and lower bounds is 125GPa (assuming that Walpole's comparison material is set to infinity). These differences are huge but it has been demonstrated that in the case of E_x, Voigt's bound produces a very accurate result compared to the meso-scale FE prediction. In the form that the theory is presented in the literature[122], Walpole's upper bound fails at predicting the Young's modulus in the fibre direction(s). This is due to the 'polarization tensor' which imposes varying strains between the matrix and reinforcement, whereas in reality the strain will be uniform. In the original references[122, 125] it is stated that the reinforcement geometry may be arbitrary. This is true of particle inclusions but appears untrue for fibre based systems in the prediction of Young's moduli in the fibre direction(s). The restriction then is that for calculating the Young's moduli in the direction of fibre/Z-pin reinforcement one must set the comparison material properties to infinity. Walpole's upper bound will then return the same result as Voigt's bound i.e. a uniform strain result which is close to reality. It is important that this restriction is known before trying to apply Walpole's bounds to any FRP.

It was demonstrated that Voigt, Reuss and Walpole predictions were close to the FE results for selected properties, but none of the bounding methods can be recommended as a robust prediction tool. Neither of the bounding methods proved to be consistently reliable at predicting the properties of Z-pinned laminates so they cannot be recommended as a simple analytical tool.

9.2 Suggestions for Future Work

9.2.1 Through-Thickness Testing

The state of through-thickness shear testing appears to be fairly robust compared to that of through-thickness tensile and compressive testing. Various test methods exist owing to the ability to use or modify existing standard in-plane shear test methods in order to characterise the through-thickness shear response of carbon/epoxy laminates. It appears that the areas of through-thickness tensile and compressive testing are suffering from a lack of standardisation. The result is that experimental data available in the literature are hard to compare and hard to trust. A key step then is to investigate the standardisation of specimens for through-thickness tensile and compressive loading. It is hoped that the current study will aid this process by showing the advantages and disadvantages of waisted, cubic and hollow cylindrical specimens. The current work gives weight to both the cubic and waisted specimens for producing results for the elastic properties. Only the waisted specimen has been recommended for strength testing. In order to present a specimen for standardisation, much more work should be carried out. The current study has tested only quasi-isotropic CFRP materials. To better judge the usefulness of the specimens other materials such as glass and Kevlar fibres and polyester and PEEK matrices should be examined. Furthermore, a range of lay-ups should be examined to assess the properties and failure mode. This is a massive undertaking, not only in terms of the time it would take but also due to the expense of the operation.

A further area of concern highlighted by the current work is the results of DeTeresa *et al*[55]. The hollow cylindrical specimen was used by DeTeresa to characterise the response of various glass and carbon fibre laminates under combined through-thickness compressive and shear loading. The results demonstrated here show that the cylindrical specimen suffers greatly from free-edge effects which considerably affect the compressive strength and could also have a severe impact on the shear response of the specimens. Further work should be conducted to analyse the specimen under shear loading in order to assess the validity of the experimental approach. However, it should be noted that for

filament wound specimens free-edge effects will not be a problem. Another avenue would be to develop and test a new specimen to analyse the material response of laminates under combined through-thickness compression and shear loading. This would demand a great deal of time but any successful outcome would no doubt significantly advance the knowledge on composite material response.

9.2.2 Z-pinned Laminate Analysis

The work on Z-pinned composites in this study has highlighted a severe lack of experimental data on these materials. As has been demonstrated in the WWFEs, it is important to benchmark analytical predictions (be it failure or property predictions) with reliable experimental data. The author believes that there is plenty of scope for new work in this field. An extremely important area of work is the study of the displacement of in-plane fibres upon the insertion of Z-pin reinforcement. It is more than likely that this is due to parameters in the manufacture process such as the type of in-plane fibre, the type of matrix, the curing temperature and the curing pressure. It would render a valuable insight if a parametric study could be carried out to observe what determines the in-plane fibre volume fraction and misalignment in the region of the Z-pin. Once the in-plane fibre volume fraction problem has been studied it is important that when experimental observations are presented the authors acknowledge the state of the in-plane fibres. This would allow one to observe the correlation between the in-plane fibre volume fraction and misalignment and the effective material properties. After this the current property prediction methods can be fully analysed and potentially developed to provide more accurate predictions.

The work on Walpole's theory showed that some extra research may be worthwhile. It is believed that the use of an anisotropic comparison material would improve the predictions as it would characterise the fibre constituent much more closely. However, this would require the development of a higher order Green's function which would require a very determined effort as the result is likely to be extremely complex.

References

1. Edison, T.A., *US Pat. 470925.* 1892.
2. Bennett, S.C. and D.J. Johnson, *Structural Heterogeneity in Carbon Fibers.* Proceedings 5th London Carbon and Graphite Conference (Society for the Chemical Industry: London), 1978. **1**: p. 377-386.
3. Hinton, M.J. and A.S. Kaddour, *The Second World Wide Failure Exercise: Benchmarking of Failure Criteria Under Triaxial Stresses for Fibre-Reinforced Polymer Composites.* Proceedings of the 16th International Conference on Composite Materials, 8-13 July, 2007(Kyoto, Japan).
4. Hinton, M.J. and P.D. Soden, *Predicting Failure in Composite Laminates: The Background to the Exercise.* Composites Science and Technology, 1998. **58**: p. 1001-1010.
5. Greenwood, J.H., *German Work on GRP Design.* Composites, 1977: p. 175-184.
6. Owen, M.J. and D.I. Rice, *Biaxial Strength Behaviour of Glass-Reinforced Polyester Resins.* Composite materials: testing and design, ASTM STP 787, ed. I. M. Daniel, 1982: p. 124-144.
7. Swanson, S.R. and A.P. Christoforou, *Progressive Failure in Carbon/Epoxylaminates Under Biaxial Stress.* Journal of Engineering Materials and Technology, Trans. ASME, 1987. **109**: p. 12-16.
8. Tang, P., *A Multiaxial Failure Criterion for Composites.* Computational Probabilistic Methods, 1988(AMD/ASME, V93, published by ASME, New York, USA): p. 87-96.
9. Soden, P.D., M.J. Hinton, and A.S. Kaddour, *A Comparison of the Predictive Capabilities of Current Failure Theories for Composite Laminates.* Composites Science and Technology, 1998. **58**: p. 1225-1254.
10. Hinton, M.J., A.S. Kaddour, and P.D. Soden, *Evaluation of Failure Prediction in Composite Laminates: Background to 'Part B' of the Exercise.* Composites Science and Technology, 2002. **62**: p. 1481-1488.
11. Hinton, M.J., A.S. Kaddour, and P.D. Soden, *A Comparison of the Predictive Capabilities of Current Failure Theories for Composite Laminates, Judged Against Experimental Evidence.* Composites Science and Technology, 2002. **62**: p. 1725-1797.
12. Eckold, G.C., *Failure Criteria for use in the Design Environment.* Composites Science and Technology, 1998. **58**(7): p. 1095-1105.
13. Edge, E.C., *Stress Based Grant-Sanders Method for Predicting Failure of Composite Laminates.* Composites Science and Technology, 1998. **58**(7): p. 1033-1041.
14. Gotsis, P.K., C.C. Chamis, and L. Miinetyan, *Prediction of Composite Laminate Fracture: Micromechanics and Progressive Fracture.* Composites Science and Technology, 1998. **58**(7): p. 1137-1149.
15. Hart-Smith, L.J., *Predictions of the Original and Truncated Maximum-Strain Failure Models for Certain Fibrous Composite Laminates.* Composites Science and Technology, 1998. **58**(7): p. 1151-1178.
16. Hart-Smith, L.J., *Predictions of a Generalised Maximum Shear-Stress Failure Criterion for Certain Fibrous Composite Laminates.* Composites Science and Technology, 1998. **58**(7): p. 1179-1208.

17. Liu, K.S. and S.W. Tsai, *A Progressive Quadratic Failure Criterion for a Laminate.* Composites Science and Technology, 1998. **58**(7): p. 1023-1032.
18. McCartney, L.N., *Predicting Transverse Crack Formation in Cross-Ply Laminates.* Composites Science and Technology, 1998. **58**(7): p. 1069-1081.
19. Puck, A. and H. Schürmann, *Failure Analysis of FRP Laminates by Means of Physically Based Phenomenological Models.* Composites Science and Technology, 1998. **58**(7): p. 1045-1067.
20. Rotem, A., *Prediction of Laminate Failure with Rotem Failure Criterion.* Composites Science and Technology, 1998. **58**(7): p. 1083-1094.
21. Sun, C.T. and J.X. Tao, *Prediction of Failure Envelopes and Stress/Strain Behaviour or Composite Laminates.* Composites Science and Technology, 1998. **58**(7): p. 1125-1136.
22. Wolfe, W.E. and T.S. Butalia, *A Strain-Energy Based Failure Criterion for Nonlinear Analysis of Composite Laminates Subjected to Biaxial Loading.* Composites Science and Technology, 1998. **58**(7): p. 1107-1124.
23. Zinoviev, P., et al., *The Strength of Multilayered Composites Under Plane Stress State.* Composites Science and Technology, 1998. **58**(7): p. 1209-1223.
24. Hinton, M.J., A.S. Kaddour, and P.D. Soden, *Evaluation of Failure Prediction in Composite Laminates: Background to 'Part C' of the Exercise.* Composites Science and Technology, 2004. **64**: p. 321-327.
25. Bogetti, T.A., et al., *Predicting the Nonlinear Response and Progressive Failure of Composite Laminates.* Composites Science and Technology, 2004. **64**: p. 329-342.
26. Cuntze, R.G. and A. Freund, *The Predictive Capability of Failure Mode Concept-Based Strength Criteria for Multidirectional Laminates.* Composites Science and Technology, 2004. **64**: p. 343-377.
27. Huang, Z.M., *A Bridging Model Prediction of the Ultimate Strenght of Composite Laminates Subjected to Biaxial Loads.* Composites Science and Technology, 2004. **64**: p. 395-448.
28. Mayes, J.S. and A.C. Hansen, *Composite Laminate Failure Analysis Using Multicontinuum Theory.* Composites Science and Technology, 2004. **64**: p. 379-394.
29. Orifici, A.C., I. Herszberg, and R.S. Thomson, *Review of Methodologies for Composite Material Modelling Incorporating Failure.* Composite Structures, 2008. **86**: p. 194-210.
30. Kaddour, A.S., et al., *Damage Theories for Fibre-Reinforced Polymer Composites: the Third World-Wide Failure Exercise (WWFE III).* Proceedings of the 16th International Conference on Composite Materials, 8-13 July, Kyoto, Japan, 2007.
31. Kaddour, A.S. and M.J. Hinton, *Failure Criteria for Polymer Composites Under 3D Stress States: The Second World-Wide Failure Exercise.* Proceedings of the 17th International Conference on Composite Materials, 27-31 July, Edinburgh, UK, 2009.
32. Kaddour, A.S., et al., *Damage Prediction in Polymer Composites: Update of Part A of the Third World-Wide Failure Exercise (WWFE-III).* Proceedings of

the 17th International Conference on Composite Materials, 27-31 July, Edinburgh, UK, 2009.
33. Daniel, I.M. and O. Isahi, *Engineering Mechanics of Composite Materials, 2nd ed.* Oxford University Press, Oxford, UK, 2006.
34. Daniel, I.M., *Composite Materials: testing & design (6th Conference).* ASTM STP 787., American Society for Testing and Materials, 1982.
35. Hodgkinson, J.M., *Mechanical Testing of Advanced Fibre Composites.* Woodhead Publishing Limited, Cambridge, UK, 2000.
36. Pendleton, R.L. and M.E. Tuttle, *Manual on Experimental Methods for Mechanical Testing of Composites.* Elsevier Science Publishers Ltd, Essex, UK, 1989.
37. Pipes, R.B. and I.M. Daniel, *Moiré Analysis of the Interlaminar Shear Edge Effects in Laminated Composites.* Journal of Composite Materials, 1971. **5**: p. 255-259.
38. Dong, S.B. and D.B. Goetschel, *Edge Effects in Laminated Composite Plates.* Journal of Applied Mechanics, 1982. **49**: p. 129-135.
39. Hsu, P.W. and C.T. Herakovich, *Edge Effects in Angle-Ply Composite Laminates.* Journal of Composite Materials, 1977. **11**(422-428).
40. Lindemann, J. and W. Becker, *Analysis of the Free-Edge Effect in Composite Laminates by the Boundary Finite Element Method.* Mechanics of Composite Materials, 2000. **36**(3): p. 207-214.
41. Pagano, N.J., *Exact Solution for Rectangular Bidirectional Composites and Sandwich Plates.* Journal of Composite Materials, 1970. **31**(1): p. 20-34.
42. Pagano, N.J., *On the Calculation of Interlaminar Normal Stress in Composite Laminates.* Journal of Composite Materials, 1974. **8**(65-81).
43. Pagano, N.J. and R.B. Pipes, *Some Observations on the Interlaminar Strength of Composite Materials.* International Journal of Mechanical Science, 1973. **15**: p. 679-688.
44. Pipes, R.B. and N.J. Pagano, *Interlaminar Stresses in Composite Laminates under Uniform Axial Extension.* Journal of Composite Materials, 1970. **4**(538-548).
45. Zhang, D., J. Ye, and D. Lam, *Free-Edge and Ply Cracking Effect in Angle-Ply Laminated Composites Subjected to In-Plane Loads.* Journal of Engineering Maechanics, 2007: p. 1268-1277.
46. Guo, Y., D. Post, and B. Han, *Thick Composites in Compression: An Experimental Study of Micromechanical Behaviour and Smeared Engineering Properties.* Journal of Composite Materials, 1992. **26**(13): p. 1930-1944.
47. Lodeiro, M.J., W.R. Broughton, and G.D. Sims, *Understanding Limitations of Though Thickness Test Methods.* Plastics, Rubber and Composites, 1999. **28**(9): p. 416-424.
48. Mespoulet, S., et al., *Design, development, and implementation of test methods for determination of through thickness properties of laminated composites.* Plastics, Rubber and Composites, 2000. **29**(9): p. 496-502.
49. Park, D.C. and D.G. Lee, *Through-Thickness Compressive Strength of Carbon-Phenolic Woven Composites.* Composite Structures, 2005. **70**: p. 403-412.
50. Kim, B.C., et al., *Through-Thickness Compressive Strength of a Carbon/Epoxy Composite Laminate.* Composite Structures, 2010. **92**: p. 480-487.

51. Roy, A.K. and R.Y. Kim, *Interlaminar Normal Stiffness and Strength of Thick Orthotropic Laminates: An Experimental Study.* Journal of Reinforced Plastics and Composites, 1994. **13**: p. 880-894.
52. Kitching, R., A.L. Tan, and T.M.N. Abu-Mansour, *The Influence of Through Thickness Properties on Glass Reinforced Plastic Laminated Structures.* Composite Structures, 1984. **2**: p. 105-151.
53. Tagarielli, V.L., et al., *The Response of a Multi-Directional Composite Laminate to Through-Thickness Loading.* Composites Science and Technology, To Be Published.
54. Ferguson, R.F., M.J. Hinton, and M.J. Hiley, *Determining the Through-Thickness Properties of FRP Materials.* Composites Science and Technology, 1997. **58**: p. 1411-1420.
55. DeTeresa, S.J., D.C. Freeman, and S.E. Groves, *The Effects of Through-Thickness Compression on the Interlaminar Shear Response of Laminated Fiber Composites.* Journal of Composite Materials, 2004. **38**(8): p. 681-697.
56. Zhao, Y., *Torque Limit for Bolted Joint for Composites Part A: TTTC Properties of Laminated Composites.* Nasa Faculty Fellowship Program Report, 2002.
57. Becker, W., *Closed-Form Solution for the Free-Edge Effect in Cross-Ply Laminates.* Composite Structures, 1993. **26**: p. 39-45.
58. Chang, C.C., et al., *Continuous Strain Finite-Element Analysis of Free-Edge Effect in Laminated Composites Specimens.* Journal of Composite Technology and Research, 1988. **10**: p. 54-64.
59. Isakson, G. and A. Levy, *Finite-Element Analysis of Interlaminar Shear in Fibrous Composites.* Journal of Composite Materials, 1971. **5**: p. 273-276.
60. Rybicki, E.F., *Approximate Three-Dimensional Solutions for Symmetric Laminates Under In-Plane Loading.* Journal of Composite Materials, 1971. **5**: p. 354-360.
61. Spilker, R.L., *A Traction-Free-Edge Hybrid-Stress Element for the Analysis of Edge Effects in Cross-Ply Laminates.* Composite Structures, 1980. **12**: p. 167-179.
62. Wang, A.S.D. and F.W. Crossman, *Some New Results on Edge Effect in Symmetric Composite Laminates.* Journal of Composite Materials, 1977. **11**: p. 92-106.
63. Wang, A.S.D. and F.W. Crossman, *Calculation of edge stresses in multi-layer laminates by substructuring.* Journal of Composite Materials, 1978. **12**: p. 76-83.
64. Wang, S.S. and I. Choi, *Boundary-Layer Effects in Composite Laminates: Part 2 - Free-Edge Stress Solutions and Basic Characteristics.* Journal of Applied Mechanics, 1982. **49**: p. 549-560.
65. Huang, S.L., R.J. Richey, and E.W. Deska, *Cross Reinforcement in a GR/EP Laminate.* American Society of Mechanical Engineers, Winter Annual Meeting, San Fracisco, California; United States; 10-15 Dec 1978(5).
66. Mignery, L.A., T.M. Tan, and C.T. Sun, *The Use of Stitching to Suppress Delamination in Laminated Composites.* Dealmination and Debonding. ASTM STP 876, W. S. Johnson, Ed., American Society for Testing and Materials, Philadelphia, United States, 1985: p. 371-385.

67. Chung, W.C., et al., *Fracture Behaviour in Stitched Multidirectional Composites.* Materials Science and Engineering, 1989. **A112**: p. 157-173.
68. Lee, C. and D. Liu, *Tensile Strength of Stitching Joint in Woven Glass Fabrics.* Journal of Engineering Materials and Technology, 1990. **112**: p. 125-130.
69. Dransfield, K., C. Baillie, and Y.-W. Mai, *Improving the Delamination Resistance of CFRP by Stitching - A Review.* Composites Science and Technology, 1994. **50**: p. 305-317.
70. Guenon, V.A., T.-W. Chou, and J.W.G. Jr, *Toughness Properties of a Three-Dimensional Carbon-Epoxy Composite.* Journal of Materials Science, 1989. **24**: p. 4168-4175.
71. Farley, G.L., B.T. Smith, and J. Maiden, *Compression Response of Thick Layer Composite Laminates with Through-the-Thickness Reinforcement.* Journal of Reinforced Plastics and Composites, 1992. **11**: p. 787-810.
72. Farley, G.L. and L.C. Dickinson, *Removal of Surface Loop from Stitched Composites Can Improve Compression and Compression-After-Impact Strengths.* Journal of Reinforced Plastics and Composites, 1992. **11**: p. 633-642.
73. Partridge, I.K. and D.D.R. Cartié, *Delamination Resistant Laminates by Z-Fiber® Pinning: Part I Manufacture and Fracture Performance.* Composites: Part A, 2005. **36**: p. 55-64.
74. Barrett, D.J., *The Mechanics of Z-Fiber Reinforcement.* Composite Structures, 1996. **36**: p. 23-32.
75. Dell'Anno, G., et al., *Exploring Mechanical Property Balance in Tufted Carbon Fabric/Epoxy Composites.* Composites: Part A, 2007. **38**(11): p. 2366-2373.
76. Hull, D. and T.W. Clyne, *An Introduction to Composite Materials: Second Edition.* Cambridge University Press, Cambridge, UK, 1996: p. 46.
77. Li, W., M. Hammad, and A. El-Shiekh, *Structural Analysis of 3-D Braided Preforms for Composites Part I: The Four-Step Preforms.* Journal of the Textile Institute, 1990. **81**(4): p. 491-514.
78. Tang, Z.X. and R. Postle, *Mechanics of Three-Dimensional Braided Structures for Composite Materials - Part I: Fabric Structure and Fibre Volume Fraction.* Composite Structures, 2000. **49**: p. 451-459.
79. Wang, Y.Q. and A.S.D. Wang, *On the Topological Yarn Structure of 3-D Rectangular and Tubular Braided Preforms.* Composites Science and Technology, 1994. **51**: p. 575-586.
80. Dexter, H.B., *Development of Textile Reinforced Composites for Aircraft Structures.* NASA Langley Research Centre Report, 1998.
81. Leong, K.H., et al., *The Potential of Knitting for Engineering Composites - A Review.* Composites: Part A, 2000. **31**: p. 197-220.
82. Leong, K.H., et al., *An Investigation of the Mechanical Performance of Weft-Knit Milano-Rib Glass/Epoxy Composites.* Composites Science and Technology, 1998. **58**: p. 239-251.
83. Rudd, C.D., M.J. Owen, and V. Middleton, *Mechanical Properties of Weft Knit Glass Fibre/Polyester Laminates.* Composites Science and Technology, 1990. **39**: p. 261-277.

84. Chou, S., H.-C. Chen, and C.-C. Lai, *The Fatigue Properties of Weft-Knit Fabric Reinforced Epoxy Resin Composites.* Composites Science and Technology, 1992. **45**: p. 283-291.
85. Dickinson, L.C., G.L. Farley, and M.K. Hinders, *Prediction of Effective Three-Dimensional Elastic Constants of Translaminar Reinforced Composites.* Journal of Composite Materials, 1999. **33**(11): p. 1002-1029.
86. Grassi, M., X. Zhang, and M. Meo, *Prediction of Stiffness and Stresses in Z-Fibre Reinforced Composite Laminates.* Composites Part A: Applied Science and Manufacturing, 2002. **33**: p. 1653-1664.
87. Naik, R.A., *TEXCAD - Textile Composite Analysis for Design, Version 1.0 User's Manual.* NASA CR 4639, 1994.
88. Naik, R.A., *Micromechanical Combined Stress Analysis-Micstran, A User Manual.* NASA CR 189694, 1992.
89. Naik, R.A. and J.H.J. Crews, *Closed-Form Analysis of Fiber-Matrix Interface Stresses Under Thermo-Mechanical Loadings.* NASA TM 107575, 1992.
90. Sun, C.T. and R.S. Vaidya, *Prediction of Composite Properties from a Representative Volume Element.* Composites Science and Technology, 1996. **56**: p. 171-179.
91. Lin, C.J. and W.S. Chan, *Stiffness of Composite Laminates with Z-fibre Reinforcement.* Proceedings of AIAA/ASME/ASCE/AHS/ASC Structures, Structural Dynamics and Materials Conference. St Louis MO, Paper No. AIAA-99-1294, 1999: p. 918-924.
92. Hu, F.Z. and C. Soutis, *Interlaminar Stresses in Composite Laminates with a Circular Hole.* Composite Structures, 1997. **37**: p. 223-232.
93. Troulis, E., *Effect of Z-Fiber® Pinning on the Mechanical Properties of Carbon Fibre/Epoxy Composites.* PhD Thesis, 2003.
94. Steeves, C.A. and N.A. Fleck, *In-Plane Properties of Composite Laminates with Through-Thickness Pin Reinforcement.* International Journal of Solids and Structures, 2006. **43**: p. 3197-3212.
95. Lomov, S.V., et al., *Meso-FE Modelling of Textile Composites: Road Map, Data Flow and Algorithms.* Composites Science and Technology, 2007. **67**: p. 1870-1891.
96. Chamis, C.C., *Mechanics of Composite Materials: Past, Present and Future.* Journal of Composites Technology and Research, 1989. **11**(1): p. 3-14.
97. Hashin, Z., *Analysis of Properties of Fibre Reinforced Composites with Anisotropic Constituents.* Journal of Applied Mechanics, 1979. **46**: p. 543-550.
98. Hashin, Z., *Analysis of Composite Materials - A Survey.* Journal of Applied Mechanics, 1983. **50**: p. 481-506.
99. Hashin, Z. and B.W. Rosen, *The Elastic Moduli of Fibre Reinforced Materials.* Journal of Applied Mechanics, 1964. **31**: p. 223-232.
100. Bogdanovich, A.E., *Multi-Scale Modeling, Stress and Failure Analyses of 3-D Woven Composites.* Journal of Materials Science, 2006. **41**(20): p. 6547-6590.
101. Li, S., *Boundary Conditions for Unit Cells from Periodic Microstructures and Their Implications.* Composites Science and Technology, 2008. **68**: p. 1962-1974.

102. Li, S., *General Unit Cells for Micromechanical Analyses of Unidirectional Composites.* Composites Part A, 2001. **32**: p. 815-826.
103. Agarwal, B.D. and L.J. Broutman, *Three-Dimensional Finite Element Analysis of Spherical Particle Composites.* Fibre Science and Technology, 1974. **7**: p. 63-77.
104. Banks-Sills, L., V. Leiderman, and D. Fang, *On the Effects of Particle Shape and Orientation on Elastic Properties of Metal Matrix Composites.* Composites Part B, 1997. **28**(465-481).
105. Bao, G., J.W. Hutchinson, and R.M. McMeeking, *Particle Reinforcement of Ductile Matrices Against Plastic Flow and Creep.* Acta Metallurgica et Materialia, 1991. **39**: p. 1871-1882.
106. Meijer, M., F. Ellyin, and Z. Xia, *Aspects of Residual Stress/Strain in Particle Reinforced Metal Matrix Composites.* Composites Part B, 2000(29-37).
107. Suzuki, T. and P.K.L. Yu, *Complex Elastic Wave Band Structures in Three-Dimensional Periodical Elastic Media.* Mechanics and Physics of Solids, 1998. **46**: p. 115-138.
108. Weissenbek, E., H.J. Bohm, and R.G. Rammerstorfer, *Micromechanical Investigations of Arrangement Effects in Particle Reinforced Metal Matrix Composites.* Computational Materials Science, 1994. **3**: p. 263-278.
109. Tang, X. and J.D. Whitcomb, *General Techniques for Exploiting Periodicity and Symmetries in Micromechanics Analysis of Textile Composites.* Journal of Composite Materials, 2003. **37**: p. 1167-1189.
110. Whitcomb, J., C.D. Chapman, and X. Tang, *Derivation of Boundary Conditions for Micromechanics Analyses of Plain and Satin Woven Composites.* Journal of Composite Materials, 2000. **34**: p. 724-747.
111. Li, S. and A. Wongsto, *Unit Cells for Micromechanical Analyses of Particle-Reinforced Composites.* Mechanics of Materials, 2004. **36**: p. 543-572.
112. Li, S., *On the Unit Cell for Micromechanical Analysis of Fibre-Reinforced Composites.* Proceedings of the Royal Society, A, 1999. **455**: p. 815-838.
113. Chamis, C.C. and G.P. Sendeckyj, *Critique on Theories Predicting Thermoelastic Properties of Fibrous Composites.* Journal of Composite Materials, 1968. **2**: p. 332-358.
114. Halpin, J.C., *Primer on Composite Materials Analysis (2nd edition).* Technomic Publishing Co., Inc., Lancaster Basel, 1992: p. 153-192.
115. McCullough, R.L., *Micro-Models for Composite Materials - Continuous Fiber Composites, Micromechanical Materials Modelling., Delaware Composites Design Encyclopedia.* Technomic Publishing Co., Inc., Lancaster Basel, 1990. **2**.
116. Reuss, A., *Berechnung der fließgrenze von mischkristallen auf grund den konstanten des einkristalls.* Z. Angew. Math. Mech, 1929. **9**(49).
117. Voigt, W., *Lehrbuch der kristallphysik.* Berlin. Teubner, 1928.
118. Hill, R., *Elastic Properties of Reinforced Solids: Some Theoretical Principles.* Journal of Mechanics and Physics of Solids, 1963. **11**: p. 357-372.
119. Thompson, L., A.S. Kaddour, and S. Li, *Use of Upper and Lower Bound Theorem for 3D Stitched Composites.* Presented at the 2nd ECCOMAS Thematic Conference on the Mechanical Response of Composites (Composites 2009), 2009.

120. Huang, Z.-M., *Simulation of the Mechanical Properties of Fibrous Composites by the Bridging Micromechanics Model.* Composites Part A, 2001. **32**: p. 143-172.
121. Huang, Z.-M., *A Unified Micromechanical Model for the Mechanical Properties of Two Constituent Composite Materials. Part I: Elastic Behaviour.* Journal of Thermoplastic Composite Materials, 2000. **13**(4): p. 252-271.
122. Walpole, L.J., *On Bounds for the Overall Elastic Moduli of Inhomogeneous Systems - I.* Journal of Mechanics and Physics of Solids, 1966. **14**: p. 151-162.
123. Walpole, L.J., *On Bounds for the Overall Elastic Moduli of Inhomogeneous Systems - II.* Journal of Mechanics and Physics of Solids, 1966. **14**: p. 289-301.
124. Brown, W.F., *Solid Mixture Permittivities.* Journal of Chemical Physics, 1955. **23**(8): p. 1514-1517.
125. Hashin, Z. and S. Shtrikman, *Note on a Variational Approach to the Theory of Composite Elastic Materials.* Journal of the Franklin Institute, 1961. **271**: p. 336-341.
126. Hashin, Z. and S. Shtrikman, *On Some Variational Principles in Anisotropic and Nonhomogeneous Elasticity.* Journal of Mechanics and Physics of Solids, 1962. **10**: p. 335-342.
127. Hashin, Z. and S. Shtrikman, *A Variational Approach to the Theory of the Elastic Behaviour of Multiphase Materials.* Journal of Mechanics and Physics of Solids, 1963. **11**: p. 127-140.
128. Chang, D.C. and G.J. Weng, *Elastic Moduli of Randomly Oriented, Chopped-Fibre Composites with Filled Resin.* Journal of Materials Science, 1979. **14**: p. 2183-2190.
129. Šejnoha, M. and J. Zeman, *On Adequacy of the Hashin-Shtrikman Variational Principles Applied to Polymer Matrix Based Random Fibrous Composites.* VIII International Conference on Computational Plasticity, Barcelona 2005, 2005.
130. Eshelby, J.D., *The Determination of the Elastic Field of an Ellipsoidal Inclusion, and Related Problems.* Proceedings of the Royal Society, A, 1957. **241**: p. 376-396.
131. Hill, R., *Progress in Applied Mechanics.* Prager Anniversary Volume, MacMillan, 1963: p. 99.
132. Love, A.E.H., *A Treatise on the Mathematical Theory of Elasticity (Fourth Edition).* Dover Publications, New York, 1944: p. 245.
133. Walpole, L.J., *The Elastic Field of an Inclusion in an Anisotropic Medium.* Proceedings of the Royal Society, A, 1967. **300**(1461): p. 270-289.
134. Mouritz, A.P., K.H. Leong, and I. Herszberg, *A Review of the Effect of Stitching on the In-Plane Mechanical Properties of Fibre-Reinforced Polymer Composites.* Composites Part A, 1997. **28A**: p. 979-991.
135. Herszberg, I. and M.K. Bannister, *Tensile Properties of Thin Stitched Carbon/Epoxy Composites, In.* Proceedings of the 5th Aust. Aero. Conference, March, 1993: p. 213-218.
136. Farley, G.L., *A Mechanism Responsible for Reducing Compression Strength of Through-the Thickness Reinforced Composite Material.* Journal of Composite Materials, 1992. **26**: p. 1784-1795.

137. Partridge, I.K. and D.D.R. Cartié, *Delamination Resistant Laminates by Z-Fibre® Pinning: Part I Manufacture and Fracture Performance.* Composites Part A, 2005. **36**: p. 55-64.
138. Mouritz, A.P. and B.N. Cox, *A Mechanistic Interpretation of the Comparative In-Plane Mechanical Properties of 3D Woven, Stitched and Pinned Composites.* Composites: Part A, 2010. **41**: p. 709-728.
139. Lau, W.S., W.B. Lee, and S.Q. Pang, *Pulsed Nd:YAG Laser Cutting of Carbon Fibre Composite Materials.* Annals of the CIRP, 1990. **39**(1): p. 179-182.
140. Soden, P.D., M.J. Hinton, and A.S. Kaddour, *Lamina Properties, Lay-up Configurations and Loading Conditions for a Range of Fibre-Reinforced Composite Laminates.* Composites Science and Technology, 1998. **58**: p. 1011-1022.
141. ASTM-D-695, *Standard Test Method for Compressive Properties of Rigid Plastics.* 1996.
142. King, T.R., et al., *Micromechanics Prediction of the Shear Strength of Carbon Fibre/Epoxy Matrix Composites: The Influence of the Matrix and Interface Strengths.* Journal of Composite Materials, 1992. **4**: p. 558-573.
143. Daniel, I.M. and J.W. Lee, *Progressive Transverse Cracking of Crossply Composite Laminates.* Journal of Composite Materials, 1990. **24**: p. 1225-1243.
144. Sun, C.T. and S.G. Zhou, *Failure of Quasi-Isotropic Laminates with Free Edges.* Journal of Reinforced Plastics and Composites, 1988. **7**: p. 515-557.
145. Mao, T.H. and M.J. Owen, *Through-the-Thickness Tensile Strength of Fiber-Reinforced Plastics.* Composite Materials: Testing and Design, (Sixth Conference). ASTM STP 787, I. M. Daniel. Ed., American Society for Testing and Materials, 1982: p. 5-18.
146. Hiel, C.C., M. Sumich, and D.P. Chappell, *A Curved Beam Test Specimen for Determining the Interlaminar Tensile Strength of a Laminated Composite.* Journal of Composite Materials, 1991. **25**: p. 854-868.
147. Jackson, W.C. and R.H. Martin, *An Interlaminar Strength Specimen.* Composite Materials: Testing and Design (Eleventh Volume), ASTM STP 1206, E. T. Camponeschi, Jr., Ed., American Society for Testing and Materials, Philadelphia, 1993: p. 333-354.
148. Wisnom, M.R. and M.I. Jones, *A Comparison Between Interlaminar and In-Plane Shear of Unidirectional Glass Fibre-Epoxy.* Advanced Composite Letters, 1994. **3**(2).
149. Avva, V.S., H.G. Allen, and K.N. Shivakumar, *Through-the-Thickness Tension Strength of 3-D Braided Composites.* Journal of Composite Materials, 1996. **30**(1): p. 51-68.
150. Cui, W., et al., *Interlaminar Tensile Strength (ILTS) Measurement of Woven Glass/Polyester Laminates Using Four-Point Curved Beam Specimen.* Composites Part A, 1996. **27**: p. 1097-1105.
151. Martin, R.H. and G.N. Sage, *Prediction of the Fatigue Strength of Bonded Joints Between Multi-Directional Laminates of CFRP.* Composite Structures, 1986. **6**: p. 141-163.
152. Lagace, P.A. and D.B. Weems, *A Through-the-Thickness Strength Specimen for Composites.* Test Methods for Design Allowables for Fibrous Composites:

2nd Volume, ASTM STP 1003, C. C. Chamis, Ed., American Society for Testing and Materials, Philadelphia, 1989: p. 197-207.
153. Abot, J.L. and I.M. Daniel, *Through-Thickness Mechanical Characterization of Woven Fabric Composites.* Journal of Composite Materials, 2004. **38**(7): p. 543-553.
154. Karkkainen, R.L., P. Moy, and J.T. Tzeng, *Through-Thickness Property Measurement of Three-Dimensional Textile Composites.* Army Research Laboratory Report ARL-TR-4765, 2009.
155. Whitney, J.M. and C.E. Browning, *On Short-Beam Shear Tests for Composite Materials.* Experimental Mechanics, 1985. **25**(3): p. 294-300.
156. Post, D., et al., *Interlaminar Shear Moduli of Cross-Ply Laminates: An Experimental Analysis.* Journal of Composite Materials, 1989. **23**: p. 264-279.
157. Tsai, C.L. and I.M. Daniel, *Determination of In-Plane and Out-of-Plane Shear Moduli of Composite Materials.* Experimental Mechanics, 1990. **30**: p. 395-299.
158. Gipple, K. and D. Hoyns, *Measurement of the Out-of-Plane Shear Response of Thick Section Composite Materials Using the V-notched Beam Specimen.* Naval Surface Warfare Center: Survivability, Structures, and Materials Directorate Technical Report, 1993.
159. Eshelby, J.D., *The Elastic Field Outside an Ellipsoidal Inclusion.* Proceedings of the Royal Society, A, 1959. **252**: p. 561-569.
160. Sokolnikoff, I.S., *Mathematical Theory of Elasticity (Second Edition).* McGraw Hill, New York, 1956: p. 337.
161. MacMillan, W.D., *The Theory of Potential.* McGraw Hill, New York, 1930.

Appendices

Appendix 1 – Summary of Through-Thickness Tensile Experimental Data Available in the Literature

Table A-1: Summary of through-thickness tensile test data

Indirect Tensile Testing								
Mao and Owen[145] (1982)	Diametrally Compressed Disc 2, 3, 4 and 6mm thick 20, 30 and 40mm diameters	Woven Roving Glass fabric Y920/625MV H Disks (40mm) V Disks (40mm) C0 Disks (20mm) C90 Disks (20mm)	 9.21 9.09 10.24 11.52	 - - - -	 - - - -	 - - - -	-	Studied the effect of disc diameter and thickness on strength results. No clear effect was seen.
Hiel *et al*[146] (1991)	Circuler C-Section Thickness = 0.914cm Depth = 2.54cm Flat section length = 1.91cm Circular section length = 3.07cm Total height = 6.1cm Circular Scarfed C-Section Depth at C-Section = 0.6cm Elliptical C-Section Specimens Thickness = 0.279cm Flat section length = 2.54cm Elliptical section length = 5.08cm Total height = 4.01cm	G40-600/5245C carbon/epoxy pre-pregs Circular C-Section Circular Scarfed C-Section "Weak" "Strong" T300/934 carbon/epoxy pre-preg Elliptical C-Section	 36.85 (23) 57.95 (7.6) 32.49 (11.8) 107.6 (9.8)	 - - - -	 - - - -	 - - - -	Failure occurred as delamination through the curved section. Failure was said to initiate from material defects such as voids. Speculated that only a small section of the elliptical specimens is subject to an interlaminar tensile stress which may have raised the strength.	'Scarfed' specimens used to reduce scatter of results. These specimens formed a 'weak' group and a 'strong' group which was attributed to the quality of the material in the specimens. Elliptical specimens used to reduce the thickness through the gauge length. Also included a study of moisture effects and fatigue testing.

Jackson and Martin[147] (1993)	L-Section Specimen Width (w) = 12.7/25.4mm Arm Length (L) = 25.4, 50.8mm Thickness = 1.96, 3.35, 3.36, 3.66, 6.61mm Inner Radius (r) = 5, 3.2, 8.5mm Plies (P) = 16, 24, 48	AS4/3501-6 carbon/epoxy Plies: 16 r = 5, L = 25.4 w = 12.7 r = 5, L = 25.4 w = 25.4 Plies: 24 r = 3.2, L = 25.4 w = 12.7 r = 3.2, L = 25.4 w = 25.4 r = 5, L = 25.4 w = 12.7 r = 5, L = 25.4 w = 25.4 r = 5, L = 50.8 w = 12.7 r = 5, L = 50.8 w = 25.4 r = 8.5, L = 25.4 w = 12.7 r = 8.5, L = 25.4 w = 25.4 Plies: 48 r = 5, L = 25.4 w = 12.7 r = 5, L = 25.4 w = 25.4	 81.4 (13.3) 81.1 (16.2) 75.5 (14.3) 47.4 (41.4) 30.0 (20.7) 35.7 (7.3) 37.0 (27.5) 40.8 (15.3) 39.7 (28.8) 29.2 (42.6) 16.7 (5.5) 17.1 (5.3)	 - - - - - - - - - - - -	 - - - - - - - - - - - -	 - - - - - - - - - - - -	In many cases, subcritical damage developed before final failure. This was more prevalent in the wider specimens. Final failure occurred when cracks developed through the centre of the curved section. Cracks were translaminar and discontinuous.	Arm length and specimen width did not greatly effect results but number of plies changed the strength result significantly. It was concluded that this was due to the prevalence of material defects in the thicker specimens.
Wisnom and Jones[148] (1994)	Hump Back Specimen Small Specimen Plies = 16 Total length = 70mm Width = 5mm Hump radius = 4mm Average Hump Thickness = 1.87mm Medium Specimen = Small specimen x 2 Large Specimen = Small specimen x 4	Ciba E glass/913 epoxy Small Medium Large	 109.4 (5.5) 95.1 (10.1) 60.9 (7.1)	 - - -	 - - -	 - - -	Very large deformations were witnessed. Failure was sudden in all cases with delamination occurring in the central curved section. In all specimens one dominant crack was present but secondary cracks and splitting was also noted.	Also conducted short beam shear tests.

Table A-1: Continued

Avva *et al*[149] (1996)	L-Section Specimen Width (w) = 38.1mm Arm Length (L) = 51.2mm Thickness (t) = 2.54mm Inner Radius (r) = 6.4mm	Braided G30-500/123 carbon/epoxy $[0_{12k}/\pm\theta_{12k}]_{45\%axial}$ ($\theta \approx 41°$) AS4/3501-6 carbon/epoxy laminate $[(45/0/-45/0)_4(45/0/-45)]_{47\%axials}$ [0] UD	24.2 28.8 40.9	- - -	- - -	- - -	Free-edge effects cause cracks in the braided and multiaxial specimens resulting in a lower through-thickness tensile failure stress.	The angle ply laminate was designed to be an equivalent laminate to the braided composite.
Cui *et al*[150] (1996)	Hump Back Specimen Plies = 8 and 20 Hump inner radius = 20mm	E-glass chopped strand mat/orthophthalic polyester (20plies) E-glass woven roving/ orthophthalic polyester (8 plies) E-glass woven roving/ isophthalic polyester (8 plies)	9.78 (22) 9.16 (6) 10.91 (15)	- - -	- - -	- - -	Delamination occurred generally near the centre line of the curved section indicating interlaminar tensile failure.	Three failure modes possible; delamination failure (desired), surface fibre fracture and interlaminar shear cracking. Scatter in results was due to voids introduced in the hand lay-up manufacture process.
Lodeiro *et al*[47] (1999)	Semicircular C-section†	T300 UD Carbon Fibre/Epoxy 2x2 Twill Glass Fabric/Epoxy	54 15	- -	- -	- -	Through-thickness tensile failure was only witnessed in the weakest materials which contained many voids and /or defects. Stronger materials showed signs of tensile and shear failure.	Concluded that the C-section specimen is not suitable for materials with a high through-thickness/in-plane strength ratio.

Table A-1: Continued

Direct Tensile Testing								
Mao and Owen[145] (1982)	I-Section Specimen 30x9x40 Dog Bone Specimen Parallel Sided Specimen	Woven Roving Glass fabric Y920/625MV I-Section Specimen Dog Bone Specimen Parallel Sided Specimen Ground Unground	 2.52 1.14 10.89 7.69	 - - - -	 - - - -	 - - - -	-	Comparison between specimens. The I-section and Dog Bone specimens were very weak when handling and in testing. Parallel sided specimen strength results compared well with diametrally compressed discs. Grinding of the parallel sided specimen surfaces increased the apparent strength.
Kitching *et al*[52] (1984)	Dog Bone Specimen Flat Waisted Specimen	E glass mat Dog Bone Specimen E glass CSM Dog Bone Specimen Flat Waisted Specimen	 - 8.76 9.04	 10.294 5.254 4.978	 - 0.173 0.18	 - - -	-	Also tested specimens under compression, torsion and 3 and 4 point bending.
Martin and Sage[151] (1986)	Waisted Specimen Height = 48mm Fillet radius = 125mm	914C-XAS pre-preg carbon/epoxy $[\pm 45/0/90]_{2s}$	 75	 -	 -	 -	Failure commonly occurred at the bond line between the specimen and the end blocks due to the difference in Poisson's ratios.	Study included static and fatigue strengths in the transverse direction as well as short beam shear fatigue tests.

Table A-1: Continued

Lagace and Weems[152] (1989)	Waisted Specimen Height = 13.4mm End tab: 12.7x12.7x1.93mm Gauge length: 6.25x6.25x3.18mm Fillet radius = 3.18mm	AS4/3501-6 $[0]_{100}$ $[0/90]_{25s}$ $[\pm45]_{25s}$	 41.0 (9.6) 43.3 (18.1) 45.3 (13.5)	 - - -	 - - -	 - - -	No fibre breakage reported. Fracture was generally limited to one ply and where it was across two plies the jump between plies was through a transverse matrix crack.	Tested to observe the effect of stacking sequence on through-thickness tensile strength. Also reported the transverse strength.
Roy and Kim[51] (1994)	Dog Bone Specimen Length = 50.8mm Parallel Sided Specimen Length = 50.8mm Width = 6.35mm Thicknesses: 1.02, 1.4, 2.54, 5.75mm	AS4/3501-6 Carbon/Epoxy [0/90] Dog Bone Specimen r=3.7§ r=6.3§ Parallel Sided Specimen t=1.02 t=1.4 t=2.54 t=5.75 [0/90/±45] Dog Bone Specimen r=3.7§ r=6.3§ Parallel Sided Specimen t=1.02 t=1.4 t=2.54 t=5.75	 51 46 47.5 60 52 39 55 46 55 55 42 42	 - - 12.98* 13.04* 12.93* 12.93* - - 12.93* 12.93* 13.86* 13.80*	 - - - 0.09 0.088 0.085 - - - 0.055 0.060 0.070	 - - - - - - - - - - - -	Free-edge effects were concluded to be present in the quasi-isotropic laminates resulting in lower E_3 values for specimens with lower thickness. Images show that fracture was limited to one or a few plies implying that matrix failure had occurred.	Studied the effects of specimen thickness. Compared strength values provided by rectangular and circular cross-section specimens.

Table A-1: Continued

Ferguson *et al*[54] (1998)	RARDE waisted specimen Height = 38mm End tab: 25x25x4mm Gauge length: 16x10x12mm Radius section: Long side, height=9mm radius = 9mm Short side, Height = 9mm Radius = 12mm	T300 Carbon/Epoxy pre-preg [0] E-G/Epoxy UD filament wound [0] E-G/Epoxy woven pre-preg [0/90] E-G/Epoxy woven fabric [0/90] E-G/Polyester random chopped filaments	70.7 (8.1) 16.7 (9.3) 61.2 (8.8) 36.0 8.2 (15)	9.52 (0.7) 23.3 (2.7) 10.2 (2.2) 11.2 5.3 (8.3)	0.011 (15) 0.101 (8.2) 0.17 (6.4) 0.18 0.25 (18)	0.47 (2.7) 0.32 (1.9) 0.16 (5.5) 0.17 0.21 (25)	Fracture always within or at one end of the gauge length in a single plane perpendicular to the gauge length.	Specimen was fragile and in the case of the E-G/Epoxy woven fabric only two specimens remained and as a result a CoV value was not calculated.
Lodeiro *et al*[47] (1999)	Parallel sided short blocks – heights: 40mm and 20mm† Circular waisted block – height: 40mm† I-Section specimens	T300 UD Carbon Fibre/Epoxy Parallel Block (40mm) Parallel Block (20mm) Circular Waisted Block (40mm) Chopped Strand Mat Parallel Block (40mm) Circular Waisted Block (40mm) 2x2 Twill Glass Fabric/Epoxy Parallel Block (40mm) Circular Waisted Block (40mm) Discontinuous Glass Fibre/Nylon 66 Parallel Block (20mm) I-Section Random Glass Fibre Mat/Polypropylene Parallel Block (20mm) I-Section	- - 71±6.0 - 9.1±2.0 - 41±8.0 - 69±7 - 5.7±1.6	9.9±0.1 9.9±0.4 - 6.3 - 11.0±0.4 - 4.4±0.1 - 3.5±0.2 -	0.019±0.002 0.020±0.002 - 0.23 - 0.19±0.01 - 0.27±0.04 - 0.16±0.04 -	0.55±0.01 0.51±0.01 - 0.23[+] - 0.19±0.001[+] - 0.41±0.02 - 0.16±0.04[+]	Parallel block failed due to a failure at the bond line between the specimen and end blocks in all but the weakest materials. The circular waisted and I-section specimens failed through tension within the gauge length.	Also presented results for through-thickness compression and shear. Parallel sided specimens and circular waisted specimens provided complementary data under tension and compression.

Table A-1: Continued

Mespoulet *et al*[48] (2000)	Parallel Sided Specimen 6x6x6mm 6x6x12mm Elliptical Waisted Specimen Height = 17mm End tab: 8x8x1.5mm Gauge length: 4x4x2mm	T300/914 carbon fibre/epoxy pre-pregs [0] UD	97 (12)	9.8 (2.4)	-	-	-	Special test jig used to avoid uneven loading. Waisted specimen used to obtain strength but no indication as to which specimen was used to obtain the modulus E_3.
Abot and Daniel[153] (2004)	Waisted Specimen	AGP370-5H/3501-6S carbon/epoxy (AS4 carbon fibres) satin weave fabric $[0]_{80}$	59.8	12.8	0.085	0.064	Images show that failure was restricted to one or a few plies indicating that specimens failed through tension.	Compared results with UD AS4/3501-6 showing improvements in all properties except tensile strength.
Karkainnen *et al*[154] (2009)	Cylindrical Specimen Height = 20mm Gauge length diameter = 30mm Fillet radius = 6mm Circular Waisted Specimen Height = 20mm End tab = 30x30mm Gauge length = 25x25mm Fillet radius = 21mm	S2 Glass/5250-4 containing through-thickness stitches Cylindrical pecimen Circular waisted specimen	20.9 27.9 25.4	8.76 11.3 10.3	- - -	- - -	In all cases failure initiated as pullout of stitches due to a bond failure between the stitch and matrix materials. Then the in-plane fibres begin to debond with the matrix.	The cylindrical specimen suffered loading problems due to the clamping mechanism slipping and so produced less consistent results compared to the waisted specimens.

Table A-1: Summary of through thickness tensile test data

Appendix 2 – Summary of Through-Thickness Shear Experimental Data Available in the Literature

Table A-2: Summary of through-thickness shear test data

Author	Specimen Design and Dimensions (length x width x height)	Material/Lay-up	Strength S_{xz} MPa (C_v (%))	Strength S_{yz} MPa (C_v (%))	G_{xz} (GPa) (C_v (%))	G_{yz} (GPa) (C_v (%))	Failure Mode	Notes
Whitney and Browning[155] (1985)	Three point bend specimen Length to height ratio of 4:1 Four point bend specimen Length to height ratios of 16:1 and 8:1 investigated	UD AS-1/3502 graphite/epoxy 3 point bend 16 ply l:h=4:1 50 ply l:h=4:1 4 point bend 16 ply l:h=16:1 24 ply l:h=16:1 UD X-AS/PEEK graphite/PEEK 4 point bend 34 ply l:h=8:1	 102 96 88 81 115	 - - - - -	 - - - - -	 - - - - -	A range of failure modes were presented. Some specimens showed initial damage leading to mixed mode failure and for specimens without initial damage the failure mode was compressive buckling or yielding due to combined compression and shear.	
Post *et al* (1989)[156]	Modified rail shear specimen Length = 38.1mm Width = 5.8mm Thickness = 7.6mm	AS4/5920 graphite/epoxy $[90_2/0]_n$	-	-	3.3	2.4	Specimens not taken to failure	Specimens cut from thick walled cylinders and Moire interferometry used for strain measuring

Tsai and Daniel[157] (1990)	Torsion plate specimen Various length, width and thickness Ply numbers 8, 16 and 32	AS4/3501-6 $[0]_8$ $[0]_{16}$ $[0]_{32}$ $[90]_8$ $[90]_{16}$ $[90]_{32}$ SiC/CAS $[0]_{24}$ $[90]_{24}$	 - - - - - - - -	 - - - - - - - -	 7.11 7.59 6.60 - - - 39.3 -	 - - - 3.54 4.00 3.79 - 31.5	No failure observations given	Formulae required to extract shear moduli. These are presented in the original reference
Hodgkinson and Bertholet[35] (1993)	Iosipescu shear specimen	XAS/913C [0] [90]	 42.6 27.4		 - -	 - -	-	Also measured in-plane shear strength
Gipple and Hoyns[158] (1994)	Iosipescu shear specimen Thickness = 140 plies	AS4/3501-6 [0] strain gauge [0] Moiré/full section gauge [0/90] strain gauge [0/90] Moiré/full section gauge	 - - - -	 32.5 (6) 32.4 (7.9) 91.3 (1.7) 91.4 (1.8)	 - - - -	 2.8 (1) 3.1 (0) 3.9 (1.5) 3.9 (2.5)	Failure mode dependent on the fibre direction	Three strain measurement methods used; strain gauge rosettes, full section gauges and Moiré interferometry
Lodeiro *et al[47]* (1999)	Iosipescu specimen dimensions from.... Double notch shear specimen dimensions from.....	T300 UD Carbon Fibre/Epoxy Iosipescu Double notch 3 point bend	 111±2 75±12 108±6	 64±9 - -	 5.3±0.2 - -	 2.9±0.3 - -	3 point bend shear strength only valid for UD laminates, other materials failed in tension. Other specimens typically failed through shear.	Shear testing is part of a thorough review of through-thickness test methods produced by Lodeiro *et al*

Table A-2: Continued

Lodeiro *et al*[47] (1999) *Continued*	Three point bend specimen dimensions from.....	Chopped Strand Mat Iosipescu Double notch 3 point bend 2x2 Twill Glass Fabric/Epoxy Iosipescu Double notch 3 point bend Discontinuous Glass Fibre/Nylon 66 Iosipescu Double notch 3 point bend Random Glass Fibre Mat/Polypropylene Iosipescu Double notch 3 point bend	 40.7±1.7 38.3±4.7 13.4±3.0 68.4±0.9 64.9±1.8 52.5±0.6 56.9±3.6 66.4±4.8 18.6±0.4 22.7±0.8 18.1±3.3 14.2±1.5	 40.7±1.7 38.3±4.7 13.4±3.0 68.4±0.9 64.9±1.8 52.5±0.6 56.9±3.6 66.4±4.8 18.6±0.4 22.7±0.8 18.1±3.3 14.2±1.5	 1.64±0.09 - - 4.12±0.14 - - 1.68±0.06 - - 1.04±0.04 - -	 1.64±0.09 - - 4.12±0.14 - - 1.68±0.06 - - 1.04±0.04 - -		
Mespoulet *et al*[48] (2000)	Modified rail shear Width = 6mm Thickness = 8mm Lengths = 25 and 16mm Waisted shear Width = 6mm Thickness = 8mm Gauge length = 6mm with 9mm tabs	T300/914 carbon/epoxy UD Rail shear UD waisted	 68 (9.4) 95 (9.8)	 48 (6.5) 70 (2.7)	 5.0 (2.2) -	 3.2 (2.0) -	Waisted specimen shown through FE analysis to be subjected to more pure shear state than the modified rail shear specimen	Waisted specimen loaded at an inclined plane. FE analysis showed that applying a closing force increases the pure shear state.

Table A-2: Continued

DeTeresa *et al* [55] (2004)	Hollow cylinder specimens – Inner diameter = 1.59cm Outer diameter = 2.1cm Fillet radius = 0.635cm Gauge length = 0.635cm	T300/F584 pre-preg $[45/0/-45/90]_{xs}$	53.1 – 62.6	-	-	-	Combined through-thickness compression and interlaminar shear tests showed large amounts of material crushing on the fracture surface. No details given on the failure surface under pure compression.	Study was to observe the effect of applying a constant through-thickness compressive load on the shear strength of composite laminates.
		IM7/8551-7 $[0/90]_{xs}$ @23°C	66.9 – 67.0	-	-	-		
		$[0/90]_{xs}$ @93°C	41.9 – 41.5	-	-	-		
		$[45/0/-45/90]_{xs}$	61.4 – 61.9	-	-	-		
		E-Glass plain-weave fabric-vinyl ester $[90_2/\pm45]_{xs}$	51.1 – 48.6	-	-	-		
		S2-glass/DER-332 $[90_2/\pm45]_{xs}$	25.3 – 24.2	-	-	-		

Table A-2: Summary of through thickness shear test data

Appendix 3 – Raw Through-Thickness Test Data

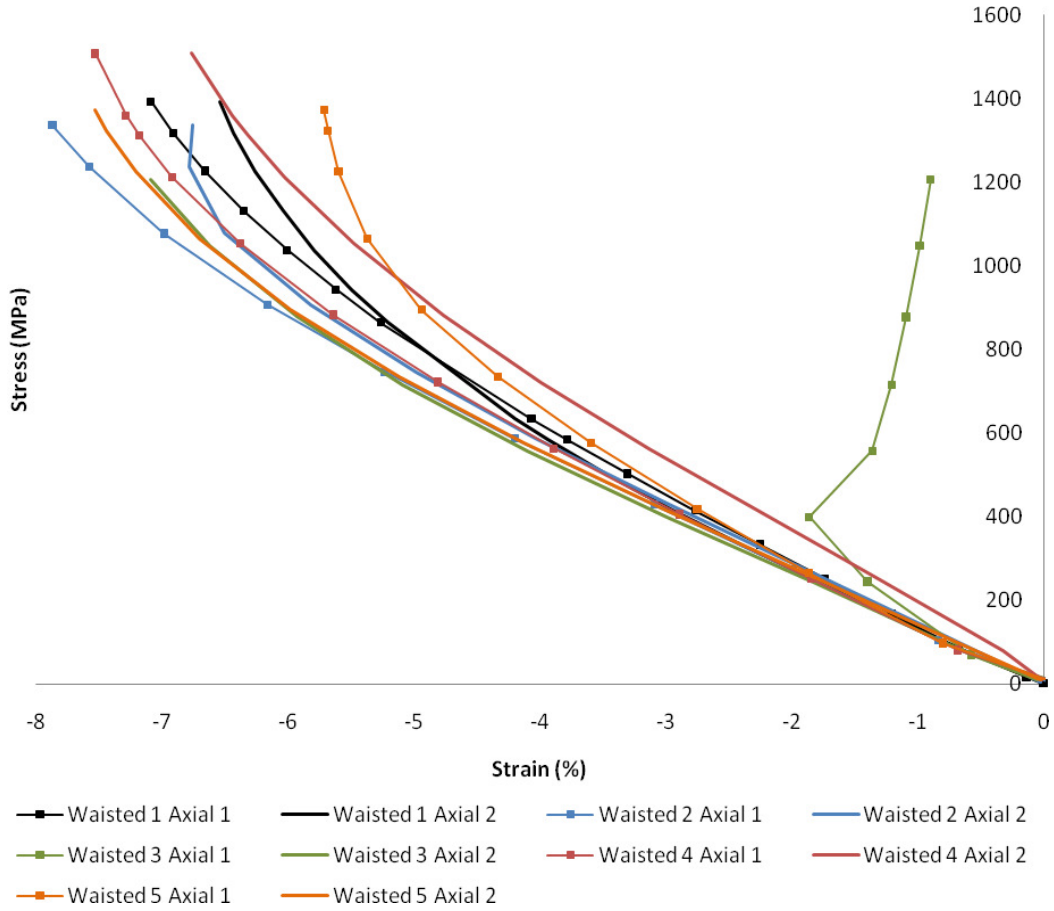

Figure A.3.1: Axial stress-strain curves for all waisted specimens

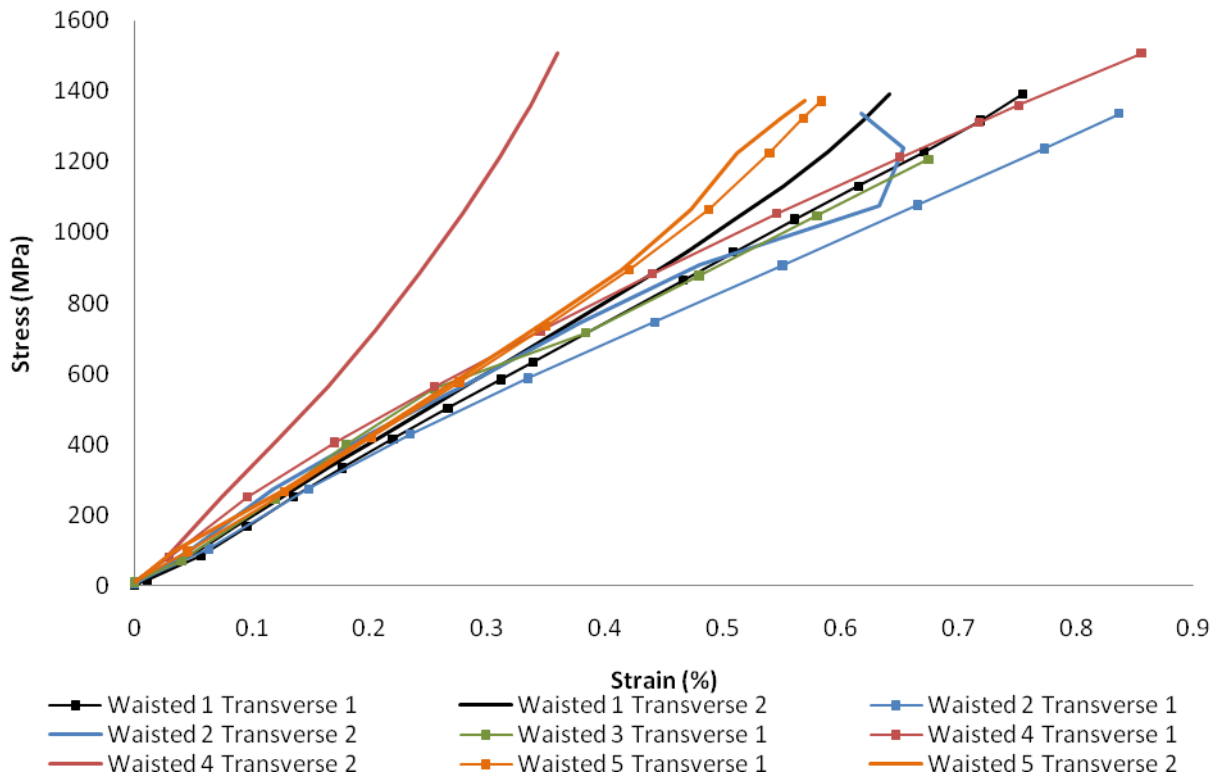

Figure A.3.2: Transverse stress-strain curves for all waisted specimens

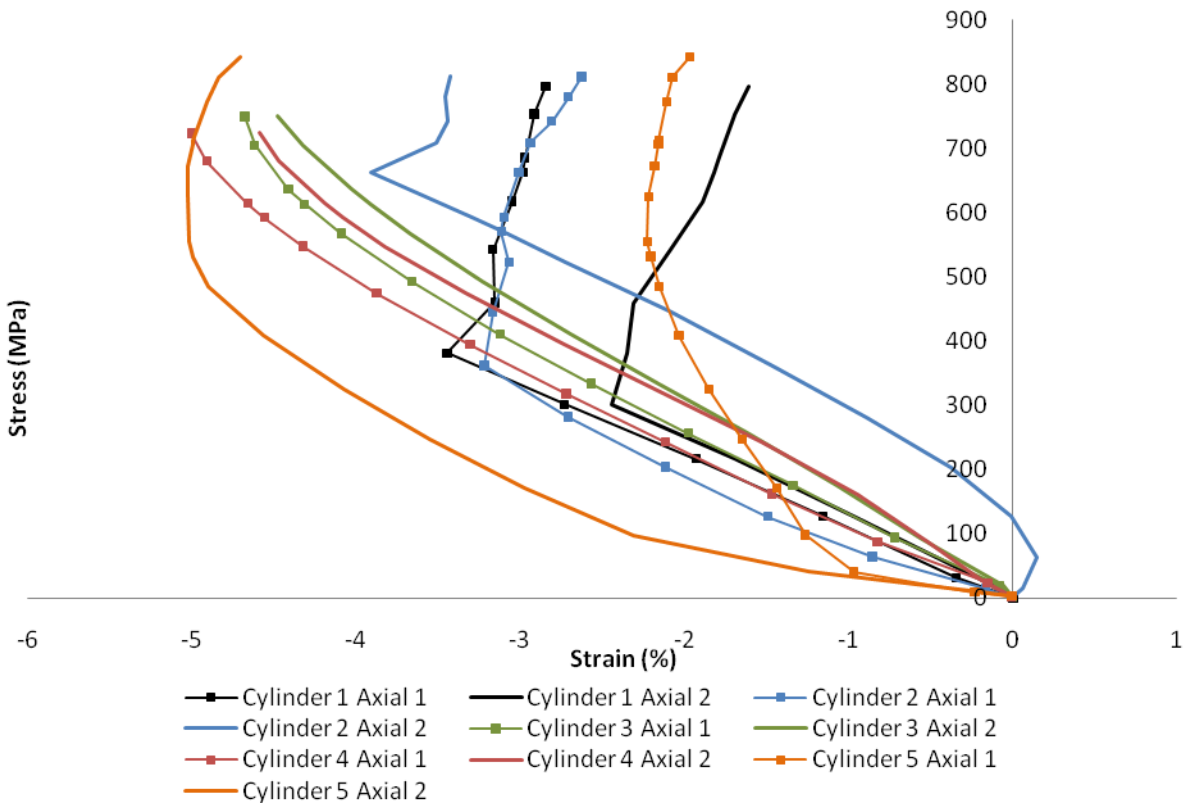

Figure A.3.3: Axial stress-strain curves for all cylindrical specimens

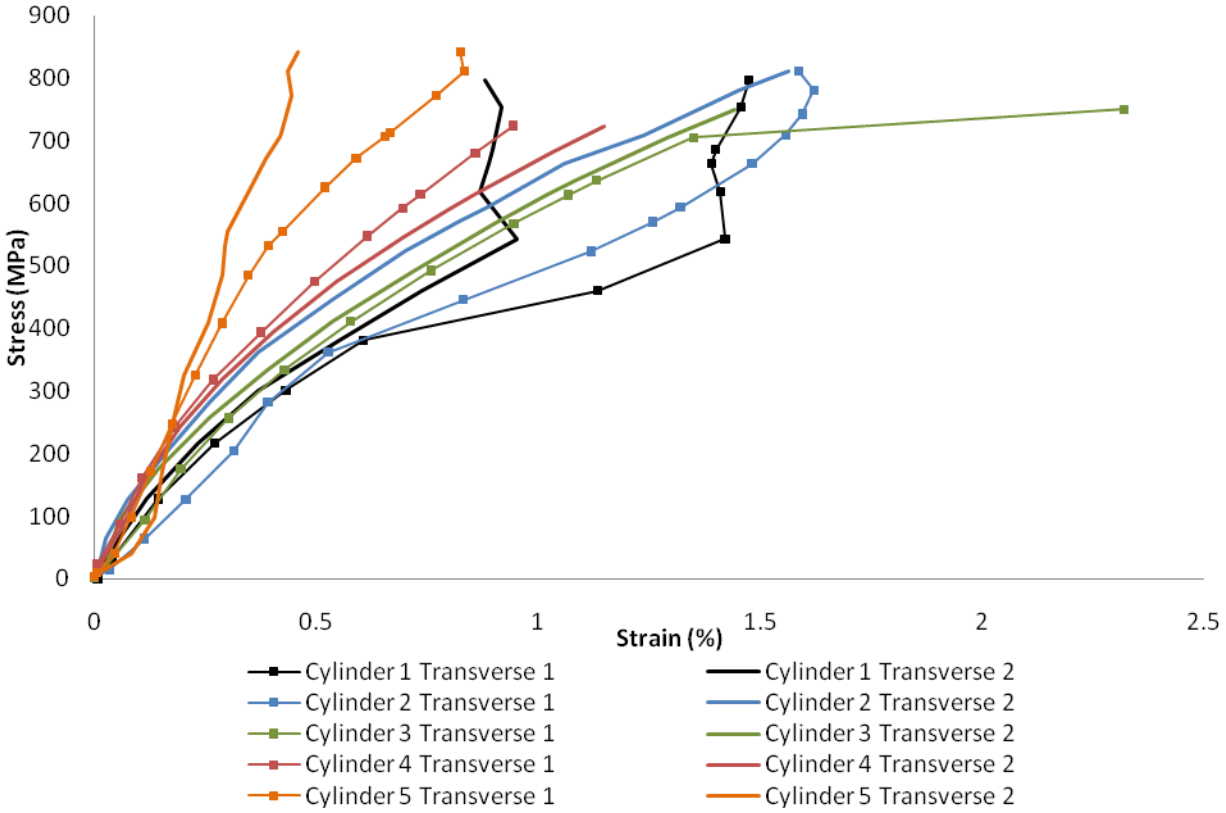

Figure A.3.4: Transverse stress-strain curves for all cylindrical specimens

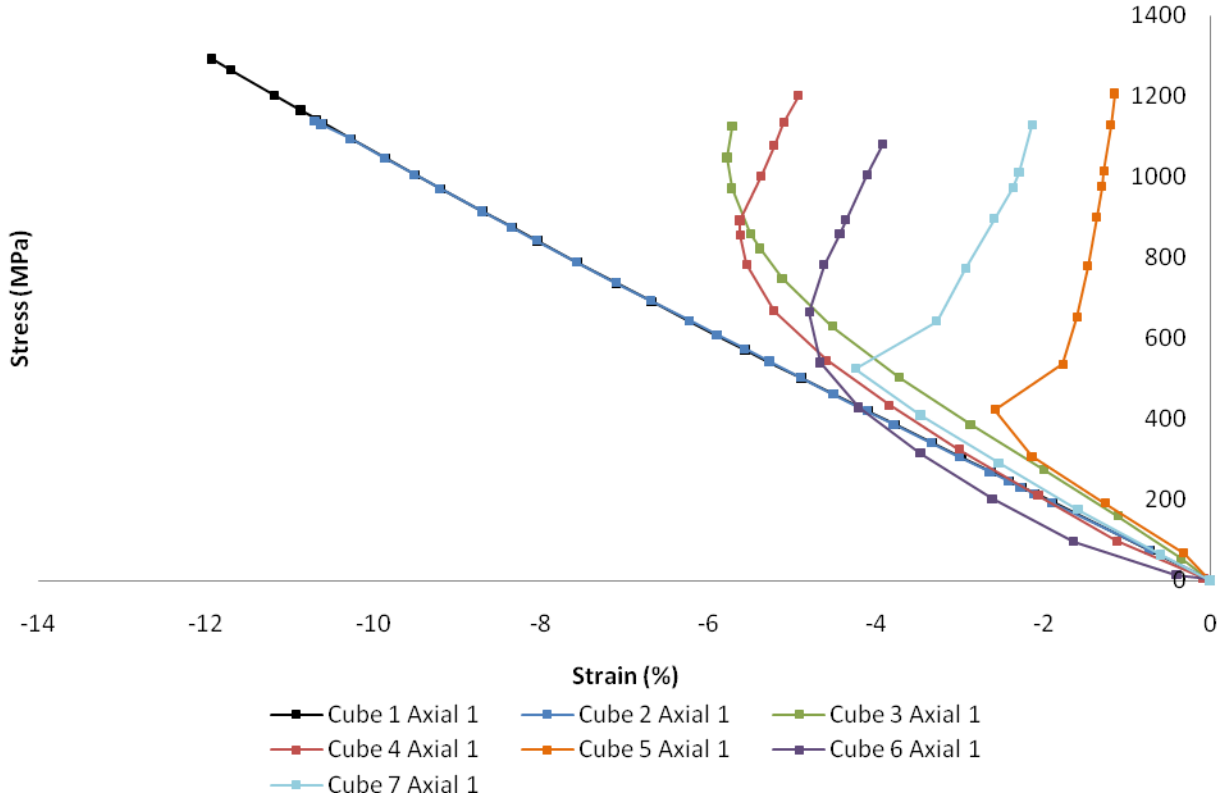

Figure A.3.5: Axial stress-strain curves for all cubic specimens

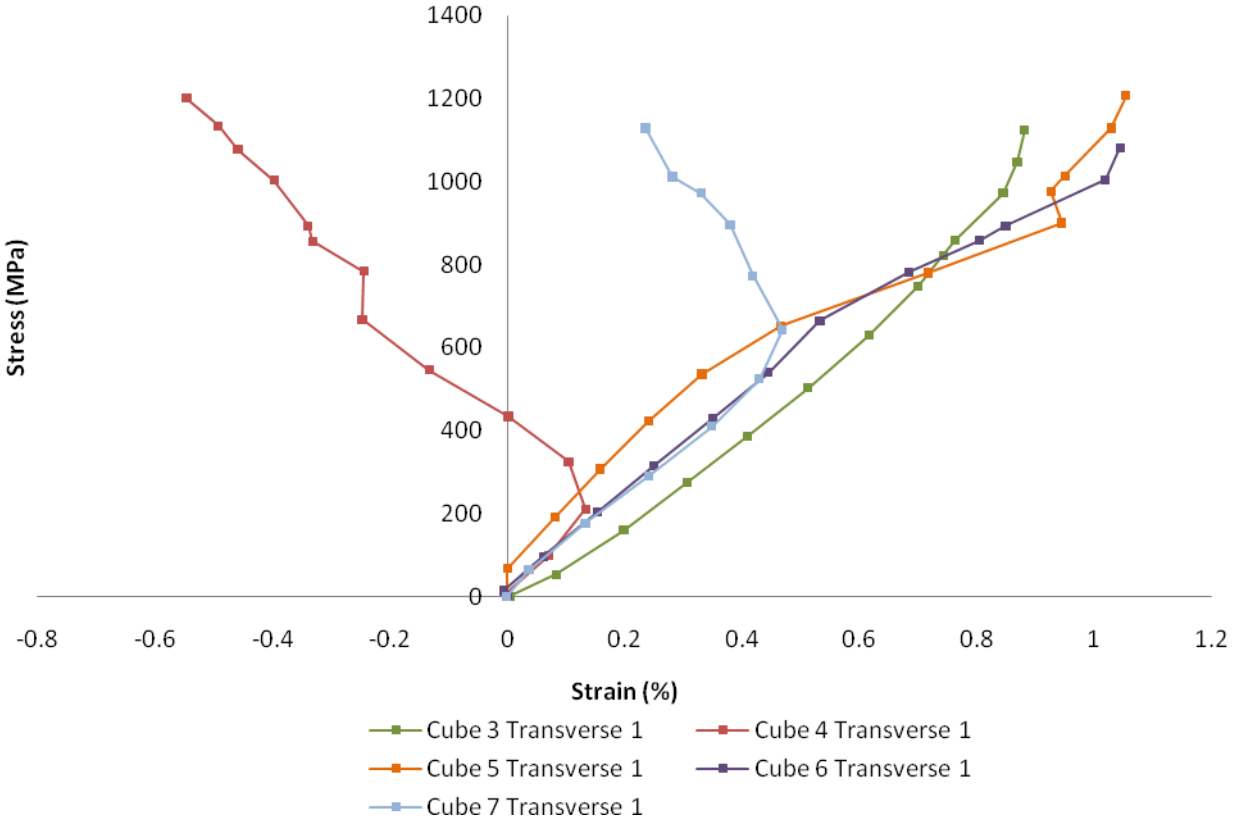

Figure A.3.6: Transverse stress-strain curves for all cubic specimens

Appendix 4 - Derivation of Walpole's Bounds

Walpole's bounds[122, 123] are used in the current study to predict to elastic properties of Z-pinned laminates. Due to the complexity of the derivation and because some parts are skipped over in the original reference a thorough account of the theory is presented here.

As discussed in Chapter 3, two boundary-value problems are stated. In the first a displacement is prescribed over the surface of the considered region. The composite material is replaced by the comparison material and a strain field ε is defined such that $\sigma^*=C_0\varepsilon+\tau$ is self equilibrated.

The second problem is similar but traction is prescribed over the surface of the considered region. A stress field σ is defined in the comparison material so that the strain field $\varepsilon^*=S_0\sigma-\eta$ can be derived from a continuous displacement.

In the present analysis approximate fields are made by choosing polarizations and these are then inserted into classic extremum principles to bound the overall energy; from this the overall moduli can also be bound. It is stated in [123] that piecewise-uniform polarization fields are the most general form from which the required averages can be calculated using the known information and the best values are noted as:

$$\begin{aligned}\tau &= \left(C_r - C_0\right)\bar{\varepsilon}_r, \\ \eta &= \left(S_0 - S_r\right)\bar{\sigma}_r\end{aligned} \qquad \textbf{A3-1}$$

where $\bar{\varepsilon}_r$ and $\bar{\sigma}_r$ are the averages over V_r of ε and σ (The real strain and stress fields within the composite). The fields, σ^* and ε^* are then specified within V_r:

$$\begin{aligned}\sigma^* &= C_0\varepsilon_r + \tau_r = C_0\varepsilon_r + \left(C_r - C_0\right)\bar{\varepsilon}_r = C_r\bar{\varepsilon}_r + C_0\left(\varepsilon_r - \bar{\varepsilon}_r\right) \\ &= C_r\bar{\varepsilon}_r + C_0\varepsilon_r^{'}\end{aligned} \qquad \textbf{A3-2}$$

similarly

$$\varepsilon^* = S_r\bar{\sigma}_r + S_0\sigma_r^{'} \qquad \textbf{A3-3}$$

where $\varepsilon_r^{'} = \varepsilon_r - \bar{\varepsilon}_r$ and $\sigma_r^{'} = \sigma_r - \bar{\sigma}_r$, as explained by Walpole these are the deviations within V_r from the averages of the approximate strain and stress fields.

In the first boundary value problem we let the surface displacement prescribed on the area of interest on the composite be compatible with a uniform strain $\bar{\varepsilon}$. The strain field ε can then be derived from a continuous displacement taking the surface values so that σ^* is self-equilibrated. Then the principles of minimum potential energy and complementary energy are (from Hill[131])

$$2U \le \sum \int_{V_r} \varepsilon_r C_r \varepsilon_r dV_r \qquad \textbf{A3-4}$$

$$2U \geq \int_{V_r} \sigma^* \left(2\bar{\varepsilon} - S_r \sigma^*\right) dV_r \qquad \textbf{A3-5}$$

where *U* is the energy.

As $\bar{\varepsilon}$ (the macroscopic strain field) and ε (the real strain field, i.e. ε_r in phase *r*) are both kinematically admissible strain fields then so is $\left(\bar{\varepsilon} - \varepsilon_r\right)$. The principle of virtual work states that the virtual work of a statically admissible stress field (self-equilibrated) on a kinematically admissible strain field is equal to the work of the external forces on the corresponding displacements. In this case the displacement field which corresponds to the strain field $\left(\bar{\varepsilon} - \varepsilon_r\right)$ has zero values on the boundary i.e. the work of external forces is zero. Therefore

$$\int \sigma^* \left(\bar{\varepsilon} - \varepsilon_r\right) dV = \sum \int_{V_r} \sigma_r^* \left(\bar{\varepsilon} - \varepsilon_r\right) dV_r = 0 \qquad \textbf{A3-6}$$

this can then be added to the right side of A3-4 without changing its value such that

$$A = \sum \int_{V_r} \varepsilon_r C_r \varepsilon_r dV_r = \sum \int_{V_r} \varepsilon_r C_r \varepsilon_r dV_r + \sum \int_{V_r} \left(\bar{\varepsilon} - \varepsilon_r\right) \sigma_r^* dV_r = 0 \qquad \textbf{A3-7}$$

Given that

$$\begin{aligned} \varepsilon_r &= \varepsilon_r' + \bar{\varepsilon}_r, \\ \tau_r &= \left(C_r - C_0\right) \bar{\varepsilon}_r \end{aligned} \qquad \textbf{A3-8}$$

Then:

$$A = \sum \int_{V_r} \left(\varepsilon_r' + \bar{\varepsilon}_r\right) C_r \left(\varepsilon_r' + \bar{\varepsilon}_r\right) dV_r + \sum \int \left(\bar{\varepsilon} - \varepsilon_r' - \bar{\varepsilon}_r\right) \left(C_r \bar{\varepsilon}_r + C_0 \varepsilon_r'\right) dV_r \qquad \textbf{A3-9}$$

Then a rearrangement can be carried out:

$$\begin{aligned} &= \sum \int_{V_r} \left(\varepsilon_r' C_r \varepsilon_r' + 2\varepsilon_r' C_r \bar{\varepsilon}_r + \bar{\varepsilon}_r C_r \bar{\varepsilon}_r + \bar{\varepsilon} C_r \bar{\varepsilon}_r + \bar{\varepsilon} C_0 \varepsilon_r' - \varepsilon_r' C_r \bar{\varepsilon}_r - \varepsilon_r' C_0 \varepsilon_r' - \bar{\varepsilon}_r C_r \bar{\varepsilon}_r - \bar{\varepsilon}_r C_0 \varepsilon_r'\right) dV_r \\ &= \sum \int_{V_r} \left(\varepsilon_r' C_r \varepsilon_r' + \varepsilon_r' C_r \bar{\varepsilon}_r + \bar{\varepsilon} C_r \bar{\varepsilon}_r + \bar{\varepsilon} C_0 \varepsilon_r' - \varepsilon_r' C_0 \varepsilon_r' - \bar{\varepsilon}_r C_0 \varepsilon_r'\right) dV_r \\ &= \sum \int_{V_r} \left(\varepsilon_r' \left(C_r - C_0\right) \varepsilon_r' + \bar{\varepsilon} C_r \bar{\varepsilon}_r + \left(\bar{\varepsilon}_r C_r + \left(\bar{\varepsilon} - \bar{\varepsilon}_r\right) C_0\right) \varepsilon_r'\right) dV_r \end{aligned}$$

A3-10

The third term in the final part of the above now vanishes because

$$\int_{V_r} \left(\bar{\varepsilon}_r C_r + \left(\bar{\varepsilon} - \bar{\varepsilon}_r\right) C_0\right) \varepsilon_r' dV_r = \left(\bar{\varepsilon}_r C_r + \left(\bar{\varepsilon} - \bar{\varepsilon}_r\right) C_0\right) \int_{V_r} \varepsilon_r' dV_r = 0 \qquad \because \quad \int_{V_r} \varepsilon_r' dV_r = 0$$

A3-11

Then one is left with

$$A = \sum \int_{V_r} \left(\varepsilon_r' \left(C_r - C_0\right) \varepsilon_r' + \bar{\varepsilon} C_r \bar{\varepsilon}_r\right) dV_r = -\sum \int_{V_r} \varepsilon_r' \left(C_0 - C_r\right) \varepsilon_r' dV_r + \sum V_r \bar{\varepsilon} C_r \bar{\varepsilon}_r \qquad \textbf{A3-12}$$

Similar to the approach used to obtain A3-7, A3-6 can also be subtracted from A3-5 without affecting the result

$$B = \sum \int_{V_r} \sigma_r^* \left(2\bar{\varepsilon}_r - S_r \sigma_r^*\right) dV = \sum \int_{V_r} \sigma_r^* \left(2\bar{\varepsilon}_r - S_r \sigma_r^*\right) dV - \sum \int \sigma_r^* \left(\bar{\varepsilon} - \varepsilon_r\right) dV \qquad \textbf{A3-13}$$

Then following the same approach as used to obtain A3-12 one is left with

$$B = \sum V_r \bar{\varepsilon} C_r \bar{\varepsilon}_r + \sum \int_{V_r} \varepsilon_r' C_0 \left(S_0 - S_r\right) C_0 \varepsilon_r' dV_r \qquad \textbf{A3-14}$$

Similar operations can be carried out for the second set of boundary value problems where the surface tractions are set to be compatible with a uniform stress $\bar{\sigma}$. The stress field, σ is then in equilibrium with the given tractions and then ε^* is a strain field derived from a continuous displacement. The potential and complementary energy can be rewritten as

$$2U \geq \sum \int_{V_r} \varepsilon^* \left(2\bar{\sigma} - C_r \varepsilon^*\right) dV_r \qquad \textbf{A3-15}$$

$$2U \leq \sum \int_{V_r} \sigma S_r \sigma dV_r \qquad \textbf{A3-16}$$

then using the equality

$$\int \left(\bar{\sigma} - \sigma\right) \varepsilon^* dV = 0 \qquad \textbf{A3-17}$$

and following the approach used to obtain A3-12 and A3-14, one obtains

$$2U \geq \sum V_r \bar{\sigma} S_r \bar{\sigma}_r + \sum \int_{V_r} \sigma_r' S_0 \left(C_0 - C_r\right) S_0 \sigma_r' dV_r \qquad \textbf{A3-18}$$

and $$2U \leq \sum V_r \bar{\sigma} S_r \bar{\sigma}_r - \sum \int_{V_r} \sigma_r' \left(S_0 - S_r\right) \sigma_r' dV_r \qquad \textbf{A3-19}$$

If the considered region is a representative volume then the inequalities will remain true if the surface values of the real and approximating fields are macroscopically compatible with the uniform values as defined in A3-1.

Following Walpole, two concentration factor tensors associated with the approximate fields are defined as

$$\begin{aligned} \bar{\varepsilon}_r &= \bar{A}_r \bar{\varepsilon}, \\ \bar{\sigma}_r &= \bar{B}_r \bar{\sigma} \end{aligned} \qquad \textbf{A3-20}$$

with $\sum c_r \bar{A}_r = I = \sum c_r \bar{B}_r$, where c_r is the constituent volume fraction (V_r/V) and I is a unit tensor with components,

$$I_{ijkl} = \frac{1}{2}\left(\delta_{ik}\delta_{jl} + \delta_{il}\delta_{jk}\right) = \begin{bmatrix} 1 & 0 & 0 & 0 & 0 & 0 \\ 0 & 1 & 0 & 0 & 0 & 0 \\ 0 & 0 & 1 & 0 & 0 & 0 \\ 0 & 0 & 0 & \frac{1}{2} & 0 & 0 \\ 0 & 0 & 0 & 0 & \frac{1}{2} & 0 \\ 0 & 0 & 0 & 0 & 0 & \frac{1}{2} \end{bmatrix} \quad \textbf{A3-21}$$

Next, define tensors $\overline{C}$ and $\overline{S}$

$$\begin{aligned} \overline{C} &= \sum c_r C_r \overline{A}_r, \\ \overline{S} &= \sum c_r S_r \overline{B}_r \end{aligned} \quad \textbf{A3-22}$$

The integrals that remain in A3-12, A3-14, A3-18 and A3-19 were then dropped by Walpole. This is required as they cannot be calculated with the information available. However, bounds on the overall energy can be produced if in one instance the comparison material is chosen such that (C_0-C_r) is semi-positive or semi-negative definite.

From A3-22, A3-12 is given as

$$2U = \overline{\varepsilon} C \overline{\varepsilon} \le -\sum \int_{V_r} \varepsilon_r^{'} \left(C_0 - C_r\right) \varepsilon_r^{'} dV_r + \sum V_r \overline{\varepsilon} C_r \overline{\varepsilon}_r \le \sum V_r \overline{\varepsilon} C_r \overline{\varepsilon}_r = \overline{\varepsilon} \overline{C} \overline{\varepsilon} \quad \textbf{A3-23}$$

if $\left(C_0 - C_r\right)$ is semi positive definite

This leads to the main theorems of Walpole's theory;

If C_0-C_r is (for all r) positive (negative) semi-definite then so is $\overline{C} - C$

If S_0-S_r is (for all r) positive (negative) semi-definite then so is $\overline{S} - S$ **A3-24**

Following from the above, the aim is to obtain the strain field ε, generated by the polarization stress τ. To do this we observe

$$\sigma^*_{ij,j} = C^0_{ijkl}\varepsilon_{kl,j} + \tau_{ij,j} \quad \textbf{A3-25}$$

Here a body force of density $\tau_{ij,j}$ is introduced into the comparison material along with body forces on the discontinuity surfaces i.e. the surfaces between fibre and matrix material. The resulting strain field in the comparison material is

$$\varepsilon = \varepsilon^I + \varepsilon^\dagger \quad \textbf{A3-26}$$

This consists of the strain field produced by the body force distributions $\varepsilon^\dagger$ and a superimposed image field ε^I which ensures that the prescribed surface

displacements are correct. The strain field $\varepsilon^{\dagger}$ produced by the distributions of body force is derived from the displacement

$$u_i^{\dagger}(r) = \int G_{ij}\left[\tau_{jk}\right] n_k dS + \int G_{ij}\tau_{jk,k} dV \qquad \textbf{A3-27}$$

where the comma (,) denotes differentiation.

The surface force $\left[\tau_{ij}\right] n_j$ comes as a result of the equilibrium conditions on the discontinuity surfaces, where [ ] indicates the discontinuity across the interface in the outward normal direction to the inclusion surface n_i. This problem was presented first by Eshelby [130] and was described as the 'subsidiary problem' by Hashin and Shtrikman [126].

To aid in the continuation of the derivation A3-28 can be rewritten as

$$u_i^{\dagger}(r) = \int_{S_r} G_{ij}\left(\tau_{ij}^{+} - \tau_{ij}^{-}\right) n_k dS + \int_{V_r} G_{ij}\frac{\partial \tau_{jk}}{\partial \xi_k} \qquad \textbf{A3-28}$$

the form of the displacement in A3-29 is adjusted by applying Gauss's formula (Divergence theorem) $\int_{\Omega} f_{i,i} d\Omega = \oint_{\partial\Omega} f_i n_i dS$,

$$= \int_{S_r} G_{ij}\tau_{ij}^{+} n_k dS - \left(\int_{S_r} G_{ij}\tau_{ij}^{-} n_k dS - \int_{V_r} G_{ij}\frac{\partial \tau_{jk}}{\partial \xi_k} dV \right) \qquad \textbf{A3-29}$$

$$= \int_{S_r} G_{ij}\tau_{ij}^{+} n_k dS - \left(\int_{V_r} \frac{\partial G_{ij}}{\partial \xi_k}\tau_{jk} dV \right) \qquad \textbf{A3-30}$$

The second term goes to the final expression as all V_r are summed together. The first term is considered as the contribution of the traction on the interface for the matrix phase. When the unit normal is reversed to become outward from the matrix phase, the term changes its sense, acquiring the negative sign required for use the divergence theorem; resulting in

$$u_i^{\dagger}(r) = -\int \frac{\partial G_{ij}}{\partial \xi_k}\tau_{jk} dV \qquad \textbf{A3-31}$$

In the present derivation it is assumed that the comparison material is chosen to be uniform and isotropic. It is also at this point that Walpole's theory deviates from the bounds approach put forward by Hashin and Shtrikman. As discussed in Chapter 3, Walpole utilises the Green's function instead of the Fourier method employed by Hashin and Shtrikman.

The Green's function used by Walpole will be derived for clarity. This step is omitted in the original reference[122]. To calculate the Green's function one must

start with the displacements *u*, *v* and *w* as given by Love[132]. Under a unit force (*x'*, *y'*, *z'*) in the *x*-direction these are

$$u_1 = -\frac{\lambda+\mu}{8\pi\mu(\lambda+2\mu)}\left(\frac{\partial^2 r}{\partial x^2} - 2\frac{\lambda+2\mu}{\lambda+\mu}\frac{1}{r}\right)$$

$$v_1 = -\frac{\lambda+\mu}{8\pi\mu(\lambda+2\mu)}\frac{\partial^2 r}{\partial x \partial y} \qquad \text{where} \quad r = \sqrt{\sum_{i=1}^{3}(x_i - \xi_i)^2}$$

$$w_1 = -\frac{\lambda+\mu}{8\pi\mu(\lambda+2\mu)}\frac{\partial^2 r}{\partial x \partial z} \qquad \textbf{A3-32}$$

these can similarly be obtained for a unit force (x', y', z') in the *y* and *z* directions

$$u_2 = -\frac{\lambda+\mu}{8\pi\mu(\lambda+2\mu)}\frac{\partial^2 r}{\partial x \partial y}$$

$$v_2 = -\frac{\lambda+\mu}{8\pi\mu(\lambda+2\mu)}\left(\frac{\partial^2 r}{\partial y^2} - 2\frac{\lambda+2\mu}{\lambda+\mu}\frac{1}{r}\right) \qquad \textbf{A3-33}$$

$$w_2 = -\frac{\lambda+\mu}{8\pi\mu(\lambda+2\mu)}\frac{\partial^2 r}{\partial y \partial z}$$

$$u_3 = -\frac{\lambda+\mu}{8\pi\mu(\lambda+2\mu)}\frac{\partial^2 r}{\partial x \partial z}$$

$$v_3 = -\frac{\lambda+\mu}{8\pi\mu(\lambda+2\mu)}\frac{\partial^2 r}{\partial y \partial z} \qquad \textbf{A3-34}$$

$$w_3 = -\frac{\lambda+\mu}{8\pi\mu(\lambda+2\mu)}\left(\frac{\partial^2 r}{\partial z^2} - 2\frac{\lambda+2\mu}{\lambda+\mu}\frac{1}{r}\right)$$

the terms in A3-32, A3-33 and A3-34 can be combined giving

$$u = -\frac{\lambda+\mu}{8\pi\mu(\lambda+2\mu)}\left(-2\frac{\lambda+2\mu}{\lambda+\mu}\frac{1}{r}F_1 + \frac{\partial^2 r}{\partial x^2}F_1 + \frac{\partial^2 r}{\partial x \partial y}F_2 + \frac{\partial^2 r}{\partial x \partial z}F_3\right)$$

$$v = -\frac{\lambda+\mu}{8\pi\mu(\lambda+2\mu)}\left(-2\frac{\lambda+2\mu}{\lambda+\mu}\frac{1}{r}F_2 + \frac{\partial^2 r}{\partial x \partial y}F_1 + \frac{\partial^2 r}{\partial y^2}F_2 + \frac{\partial^2 r}{\partial y \partial z}F_3\right) \qquad \textbf{A3-35}$$

$$w = -\frac{\lambda+\mu}{8\pi\mu(\lambda+2\mu)}\left(-2\frac{\lambda+2\mu}{\lambda+\mu}\frac{1}{r}F_3 + \frac{\partial^2 r}{\partial x \partial z}F_1 + \frac{\partial^2 r}{\partial y \partial z}F_2 + \frac{\partial^2 r}{\partial z^2}F_3\right)$$

by manipulating the first term in each of the three equations in A3-35 a further generalisation can be reached

$$u_i = \frac{1}{4\pi\mu}\frac{1}{r}F_i - \frac{\lambda+\mu}{8\pi\mu(\lambda+2\mu)}\frac{\partial^2 r}{\partial x_i \partial x_j}F_j \qquad \textbf{A3-36}$$

This same form was found by Eshelby [159] and an alternative form was presented by Sokolnikoff [160]. The form of Sokolnikoff is shown below with proof that it is the same as that presented by Eshelby and Walpole.

The presentation by Sokolnikoff [160] is

$$u_i = \frac{\lambda+3\mu}{8\pi\mu(\lambda+2\mu)}\frac{F_i}{r} + \frac{\lambda+\mu}{8\pi\mu(\lambda+2\mu)}\frac{(x_i-\xi_i)(x_j-\xi_j)}{r^3}F_j \qquad \textbf{A3-37}$$

It can be proven that these two forms are in fact the same since

$$\frac{\partial r}{\partial x_i} = \frac{\partial}{\partial x_i}\sqrt{(x_k-\xi_k)(x_k-\xi_k)} = \frac{(x_i-\xi_i)}{\sqrt{(x_k-\xi_k)(x_k-\xi_k)}} = \frac{(x_i-\xi_i)}{r}$$
$$\frac{\partial^2 r}{\partial x_i \partial x_j} = \frac{\partial}{\partial x_j}\frac{\partial r}{\partial x_i} = \frac{\delta_{ij}}{r} - \frac{(x_i-\xi_i)(x_j-\xi_j)}{r^3} \qquad \textbf{A3-38}$$

Then reverting to the Eshelby and Walpole presentation and introducing the terms expressed in A3-36 one finds

$$\begin{aligned}
u_i &= \frac{1}{4\pi\mu}\frac{1}{r}F_i - \frac{\lambda+\mu}{8\pi\mu(\lambda+2\mu)}\frac{\partial^2 r}{\partial x_i \partial x_j}F_j \\
&= \frac{1}{4\pi\mu}\frac{1}{r}F_i - \frac{\lambda+\mu}{8\pi\mu(\lambda+2\mu)}\left(\frac{\delta_{ij}}{r} - \frac{(x_i-\xi_i)(x_j-\xi_j)}{r^3}\right)F_j \\
&= \frac{1}{4\pi\mu}\frac{1}{r}F_i - \frac{\lambda+\mu}{8\pi\mu(\lambda+2\mu)}\frac{1}{r}F_i + \frac{\lambda+\mu}{8\pi\mu(\lambda+2\mu)}\frac{(x_i-\xi_i)(x_j-\xi_j)}{r^3}F_j \\
&= \frac{1}{8\pi\mu}\left(2 - \frac{\lambda+\mu}{\lambda+2\mu}\right)\frac{1}{r}F_i + \frac{\lambda+\mu}{8\pi\mu(\lambda+2\mu)}\frac{(x_i-\xi_i)(x_j-\xi_j)}{r^3}F_j \\
&= \frac{\lambda+3\mu}{8\pi\mu(\lambda+2\mu)}\frac{1}{r}F_i + \frac{\lambda+\mu}{8\pi\mu(\lambda+2\mu)}\frac{(x_i-\xi_i)(x_j-\xi_j)}{r^3}F_j
\end{aligned} \qquad \textbf{A3-39}$$

The final term is then the same as that given by Sokolnikoff.

Pursuing with Walpole's theory, the displacement given in A3-36 can be used to give the Green's function as used by Walpole

$$G_{il} = \frac{1}{4\pi\mu_0}\frac{\delta_{il}}{r} - \frac{(\lambda_0+\mu_0)}{8\pi\mu_0(\lambda_0+2\mu_0)}\frac{\partial^2 r}{\partial x_i \partial x_l} \qquad \textbf{A3-40}$$

where κ_0 and μ_0 are the comparison material bulk and shear modulus respectively.

To obtain the strain field ε_{ij} one must revert to A3-31 and differentiate

$$u^{\dagger}_{i,j}(x) = \frac{\partial}{\partial x_j}\left(-\int_V \frac{\partial G_{il}}{\partial \xi_k}\tau_{lk}dV\right) = -\int_V \frac{\partial^2 G_{il}}{\partial x_j \partial \xi_k}\tau_{lk}dV \qquad \textbf{A3-41}$$

applying A3-40 to the right hand side of A3-41

$$\frac{\partial^2 G_{il}}{\partial x_j \partial \xi_k} = \frac{\delta_{il}}{4\pi\mu}\frac{\partial^2}{\partial x_j \partial \xi_k}\left(\frac{1}{r}\right) - \frac{(\lambda+\mu)}{8\pi\mu(\lambda+2\mu)}\frac{\partial^4 r}{\partial x_i \partial x_j \partial \xi_k \partial x_l} \qquad \textbf{A3-42}$$

$$= -\frac{\delta_{il}}{4\pi\mu}\frac{\partial^2}{\partial x_j \partial x_k}\left(\frac{1}{r}\right) + \frac{(\lambda+\mu)}{8\pi\mu(\lambda+2\mu)}\frac{\partial^4 r}{\partial x_i \partial x_j \partial x_k \partial x_l} \qquad \textbf{A3-43}$$

$$u^{\dagger}_{i,j}(x) = -\int_V \left(-\frac{\delta_{il}}{4\pi\mu}\frac{\partial^2}{\partial x_j \partial x_k}\left(\frac{1}{r}\right) + \frac{(\lambda+\mu)}{8\pi\mu(\lambda+2\mu)}\frac{\partial^4 r}{\partial x_i \partial x_j \partial x_k \partial x_l}\right)\tau_{kl}dV \qquad \textbf{A3-44}$$

$$= \int_V \left(\frac{\delta_{il}}{4\pi\mu}\frac{\partial^2}{\partial x_j \partial x_k}\left(\frac{1}{r}\right) - \frac{(\lambda+\mu)}{8\pi\mu(\lambda+2\mu)}\frac{\partial^4 r}{\partial x_i \partial x_j \partial x_k \partial x_l}\right)\tau_{kl}dV \qquad \textbf{A3-45}$$

the strain field is then

$$\varepsilon^{\dagger}_{ij} = \frac{1}{2}\left(u^{\dagger}_{i,j}(x) + u^{\dagger}_{j,i}(x)\right) \qquad \textbf{A3-46}$$

Applying A3-45 with the above

$$= \frac{1}{8\pi\mu}\int_V \left(\delta_{il}\frac{\partial^2}{\partial x_j \partial x_k}\left(\frac{1}{r}\right) + \delta_{jl}\frac{\partial^2}{\partial x_i \partial x_k}\left(\frac{1}{r}\right) - \frac{(\lambda+\mu)}{(\lambda+2\mu)}\frac{\partial^4 r}{\partial x_i \partial x_j \partial x_k \partial x_l}\right)\tau_{kl}dV \qquad \textbf{A3-47}$$

$$= \frac{1}{8\pi\mu}\int_V \left(\tau_{ik}\frac{\partial^2}{\partial x_j \partial x_k}\left(\frac{1}{r}\right) + \tau_{jk}\frac{\partial^2}{\partial x_i \partial x_k}\left(\frac{1}{r}\right) - \frac{(\lambda+\mu)\tau_{kl}}{(\lambda+2\mu)}\frac{\partial^4 r}{\partial x_i \partial x_j \partial x_k \partial x_l}\right)dV \qquad \textbf{A3-48}$$

$$= -\frac{1}{2\mu}\left(\tau_{ik}\frac{\partial^2}{\partial x_j \partial x_k} + \tau_{jk}\frac{\partial^2}{\partial x_i \partial x_k}\right)\left(-\frac{1}{4\pi}\int_V \frac{dV}{r}\right) + \frac{(\lambda+\mu)}{\mu(\lambda+2\mu)}\tau_{kl}\frac{\partial^4}{\partial x_i \partial x_j \partial x_k \partial x_l}\left(-\frac{1}{8\pi}\int_V r dV\right) \qquad \textbf{A3-49}$$

Simplifying the integral terms A3-49 becomes

$$\varepsilon^{\dagger}_{ij} = -\frac{1}{2\mu}\left(\tau_{ik}\phi_{,jk} + \tau_{jk}\phi_{,ik}\right) + \frac{(\lambda+\mu)}{\mu(\lambda+2\mu)}\tau_{kl}\psi_{,ijkl} \qquad \textbf{A3-50}$$

where

$$\phi_{,jk} = -\frac{1}{4\pi}\int_V \frac{dV}{r} \qquad \textbf{A3-51}$$

$$\psi_{,ijkl} = -\frac{1}{8\pi}\int_V r dV \qquad \textbf{A3-52}$$

these are the harmonic and biharmonic potential respectively shown by MacMillan[161]. These have the properties

$$\nabla^4 \psi^r = \nabla^2 \phi^r = \delta_{rs} \qquad \textbf{A3-53}$$

inside V_s

The proof of this is not supplied by Walpole but is provided here

$$\nabla^2 \psi = \psi_{,ii} = \nabla^2 \left(-\frac{1}{8\pi} \int_V r dV \right) \qquad \textbf{A3-54}$$

$$= \frac{\partial^2}{\partial x_i \partial x_i'} \left(-\frac{1}{8\pi} \int_V r dV \right) \qquad \textbf{A3-55}$$

$$= -\frac{1}{8\pi} \int_V \frac{\partial^2 r}{\partial x_i \partial x_i} dV \qquad \textbf{A3-56}$$

$$= -\frac{1}{8\pi} \int_V \frac{2}{r} dV = \phi \qquad \textbf{A3-57}$$

then

$$\nabla^2 \phi = \phi_{,ii} = \delta_{rs} \qquad \textbf{A3-58}$$

Now the strain field calculation in A3-50 can be rewritten using the relationship $\lambda = \kappa - \frac{2}{3}\mu$ and adding the image strain ε^I as stipulated in A3-26 giving

$$\varepsilon_{ij} = \frac{\kappa_0 + \frac{1}{3}\mu_0}{\mu_0 \left(\kappa_0 + \frac{4}{3}\mu_0 \right)} \left(\sum \tau_{kl}^r \psi_{,ijkl}^r \right) - \frac{1}{2\mu_0} \sum \left(\tau_{ik}^r \phi_{,kj}^r + \tau_{jk}^r \phi_{,ki}^r \right) + \varepsilon_{ij}^I \qquad \textbf{A3-59}$$

similar to this the stress field σ can also be presented. To obtain the stress field one must start with the basic formulation

$$\sigma = C_0 (\eta + \varepsilon) = C_0 \left(\eta + \varepsilon^\dagger + \varepsilon^I \right) = \sigma^\dagger + \sigma^I \qquad \textbf{A3-60}$$

where $\sigma^I = C_0 \varepsilon^I$ and $\sigma^\dagger = C_0 \left(\eta + \varepsilon^\dagger \right)$

taking $\sigma^\dagger$

$$\left(\sigma_{ij}^\dagger \right)^s = 2\mu_0 \left(\eta_{ij}^s + \left(\varepsilon_{ij}^\dagger \right)^s \right) + \left(\kappa_0 - \frac{2}{3}\mu_0 \right) \delta_{ij} \left(\eta_{kk}^s + \left(\varepsilon_{kk}^\dagger \right)^s \right) \qquad \textbf{A3-61}$$

By manipulating the equation and adding the image stress we arrive at

$$\sigma_{ij}=\frac{2\mu_0\left(\kappa_0-\frac{2}{3}\mu_0\right)}{\left(\kappa_0+\frac{4}{3}\mu_0\right)}\left(\underline{\frac{1}{2\mu_0}\left(\left(\kappa_0+\frac{4}{3}\mu_0\right)\eta^s_{kk}-\left(\kappa_0-\frac{2}{3}\mu_0\right)\sum\eta^r_{kk}\right)}\delta_{ij}-\delta_{ij}\sum\eta^r_{kl}\phi^r_{,kl}-\sum\eta^r_{kk}\phi^r_{,ij}\right)$$

$$+2\mu_0\left(\eta^s_{ij}-\sum\left(\eta^r_{ik}\phi^r_{,jk}+\eta^r_{jk}\phi^r_{,ik}\right)\right)+\frac{4\mu_0\left(\kappa_0+\frac{1}{3}\mu_0\right)}{\left(\kappa_0+\frac{4}{3}\mu_0\right)}\sum\eta^r_{kl}\psi^r_{,ijkl}+\sigma^I_{ij}$$

A3-62

There appears to be a disagreement here with Walpole's calculation regarding the underlined term (η_{kk}) in A3-62. This is seen in the final result in above, however, the term is dropped later on so it may be an unexplained abbreviation used by Walpole.

$$\sigma_{ij}=\frac{2\mu_0\left(\kappa_0-\frac{2}{3}\mu_0\right)}{\left(\kappa_0+\frac{4}{3}\mu_0\right)}\left[\underline{\eta_{kk}}\delta_{ij}-\left(\sum\eta^r_{kl}\phi^r_{,kl}\right)\delta_{ij}-\left(\sum\eta^r_{kk}\phi^r_{,ij}\right)\right]$$

$$+2\mu_0\left[\eta_{ij}-\sum\left(\eta^r_{ik}\phi^r_{,jk}+\eta^r_{jk}\phi^r_{,ik}\right)\right]+\frac{4\mu_0\left(\kappa_0+\frac{1}{3}\mu_0\right)}{\left(\kappa_0+\frac{4}{3}\mu_0\right)}\left(\sum\eta^r_{kl}\psi^r_{,ijkl}\right)+\sigma^I_{ij}$$

A3-63

The average fields required in A3-23 may now be evaluated. Following the strain formation, firstly assume that the average of $\psi^r_{,ijkl}$ over V_s can be noted as $\left\{\psi^r_{,ijkl}\right\}_s$. Ψ^r is distributed in an isotropic and uniform manner; hence the average value of $\left\{\psi^r_{,ijkl}\right\}_s$ must be a fourth order isotropic tensor, symmetric with any change of the subscripts. Using A3-53 the isotropic tensor is determined as:

$$\left\{\psi^r_{,ijkl}\right\}_s=\frac{1}{15}\delta_{rs}\left(\delta_{ij}\delta_{kl}+\delta_{ik}\delta_{jl}+\delta_{il}\delta_{jk}\right)$$ **A3-64**

and similarly

$$\left\{\phi^r_{,ij}\right\}_s=\frac{1}{3}\delta_{rs}\delta_{ij}$$ **A3-65**

Substitution of A3-64, A3-65 and A3-32 into A3-59 gives

$$\bar{\varepsilon}_r=-P_0\tau^r+\varepsilon^I=P_0\left(C_0-C_r\right)\bar{\varepsilon}_r+\varepsilon^I$$ **A3-66**

where $P_o^{-1}=C_0^*+C_0$

C_0* is referred to as the 'overall constraint tensor' by Walpole and is defined as

$$C_0{}^*{}_{ijkl} = \kappa_o^* \delta_{ij}\delta_{kl} + \mu_0^* \left(\delta_{ik}\delta_{jl} + \delta_{il}\delta_{jk} - \frac{2}{3}\delta_{ij}\delta_{kl} \right) \quad \textbf{A3-67}$$

where $\mu_0{}^*$ and $\kappa_0{}^*$ are the comparison material overall constraint shear and bulk moduli respectively, given by

$$\mu_0^* = \frac{3}{2}\left(\frac{1}{\mu_0} + \frac{10}{9\kappa_0 + 8\mu_0} \right)^{-1} \quad \textbf{A3-68}$$

$$\kappa_0^* = \frac{4}{3}\mu_0 \quad \textbf{A3-69}$$

For simplification of A3-67 the terms *I* and *J* can be introduced

$$\delta_{ij}\delta_{kl} = J \quad \textbf{A3-70}$$

$$\delta_{ik}\delta_{jl} + \delta_{il}\delta_{jk} = I \quad \textbf{A3-71}$$

where *I* is as in A3-21 and

$$J = \begin{bmatrix} 1 & 1 & 1 & 0 & 0 & 0 \\ 1 & 1 & 1 & 0 & 0 & 0 \\ 1 & 1 & 1 & 0 & 0 & 0 \\ 0 & 0 & 0 & 0 & 0 & 0 \\ 0 & 0 & 0 & 0 & 0 & 0 \\ 0 & 0 & 0 & 0 & 0 & 0 \end{bmatrix} \quad \textbf{A3-72}$$

Progressing, A3-66 can be expressed as

$$\overline{\varepsilon}_r = A_r \varepsilon^I \quad \textbf{A3-73}$$

where

$$A_r = \left[I + P_0 \left(C_r - C_0 \right) \right]^{-1} \quad \textbf{A3-74}$$

the formulation of A_r may then be manipulated to give

$$\left(C_0^* + C_r \right) A_r = \left(C_0^* + C_0 \right) \quad \textbf{A3-75}$$

From A3-20, $\overline{\varepsilon}_r = \overline{A}_r \overline{\varepsilon}$, where $\sum c_r \overline{A}_r = I$. Therefore $\overline{\varepsilon}_r$ this may be rewritten as:

$$\overline{\varepsilon}_r = A_r \varepsilon^I = A_r \left(\sum c_r A_r \right)^{-1} \overline{\varepsilon} \quad \textbf{A3-76}$$

Substitution of the image strain in A3-76 into A3-73 allows the concentration factor A_r to be calculated and from this, the effective compliance matrix $\overline{C}$ can be obtained. The final usable form to obtain $\overline{C}$ is created by the following mathematical manipulation

$$\bar{C} = \sum c_r C_r A_r \left(\sum c_r A_r \right)^{-1} \quad \textbf{A3-77}$$

$$\bar{C} = \sum c_r \left(C_0^* + C_r \right) A_r \left(\sum c_r A_r \right)^{-1} - \sum c_r C_0^* A_r \left(\sum c_r A_r \right)^{-1} \quad \textbf{A3-78}$$

$$\bar{C} = \sum c_r \left(C_0^* + C_0 \right) \left(\sum c_r A_r \right)^{-1} - C_0^* \quad \textbf{A3-79}$$

$$\bar{C} = \left(C_0^* + C_r \right) A_r \left(\sum c_r A_r \right)^{-1} - C_0^* \quad \textbf{A3-80}$$

$$\bar{C} = \left(C_0^* + C_r \right)^{-1} \sum c_r \left(C_0^* + C_r \right) \bar{A}_r - C_0^* = \bar{A}_r - C_0^* \quad \textbf{A3-81}$$

$$\sum c_r \bar{C} = \sum \left(c_r \left(C_0^* + C_r \right)^{-1} \sum c_r \left(C_0^* + C_r \right) \bar{A}_r \right) - \sum c_r C_0^* = \sum c_r \bar{A}_r - \sum c_r C_0^* \quad \textbf{A3-82}$$

$$\sum c_r \bar{C} = \left(\sum c_r \left(C_0^* + C_r \right)^{-1} \right) \left(\sum c_r \left(C_0^* + C_r \right) \bar{A}_r \right) - \sum c_r C_0^* = I - \sum c_r C_0^* \quad \textbf{A3-83}$$

$$\left(\sum c_r \right) \bar{C} = \sum c_r \left(C_0^* + C_r \right) \bar{A}_r - \sum c_r C_0^* = \left(\sum c_r \left(C_0^* + C_r \right)^{-1} \right)^{-1} - \left(\sum c_r \right) C_0^* \quad \textbf{A3-84}$$

$$\bar{C} = \left(\sum c_r \left(C_0^* + C_r \right)^{-1} \right)^{-1} - C_0^* \quad \textbf{A3-85}$$

Equation A3-85 is now sufficient to obtain bounds on the elastic properties of a composite material following the theorems set out by Walpole A3-24

Denote $\bar{C}$ as $\bar{C}^p$ when $\left(C_0 - C_r \right)$ is positive semi definite for all *r*. The theorem says that $\left(\bar{C}^p - C \right)$ is also positive semi definite, i.e. $\bar{\varepsilon} \bar{C}^p \bar{\varepsilon} \geq \bar{\varepsilon} C \bar{\varepsilon}$.

Denote $\bar{C}$ as $\bar{C}^n$ when $\left(C_0 - C_r \right)$ is negative semi definite for all *r*. The theorem says that $\left(\bar{C}^p - C \right)$ is also negative semi definite, i.e. $\bar{\varepsilon} \bar{C}^n \bar{\varepsilon} \leq \bar{\varepsilon} C \bar{\varepsilon}$.

Thus, $\bar{\varepsilon} \bar{C}^n \bar{\varepsilon} \leq \bar{\varepsilon} C \bar{\varepsilon} \leq \bar{\varepsilon} \bar{C}^p \bar{\varepsilon}$